Development of the Quantum Lattice Boltzmann method for simulation of quantum electrodynamics with applications to graphene

Denis Lapitski

St Anne's College

University of Oxford

A thesis submitted for the degree of

Doctor of Philosophy

Michaelmas 2012

Acknowledgements

Foremost, I would like to thank my supervisor, Paul Dellar, for his guidance throughout this research project. Furthermore, I would like to thank Sauro Succi and Silvia Palpacelli for sharing their findings about errors in the multidimensional Quantum Lattice Boltzmann scheme, and thank Tim Reis for useful discussions on the hydrodynamic Lattice Boltzmann Method. Also, I must extend a warm thank you to my family, my friends, and my wonderful girlfriend, Alena, for their continued support and encouragement.

Abstract

Development of the Quantum Lattice Boltzmann method for simulation of quantum electrodynamics with applications to graphene

Denis Lapitski
St. Anne's College
DPhil, Applied Mathematics
Michaelmas Term 2012

We investigate the simulations of the the Schrödinger equation using the one-dimensional quantum lattice Boltzmann (QLB) scheme and the irregular behaviour of solution. We isolate error due to approximation of the Schrödinger solution with the non-relativistic limit of the Dirac equation and numerical error in solving the Dirac equation. Detailed analysis of the original scheme showed it to be first order accurate. By discretizing the Dirac equation consistently on both sides we derive a second order accurate QLB scheme with the same evolution algorithm as the original and requiring only a one-time unitary transformation of the initial conditions and final output. We show that initializing the scheme in a way that is consistent with the non-relativistic limit supresses the oscillations around the Schrödinger solution. However, we find the QLB scheme better suited to simulation of relativistic quantum systems governed by the Dirac equation and apply it to the Klein paradox. We reproduce the quantum tunnelling results of previous research and show second order convergence to the theoretical wave packet transmission probability. After identifying and correcting the error in the multidimensional extension of the original QLB scheme that produced asymmetric solutions, we expand our second order QLB scheme to multiple dimensions. Next we use the QLB scheme to simulate Klein tunnelling of massless charge carriers in graphene, compare with theoretical solutions and study the dependence of charge transmission on the incidence angle, wave packet and potential barrier shape. To do this we derive a representation of the Dirac-like equation governing charge carriers in graphene for the one-dimensional QLB scheme, and derive a two-dimensional second order graphene QLB scheme for more accurate simulation of wave packets. We demonstrate charge confinement in a graphene device using a configuration of multiple smooth potential barriers, thereby achieving a high ratio of on/off current with potential application in graphene field effect transistors for logic devices. To allow simulation in magnetic or pseudo-magnetic fields created by deformation of graphene, we expand the scheme to include vector potentials. In addition, we derive QLB schemes for bilayer graphene and the non-linear Dirac equation governing Bose-Einstein condensates in hexagonal optical lattices.

Chapter 2

In subsection 2.1.3, the eigenvector and eigenvalue calculations on page 26 were first performed by P. Dellar, not including the power series expansion of error in equations 2.32-2.36. Some of the results in this subsection were subsequently found to be in a paper by Strauch (2007)[1] *on the apparently unrelated topic of discrete time quantum walks. In subsection 2.2.1 and 2.2.5 the discretization calculations were first performed by P. Dellar. Figure 2.7 generated by P. Dellar using his computations.*

Chapter 3

In subsection 3.1.2 the use of initial wave packets composed as superpositions of plane waves was suggested by P. Dellar, and calculation of the integral expression for transmission coefficient in equations 3.18-3.19 was done by P. Dellar.

Chapter 5

In section 5.4, calculation of the transmission coefficient by integration of Fourier mods to exclude wave numbers that produce evanescent waves as described at the bottom of page 117 was suggested by P. Dellar. Figure 5.8 uses data from computations performed by P. Dellar.

Chapter 7

In section 7.1, use of decoupled two-component form as in equation 7.2 in the derivation was suggested by P. Dellar. After the NLDE QLB was derived, P. Dellar's independent implementation based on the graphene QLB algorithm first established second order convergence.

[1] Strauch, F. W., Relativistic effects and rigorous limits for discrete- and continuous-time quantum walks, *J. Math. Phys.* **48**, 082102 (2007)

Contents

List of Figures

Chapter 1

Introduction

The subject of my research is a new numerical method for simulation of relativistic quantum systems called the quantum lattice Boltzmann method, its development and application. It was first proposed in 1993 by Succi and Benzi [101], and is based on the lattice Boltzmann method for fluid simulation, which is also a relatively new addition to the field of computational fluid dynamics itself and is being successfully used in both academic and commercial applications as an alternative to numerical solutions of the Navier-Stokes equations. This 'predecessor' is also the source of the name of the scheme we are considering - 'Quantum Lattice Boltzmann' was named after a method that solves the Boltzmann equation, and technically it should be called the 'Quantum Lattice Dirac' or the 'Lattice Dirac Method' since we are solving the Dirac equation, but the original name has stuck and we shall continue with it. After much more recent further research by Succi and Palpacelli [78, 79] the quantum lattice Boltzmann method was shown to follow the evolution of non-relativistic quantum systems governed by the Schrödinger equation, but was still left in its development stages, lacked definite measures of its rate of convergence, and, as was later discovered, had problems preserving spherical symmetry in its three-dimensional form. Nevertheless, it was shown to have a lot of potential for efficient and accurate numerical simulation of relativistic quantum systems as an explicit scheme exhibiting unitary evolution, unconditional stability, linear scaling of the time step with the mesh spacing, and a natural amenability to parallel processing. As we will show, unlike finite difference and finite element schemes for the Dirac equation, the quantum lattice Boltzmann scheme also does not suffer from the fermion doubling problem and can serve as an alternative to the spectral methods currently used for numerical solutions of the Dirac equation.

This research was first motivated by reported unusual errors in the quantum lattice Boltzmann scheme applied to simulating Schrödinger equation, after investigating them we found that applying the scheme to simulation of quantum electrodynamics systems governed by the Dirac equation directly would be a more fruitful approach, and it will be the focus of the work presented. We start with a general description of the lattice Boltzmann method (LBM) for hydrodynamics and its development in this first chapter, moving on to the quantum lattice Boltzmann (QLB) as originally derived in the second section, drawing parallels to source of inspiration for the original idea in the lattice Boltzmann method. Chapter two describes our error analysis of the existing QLB method in one dimension, showing it to be generally first order accurate and isolating two sources of error in comparison with the Schrödinger equation solutions. We present our modification of the underlying discretization for the scheme that improves global accuracy in solving the Dirac equation to second order, show the scheme to be free from the fermion doubling problem, and explore a new initialization set up that is more appropriate for simulating non-relativistic systems and suppresses the large oscillations around the Schrödinger solution. Since the QLB scheme is solving the Dirac equation and not the Schrödinger equation, we find it more suitable for application to quantum systems governed by the Dirac equation and therefore, we test the second order QLB scheme in chapter three by simulating a relativistic quantum tunnelling system and the Klein paradox in one dimension. We show it to correctly reproduce the unusual relativistic tunnelling behaviour and investigate the simulation of Zitterbewegung oscillations, which are also only present in Dirac equation solutions, and show the scheme to simulate them accurately by comparing with theoretical wave packet tunnelling calculations.

The fourth chapter discusses the extension of the QLB to multiple dimensions. We recover the isotropy of the scheme by correcting a mistake in the previous derivation, and make the required modification to maintain the second order of convergence we obtained in the one-dimensional version, as well as correct transformation between the QLB and the standard components of the Dirac wave function. In chapter five we apply the QLB scheme to graphene - a new purely two-dimensional material with interesting electronic and physical properties and remarkable potential for application in technology. We first use our one-dimensional QLB scheme to simulate two dimensional Klein tunnelling dynamics in graphene, made possible by the zero effective mass of graphene's charge carriers and a transformation of the equation governing them.

Moving forward, we adapt the two-dimensional QLB scheme to solve the Dirac-like equation governing charge carriers at low energies in graphene and study the transmission through a potential barrier by 'Klein tunnelling' in graphene, investigating the effects of angles of incidence on the transmission coefficient for wave packets. We also expand the graphene QLB scheme to simulate systems with non-zero magnetic fields by incorporating the effects of the vector potential terms and confirm the accuracy and convergence of the solutions. In chapter six we propose and simulate a potential configuration that would allow charge confinement in unmodified monolayer graphene designed to block the flow of current in a graphene device. This would allow for a large ratio of on/off current for the possible application of monolayer graphene in high frequency field effect transistors. Chapter seven extends the scheme to the nonlinear Dirac equation governing Bose-Einstein condensates in graphene-like hexagonal optical lattices. The last chapter summarizes the main results of the completed work and outlines the directions for possible further research with the quantum lattice Boltzmann method.

1.1 Lattice Boltzmann method for fluid simulation

The lattice Boltzmann method is an alternative approach to fluid simulation that is different from classical CFD solvers in several ways. The most significant difference is in the fact that it is a bottom-up approach based on models of molecular interactions in the fluid, and as such, it already contains much of the underlying physics of the fluid built into the model [19, 20]. Instead of the macroscopic quantities of density, momentum and energy that numerical calculations based on the Navier-Stokes PDEs aim to approximate, LBM solves for a set of particle distribution functions with different velocities in the fluid. The macroscopic variables are then given as moments of the distribution functions. In its discretization of the Boltzmann equation, LBM is concerned with the values of the distribution functions at lattice cites, given by the space-discretizing grid, instead of average values of a macroscopic variable over a cell. Because of the lattice structure of the discretized domain, the scheme is well suited to deal with complex geometries. It is simple in its numerical algorithms, and can easily take advantage of parallel computing in its numerical implementation due to the local nature of simulated particle collisions at each lattice cite - the evolution of the

distribution function values in a particular region depends only on the surrounding lattice sites.

The starting point of the lattice Boltzmann method, the Boltzmann equation, is derived from kinetic theory by statistically averaging the motion and interaction of molecules into single-particle distribution functions $f(\boldsymbol{x}, \boldsymbol{v}, t)$ [50, 68]. Each distribution function f corresponds to the probability of finding a molecule with velocity $\boldsymbol{v}$, around position $\boldsymbol{x}$, at time t. Assuming no external forces on the fluid, the Boltzmann equation can be written as follows,

$$\partial_t f + \boldsymbol{v} \cdot \nabla f = C[f, f], \tag{1.1}$$

where $C[f, f]$ is a complex collision operator governing the interaction of distribution functions. The macroscopic quantities of the fluid flow are given as moments of the distribution functions,

$$\rho(\boldsymbol{x}, t) = \int f(\boldsymbol{x}, \boldsymbol{v}, t)\, d\boldsymbol{v}, \tag{1.2a}$$

$$\boldsymbol{u}(\boldsymbol{x}, t) = \frac{1}{\rho(\boldsymbol{x}, t)} \int f(\boldsymbol{x}, \boldsymbol{v}, t)\, \boldsymbol{v} d\boldsymbol{v}, \tag{1.2b}$$

$$\theta(\boldsymbol{x}, t) = \frac{1}{3\rho(\boldsymbol{x}, t)} \int f(\boldsymbol{x}, \boldsymbol{v}, t)\, (\boldsymbol{v} - \boldsymbol{u})^2\, d\boldsymbol{v}, \tag{1.2c}$$

and are conserved by the collision operator $C[f, f]$. The effect of the collision operator is to bring the distribution functions f closer towards the Maxwell-Boltzmann equilibrium distribution that is given by

$$f^{eq}(\boldsymbol{v}) = \frac{\rho}{(2\pi\theta)^{3/2}} e^{\frac{-(\boldsymbol{v}-\boldsymbol{u})^2}{2\theta}}, \tag{1.3}$$

where θ is the temperature and $\boldsymbol{u}$ is the mean velocity of the fluid. The Maxwell-Boltzmann distribution is such that it maximizes the entropy of the system, as derived by Boltzmann, and given by the H-functional,

$$H(t) = -\int f \ln f d\boldsymbol{v}. \tag{1.4}$$

In general the complex collision operator $C[f, f]$ is approximated by the simple Bhatnagar-Gross-Krook (BGK) collision operator [6] with a single relaxation time τ that was first proposed by Qian in his PhD thesis [83, 84], and is a function of the difference between the current distribution function and the equilibrium distribution

function. It simplified the computation of the particle collisions and equation manipulation while retaining the conservation properties of the collisions. With the BGK collision operator the Boltzmann equation becomes

$$\partial_t f + \boldsymbol{v} \cdot \nabla f = \frac{1}{\tau} \left(f^{eq} - f \right), \tag{1.5}$$

where the relaxation time τ is dependent on the distribution function and governed by the viscosity of the fluid. This relaxation to the equilibrium distribution maintains mass and momentum conservation, and the Navier-Stokes hydrodynamics can be recovered through application of the Chapman-Enskog expansion to the Boltzmann equation in this form [19, 106], which we will come back to below.

The next step towards the lattice Boltzmann equation is the discretization of time, position, and phase (velocity) space. We define a finite number of velocities $\boldsymbol{v}_i$, $i = 0, ..., n$, that will allows the method to accurately reproduce macroscopic fluid behaviour in continuous phase space. The density, macroscopic velocity, and temperature are now defined as sums over the finite set of distribution functions f_i for discrete of velocities instead of integrals,

$$\rho \left(\boldsymbol{x}, t \right) = \sum_{i=0}^{n} f_i \left(\boldsymbol{x}, t \right), \tag{1.6a}$$

$$\boldsymbol{u} \left(\boldsymbol{x}, t \right) = \frac{1}{\rho \left(\boldsymbol{x}, t \right)} \sum_{i=0}^{n} f_i \left(\boldsymbol{x}, t \right) \boldsymbol{v}_i, \tag{1.6b}$$

$$\theta \left(\boldsymbol{x}, t \right) = \frac{1}{3\rho \left(\boldsymbol{x}, t \right)} \sum_{i=0}^{n} f_i \left(\boldsymbol{x}, t \right) \left(\boldsymbol{v}_i - \boldsymbol{u} \right)^2, \tag{1.6c}$$

and the second moment

$$\Pi \left(\boldsymbol{x}, t \right) = \sum_{i=0}^{n} f_i \left(\boldsymbol{x}, t \right) \boldsymbol{v}_i \boldsymbol{v}_i \tag{1.7}$$

is the momentum flux, it is not conserved by the collisions.

The discrete Boltzmann-BGK equation then reads

$$\partial_t f_i + \boldsymbol{v}_i \cdot \nabla f_i = \frac{1}{\tau} \left(f_i^{eq} - f_i \right). \tag{1.8}$$

and the equilibrium distribution is defined separately for each discrete velocity,

$$f_i^{eq} = \omega_i \rho \left[1 + \frac{1}{\theta} \left(\boldsymbol{v}_i \cdot \boldsymbol{u} \right)^2 + \frac{1}{2\theta^2} \left(\boldsymbol{v}_i \cdot \boldsymbol{u} \right)^2 - \frac{1}{2\theta} |u|^2 \right], \tag{1.9}$$

where ω_i's are the weights of the discrete velocities that depend on their number and configuration. The f_i^{eq}'s are constructed such that the moments of this discrete equilibrium distribution also give the macroscopic variables,

$$\rho(\boldsymbol{x},t) = \sum_{i=0}^{n} f_i^{eq}(\boldsymbol{x},t), \tag{1.10a}$$

$$\boldsymbol{u}(\boldsymbol{x},t) = \frac{1}{\rho(\boldsymbol{x},t)} \sum_{i=0}^{n} f_i^{eq}(\boldsymbol{x},t)\,\boldsymbol{v}_i, \tag{1.10b}$$

$$\Pi(\boldsymbol{x},t) = \sum_{i=0}^{n} f_i^{eq}(\boldsymbol{x},\boldsymbol{v}_i,t)\,\boldsymbol{v}_i\boldsymbol{v}_i, \tag{1.10c}$$

like the Maxwell-Boltzmann equilibrium distribution. The temperature θ is assumed constant for simplicity – thermal LBM schemes require more complex collision operators [48, 100]. Note that the equilibrium distribution f_i^{eq} is a function of the distribution function $f_i(\boldsymbol{x},t)$ through the macroscopic velocity $\boldsymbol{u}$ and density ρ, and has to be recalculated at every timestep in the simulation, once we have discretized the time and space.

Particular phase space LBM discretizations are designated as $DaQb$-lattices, where a is the number of spatial dimensions in the model, and b is the number of discrete velocities defined. The choice of velocities and their number is not arbitrary, they must provide sufficient lattice symmetry to reproduce Navier-Stokes hydrodynamics. Often used lattice configurations are $D2Q9$ and $D3Q19$ (shown in Figure 1.1), as well as $D1Q5$, $D3Q15$, and $D3Q27$. For example, the equilibrium distribution weights ω_i for the $D2Q9$ two-dimensional square lattice are $\omega_0 = 16/36$ for zero velocity, $\omega_{1,2,3,4} = 4/36$ for the horizontal and vertical velocities (magnitude 1), and $\omega_{5,6,7,8} = 1/36$ for the diagonal velocities (magnitude $\sqrt{2}$); the weights for the $D3Q19$ lattice are 12/36, 2/36, and 1/36 for the velocities of magnitude 0,1, and $\sqrt{2}$ respectively [100].

As mentioned before, the Navier-Stokes hydrodynamics are derived by looking for slowly varying solutions of the discrete Boltzmann equation (1.8), similar to the continuous Boltzmann-BGK equation [19, 24]. The distributions f_i are written in terms of small deviations from the equilibrium distribution, expanding for small ϵ,

$$f_i = f_i^{eq} + \epsilon f_i^1 + \epsilon^2 f_i^2 + \mathcal{O}\left(\epsilon^3\right), \tag{1.11}$$

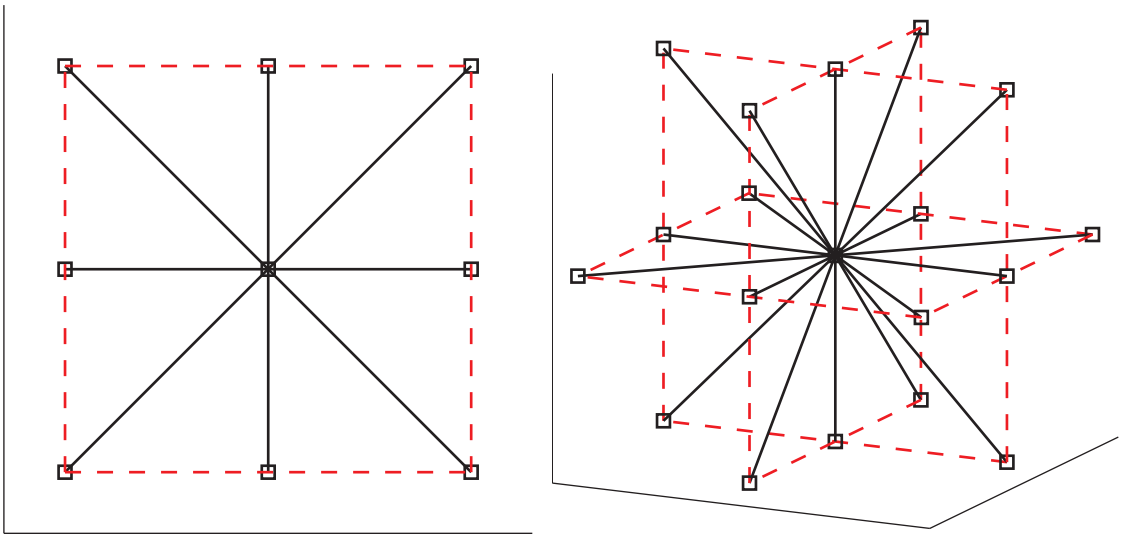

Figure 1.1: A diagram of a D2Q9 (left) and a D3Q19 (right) lattice, solid lines show direction of discrete velocities.

such that the corrections to the equilibrium in total do not contribute to the density and velocity moments,

$$\sum_{i=0}^{n} f_i^k(\boldsymbol{x},t) = 0, \qquad \sum_{i=0}^{n} f_i^k(\boldsymbol{x},t)\,\boldsymbol{v}_i = 0, \qquad k = 1,2,... \tag{1.12}$$

The Champan-Enskog multiscale expansion is applied to the derivatives

$$\frac{\partial}{\partial t} = \epsilon\frac{\partial}{\partial t_1} + \epsilon^2\frac{\partial}{\partial t_2}, \tag{1.13}$$

where the time scale t_2 is much slower that t_1. Then substituting the expansions into the discrete Boltzmann equation (1.8) and taking moments leads to Navier-Stokes equations.

A derivation of the lattice Boltzmann equation directly from the Boltzmann equation that we present below was not the original way of development of the LBM scheme, and has been derived recently [49, 2] to serve as another validation of LBM as a method for fluid simulation rigorously grounded in the physical laws of kinetic theory, but it is a more straightforward approach. To derive the lattice Boltzmann equation they start from the discrete Boltzmann equation with the BGK collision operator (1.8) and integrate along a characteristic on the left-hand side,

$$\int_0^{\Delta t} \frac{d}{ds}[f_i(\boldsymbol{x}+\boldsymbol{v}_i s, t+s)]ds = \int_0^{\Delta t} \frac{1}{\tau}\left(f_i^{eq}(\boldsymbol{x}+\boldsymbol{v}_i s, t+s) - f_i(\boldsymbol{x}+\boldsymbol{v}_i s, t+s)\right)ds, \tag{1.14}$$

and evaluate the right-hand side using the second order accurate trapezoidal rule,

$$f_i\left(\boldsymbol{x}+\boldsymbol{v}_i\Delta t, t+\Delta t\right)-f_i\left(\boldsymbol{x},t\right)=\frac{1}{2}\Delta t\left(C_i^{BGK}\left(\boldsymbol{x}+\boldsymbol{v}_i\Delta t, t+\Delta t\right)+C_i^{BGK}\left(\boldsymbol{x},t\right)\right), \tag{1.15}$$

where C_i^{BGK} is the BGK collision term,

$$C_i^{BGK}\left(\boldsymbol{x},t\right)=\frac{1}{\tau}\left(f_i^{eq}\left(\boldsymbol{x},t\right)-f_i\left(\boldsymbol{x},t\right)\right). \tag{1.16}$$

This gives us an implicit equation for the evolved distribution functions. Making a change of variables proposed by He, Chen and Doolen [48], we define a new probability density

$$\bar{f}_i\left(\boldsymbol{x},t\right)=f_i\left(\boldsymbol{x},t\right)-\frac{\Delta t}{2\tau}\left(f_i^{eq}\left(\boldsymbol{x},t\right)-f_i\left(\boldsymbol{x},t\right)\right) \tag{1.17}$$

and the implicit system (1.15) simplifies to the explicit lattice Boltzmann equation

$$\bar{f}_i\left(\boldsymbol{x}+\Delta x, t+\Delta t\right)-\bar{f}_i\left(\boldsymbol{x},t\right)=\frac{\Delta t}{\tau+\Delta t/2}\left(\bar{f}_i^{eq}\left(\boldsymbol{x},t\right)-\bar{f}_i\left(\boldsymbol{x},t\right)\right), \tag{1.18}$$

where Δx is the distance between neighboring lattice points and Δt is the size of the timesteps [24] and moments of the $\bar{f}_i$ distribution functions give the same macroscopic variables as moments of the original f_i, the collision term in (1.17) does not contribute anything to the moments because the collisions conserve mass and momentum. We can therefore replace the f_i's by $\bar{f}_i$'s completely to have an explicit set of equation evolving the probability densities at each lattice site.

Historically, however, LBM developed from another, more basic, approach to fluid simulation based on molecular interactions - lattice gas cellular automata (LGCA). It has been found that a very crude model of particle motion on a microscopic scale can reproduce realistic fluid behavior on a macroscopic scale [100], and the discovery generated a lot promise at the time. A particular model of this kind, the Frisch-Hasslache-Pomeau automaton [35], uses a regular hexagonal lattice with six possible velocities and is able to reproduce the Navier-Stokes dynamics. LGCA models the molecular interactions with discrete particles hopping from their current lattice cite to a neighboring cite along one of the discrete directions in a single streaming timestep, with only a single allowed magnitude of velocity and the same mass given to all particles [20]. No two particles are allowed to move along the same direction at the same time, and if two particles are streamed to the same lattice node in the same timestep, an collision takes place, scattering particles along different velocities while conserving total mass, given by the number of particles, and momentum.

Because LGCA requires no more than one particle to occupy each node, the state of the system is described with Boolean variables and the macroscopic fluid simulation is exact, free of round-off error. Another advantage of LGCA is the intrinsic parallelism of computation, because the collisions in one site of the domain are independent of the collisions in other parts of the fluid at any given time. However, LGCA suffers from several drawbacks, such as statistical noise, quickly growing complexity, and lack of Galilean invariance [100]. Once realized, these disadvantages slowed its further development and the efforts to overcome them have resulted in the development of the lattice Boltzmann method. The key difference in the LBM is the replacement of single particles occupying particular lattice nodes with distribution functions f_i. This removes statistical noise from the LGCA simulations, and introduces round-off error, but retains the locality of collisions and ability to easily adapt the scheme to parallel computation.

There have also been studies of the quantum version of the lattice gas automata (QLGA) to investigate their implementation on quantum computers [69, 70]. QLGA is constructed as a regular one dimensional lattice populated with left and right moving particles, with a complex probability amplitude at each lattice cite. Each cell moves along its designated velocity in the first half of the timestep, and interact in the second, collision, half of the timestep to determine new probability density. The collisions are unitary, so that the norm squared of the amplitude is preserved throughout the evolution [69]. The amplitudes of the left and right going particles can be used to represent two components of the one dimensional Dirac equation, with the evolution given by

$$\psi_{t+1}(x) = \begin{pmatrix} 0 & i\sin\theta \\ 0 & \cos\theta \end{pmatrix} \psi_t(x-1) + \begin{pmatrix} \cos\theta & 0 \\ i\sin\theta & 0 \end{pmatrix} \psi_t(x+1) \tag{1.19}$$

where $\tan\theta$ corresponds to the particle mass. This is a particular QLGA evolution that is equivalent to the Succi-Benzi QLB equation in one dimension [70], and is also equivalent to the one dimensional version of the Bialynicki-Birula's quantum cellular automata [7]. A closely related algoritm of a discrete time quantum walk is also equivalent to the one dimensional Dirac equation solved by the Succi-Benzi QLB [98]. Unlike a classical random walk, the 'coin flip' that decides whether the particle moves left or right does not have a single outcome, instead it is a superposition of states that evolves left going and a right going wave function components, resulting in a disperion proportional to t instead of $\sqrt{t}$ and matching the spreading of a wave packet

governed by the Dirac equation [97]. A different QLG model based on the many-body Schrödinger equation was proposed by Boghosian and Taylor [9], and shown to be capable of simulating any number of particles in three dimensions. However, it is impractical to implement on a classical computer for more than a few particles due to high complexity and computation cost. Full utility of these QLGA algorithms can be realized on a potential quantum computer.

A unitary quantum lattice gas algorithm was used by Yepez [110] to study quantum turbulence in Bose-Einstein condensates governed by the Gross-Pitaevskii equation, with three dimensional simulations on grids of up to 5760^3 lattice cites. The scheme evolves a two component wave function by alternating collision and streaming steps that transform the wave function components and shift along the three axis of the lattice similar to the QLB, with the two evolved components then used to recover the Gross-Pitaevskii and reconstruct the single-component wave function.

1.2 Numerical schemes for the Dirac equation

As we will show in the error analysis in the next chapter, the QLB scheme is not particularly well suited to solving the Schrödinger equation due to additional approximation errors, limits on the energy of the particle and the electric potentials of the system, and oscillating nature of the solution that is not characteristic to wave functions described by the Schrödinger equation. A detailed study of the quantum lattice Boltzmann scheme can only be done when thinking about it as a Dirac equation solver, and it is of more merit in this role, since numerical solutions of the Dirac equation are more demanding in terms of computational time and memory requirements due to high temporal resolution and multi-component solutions [71].

First attempts at numerical solution of the Dirac equation were done in nuclear physics to simulate heavy-ion collisions [4, 11]

Finite-difference and finite-element schemes for solving the Dirac equation suffer from the so-called fermion doubling problem, where the discretization of the spatial dimensions leads to more than one momentum value satisfying the discrete version of the expression for the energy of the particle [74, 10]. This can result in the solutions producing incorrect group velocities of the wave packet. There are however ways to transform the Dirac equation in such a way as to eliminate the double solutions [13], or using backward and forward differences to discretize the top and bottom components

of the wave functions can suppress fermion doubling [10]. As we will see in section 2.2.1, this approach of different discretization of the spatial derivatives is also part of the QLB method.

The currently widely used method for numerically solving the Dirac equation is based on the evolution of the wave function alternatively in position and momentum space for each timestep using the split operator technique [34, 32] and Fast Fourier Transforms to transform the wave function in each timestep [12]. Each of the spatial variables are discretized into N_x, N_y, N_z points and time is discretized into timesteps of size Δt. The Hamiltonian is split into two parts that are used to evolve the wave function one after another as follows,

$$\Psi\left(t+\Delta t\right)=\exp\left(-i\frac{1}{2}\Delta t H_r\right)\mathcal{F}^{-1}\exp\left(-i\Delta t H_k\right)\mathcal{F}\exp\left(-i\frac{1}{2}\Delta t H_r\right)\Psi\left(\Delta t\right)+\mathcal{O}\left(\Delta t^3\right), \tag{1.20}$$

where H_r and H_k are collections of the position-dependant and momentum-dependant terms of the Hamiltonain and $\mathcal{F}$ is the Fast Fourier Transform. In such a splitting of the noncommuting operators each timestep is third order accurate in Δt, resulting in second order global accuracy as many timesteps are accumulated in the evolution of the wave function. It is also possible to split the operators further, leading to a fifth order accuracy of each timestep, and the numerical efficiency of the two approaches are investigated by Braun et. al. [12]. We will use this spectral solution to confirm convergence of the QLB scheme throughout this work. It's application in one dimension is described in more detail in section 2.1.3, and in two dimensions in section 5.5.

The quantum lattice Boltzmann scheme is in a unique position among the two approaches to numerical solution of the Dirac equation, unlike other finite difference schemes it does not suffer from the fermion-doubling problem, as we will show in section 2.2.6, and unlike the spectral method it is well suited to take advantage of a parallel implementation due to the local nature of its collisions.

1.3 Original Quantum Lattice Boltzmann scheme

The lattice Boltzmann method for fluid simulation has been successfully adapted to numerous applications since its introduction as an alternative tool for fast and accurate computation of fluid behaviour [19, 100]. A more recent development, initially motivated by qualitative parallels between fluid mechanics and quantum mechanics,

was the adaptation of the lattice Boltzmann method to simulation of quantum phenomena [101]. As we will show below, the mathematical basis for the development of the quantum lattice Boltzmann (QLB) scheme by Succi and co-workers lies in the analogy that can be drawn between the relativistic Dirac equation and the discrete Boltzmann equation of kinetic theory [101, 99]. The original one dimensional QLB scheme aimed to simulate evolution of quantum systems governed to the Schrödinger equation, which can be derived as a non-relativistic limit of the Dirac equation, analogous to the Navier-Stokes equations being a slowly varying limit of the Boltzmann equation that is solved by the lattice Boltzmann method.

1.3.1 Boltzmann equation - Dirac equation parallels

The Dirac equation describes the evolution of a three-dimensional quadrispinor wave function that contains four complex components, $\Psi = [\psi_1, \psi_2, \psi_3, \psi_4]$, and is given by

$$i\hbar\frac{\partial}{\partial t}\Psi = \boldsymbol{H}\Psi \qquad \boldsymbol{H} = c\boldsymbol{\alpha}\cdot(\boldsymbol{p} - q\boldsymbol{A}) + \beta mc^2 + qV. \tag{1.21}$$

Derived by Paul Dirac in 1928 [27], it is a fundamental wave function equation that, unlike the Schrödinger equation, is consistent with the principles of relativity as well as quantum mechanics. In his derivation, Dirac realized that to get an equation first order in time and space that, when squared, would reproduce the relativistic expression for energy

$$E = \sqrt{p^2c^2 + m^2c^4} \qquad E = i\hbar\frac{\partial}{\partial t}, \tag{1.22}$$

the quantities $\alpha_{x,y,z}$ and β would have to satisfy relations that would allow the cross terms to cancel and squares of them be equal to identity [27],

$$\alpha_{x,y,z}^2 = \beta^2 = I \qquad \alpha_i\alpha_j + \alpha_j\alpha_i = 0 \qquad \alpha_i\beta + \beta\alpha_i = 0, \tag{1.23}$$

and to do this they have to be 4×4 matrices, therefore forcing the wave function Ψ to be made up of four components. The rest of the parameters in the Dirac equation are given as follows - $\boldsymbol{A}$ is the magnetic vector potential, V is the scalar potential, q is the modulus of the particle charge, c is the speed of light, and $\hbar$ is Planck's constant. For simplicity only zero magnetic vector potential was considered at this point, setting $\boldsymbol{A} = 0$ for simplicity. Writing out the momentum operator $\boldsymbol{p} = -i\hbar\boldsymbol{\nabla}$ and applying the Dirac Hamiltonian we get,

$$\left(\partial_t + c\alpha^x\partial_x + c\alpha^y\partial_y + c\alpha^z\partial_z + \frac{1}{\hbar}i\beta mc^2 + \frac{1}{\hbar}iqV\right)\Psi = 0. \tag{1.24}$$

The matrices $\alpha_{x,y,z}$ and β are given by

$$\alpha_i = \begin{pmatrix} 0 & \sigma_i \\ \sigma_i & 0 \end{pmatrix} \qquad \beta = \begin{pmatrix} I & 0 \\ 0 & -I \end{pmatrix}, \tag{1.25}$$

where I is the 2×2 identity matrix and σ_i's are the Pauli matrices [81] given by

$$\sigma_x = \begin{pmatrix} 0 & 1 \\ 1 & 0 \end{pmatrix} \qquad \sigma_y = \begin{pmatrix} 0 & -i \\ i & 0 \end{pmatrix} \qquad \sigma_z = \begin{pmatrix} 1 & 0 \\ 0 & -1 \end{pmatrix}, \tag{1.26}$$

that satisfy the commutation relation $[\sigma_i, \sigma_j] = 2i\epsilon_{ijk}\sigma^k$, where ϵ_{ijk} is the alternating Levi-Civita tensor [5].

The motivation for using the Dirac equation as a basis for a quantum lattice Boltzmann scheme may be seen by the similarity between the relativistic equation,

$$i\hbar\partial_t\Psi + i\hbar c^2\alpha \cdot \nabla\Psi = \beta mc^2\Psi + qV\Psi. \tag{1.27}$$

and the discrete Boltzmann equation with a matrix collision operator,

$$\partial_t f_i + \boldsymbol{\xi}_i \cdot \nabla f_i = \Omega_{ij}\left(f_j - f_j^{(\mathrm{eq})}\right). \tag{1.28}$$

The distribution functions f_i are analogous to the complex components ψ_i of the quadrispinor, the set of discrete velocities $\boldsymbol{\xi}_i$ is analogous to the set of streaming matrices $\alpha_{ij}^x, \beta_{ij}, -\alpha_{ij}^z$, and the collision matrix Ω_{ij} is analogous to the βmc^2 matrix on the right hand side of the Dirac equation. In addition, both equations contain only first derivatives in space and time, while the Navier–Stokes and Schrödinger equations (which can be derived as limits of the Boltzmann and Dirac equations respectively) both contain a mixture of first derivatives in time and first *and* second derivatives in space. The analogy is not as exact in three dimensions because it is not possible to simultaneously diagonalize all three $\boldsymbol{\alpha}^{x,y,z}$ matrices, and further details on how to overcome this are given in Chapter 4, but in one dimension it is possible to diagonalize one of the Dirac matrices to act as a streaming operator.

It is more convenient to use the form of the Dirac equation where the coefficients are all real, called the Majorana form, which we derive below. Expanding the momentum operator $\boldsymbol{p} = -i\hbar c\boldsymbol{\nabla}$, and dividing through by $i\hbar$ gives

$$\left(\partial_t + c\alpha_x\partial_x + c\alpha_y\partial_y + c\alpha_z\partial_z + \frac{1}{\hbar}i\beta mc^2 + \frac{1}{\hbar}iqV\right)\Psi = 0 \tag{1.29}$$

To eliminate the imaginary quantities α_y and $i\beta$ we perform a transformation of $\Psi' = U\Psi$, where

$$U = \frac{1}{\sqrt{2}}\left(\alpha_y + \beta\right) = U^{-1}. \tag{1.30}$$

The imaginary matrix α_y and the real matrix β are then interchanged, $\alpha'_x = U\alpha_x U = -\alpha_x$, $\alpha'_z = -\alpha_z$, and we get the Majorana form of the Dirac equation,

$$\left(\partial_t - c\alpha_x\partial_x + c\beta\partial_y - c\alpha_z\partial_z + i\omega_c\alpha_y - iqV/\hbar\right)\Psi' = 0, \tag{1.31}$$

where $\omega_c = mc^2/\hbar$ is the Compton frequency for a particle of mass m, and all the coefficients are real [5].

In one dimension, considering a free particle for simplicity at this point, we set $V = 0$ and the Dirac equation simplifies to

$$\partial_t u + c\partial_z u = \omega_c d, \tag{1.32a}$$

$$\partial_t d - c\partial_z d = -\omega_c u, \tag{1.32b}$$

where u and d are the two wave function components of the Dirac quadrispinor wave function $\Psi = [u_1, d_1, d_2, u_2]$ that are streaming in opposite directions along the z-axis with speeds $\pm c$, defined as the 'up' and 'down' components. There is no distinction between u_1 and u_2, or between d_1 and d_2 in one dimension, so we omit the spinorial indices to end up with a two component wave function.

1.3.2 Schrödinger equation as a limit of the Dirac equation

The Schrödinger equation can be derived from a non-relativistic limit of the Dirac equation in a similar way that the Navier–Stokes equations may be derived from the discrete Boltzmann equation (1.28). As the LBM (solving on the discrete Boltzmann equation) is used to simulate the Navier-Stokes hydrodynamics, so is the QLB (solving on the Dirac equation) was originally designed to simulate evolution of quantum systems according to the Schrödinger equation.

To begin the derivation we introduce a pair of transformed wave functions,

$$\Phi^+ = \frac{1}{\sqrt{2}}\left(u + id\right), \qquad \Phi^- = \frac{1}{\sqrt{2}}\left(u - id\right), \tag{1.33}$$

where Φ^+ is the symmetric and Φ^- the anti-symmetric mode [5]. Rewriting the one-dimensional Dirac equation (1.32) in these variables we get

$$\partial_t\Phi^+ + c\partial_z\Phi^- = -i\omega_c\Phi^+, \tag{1.34a}$$

$$\partial_t\Phi^- + c\partial_z\Phi^+ = i\omega_c\Phi^-. \tag{1.34b}$$

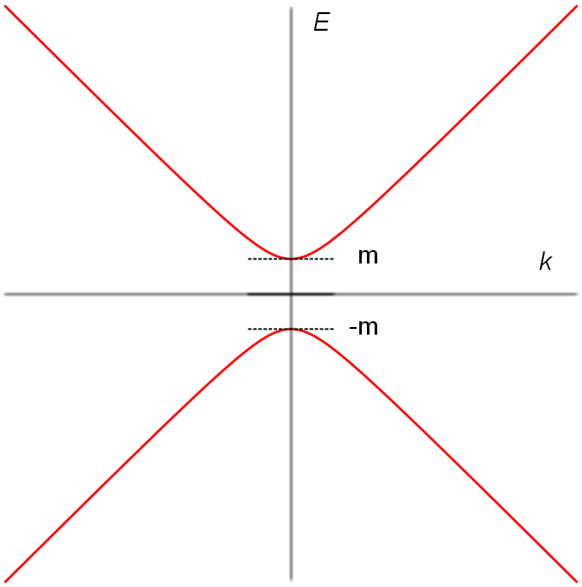

Figure 1.2: Positive and negative energy levels given by particle mass and momentum, $E = \sqrt{k^2 + m^2}$. Taking the non-relativistic limit of the Dirac equation brings the horizontal zero energy axis up to the positive rest energy level m, in $c = \hbar = 1$ units.

We need to subtract off the rest energy of the particle to go to the non-relativistic limit [5], corresponding to an energy shift equal to the rest energy $E_0 = mc^2$ (see Figure 1.2). To do this we rewrite the wave function as follows,

$$\Phi^{\pm}(z,t) = \phi^{\pm}(z,t)\, e^{-i\omega_c t}, . \tag{1.35}$$

In energy eigenstates this operation corresponds to the following representation,

$$\Phi^{\pm}(x,t) = \tilde{\phi}^{\pm}(z)\, e^{-iEt/\hbar} = \tilde{\phi}^{\pm}(z)\, e^{-i\left(E' + mc^2\right)t/\hbar} \tag{1.36}$$

where E' is the energy due to momentum and mc^2 is the particle rest energy. Then substituting (1.35) into (1.34) we get

$$\partial_t \phi^+ + c\partial_z \phi^- = 0, \tag{1.37a}$$

$$\partial_t \phi^- + c\partial_z \phi^+ = 2i\omega_c \phi^-. \tag{1.37b}$$

The collision term now only affects the ϕ^- variable. By analogy with the derivation of hydrodynamics from moments of the discrete Boltzmann equation, we refer to ϕ^+ as the slow, or hydrodynamic, variable, and ϕ^- as the fast, or non hydrodynamic, variable. As in the derivation of the Navier–Stokes equations from kinetic theory, the derivation of the Schrödinger equation follows from eliminating the fast

variable to obtain a closed evolution equation for the slow variable alone [105, 106, 23]. In quantum theory the fast variable generically undergoes rapid oscillations, rather than the rapid decay to equilibrium found in classical kinetic theory, but the same mathematical approach may be applied to both [105].

The adiabatic assumption

$$\left|\partial_t \phi^-\right| \ll 2\omega_c \left|\phi^-\right|, \tag{1.38}$$

corresponds to the kinetic energy due to momentum being much less than the rest energy due to mass, and holds in the non-relativistic limit when the ratio of particle velocity v to the speed of light is much less than one, $v/c \ll 1$. This allows us to solve (1.37b) for ϕ^- in terms of the spatial derivative of ϕ^+,

$$\phi^- = \frac{c}{2i\omega_c}\partial_z \phi^+. \tag{1.39}$$

Substituting this relation into the evolution equation (1.37a) for ϕ^+ leads to the one-dimensional Schrödinger equation for a free particle,

$$i\hbar\partial_t \phi^+ = -\frac{\hbar^2}{2m}\partial_{zz}\phi^+. \tag{1.40}$$

Therefore, the QLB can be used to simulate non-relativistic quantum mechanical systems at low energies, as long as the adiabatic assumption (1.38) holds, and this was the initial goal of the scheme [99].

1.3.3 Existing quantum lattice Boltzmann scheme

The Succi–Benzi quantum lattice Boltzmann discretization of the one-dimensional Dirac equation for a free particle (1.32) is obtained by integrating along the characteristics of u and d and approximating the right hand side integral using the trapezoidal rule [101, 99]. The integration along characteristics and discretization is done in a way that results in explicit equations for $u\,(t+\Delta t)$ and $d\,(t+\Delta t)$, and the QLB evolution of the wave function components is written as

$$u\,(x+\Delta x, t+\Delta t) = a\,u\,(x,t) + b\,d\,(x,t) \tag{1.41a}$$

$$d\,(x-\Delta x, t+\Delta t) = a\,d\,(x,t) - b\,u\,(x,t)\,, \tag{1.41b}$$

in the so-called natural units with $c = 1$ and $\hbar = 1$. The constants a and b appearing on the right hand side are given by

$$a = \frac{1-\frac{1}{4}m^2\Delta t^2}{1+\frac{1}{4}m^2\Delta t^2}, \qquad b = \frac{m\Delta t}{1+\frac{1}{4}m^2\Delta t^2}. \tag{1.42}$$

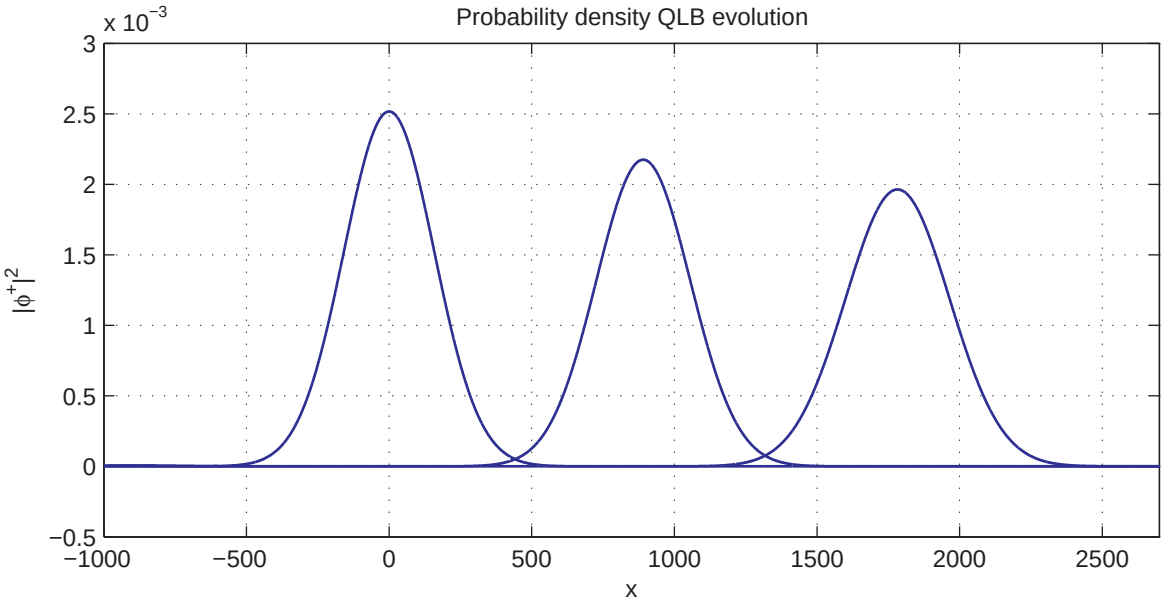

Figure 1.3: Probability density of the slow hydrodynamic mode, $|\phi^+|^2$, at times $t = 0, 2000, 4000$ in lattice units, showing wave packet propagation and dispersion behaviour.

They satisfy the relation $a^2 + b^2 = 1$, so the collision terms on the right hand side of (1.41) are equivalent to multiplication by a unitary matrix and conserve the total probability distribution $|\Psi^2| = |\phi^+|^2 + |\phi^-|^2$. The overall scheme, combining streaming and collisions, is therefore unitary and unconditionally stable.

The QLB scheme is used to evolve the wave functions u and d before composing them into ϕ^+ that simulates the evolution of a wave function under the Schrödinger equation. Setting u_0 and $d_0 = -iu_0$ to Gaussian wave packets

$$u_0 = (2\pi T_0)^{-\frac{1}{4}} \, e^{-\frac{z^2}{4T_0}} e^{ik_0 z} \tag{1.43}$$

centered at $z = 0$ and with initial momentum $p_0 = k_0\hbar$ we can see the expected drift and diffusion behaviour of $|\phi^+|^2$ probability distribution in Figure 1.3.

One of the attractive features of QLB, inherited from the lattice Boltzmann models, is the simplicity of its algorithms. A MATLAB implementation of a single timestep looks like the following,

```
% collision step
    uc=a.*u+b.*d;
    dc=a.*d-b.*u;
```

```
% streaming step
    u=circshift(uc',1)';
    d=circshift(dc',-1)';
```

where the wave function is initialized with u and d, the factors a and b depend on the quantum system and discretization parameters, and the domain has been uniformly discretized to the desired degree of accuracy.

More details on running such non-relativistic QLB simulations, and comparisons with solutions of the Schrödinger equation, may be found in Refs. [101, 99, 78, 79, 104]. However, it is important to note that discrepancies between the outcome of a QLB simulation and the exact solution of the Schrödinger equation will arise from two different sources. There are numerical errors in the approximation of the Dirac equation by the QLB scheme, and there are further errors between the exact solution of the Dirac equation, and of the Schrödinger equation as its non-relativistic limit. We first would like to analyze the former, and our analysis is presented in the next chapter.

Chapter 2

QLB analysis in one dimension

2.1 Error analysis of the Succi-Benzi QLB scheme

Recently Valdivieso and Muñoz [104] compared Succi's QLB scheme with the one-dimensional scheme proposed by Meyer [69, 70] in their ability to simulate the evolution of a wave function under the Schrödinger equation and found their numerical solutions to exhibit unexpected behaviour. In particular, they noticed oscillation of the QLB solution that are not present in the analytical solution under Schrödinger evolution, and sensitivity of the error in mean displacement and width of the wave packet to particle mass and velocity – parameters that should not affect the errors. Previously, Palpacelli and Succi [78] reported some basic convergence results of the multidimensional QLB method to the analytic solution, but they were inconclusive. In one dimension it was only shown that qualitatively the QLB solutions approach the analytic solutions with doubling of the grid size [79], but no analytical error analysis was performed. These open questions motivated the investigation of the Succi-Benzi quantum lattice Boltzmann and its error analysis. We investigate the accuracy of the QLB scheme by comparing it with the exact solutions of the Schrödinger and Dirac equation.

2.1.1 Schrödinger equation solution

We use Fourier transforms to calculate the time evolution of a free Gaussian wave packet under the Schrödinger equation (1.40), using the symmetric pair of Fourier transforms defined as

$$F\left[f\left(x\right)\right]=\widehat{f}\left(k\right)=\int_{-\infty}^{\infty}e^{-ikx}f\left(x\right)\frac{dx}{\sqrt{2\pi}} \tag{2.1}$$

$$F^{-1}\left[\widehat{f}(k)\right] = f(x) = \int_{-\infty}^{\infty} e^{ikx}\widehat{f}(k)\,\frac{dk}{\sqrt{2\pi}} \tag{2.2}$$

Applying F to both sides of the Schrödinger equation (1.40), integrating by parts and evaluating $\frac{\partial}{\partial x}\phi^+|_{x=-\infty} = \frac{\partial}{\partial x}\phi^+|_{x=\infty} = 0$ we get

$$i\hbar\partial_t F\left[\phi^+\right] = -\frac{\hbar^2}{2m}\frac{1}{\sqrt{2\pi}}\left[ik\int_{-\infty}^{\infty} e^{-ikx}\partial_x\phi^+ dx\right] \tag{2.3}$$

Applying integration by parts once again, making the same evaluation of the derivative at $\pm\infty$ and letting $F[\phi^+] = \widehat{f}(k)$ we see the Schrödinger equation transform into the following ordinary differential equation,

$$\partial_t\widehat{f}(k) = -\frac{i\hbar k^2}{2m}\widehat{f}(k)\,, \tag{2.4}$$

with a solution in terms of $\widehat{f_0}(k) = F\left[\phi_0^+\right]$, the Fourier transform of the initial wavepacket ϕ_0^+,

$$\widehat{f}(k) = e^{-\frac{i\hbar k^2 t}{2m}}\widehat{f_0}(k)\,. \tag{2.5}$$

To get the time evolution of the wave packet $\phi^+(x,t)$ we take the inverse Fourier transform

$$\phi^+(x,t) = F^{-1}\left[\widehat{f}(k)\right] = \int_{-\infty}^{\infty} e^{ikx}e^{-\frac{i\hbar k^2}{2m}t}\widehat{f_0}(k)\,\frac{dk}{\sqrt{2\pi}} \tag{2.6}$$

where $\widehat{f_0}(k) = F[\phi^+(x,0)]$. Let our initial wave packet be given by

$$\psi_0(x;T_0,x_0,k_0) = (2\pi T_0)^{-\frac{1}{4}}\,e^{-\frac{x^2}{4T_0}}e^{ik_0x}, \tag{2.7}$$

centered at $x_0 = 0$, with initial momentum $p_0 = k_0\hbar$, and initial spread of the probability distribution $\sigma = \sqrt{T_0}$. In Fourier space this initial wave packet is given by

$$\widehat{f_0}(k) = \left(\frac{2T_0}{\pi}\right)^{\frac{1}{4}} e^{-T_0(k-k_0)^2} \tag{2.8}$$

To get the time evolution of the wavepacket $\phi^+(x,t)$ we now evaluate (2.6) by taking inverse Fourier transform, and after simplification obtain,

$$\phi^+(x,t) = \left(\frac{2}{4\pi T\left(1+\frac{i\hbar t}{2mT_0}\right)^2}\right)^{\frac{1}{4}} \exp\left(\frac{-x^2+4ixk_0T_0-2iT_0k_0^2\hbar t/m}{4T_0\left(1+\frac{i\hbar t}{2mT_0}\right)}\right) \tag{2.9}$$

and can use this solution to compare with with the ϕ^+ composed from the u and d components given by the QLB scheme using the transformation (1.33).

2.1.2 Dirac equation solution in Fourier space

We can derive a solution of the Dirac equation by using the same approach of transforming and evolving in Fourier space. In natural units ($c = 1$ and $\hbar = 1$) the one-dimensional Dirac equation (1.32) becomes

$$\partial_t u + \partial_z u = m\, d, \tag{2.10a}$$

$$\partial_t d - \partial_z d = -m\, u. \tag{2.10b}$$

Taking Fourier transforms of the equations with respect to z leads to

$$\partial_t \hat{u} = -ik\hat{u} + m\,\hat{d} \tag{2.11a}$$

$$\partial_t \hat{d} = ik\hat{d} - m\,\hat{u} \tag{2.11b}$$

where $\hat{u}$ and $\hat{d}$ are the spatial Fourier transforms of u and d, as defined by (2.1) and (2.2). We rewrite equations (2.11) in matrix notation as

$$\begin{pmatrix} \partial_t \hat{u} \\ \partial_t \hat{d} \end{pmatrix} = \begin{pmatrix} -ik & m \\ -m & ik \end{pmatrix} \begin{pmatrix} \hat{u} \\ \hat{d} \end{pmatrix}, \tag{2.12}$$

and their solution is given by the exponential of the matrix

$$\mathsf{M} = \begin{pmatrix} -ik & m \\ -m & ik \end{pmatrix} \tag{2.13}$$

to be

$$\begin{pmatrix} \hat{u} \\ \hat{d} \end{pmatrix} = e^{\mathsf{M}t} \begin{pmatrix} \hat{u}_0 \\ \hat{d}_0 \end{pmatrix} = \begin{pmatrix} \cos\Omega t - \frac{ik}{\Omega}\sin\Omega t & \frac{m}{\Omega}\sin\Omega t \\ -\frac{m}{\Omega}\sin\Omega t & \cos\Omega t + \frac{ik}{\Omega}\sin\Omega t \end{pmatrix} \begin{pmatrix} \hat{u}_0 \\ \hat{d}_0 \end{pmatrix}, \tag{2.14}$$

where $\Omega = \sqrt{k^2 + m^2}$ is the relativistic energy, and $\hat{u}_0$ and $\hat{d}_0$ are the initial wave function components. It is not possible to evaluate the inverse Fourier transform integrals of equations (2.14) analytically to get explicit equations for for $u(x,t)$ and $d(x,t)$ as we did for the Schrödinger equation, but we can compute accurate numerical approximations by using Fast Fourier Transforms. Transforming the wave function into momentum space this way allows the spatial derivatives to be approximated to exponential in n order of accuracy, where n is the number of grid points [32].

Thus we can compare the evolution of ϕ^+_{QLB} as given by the QLB scheme output of u and d components and composed using the transformation

$$\phi^+ = \frac{1}{\sqrt{2}}\,(u + id)\,, \tag{2.15}$$

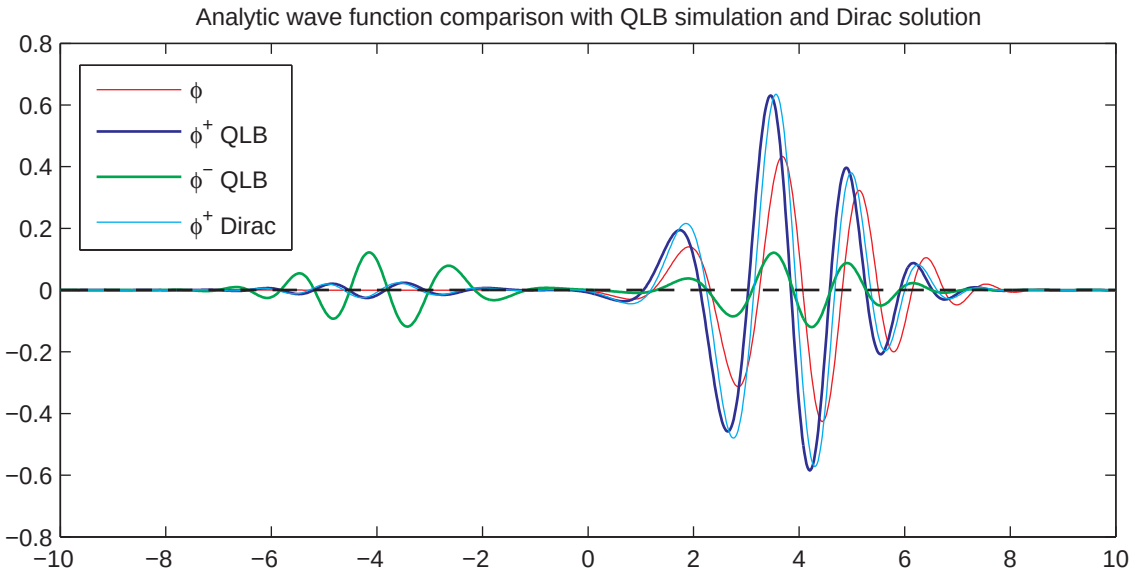

Figure 2.1: Evolution the ϕ^+ wave function under the QLB scheme (dark blue), Dirac equation (light blue), and Schrödinger equation (red) shows the differences between three solutions. The second component ϕ^- of the QLB solution (green) is lower amplitude and has a more significant portion in the left going part of the wave function.

to the solution of the Dirac equation from the inverse fast Fourier transform of equation (2.14) also giving a pair of components to compose into ϕ^+_{Dirac} by the above transformation, and the ϕ_{Schr} given by exact solution of the Schrödinger equation (2.9). The result of such a comparison can be seen in Figure 2.1, where the evolved wave functions are plotted. The QLB ϕ^+ wave function follows closely the Dirac ϕ^+, however both are noticeably different from the wave function according to the Schrödinger equation. We can see that it is more reasonable to study the accuracy of the QLB scheme by comparison with the Dirac solution, due to significant additional approximation errors that are present between the Schrödinger and the QLB solutions. We can also see the low amplitude oscillations of the ϕ^- simulated with the QLB, that is not present in the single-component wave function Schrödinger solution at all. Note also that the QLB simulations (and Dirac solution) show a portion of the wave packet, composed mostly of the ϕ^- component, moving to the left of the initial position.

Comparing the probability density evolution of $|\phi^+|^2$, the slow mode, in Figure 2.2 we see similar results. The solution computed by the QLB scheme is very close to the solution of the Dirac equation obtained from the Fast Fourier Transforms, but there

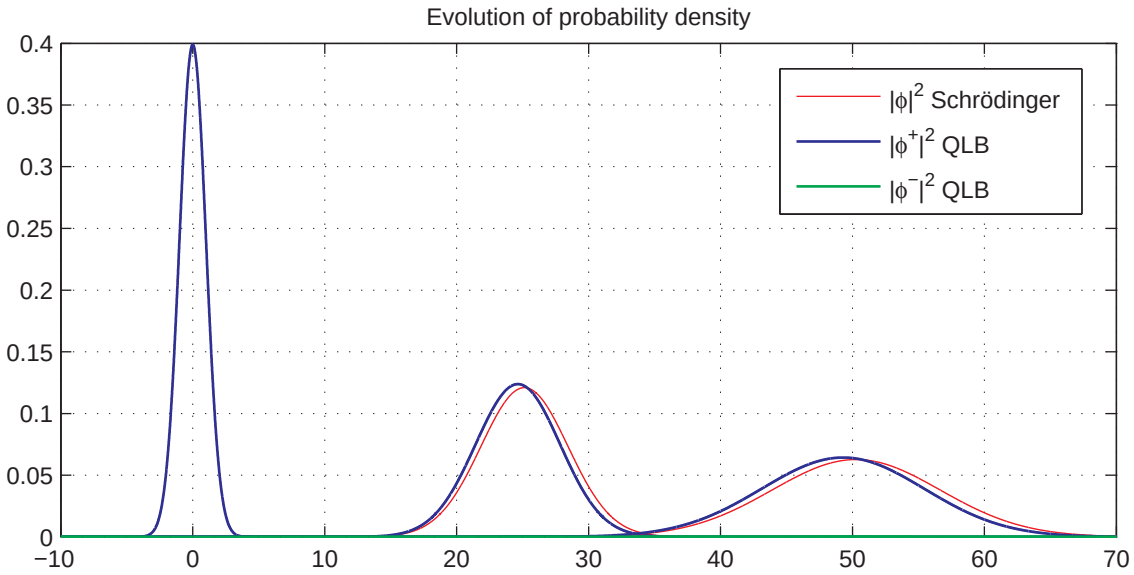

Figure 2.2: Evolution of wave function probability density under the QLB scheme (dark blue), Dirac equation (light blue), and Schrödinger equation (red) shown as initialized and two subsequent times, as the wave packet drifts to the right and disperses.

is a larger, and growing, discrepancy between both these solutions and the solution of the Schrödinger equation under the same parameters and initial conditions. We also find the global norm of the slow and fast modes to be at unit value

$$|\phi^+|^2 + |\phi^-|^2 = |\phi_{Schr}|^2 = 1 \tag{2.16}$$

as expected for normalized Schrödinger and Dirac wave functions. However a fraction of probability density oscillates between $\|\phi^+\|^2$ and $\|\phi^-\|^2$, introducing additional approximation error when trying to solve for the Schrödinger wave function. Reducing the amplitude of $|\phi^-|^2$ will then cause the discrepancy between the ϕ^+ calculated with QLB and the Schrödinger ϕ^+ to decrease. The slower the particle speeds we consider, the better will the QLB simulation describe the non-relativistic limit of the Dirac equation, and wave function evolution according to the Schrödinger equation evolution. This explains the QLB scheme's dependence on particle mass and speed in predicting the mean displacement and variance of the Schrödinger equation solution that was reported by Valdivieso & Muñoz [104]. It is not a property of the QLB scheme itself, but of the approximation to the Dirac equation on which it is based.

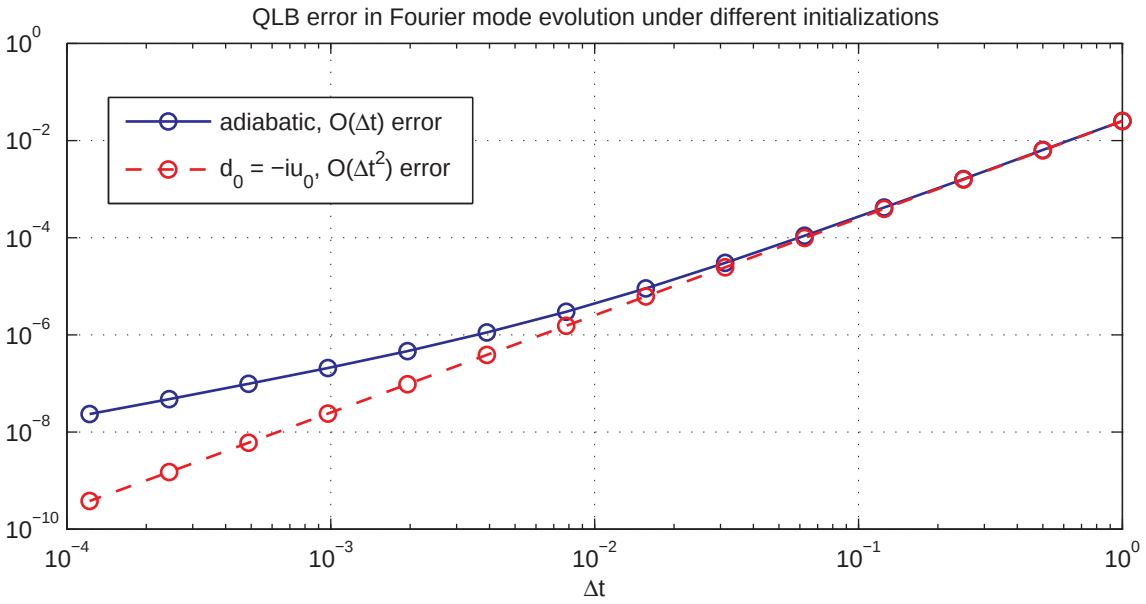

Figure 2.3: The error in ϕ^+ between the first order QLB scheme and the exact solution of the Dirac equation shows second order convergence under the $d_0 = -iu_o$ initialization and first order convergence under the adiabatic initialization.

2.1.3 Evolution of Fourier modes

To analyze the errors quantitatively we investigate the evolution of individual Fourier modes with definite energy under the QLB scheme, and compare with the evolution under the exact Dirac equation as given by (2.14). Substituting $u(z,t) = \hat{u}(t)e^{ikz}$ and $d(z,t) = \hat{d}(t)e^{ikz}$ for fixed k into the QLB scheme (1.41), we obtain

$$\begin{pmatrix} \hat{u}(t+\Delta t) \\ \hat{d}(t+\Delta t) \end{pmatrix} = \mathsf{E}_{\mathrm{QLB}} \begin{pmatrix} \hat{u}(t) \\ \hat{d}(t) \end{pmatrix} \tag{2.17}$$

in terms of the evolution matrix

$$\mathsf{E}_{\mathrm{QLB}} = \frac{1}{1+\frac{1}{4}m^2\Delta t^2} \begin{pmatrix} e^{-ik\Delta t}\left(1-\frac{1}{4}m^2\Delta t^2\right) & e^{-ik\Delta t}m\Delta t \\ -e^{ik\Delta t}m\Delta t & e^{ik\Delta t}\left(1-\frac{1}{4}m^2\Delta t^2\right) \end{pmatrix}, \tag{2.18}$$

where $\Delta z = \Delta t$ for $c = 1$. The exact evolution matrix of the Dirac equation in Fourier space is given by

$$\mathsf{E} = e^{\mathsf{M}\Delta t} = \begin{pmatrix} \cos\Omega\Delta t - \frac{ik}{\Omega}\sin\Omega\Delta t & \frac{m}{\Omega}\sin\Omega\Delta t \\ -\frac{m}{\Omega}\sin\Omega\Delta t & \cos\Omega\Delta t + \frac{ik}{\Omega}\sin\Omega\Delta t \end{pmatrix}, \tag{2.19}$$

which is the matrix (2.13) we derived above. The coefficients of the matrix $\mathsf{E}_{\mathrm{QLB}}$ agree up to and including terms of $\mathcal{O}(\Delta t)$ with those of the matrix E, and we should

therefore expect first order global accuracy from the QLB scheme. However, when we plot the error in ϕ^+ for a range of Δt values we see the error decrease as Δt^2, shown in Figure 2.3. This unusual behavior is observed when, following Succi [2], we initialize the QLB scheme with the second component of the wave function equal to $d_0 = -iu_0$. Furthermore, only $\phi^+ = \frac{1}{\sqrt{2}}(u + id)$ converges at second order – the errors in the u and d themselves decrease only as Δt. We also note that using the $d_0 = -iu_0$ initial condition sets the second wave function component to zero,

$$\phi^- = \frac{1}{\sqrt{2}}(u - id)\, e^{-imt} = 0, \tag{2.20}$$

while the adiabatic assumption that leads from the Dirac equation to the Schrödinger equation corresponds to the relationship between ϕ^- and ϕ^+ derived given in equation (1.39),

$$\phi^- = \frac{c}{2i\omega_c}\partial_z \phi^+. \tag{2.21}$$

and it is generally not equal to zero. Initializing the scheme with any other relationship between u_0 and d_0 causes the error in ϕ^+ to decrease as Δt, as is shown in the second plot in Figure 2.3. The error begins decreasing as Δt^2 for larger values of Δt but as they get sufficiently small the $\mathcal{O}(\Delta t)$ term in the error becomes dominant and the error continues to decrease as Δt.

To examine this behavior of the scheme more closely we express the final error in ϕ^+ after $n = t_{\text{final}}/\Delta t$ timesteps analytically in terms of the initial wave function components u_0 and d_0 as follows

$$\Delta\phi^+ = \begin{bmatrix} \frac{1}{\sqrt{2}} & \frac{i}{\sqrt{2}} \end{bmatrix} \left((\mathsf{E})^n \begin{bmatrix} u_0 \\ d_0 \end{bmatrix} - (\mathsf{E}_{\text{QLB}})^n \begin{bmatrix} u_0 \\ d_0 \end{bmatrix} \right). \tag{2.22}$$

To expand and simplify the expression we find the eigenvalues and eigenvectors of matrices $(\mathsf{E})^n$ and $(\mathsf{E}_{\text{QLB}})^n$, and rewrite the initial wave function in terms of the eigenvectors, such that

$$\begin{bmatrix} u_0 \\ d_0 \end{bmatrix} = A_1\mu_+ + A_2\mu_-, \qquad (\mathsf{E})^n \begin{bmatrix} u_0 \\ d_0 \end{bmatrix} = \lambda_+^n A_1\mu_+ + \lambda_-^n A_2\mu_-, \tag{2.23}$$

where $\lambda_\pm$ are the eigenvalues, $\mu_\pm$ are the eigenvectors, and A_1 and A_2 are coefficients that we can calculate given initial u_0 and d_0. The eigenvalues of E are equal to

$$\lambda_\pm = \exp(\pm i\Omega\Delta t), \tag{2.24}$$

and the eigenvectors are

$$\mu_{\pm} = \begin{pmatrix} \frac{i}{m}\left(k \pm \Omega\right) \\ 1 \end{pmatrix}. \tag{2.25}$$

where $\Omega = \sqrt{k^2 + m^2}$ as before. Like E, the $\mathsf{E}_{\mathrm{QLB}}$ matrix is of the form

$$\begin{pmatrix} p & q \\ -q^* & p^* \end{pmatrix} \tag{2.26}$$

where p^* is the complex conjugate of p. The eigenvalues of a matrix of this form are given by

$$\lambda_{\pm} = \mathrm{Re}\, p \pm i \left((\mathrm{Im}\, p)^2 + |q|^2 \right)^{\frac{1}{2}}, \tag{2.27}$$

and if the matrix is unitary and $|p|^2 + |q|^2 = 1$, as is the case for $\mathsf{E}_{\mathrm{QLB}}$, the formula reduces to

$$\lambda_{\pm} = \mathrm{Re}\, p \pm i \left(1 - (\mathrm{Re}\, p)^2 \right)^{\frac{1}{2}}, \tag{2.28}$$

So the eigenvalues of $\mathsf{E}_{\mathrm{QLB}}$ are given by

$$\tilde{\lambda}_{\pm} = \cos\left(k\Delta t\right) \left(\frac{1 - \frac{1}{4}m^2\Delta t^2}{1 + \frac{1}{4}m^2\Delta t^2} \right) \pm i \left(1 - \cos^2\left(k\Delta t\right) \left(\frac{1 - \frac{1}{4}m^2\Delta t^2}{1 + \frac{1}{4}m^2\Delta t^2} \right)^2 \right)^{\frac{1}{2}}. \tag{2.29}$$

We may rewrite them in the same form as eigenvectors of E as

$$\lambda_{\pm} = \exp(\pm i\tilde{\Omega}\Delta t), \tag{2.30}$$

where

$$\tilde{\Omega} = \frac{1}{\Delta t} \cos^{-1} \left\{ \cos\left(k\Delta t\right) \left(\frac{1 - \frac{1}{4}m^2\Delta t^2}{1 + \frac{1}{4}m^2\Delta t^2} \right) \right\}. \tag{2.31}$$

Expanding $\tilde{\Omega}$ around $\Delta t = 0$ we get

$$\tilde{\Omega} = \sqrt{m^2 + k^2} - \frac{m^4 + 2m^2k^2}{12\sqrt{m^2 + k^2}} \Delta t^2 + \mathcal{O}(\Delta t^4). \tag{2.32}$$

The eigenvalues agree with those of the exact Dirac equation with $\mathcal{O}(\Delta t^2)$ error,

$$\tilde{\Omega} = \Omega + \mathcal{O}(\Delta t^2), \tag{2.33}$$

and therefore the relativistic energy according to the QLB scheme $\tilde{\Omega}$ is second order convergent to the theoretical energy Ω. The corresponding eigenvectors of $\mathsf{E}_{\mathrm{QLB}}$ are

$$\begin{pmatrix} \dfrac{q}{\lambda - p} \\ \\ 1 \end{pmatrix}, \tag{2.34}$$

with the following expansion

$$\begin{pmatrix} \frac{i}{m}\left(k \pm \tilde{\Omega}\right) + \frac{i}{2m}\left(\left(k \pm \tilde{\Omega}\right)^2 - m^2\right)\Delta t + \mathcal{O}(\Delta t^2) \\ 1 \end{pmatrix}, \tag{2.35}$$

that only agrees up to $\mathcal{O}(\Delta t)$ with the eigenvectors of the exact Dirac equation. Given second order accuracy of the eigenvalues and first order accuracy of the eigenvectors, we would expect first order global accuracy of the QLB scheme and not the second order accuracy which we observed in ϕ^+ above. Expressing the u and d wave functions in as linear combinations of the eigenvectors and using the eigenvalues to compute $(\mathsf{E}_{\mathrm{QLB}})^n$ and $(\mathsf{E})^n$, we find the error in ϕ^+ after n timesteps to be given by

$$\Delta\phi^+ = -\frac{km}{\sqrt{2}\Omega}\left(d_0 + iu_0\right)\sin\left(\Omega t_{final}\right)\Delta t + \mathcal{O}\left(\Delta t^2\right) \tag{2.36}$$

After n timesteps the $\mathcal{O}(\Delta t^2)$ local errors in each timestep accumulate to give an $\mathcal{O}\left(\Delta t\right)$ global error. But in the case of the $d_0 = -iu_0$ initial condition, the $\mathcal{O}(\Delta t)$ error term disappears completely and total error in ϕ^+ accumulates to only $\mathcal{O}\left(\Delta t^2\right)$, while the errors in u, d, and ϕ^- remain of $\mathcal{O}\left(\Delta t\right)$. Although initializing the QLB scheme with $d_0 = -iu_0$ causes it to converge significantly faster as the mesh size is refined, it may not be converging to the right physical solution since it does not match the adiabatic assumption.

2.2 Second order QLB scheme

2.2.1 Discretization of the 1D Dirac equation

In their derivation of the quantum lattice Boltzmann scheme Succi and colleagues [1,2] discretize the Dirac equation by replacing the spatial derivatives with one-sided discrete differences taken along the streaming direction. The u wave function on one side of the equation is discretized along the upward characteristic, as shown in Figure 2.4, and the d wave function on the other side of the equation is discretized along the opposite, downward direction.

This introduces additional error into the scheme because the two sides of the equation are integrated along different directions, $z + \Delta z$ and $z - \Delta z$. However, this discretization leads to a pair of equations,

$$u\left(z + \Delta z, t + \Delta t\right) - u\left(z, t\right) = \tfrac{1}{2}m\Delta t\left(d\left(z - \Delta z, t + \Delta t\right) + d\left(z, t\right)\right), \tag{2.37a}$$

$$d\left(z - \Delta z, t + \Delta t\right) - d\left(z, t\right) = -\tfrac{1}{2}m\Delta t\left(u\left(z + \Delta z, t + \Delta t\right) + u\left(z, t\right)\right), \tag{2.37b}$$

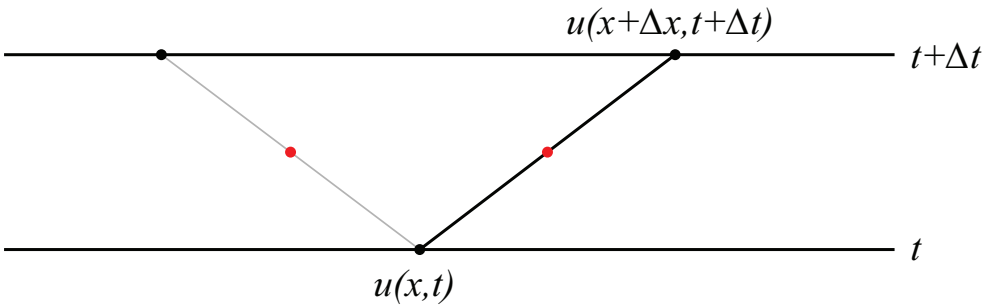

Figure 2.4: Discretization of the u and d wave functions along different characteristics on different sides of the equation.

that may be solved explicitly for the wave functions $u(z+\Delta z, t+\Delta t)$ and $d(z-\Delta z, t+\Delta t)$ at the next timestep. This solution is the Succi–Benzi QLB scheme given by equations (1.41), the original QLB scheme. As we found, the scheme is $\mathcal{O}(\Delta t)$ accurate, except in the special case of $d_0 = -iu_0$. The relatively low accuracy is due to d being evaluated at $(z-\Delta z, t+\Delta t)$ on the right hand side of (2.37), rather than at $(z+\Delta z, t+\Delta t)$ like u on the left hand side.

We now introduce a second order quantum lattice Boltzmann scheme by integrating the one-dimensional Dirac equation consistently along the same characteristic on both sides of the equation to obtain the following pair of equations,

$$u\left(z+\Delta z, t+\Delta t\right) - u\left(z,t\right) = \tfrac{1}{2}m\Delta t\left(d\left(z+\Delta z, t+\Delta t\right) + d\left(z,t\right)\right), \qquad (2.38a)$$

$$d\left(z-\Delta z, t+\Delta t\right) - d\left(z,t\right) = -\tfrac{1}{2}m\Delta t\left(u\left(z-\Delta z, t+\Delta t\right) + u\left(z,t\right)\right). \qquad (2.38b)$$

Both sides of equation (2.38a) are integrated along the u-propagated characteristic and both sides of equation (2.38b) are integrated along the d-propagated characteristic. The $d(z-\Delta z, t+\Delta t)$ on the right hand side of the previous equation (2.37a) has become $d(z+\Delta z, t+\Delta t)$ on the right hand side of (2.38a), and similarly the previous $u(z+\Delta z, t+\Delta t)$ has become $u(z-\Delta z, t+\Delta t)$ in equation (2.38b).

With these modifications, the pair of equations (2.38) approximate the original Dirac equation up to and including terms of $\mathcal{O}(\Delta t^2)$, but we can no longer solve them explicitly for u and d at time $t+\Delta t$. We may, however, transform these discrete equations into an explicit system by a change of variables, analogous to the transformation from f_i to $\overline{f}_i$ introduced by He, Chen and Doolen [48] in their derivation of lattice Boltzmann hydrodynamics. We take the new variables to be

$$\bar{u}\left(z,t\right) = \frac{u\left(z,t\right) - \frac{1}{2}m\Delta t\, d\left(z,t\right)}{\left(1+\frac{1}{4}m^2\Delta t^2\right)^{1/2}}, \quad \bar{d}\left(z,t\right) = \frac{d\left(z,t\right) + \frac{1}{2}m\Delta t\, u\left(z,t\right)}{\left(1+\frac{1}{4}m^2\Delta t^2\right)^{1/2}}. \qquad (2.39)$$

To maintain norm-preservation of the scheme, we also introduced an extra constant factor of $\left(1+\frac{1}{4}m^2\Delta t^2\right)^{-1/2}$ so that the $\overline{u}$ and $\overline{d}$ variables are related to u and d by a unitary transformation,

$$\begin{pmatrix}\overline{u}\\ \overline{d}\end{pmatrix} = \mathsf{B}\begin{pmatrix}u\\ d\end{pmatrix} \tag{2.40}$$

where the "barring matrix" is

$$\mathsf{B} = \left(1+\tfrac{1}{4}m^2\Delta t^2\right)^{-1/2}\begin{pmatrix}1 & -\frac{1}{2}m\Delta t\\ \frac{1}{2}m\Delta t & 1\end{pmatrix}. \tag{2.41}$$

This change of variables transforms the pair of equations (2.38) into an explicit system which can be solved for the evolved $\overline{u}$ and $\overline{d}$ to give

$$\overline{u}\,(z+\Delta z, t+\Delta t) = a\,\overline{u}\,(z,t) + b\,\overline{d}\,(z,t) \tag{2.42a}$$

$$\overline{d}\,(z-\Delta z, t+\Delta t) = a\,\overline{d}\,(z,t) - b\,\overline{u}\,(z,t)\,, \tag{2.42b}$$

which is exactly the same as the Succi–Benzi scheme, with the same values of collision constants a and b,

$$a = \frac{1-\frac{1}{4}m^2\Delta t^2}{1+\frac{1}{4}m^2\Delta t^2}, \qquad b = \frac{m\Delta t}{1+\frac{1}{4}m^2\Delta t^2}. \tag{2.43}$$

but applied to the barred variables $\overline{u}$ and $\overline{d}$ instead of u and d. We can invert the transformation (2.40) to recover the original u and d components,

$$\begin{pmatrix}u\\ d\end{pmatrix} = \mathsf{B}^{-1}\begin{pmatrix}\overline{u}\\ \overline{d}\end{pmatrix}, \tag{2.44}$$

where $\mathsf{B}^{-1} = \mathsf{B}^{\mathsf{T}}$ because B is real and unitary.

We have thus derived a second order QLB scheme that, compared with the original QLB scheme, requires only a one-time modification of the initial conditions and final output to obtain global second order accuracy of solutions, which we confirm in the error analysis below.

2.2.2 Convergence of the second order QLB scheme

Applying the Fourier mode error analysis to the second order QLB scheme, we can write the evolution of $\hat{u}$ and $\hat{d}$ under a single timestep of this second order QLB scheme as given by

$$\begin{pmatrix}\hat{u}(t+\Delta t)\\ \hat{d}(t+\Delta t)\end{pmatrix} = \mathsf{B}^{-1}\mathsf{E}_{\mathrm{QLB}}\mathsf{B}\begin{pmatrix}\hat{u}(t)\\ \hat{d}(t)\end{pmatrix}. \tag{2.45}$$

The coefficients of the matrix $\mathsf{B}^{-1}\mathsf{E}_{\mathrm{QLB}}\mathsf{B}$ now agree up to and including terms of $\mathcal{O}(\Delta t^2)$ with the coefficients of the exact evolution matrix E, which is one power of Δt better than before. Therefore we expect this second order QLB scheme to be second order accurate for u and d as well as for ϕ^+, and for generic initial conditions as well as the special case with $d_0 = -iu_0$.

The error between the second order QLB scheme and the exact Dirac solution after n timesteps is given by

$$\begin{pmatrix} \Delta\hat{u} \\ \Delta\hat{d} \end{pmatrix} = \left[(\mathsf{E})^n - \mathsf{B}^{-1}(\mathsf{E}_{\mathrm{QLB}})^n\mathsf{B}\right] \begin{pmatrix} \hat{u}_0 \\ \hat{d}_0 \end{pmatrix}, \tag{2.46}$$

where again we can write $\hat{u}$ and $\hat{d}$ as linear combinations of eigenvectors and use eigenvalues to express $(\mathsf{E})^n$ and $(\mathsf{E}_{\mathrm{QLB}})^n$. Expanding for small Δt we find the errors in $\hat{u}$ and $\hat{d}$ after n timesteps to be

$$\begin{aligned} \Delta\hat{u} = \frac{m}{12\Omega^3}[&m\Omega\left(2k^2+m^2\right)t_{final}\left(dm-iku\right)\cos\left(\Omega t_{final}\right)+ \\ &(d(4k^4+3k^2m^2)-mu(-ik\left(4k^2+3m^2\right)+, \\ &\Omega^2(2k^2+m^2)t_{final}))\sin(\Omega t_{final})]\Delta t^2+\mathcal{O}(\Delta t^4), \end{aligned} \tag{2.47}$$

$$\begin{aligned} \Delta\hat{d} = \frac{m}{12\Omega^3}[&m\Omega\left(2k^2+m^2\right)t_{final}\left(-id+mu\right)\cos\left(\Omega t_{final}\right)- \\ &(u(4k^4+3k^2m^2)+md(ik(4k^2+3m^2)+ \\ &\Omega^2(2k^2+m^2)t_{final}))\sin(\Omega t_{final})]\Delta t^2+\mathcal{O}(\Delta t^4), \end{aligned} \tag{2.48}$$

where $t_f = n\Delta t$. The resulting error in ϕ^+ therefore also decreases as $\mathcal{O}(\Delta t^2)$ with refinement of the mesh for all initial conditions and the scheme is globally second order accurate.

2.2.3 Adiabatic initialization

To investigate the effects of initializing the QLB scheme with u_0 and d_0 that obey the adiabatic condition,

$$\phi^- = \frac{c}{2i\omega_c}\partial_z\phi^+, \tag{2.49}$$

we compare the ϕ^- calculated from the Schrödinger equation ϕ^+ solution (2.9) by the above differentiation formula with the ϕ^- calculated using the second order QLB

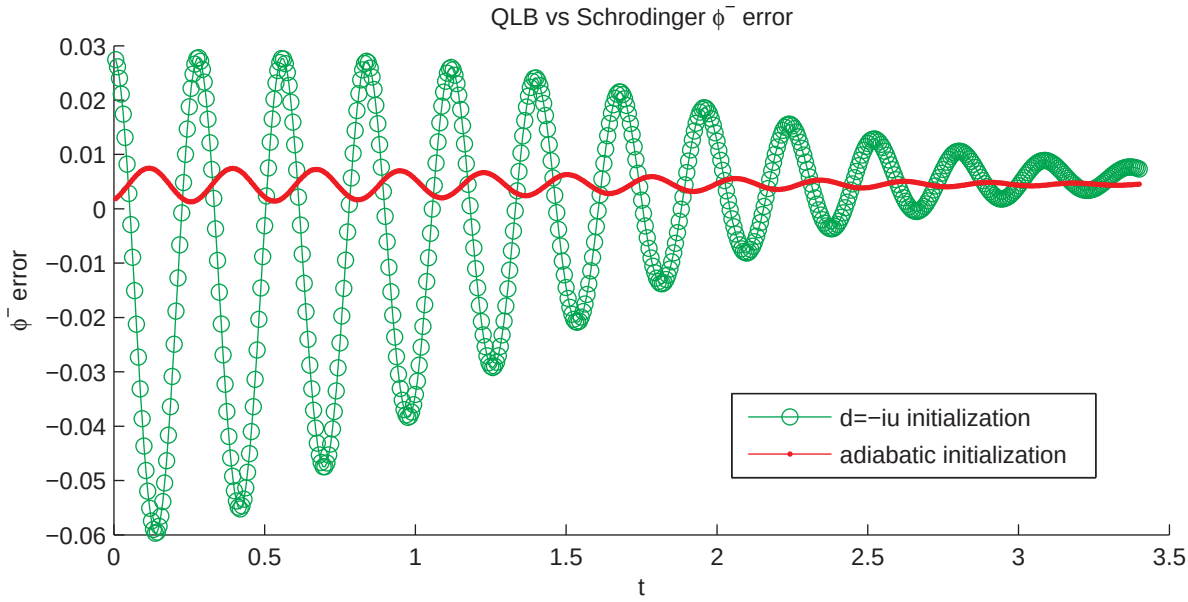

Figure 2.5: Comparison of the ϕ^- wave function component based on the Schrödinger solution with the ϕ^- calculated using the second order QLB scheme with two sets of initial conditions. Adiabatic initialization drastically reduces the amplitude of error oscillations compared with the $d_0 = -iu_0$ initialization.

scheme with two different initializations. The first one is the $d_0 = -iu_0$ initialization used by Succi et. al., where u_0 is given by a Gaussian wave packet (2.7).

The second simulation with the second order QLB scheme is initialized with u_0 and d_0 that obey the adiabatic relationship (2.49). To derive such u_0 and d_0 we set the initial wave function component ϕ_0^+ to the same Gaussian wave packet, and the initial ϕ_0^- given by (2.49),

$$\phi^+ = \eta \frac{1}{2} \left(2\pi T_0\right)^{-\frac{1}{4}} e^{-\frac{(z-z_0)^2}{4T_0}} e^{ik_0 z} \tag{2.50a}$$

$$\phi^- = \frac{c}{2i\omega_c} \partial_z \phi^+ = \left(\frac{k_0}{2m} + \frac{i\,(z-z_0)}{4mT_0} \right) \phi^+ \tag{2.50b}$$

where z_0 is the initial wave packet position and η is a normalization factor required to set the total probability density $|\phi_0^+|^2 + |\phi_0^-|^2 = 11$,

$$\eta = \sqrt{\frac{32m^2T_0}{1 + 4k_0^2T_0 + 16m^2T_0}}. \tag{2.51}$$

The u_0 and d_0 components of the wave function are then given by the inverse of the transformation (1.33) from ϕ_0^+ and ϕ_0^-,

$$u = \frac{(\phi^+ + \phi^-)}{\sqrt{2}}, \qquad d = -i\frac{(\phi^+ - \phi^-)}{\sqrt{2}}, \tag{2.52}$$

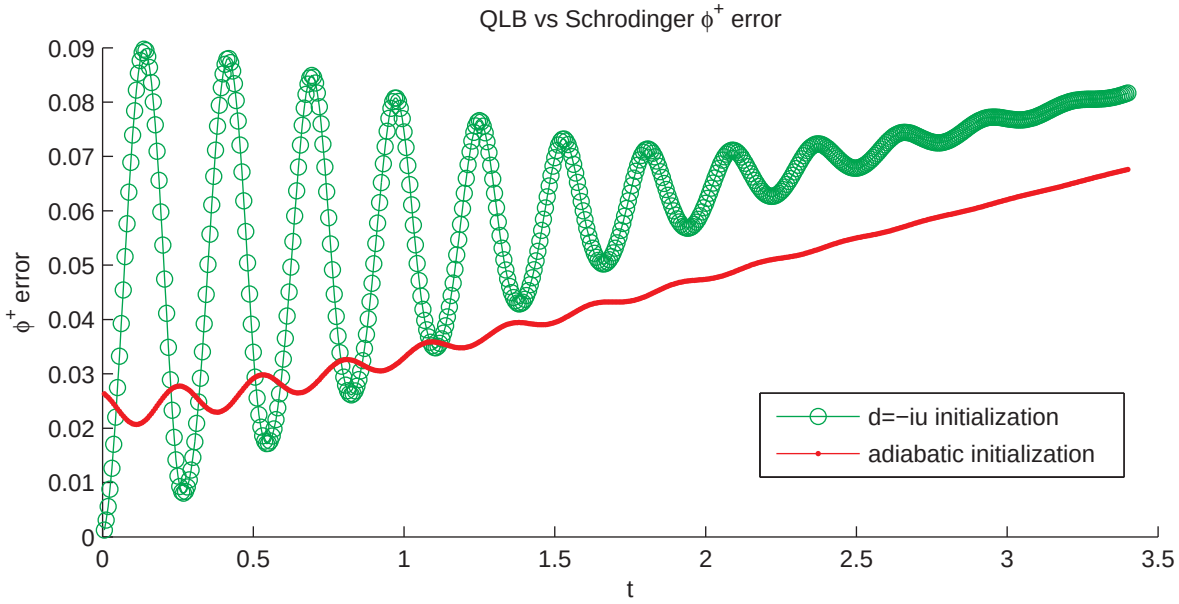

Figure 2.6: Comparison of ϕ^+ error between the QLB scheme and the Schrödinger solution under two different initializations. The oscillations of the error are suppressed by the adiabatic initialization.

and are transformed into initial values for $\overline{u}$ and $\overline{d}$ with the 'barring' matrix B before applying the collision and streaming steps of the QLB simulation. The results can be seen in Figure 2.5, with error defined as the maximum difference between the second order QLB scheme solution and the Schrödinger values of $|\phi^-|^2$ along the simulated region. In the case of adiabatic initialization the simulated ϕ^- follows the Schrödinger ϕ^- very closely, while initializing with $d_0 = -iu_0$ (corresponding to $\phi^- = 0$) causes high amplitude oscillations around the true value. The $\phi^- = 0$ initialization also increases the amplitude of oscillations in the error between ϕ^+_{QLB} and the true Schrödinger ϕ^+, as shown in Figure 2.6. The error grows with time without high amplitude oscillations when the QLB scheme is initialized correctly with the adiabatic condition.

We can surmise that the oscillations in the QLB solution reported by Valdivieso & Muñoz [104] are related to the initialization of the scheme, and they can be removed by using the adiabatic initialization.

2.2.4 Introduction of an external potential

Up to now we have been considering simulation of a free particle for the sake of simplicity, but now we take the more general case of a non-zero potential and see if the discretization approach we used to improve the order of accuracy of the scheme in the free-particle case can allow us to do the same. With the introduction of an external potential $g = qV(x)/\hbar$, where q is the particle charge, the one dimensional time-dependant Dirac equation becomes

$$\partial_t u + c\partial_x u = \omega_c d + igu \tag{2.53a}$$

$$\partial_t d - c\partial_x d = -\omega_c u + igd. \tag{2.53b}$$

As before, we may derive the Schrödinger equation from a non-relativistic limit of the Dirac equation (2.53a) with the introduction of a pair of transformed wave functions,

$$\Phi^+ = \frac{1}{\sqrt{2}}\left(u + id\right), \qquad \Phi^- = \frac{1}{\sqrt{2}}\left(u - id\right), \tag{2.54}$$

where Φ^+ is the symmetric and Φ^- the anti-symmetric mode [5]. The Dirac equation then becomes

$$\partial_t \Phi^+ + c\partial_z \Phi^- = -i\omega_c \Phi^+ + ig\Phi^+, \tag{2.55a}$$

$$\partial_t \Phi^- + c\partial_z \Phi^+ = i\omega_c \Phi^- + ig\Phi^-. \tag{2.55b}$$

We perform an energy shift, effectively subtracting off the rest energy $E_0 = mc^2$ [5] by writing

$$\Phi^{\pm}(z,t) = \phi^{\pm}(z,t)\, e^{-i\omega_c t}, \tag{2.56}$$

Then substituting (2.56) into (2.55) we get

$$\partial_t \phi^+ + c\partial_z \phi^- = ig\phi^+, \tag{2.57a}$$

$$\partial_t \phi^- + c\partial_z \phi^+ = 2i\omega_c \phi^- + ig\phi^-. \tag{2.57b}$$

Assuming adiabaticity ($|\partial_t \phi^-| \ll 2\omega_c |\phi^-|$) and weak enough coupling ($|g| \ll \omega_c$), so that (2.57b) is approximated by

$$\phi^- = \frac{c}{2i\omega_c}\partial_z \phi^+, \tag{2.58}$$

we substitute (2.57b) into (2.57a) to get the Schrödinger equation for a non-relativistic particle in an external potential

$$i\hbar\partial_t \phi^+ = -\frac{\hbar^2}{2m}\partial_{zz}\phi^+ - qV(z)\phi^+. \tag{2.59}$$

For more details on this derivation we refer the reader to standard quantum mechanics textbooks [5].

The QLB scheme with a potential remains the same as in equations (1.41), and the collision coefficients a and b become [99]

$$a = \frac{1 - \frac{1}{4}\Delta t^2(m^2 - g^2)}{1 + \frac{1}{4}\Delta t^2(m^2 - g^2) - ig\Delta t} \qquad b = \frac{m\Delta t}{1 + \frac{1}{4}\Delta t^2(m^2 - g^2) - ig\Delta t} \tag{2.60}$$

in $c = \hbar = 1$ units. It is derived by solving the following pair of discrete equations for evolved u and d,

$$\begin{aligned} u\left(z + \Delta z, t + \Delta t\right) - u\left(z, t\right) &= \tfrac{1}{2} m\Delta t \left(d\left(z - \Delta z, t + \Delta t\right) + d\left(z, t\right)\right) \\ &\quad + i\tfrac{1}{2} g(z,t)\Delta t \left(u\left(z + \Delta z, t + \Delta t\right) + u\left(z, t\right)\right), \qquad (2.61a) \\ d\left(z - \Delta z, t + \Delta t\right) - d\left(z, t\right) &= -\tfrac{1}{2} m\Delta t \left(u\left(z + \Delta z, t + \Delta t\right) + u\left(z, t\right)\right) \\ &\quad + i\tfrac{1}{2} g(z,t)\Delta t \left(d\left(z - \Delta z, t + \Delta t\right) + d(z,t)\right), \qquad (2.61b) \end{aligned}$$

which are obtained by integration along crossed characteristics of equations (2.53a) and (2.53b), as described before. Note that for this discretization to produce explicit equations the potential g is be kept constant across the timestep and mesh size, and evaluated only at (z, t) even though u and d are evaluated at both ends of the characteristics, at $(z \pm \Delta z, t + \Delta t)$ as well as at (z, t).

2.2.5 Second order QLB scheme with a potential

To derive a second order QLB scheme as for the free particle case, we discretize the Dirac equations consistently along the same characteristics on both sides of the equations (2.53a) and (2.53b) to get the following pair of discrete equations

$$\begin{aligned} u\left(z + \Delta z, t + \Delta t\right) - u\left(z, t\right) &= \tfrac{1}{2} m\Delta t \left(d\left(z + \Delta z, t + \Delta t\right) + d\left(z, t\right)\right) \\ &\quad + \tfrac{1}{2} i\Delta t \left(g(z + \Delta z, t + \Delta t) u\left(z + \Delta z, t + \Delta t\right) + g(z,t) u\left(z, t\right)\right), \qquad (2.62a) \\ d\left(z - \Delta z, t + \Delta t\right) - d\left(z, t\right) &= -\tfrac{1}{2} m\Delta t \left(u\left(z - \Delta z, t + \Delta t\right) + u\left(z, t\right)\right) \\ &\quad + \tfrac{1}{2} i\Delta t \left(g(d - \Delta z, t + \Delta t) d\left(z - \Delta z, t + \Delta t\right) + g(z,t) d\left(z, t\right)\right). \qquad (2.62b) \end{aligned}$$

We introduce $\overline{u}$ and $\overline{d}$ variables defined as

$$\begin{aligned} \overline{u}\left(z, t\right) &= \left(1 - \tfrac{1}{2} i\Delta t g(z,t)\right) u\left(z, t\right) - \tfrac{1}{2} m\Delta t d\left(z, t\right), \qquad (2.63a) \\ \overline{d}\left(z, t\right) &= \left(1 - \tfrac{1}{2} i\Delta t g(z,t)\right) d\left(z, t\right) + \tfrac{1}{2} m\Delta t u\left(z, t\right), \qquad (2.63b) \end{aligned}$$

and solve the now explicit discrete equations for the evolved $\bar{u}$ and $\bar{d}$ get

$$\overline{u}\,(z+\Delta z, t+\Delta t) = a\,\overline{u}\,(z,t) + b\,\overline{d}\,(z,t) \tag{2.64a}$$

$$\overline{d}\,(z-\Delta z, t+\Delta t) = a\,\overline{d}\,(z,t) - b\,\overline{u}\,(z,t)\,, \tag{2.64b}$$

where the values of a and b are given by as for the original QLB scheme

$$a = \frac{1-\frac{1}{4}\Delta t^2(m^2-g^2)}{1+\frac{1}{4}\Delta t^2(m^2-g^2)-ig\Delta t} \qquad b = \frac{m\Delta t}{1+\frac{1}{4}\Delta t^2(m^2-g^2)-ig\Delta t}, \tag{2.65}$$

and satisfy $|a|^2+|b|^2=1$. As for the free particle, it is exactly the same QLB scheme as the one derived by Succi and Benzi, only for $\bar{u}$ and $\bar{d}$ instead of u and d. We also do not need to make the additional approximation of $g\,(x+\Delta t, t+\Delta t) = g\,(x-\Delta x, t+\Delta t) = g\,(x,t)$ that is made in deriving the original QLB scheme. The (unscaled) matrix $\tilde{\mathsf{B}}$ to transform u and d into $\overline{u}$ and $\overline{d}$ is

$$\tilde{\mathsf{B}} = \begin{pmatrix} 1-\frac{1}{2}ig\Delta t & -\frac{1}{2}m\Delta t \\ \frac{1}{2}m\Delta t & 1-\frac{1}{2}ig\Delta t \end{pmatrix}. \tag{2.66}$$

This matrix is not unitary, even after possible rescaling. We can, however, make an $\mathcal{O}\,(\Delta t^2)$ approximation to $\tilde{\mathsf{B}}$ written as

$$\mathsf{B}' = e^{-\frac{1}{2}ig\Delta t}\begin{pmatrix} 1 & -\frac{1}{2}m\Delta t \\ \frac{1}{2}m\Delta t & 1 \end{pmatrix}, \tag{2.67}$$

and rescale by $\left(1+\frac{1}{4}m^2\Delta t^2\right)^{-\frac{1}{2}}$ to get a unitary 'barring' matrix

$$\mathsf{B} = e^{-\frac{1}{2}ig\Delta t}\left(1+\tfrac{1}{4}m^2\Delta t^2\right)^{-\frac{1}{2}}\begin{pmatrix} 1 & -\frac{1}{2}m\Delta t \\ \frac{1}{2}m\Delta t & 1 \end{pmatrix}. \tag{2.68}$$

We then use B and its inverse to transform between barred and un-barred u and d in the QLB computations. The extra error introduced by the approximation is consistent with the global $\mathcal{O}\,(\Delta t^2)$ truncation error of the QLB scheme and does not degrade the order of convergence of the simulations. Note that the barring matrix is now a function of position (and possibly time) through $g(x,t)$.

For the special case of a constant potential we can again write down the evolution matrices in momentum space, excluding the initial 'barring' and final 'unbarring' transformations of the second order scheme,

$$\mathsf{E}_{\mathrm{g}} = e^{ig\Delta t}\begin{pmatrix} \cos\Omega\Delta t - \frac{ik}{\Omega}\sin\Omega\Delta t & \frac{m}{\Omega}\sin\Omega\Delta t \\ -\frac{m}{\Omega}\sin\Omega\Delta t & \cos\Omega\Delta t + \frac{ik}{\Omega}\sin\Omega\Delta t \end{pmatrix} \tag{2.69}$$

$$\tilde{\mathsf{E}}_{\mathrm{g}} = \begin{pmatrix} \frac{e^{-ik\Delta t}\left(1-\frac{1}{4}\Delta t^2\left(m^2-g^2\right)\right)}{1+\frac{1}{4}\Delta t^2(m^2-g^2)-ig\Delta t} & \frac{e^{-ik\Delta t}m\Delta t}{1+\frac{1}{4}\Delta t^2(m^2-g^2)-ig\Delta t} \\ \frac{-e^{ik\Delta t}m\Delta t}{1+\frac{1}{4}\Delta t^2(m^2-g^2)-ig\Delta t} & \frac{e^{ik\Delta t}\left(1-\frac{1}{4}\Delta t^2\left(m^2-g^2\right)\right)}{1+\frac{1}{4}\Delta t^2(m^2-g^2)-ig\Delta t} \end{pmatrix}, \tag{2.70}$$

The eigenvalues of E_{g} are

$$\lambda_{\mathrm{g},\pm} = \exp\left(i(g \pm \Omega)\Delta t\right), \tag{2.71}$$

and the eigenvectors are given by (2.25) as before. The matrix $\tilde{\mathsf{E}}_{\mathrm{g}}$ is of the form

$$\frac{|r|}{r}\begin{pmatrix} p & q \\ -q^* & p^* \end{pmatrix} \tag{2.72}$$

where $r = 1 + \frac{1}{4}\Delta t^2(m^2 - g^2) - ig\Delta t$ and matrix terms have $|r|$ in their denominators. Using (2.28) we can express its eigenvalues as

$$\tilde{\lambda}_{\mathrm{g},\pm} = \exp(i(\tilde{g} \pm \tilde{\Omega})\Delta t). \tag{2.73}$$

where

$$\tilde{g}\Delta t = \tan^{-1}\left(\frac{g\Delta t}{1 + \frac{1}{4}\Delta t^2\left(m^2 - g^2\right)}\right), \tag{2.74}$$

and

$$\tilde{\Omega}\Delta t = \cos^{-1}\left(\mathrm{Re}\, p\right) = \cos^{-1}\left(\frac{\cos\left(k\Delta t\right)\left(1 - \frac{1}{4}\Delta t^2\left(m^2 - g^2\right)\right)}{|1 + \frac{1}{4}\Delta t^2(m^2 - g^2) - ig\Delta t|}\right). \tag{2.75}$$

The series expansion of the argument is

$$\begin{aligned} \tilde{g} \pm \tilde{\Omega} = &\left(g - \frac{g^3 + 3gm^2}{12}\Delta t^2 + \mathcal{O}(\Delta t^4)\right) \\ &\pm \left(\sqrt{m^2 + k^2} - \frac{3g^2m^2 + 2k^2m^2 + m^4}{12\sqrt{m^2 + k^2}}\Delta t^2 + \mathcal{O}(\Delta t^4)\right). \end{aligned} \tag{2.76}$$

and the eigenvector is

$$\begin{pmatrix} \frac{i}{m}\left(k \pm \Omega\right) + \frac{k}{m}\left(k \pm \Omega\right)\Delta t + \mathcal{O}(\Delta t^2) \\ \\ 1 \end{pmatrix}, \tag{2.77}$$

As in the free particle case, the dispersion relation agrees with that of the exact Dirac equation with $\mathcal{O}(\Delta t^2)$ error and the eigenvectors agree only up to $\mathcal{O}(\Delta t)$. We can write down an expression for the error as we did for the zero potential case, equation (2.46).

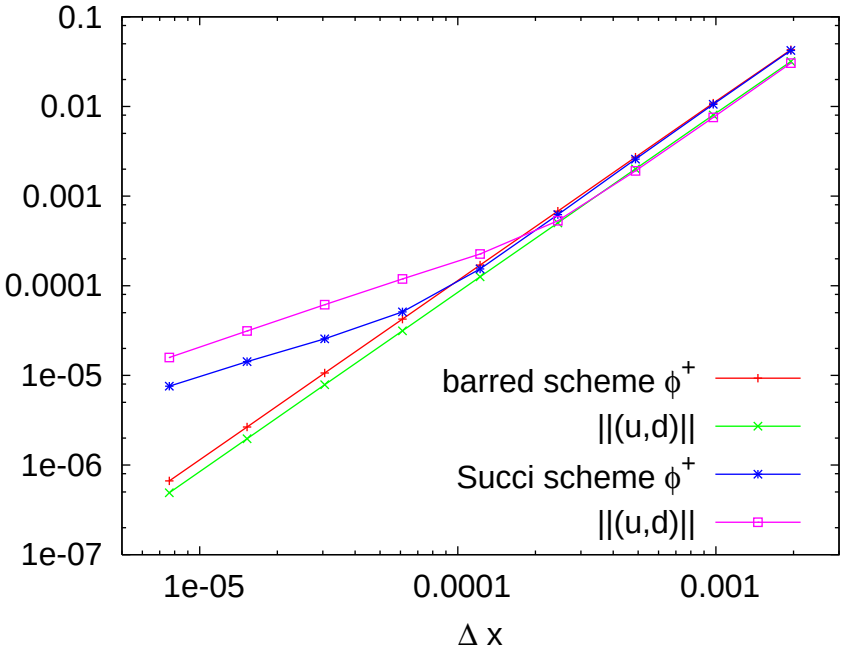

Figure 2.7: Comparison of ϕ^+ error with the original and the second order QLB scheme in the case of a spatially varying potential. (Figure by P. Dellar, generated using spectral solutions of the Dirac equation)

The error behaves the same as in the case of zero potential – u and d are $\mathcal{O}(\Delta t^2)$ accurate in the second order scheme, Succi's original scheme has ϕ^+ that is $\mathcal{O}(\Delta t^2)$ accurate when initialised with $d_0 = -iu_0$, but u and d are only $\mathcal{O}(\Delta t)$ accurate.

The behaviour of the error in the more general case of a spatially varying potential can be seen in Figure 2.7. The original QLB scheme converges to the solution of the Dirac equation as $\mathcal{O}(\Delta t)$, even when initialized with $d_0 = -iu_0$. The second order QLB scheme converges as $\mathcal{O}(\Delta t^2)$.

2.2.6 QLB scaling and accuracy requirements

In this subsection we clarify the conversion from the physical units in the equations simulated by the QLB to the lattice units and parameters used in the algorithms of the simulation, and what discretization requirements exist to maintain accuracy of solutions. The scaling we use for the QLB simulations is slightly different from that employed by Succi and co-workers [80] in that we do not use an un-physical value for the speed of light c and we do not have to maintain $\Delta t = \Delta x$ in the algorithm. The physical quantities we have are

$\tilde{m}$ (particle mass),

$\tilde{V}$ (external potential),
$\tilde{q}$ (particle charge, $g = qV$),
$\tilde{k_0}$ (wavenumber, $\tilde{p_0} = \hbar\tilde{k_0}$ initial momentum),
$\tilde{L}$ (domain length),
$\tilde{\Delta_0}$ (initial wave packet width),
$\tilde{t}$ (time).

We rescale the physical time and space in the Dirac equation by t_0 and z_0, so that the non-dimensional quantities are

$$t = \frac{\tilde{t}}{t_0} \quad z = \frac{\tilde{z}}{z_0} \tag{2.78}$$

and we get

$$\partial_t \Psi + c\frac{t_0}{z_0}\partial_z \Psi = t_0\omega_c \Psi + t_0 iqV\Psi. \tag{2.79}$$

which, assuming $ct_0 = z_0$, becomes

$$\partial_t \Psi + \partial_z \Psi = t_0\omega_c \Psi + t_0 ig\Psi. \tag{2.80}$$

The simulation parameters are then defined as

$m = t_0\omega_c$,
$g = t_0 q\tilde{V}$,
$k_0 = z_0\tilde{k}_0$
$L = \tilde{L}/z_0$,
$\Delta_0 = \tilde{\Delta}_0/z_0$,

and step size given by

$$\Delta z = L/n \qquad \Delta t = \frac{z_0\Delta z}{t_0 c} = \Delta z, \tag{2.81}$$

where n is the mesh size. Note that the scheme's accuracy is subject to the timestep Δt being small enough to resolve the Compton frequency of the simulated particle – the requirement is $\omega_c\Delta t \leq 1$. Equivalently, Δx should be small enough to resolve the de Broglie wavelength that is associated with the particle momentum, $\lambda = 2\pi\hbar/p$.

To display the effect of $\omega_c\Delta t$ approaching 1 we plot both dispersion relations $\Omega = E = \sqrt{m^2 + k^2}$ and $\tilde{\Omega}$ given by (2.31) in Figure 2.8 and observe the close agreement between the two up to the maximum wave number possible on a particular grid, given by $k_{max} = \frac{\pi}{\Delta z}$. The agreement breaks down as $m\Delta t$ approaches 1, at which point the QLB dispersion relation no longer gives the correct particle energy and the scheme is no longer able to resolve the wave function evolution correctly.

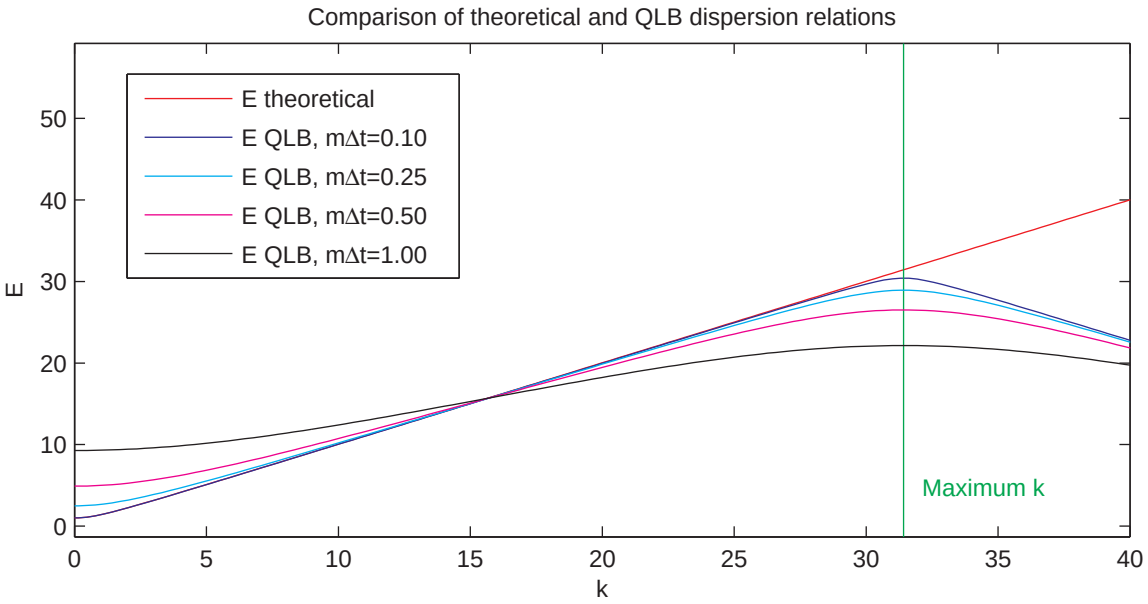

Figure 2.8: Comparison of energy as a function of the wave number as given by relativistic quantum theory and QLB algorithm, shows good agreement between the two. The agreement breaks down as we approach the limit of $m\Delta t \leq 1$.

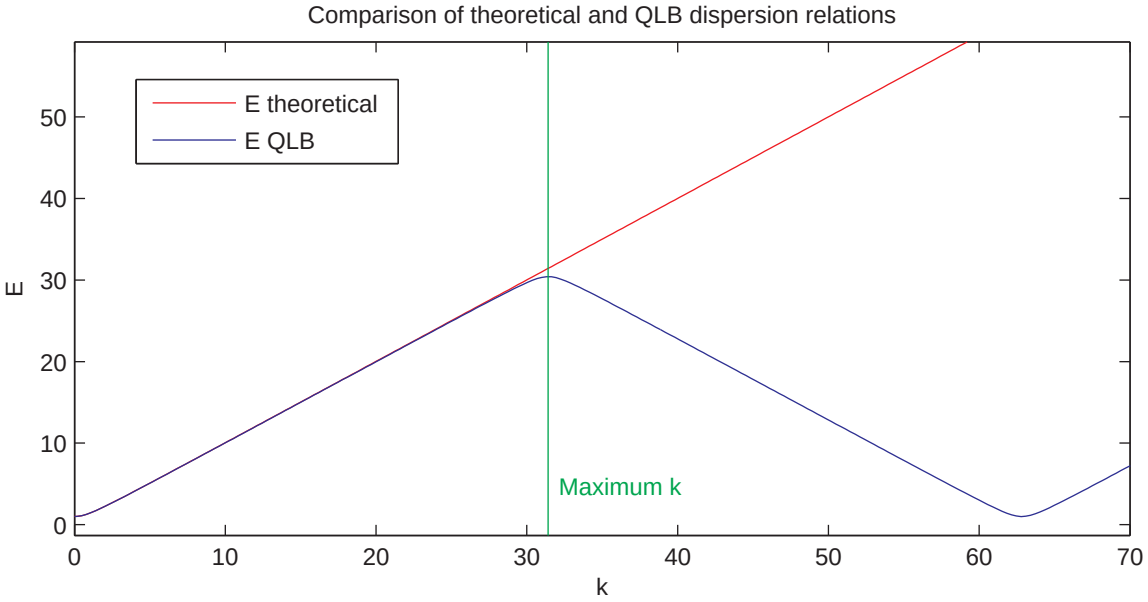

Figure 2.9: Comparison of energy as a function of the wave number as given by quantum theory and QLB, shows a single value of the energy for each value of the momentum in the range of possible discrete k values, identifying a lack of the fermion doubling problem in the QLB scheme.

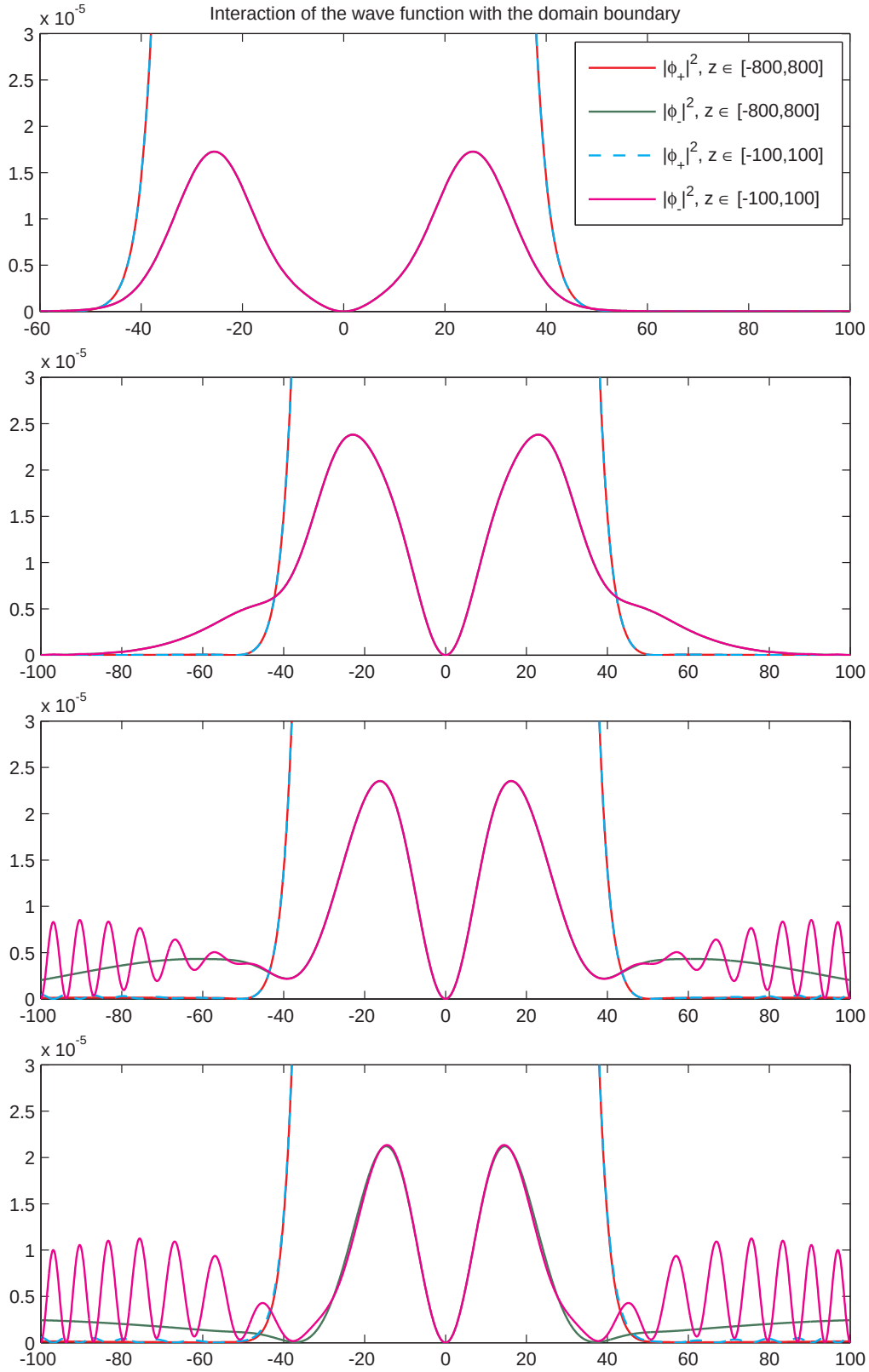

Figure 2.10: Plots of evolving probability density at successive times shows interaction of the wave function with the domain boundary results in a standing wave pattern. Increasing the domain size allows the wave function to evolve freely and results in the correct behaviour.

We can also observe another advantage of the QLB method from plots of the dispersion relation. Finite difference and finite element numerical schemes for the Dirac equation suffer from the so-called fermion doubling problem [13, 71], caused by the methods' dispersion relations allowing two wave different numbers to produce a single energy value and leading to unphysical solutions of the Dirac equation, since theoretically an energy value $E = \sqrt{m^2 + k^2}$ is determined by a single wave number $|k|$. In Figure 2.9 we can see that the QLB dispersion relation increases monotonically up to the maximum wave number for a given grid size, and therefore the QLB scheme is free from this defect.

We also would like to point out an example of the unphysical behaviour of the wave function that can result from limits of the simulation domain being insufficiently large allow for unrestricted dispersion of the evolving wave functions. Simulating confined wave packets in a harmonic potential correctly reproduces a lack of dispersion of the wave packet, composed mostly of the positive energy component of the wave function and confined by the repelling potential on both sides. However the negative energy component, although small in magnitude, will be attracted by the positive potential and reach the sides of the domain. Given periodic boundary conditions of our simulations, this can result in a standing wave pattern developing at the edges of the domain as the wave function attempts to travel beyond the boundaries and is met with a symmetrical wave function incoming from the other side. Increasing the domain resolves the problem, as shown in Figure 2.10. In this example the negative energy component is three to four orders of magnitude smaller than the positive energy component.

Chapter 3

QLB simulation in one dimension

Having shown that the QLB scheme is more suited to simulation of systems governed by the Dirac equation than the Schrödinger equation due to additional errors introduced by the non-relativistic approximation and the limits requiring kinetic energy and external potential to be much smaller than particle mass, we use a relativistic quantum system to further study the quantum lattice Boltzmann scheme. In this section we present the results of QLB simulations of a wave packet incident onto a step potential of variable height in one dimension, and compare with our theoretical calculations and previous numerical results in the literature. In particular, we are interested in the simulation of the so-called Klein paradox – a relativistic quantum tunnelling phenomenon that occurs under a critical potential height that is greater than twice the particle energy. A quantum particle incident onto a potential step or barrier has a chance of tunnelling through the barrier given by the transmission probability, and a chance to be reflected given by the reflection probability. In non-relativistic quantum tunnelling, as governed by the Schrödinger equation, the transmission coefficient decays as the height of the potential is increased and becomes zero as the waves of the wave function become evanescent inside the potential. When Klein studied [54] the evolution of the same system in relativistic systems according to then newly derived Dirac equation, he found that as the potential height increased further and further, there once again appeared a non-zero probability of transmission, interpreted as a negative energy wave function excited by the interaction of the incident particle with the strong potential [1].

3.1 Quantum tunnelling and the Klein paradox

Although thoroughly studied over the years since its publication in 1929 [54], the Klein paradox had not been observed experimentally due to the very high potentials it requires to manifest itself in the behaviour of elementary particles, such as positron production around unstable super-heavy nuclei, for example. However, with the recent discovery and isolation of monolayers of graphite in a laboratory by Novoselov and Geim, it became possible to observe Klein tunnelling in an accessible 'tabletop' experiment [63, 3, 82]. The Klein paradox was also observed with trapped ions used to simulate relativistic quantum systems [39]. Since the Klein tunnelling phenomenon has been recently experimentally confirmed, interest in this topic has grown considerably. The one-atom thick monolayer of graphite is called graphene, and we will discuss its properties and application of QLB scheme to simulation of its charge carriers in more detail in a subsequent chapter.

Strictly speaking 'Klein tunnelling' is not a tunnelling effect in the traditional quantum mechanical meaning because it does not rely on the carrying of the probability density by evanescent waves entering classically forbidden regions [3]. Instead, the incident positive energy wave function is matched inside the potential with a negative energy wave function that is excited into the positive energy range by the strong potential. But we stick with the accepted terminology to avoid confusion and under 'Klein tunnelling' imply this kind of transition. Before presenting the simulation results, we discuss the theoretical analysis of the Klein paradox in the next section.

3.1.1 Potential step plane wave tunnelling

Quantum tunnelling theory is traditionally formulated in terms of plane waves, with transmission and reflection coefficients corresponding to probability currents. We start with the one-dimensional standard form of the Dirac equation (1.21),

$$(\partial_t + c\boldsymbol{\alpha}_z\partial_z)\begin{pmatrix}\Phi_1^+\\ \Phi_2^+\\ \Phi_1^-\\ \Phi_2^-\end{pmatrix} = (-i\omega_c\boldsymbol{\beta} + ig)\begin{pmatrix}\Phi_1^+\\ \Phi_2^+\\ \Phi_1^-\\ \Phi_2^-\end{pmatrix} \tag{3.1}$$

where $\omega_c = mc^2/\hbar$ is the Compton frequency, and $g \equiv qV(z)/\hbar$. The top two components of the wave function are spin up and down positive energy components, and

the bottom two negative energy components go to zero as we approach the limit of low energies, where the system can be described by the non-relativistic Schrödinger equation. We consider plane wave solutions to this equation, with no dependence on x or y coordinates. Because there are no spin flipping processes with the only momentum component in the direction of the one dimension [40] we can drop the spin index and reduce the system to two equations in one dimension,

$$\partial_t \begin{pmatrix} \Phi^+ \\ \Phi^- \end{pmatrix} + c \begin{pmatrix} 0 & 1 \\ 1 & 0 \end{pmatrix} \partial_z \begin{pmatrix} \Phi^+ \\ \Phi^- \end{pmatrix} = \begin{pmatrix} i\left(g - \omega_c\right) & 0 \\ 0 & i\left(g + \omega_c\right) \end{pmatrix} \begin{pmatrix} \Phi^+ \\ \Phi^- \end{pmatrix}. \tag{3.2}$$

The probability density ρ and probability current j^z for this wave function $\Psi = \left(\Phi^+ \ \Phi^-\right)^T$ are given by

$$j^z = \Psi^\dagger \begin{pmatrix} 0 & 1 \\ 1 & 0 \end{pmatrix} \Psi, \qquad \rho = \Psi^\dagger \Psi, \tag{3.3}$$

where the $\Psi^\dagger$ represents a Hermitian conjugate of the wave function, and the total probability is conserved, $\partial_t \rho + \partial_z j^z = 0$. The right-going incident and left-going reflected plane waves for a potential step are given by

$$\psi_I\left(z\right) = e^{ikz} \begin{pmatrix} 1 \\ \frac{k}{E+m} \end{pmatrix} \quad \psi_R\left(z\right) = re^{-ikz} \begin{pmatrix} 1 \\ \frac{-k}{E+m} \end{pmatrix}, \tag{3.4}$$

where r is the amplitude of the reflected wave. The transmitted plane wave and its wave number are given by

$$\psi_T\left(z\right) = \tau e^{iqz} \begin{pmatrix} 1 \\ \frac{q}{E-V+m} \end{pmatrix} \qquad q = \pm\sqrt{\left(E-V\right)^2 - m^2}, \tag{3.5}$$

where τ is the amplitude of the transmitted wave [89]. We can derive a relationship between the reflected and transmitted wave amplitudes from the continuity of the wave function at the potential step,

$$1 + r = \tau \qquad 1 - r = \kappa\tau. \tag{3.6}$$

The kinematic factor κ is

$$\kappa = \frac{q\left(E+m\right)}{k\left(E-V+m\right)}. \tag{3.7}$$

The transmitted wave function is composed of negative energy states when the potential barrier is greater than twice the particle energy and high enough to excite them inside the barrier. For negative energy states the direction of momentum is anti-parallel to the direction of motion, so to get the correct right-going probability

current and the correct group velocity inside the potential we need $q < 0$ and therefore take the negative root in (3.5). This allows a simplification of κ,

$$\kappa = \sqrt{\frac{(V - E + m)(E + m)}{(V - E - m)(E - m)}}. \tag{3.8}$$

Using definition (3.3) we write down the probability currents for these plane waves,

$$j_I = \frac{2k}{E + m} \qquad j_R = -\frac{2|r|^2 k}{E + m} \qquad j_T = \frac{2|\tau|^2 q}{E - V + m}, \tag{3.9}$$

with right-going currents defined positive and left-going current negative. In the $z < 0$ region the total probability current is equal to $j_I + j_R$, and in the $z > 0$ region inside the potential the current is j_T. The reflection and transmission coefficients are defined as ratios of probability currents,

$$R_{Step} = \left|\frac{j_R}{j_I}\right| = |r|^2 = \left(\frac{1 - \kappa}{1 + \kappa}\right)^2 \qquad T_{Step} = \left|\frac{j_T}{j_I}\right| = |\tau|^2 \kappa = \frac{4\kappa}{(1 + \kappa)^2}, \tag{3.10}$$

where the total probability current is conserved because $R_{Step} + T_{Step} = 1$ [1].

3.1.2 Wave packet transmission

In simulation of real particles that are represented by wave packets instead of plane waves the wave packet is split into a reflected and a transmitted component, with the transmission coefficient equal to the total probability density that passes through the barrier. For a more quantitative error analysis of the Klein paradox QLB wave packet simulation we would like to compare the measured total probability density transmitted in the simulations with the theoretical transmission coefficient for a wave packet, and study the convergence to the theoretical value.

The transmission coefficient given by (3.10) is for a momentum eigenstate with a definite wave number k. We can calculate the transmission coefficient for our initial wave packet by expressing the wave packet as a superposition of right-going eigenstates, similar to the approach taken by Nitta et. al. to construct their wave packet [44]. Using the incident plane waves given by (3.4) we write our initial wave packet, normalized to $\int_{-\infty}^{\infty} |\Psi_0|^2 \, dx = 1$, as

$$\Psi_0(z) = \begin{pmatrix} \Phi_0^+ \\ \Phi_0^- \end{pmatrix} = \int_{-\infty}^{\infty} \hat{\Phi}_0^+(k) \begin{pmatrix} 1 \\ \frac{k}{E(k)+m} \end{pmatrix} e^{ikz} dk, \tag{3.11}$$

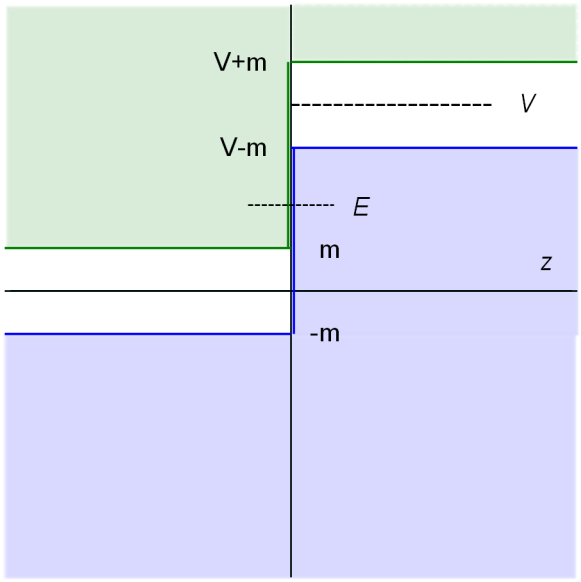

Figure 3.1: Relative energies on the left and right side of the potential step (right). An electron with energy E scattering off a potential step of height V. Shaded regions show positive (top, green) and negative (bottom, blue) energy continuum. In the region $z > 0$ the strong ($V > 2m$) potential is able to excite negative energy states up to positive energy, and if the energy of the incoming particle falls in the region where the positive energy on the left and the excited negative energy on the right overlap, Klein tunnelling occurs. The three cases we simulate correspond to the $E > V + m$, $V - m < E < V + m$, and $m < E < V - m$ regions in the Figure.

where $\hat{\Phi}_0^+(k)$ is the Fourier transform of the initial u component given as a real space Gaussian wave packet. It gives the distribution of wave numbers making up the wave packet. We use a unitary Fourier transform that is given by

$$\hat{\Phi}_0^+ = \frac{1}{\sqrt{2\pi}} \int_{-\infty}^{\infty} \Phi_0^+(z)\, e^{-ikz} dz. \tag{3.12}$$

The initial wave packet is given by

$$\Phi_0^+ = \eta \frac{1}{(2\pi\Delta^2)^{1/4}} e^{\frac{-(z-z_0)^2}{4\Delta^2} + ik_0 z}, \tag{3.13}$$

where η is a normalization factor

$$\eta = \sqrt{\frac{32m^2\Delta^2}{1 + 4k_0^2\Delta^2 + 16m^2\Delta^2}}. \tag{3.14}$$

The greater the width of the initial wave packet in real space, the narrower is its distribution in momentum space, and the smaller is the range of wave numbers necessary

to create it. Note that as k approaches zero, $\frac{k}{E+m}$ in the negative energy component of the plane wave solution (3.4) approaches $\frac{k}{2m}$, and our initial wave packet approaches the adiabatic assumption $\phi^- = \frac{c}{2i\omega_c}\partial_z\phi^+$ made in the above derivation of the Schrödinger equation as the non-relativistic limit of the Dirac equation (2.58).

We can then express the reflected and transmitted wave functions $\Psi_R(z,t)$ and $\Psi_T(z,t)$ as superpositions of reflected and transmitted plane waves. The evolution of a plane wave eigenstate is given by multiplication by e^{-iEt}, so we can calculate the evolution of the wave packet as a superposition of evolving plane waves,

$$\Psi_R(z,t) = \int_{-\infty}^{\infty} r(k)\,\hat{\Phi}_0^+(k)\,e^{-ikz-iE(k)t}\begin{pmatrix}1\\ \frac{-k}{E(k)+m}\end{pmatrix}dk. \tag{3.15}$$

$$\Psi_T(z,t) = \int_{-\infty}^{\infty} \tau(k)\,\hat{\Phi}_0^+(k)\,e^{iq(k)z-iE(k)t}\begin{pmatrix}1\\ \frac{q(k)}{E(k)+m-V_0}\end{pmatrix}dk. \tag{3.16}$$

Using Plancharel's Theorem

$$\int_{-\infty}^{\infty}|\Psi(z)|^2dz = \int_{-\infty}^{\infty}|\hat{\Psi}(k)|^2dk, \tag{3.17}$$

we can then calculate the total reflection and transmission probability by integrating the probability distribution $|\Psi|^2$ of the reflected and transmitted wave packets Ψ_R and Ψ_T in momentum space as follows,

$$\int_{-\infty}^{\infty}|\Psi_R|^2dx = \int_{-\infty}^{\infty}|\Phi_R^+|^2+|\Phi_R^-|^2dx = \int_{-\infty}^{\infty}\left|\hat{\Phi}_0^+(k)\right|^2\left(1+\left(\frac{-k}{E(k)+m}\right)^2\right)|r(k)|^2\,dk, \tag{3.18}$$

$$\int_{-\infty}^{\infty}|\Psi_T|^2dx = \int_{-\infty}^{\infty}|\Phi_T^+|^2+|\Phi_T^-|^2dx = \int_{-\infty}^{\infty}\left|\hat{\Phi}_0^+(q)\right|^2\left(1+\left(\frac{q}{E(q)+m-V_0}\right)^2\right)|\tau(q)|^2\,dq, \tag{3.19}$$

where q is a function of k as given by equation (3.5). The sum of the total reflected and transmitted probabilities is equal to one, so the transmission coefficient for a wave packet may be written as

$$T_{Wavepacket} = 1-\int_{-\infty}^{\infty}|\Psi_R|^2dz, \tag{3.20}$$

and that is the formula we will use to calculate the theoretical transmission.

3.1.3 Potential barrier

We can also write down the plane wave solutions for tunnelling through a rectangular potential barrier of finite width d in a similar way,

$$\psi_I(z) = e^{ikz}\begin{pmatrix}1\\ \frac{k}{E+m}\end{pmatrix} \quad \psi_R(z) = re^{-ikz}\begin{pmatrix}1\\ \frac{-k}{E+m}\end{pmatrix} \tag{3.21}$$

$$\psi_B(z) = b_1 e^{iqz}\begin{pmatrix} 1 \\ \frac{q}{E+m-V_0} \end{pmatrix} + b_2 e^{-iqz}\begin{pmatrix} 1 \\ \frac{-q}{E+m-V_0} \end{pmatrix} \tag{3.22}$$

$$\psi_T(z) = \tau e^{ikz}\begin{pmatrix} 1 \\ \frac{k}{E+m} \end{pmatrix} \qquad q = \pm\sqrt{(E-V)^2 - m^2}, \tag{3.23}$$

where b_1 and b_2 are amplitudes of the left-going and right-going waves inside the barrier [89]. We derive equations for the plane wave amplitudes from the boundary conditions that require matching wave function values at the boundaries between the outside and inside of the potential barrier,

$$1 + r = b_1 + b_2 \qquad \frac{k(1-r)}{E+m} = \frac{q(b_1 - b_2)}{E+m-V_0}, \tag{3.24}$$

$$\tau e^{ika} = b_1 e^{iqa} + b_2 e^{-iqa} \qquad \frac{\tau k e^{ika}}{E+m} = \frac{q(b_1 e^{iqa} - b_2 e^{-iqa})}{E+m-V_0}. \tag{3.25}$$

As before for the potential step, we calculate the probability currents using (3.3),

$$j_{in} = \frac{2k}{E+m} \qquad j_{refl} = -\frac{2|r|^2 k}{E+m} \qquad j_{trans} = \frac{2|\tau|^2 k}{E+m} \tag{3.26}$$

and write down the reflection and transmission probabilities,

$$R_{Barrier} = \left|\frac{j_{refl}}{j_{in}}\right| = |r|^2 \qquad T_{Barrier} = \left|\frac{j_{trans}}{j_{in}}\right| = |\tau|^2. \tag{3.27}$$

Solving (3.21)-(3.23) for the amplitude of the transmitted wave we get the plane wave transmission coefficient for a potential barrier,

$$T_{Barrier1D} = \frac{4\kappa^2}{4\kappa^2 + (1-\kappa^2)^2 \sin^2(qd)}, \tag{3.28}$$

where kinematic factor κ is given by (3.7) and the transmitted momentum inside the potential q by (3.5) as before. Note that for a given barrier height and energy of the incident particle, particular barrier widths cause a transmission resonance to occurs - when $qd = n\pi$ we have $\sin(qd) = 0$ and the transmission coefficient is equal to 1 [1]. This effect is analogous to Fabry-Perot resonances in optical systems, the waves interfere constructively when a half-integer number of wavelengths ($2\pi/q$) fit inside the barrier [3]. We can then use the same approach with Plancharel's Theorem to calculate the wave packet transmission coefficient for tunnelling through a barrier.

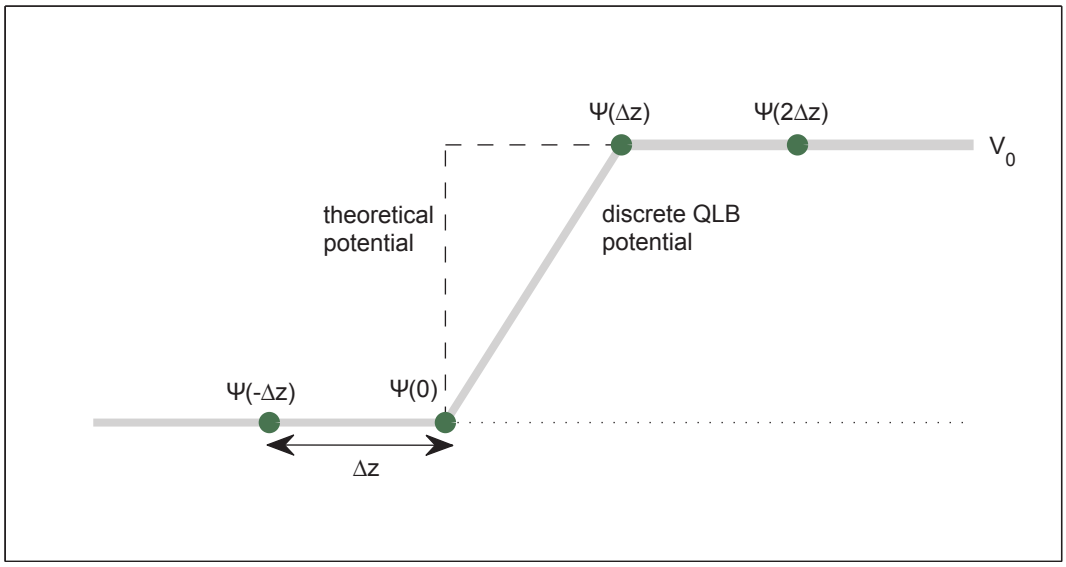

Figure 3.2: A scheme of the discrete potential step as defined in the QLB algorithm, with values on the left and right of the barrier given by plane wave solutions, and solved for wave function values points $z = 0$ and $z = \Delta z$.

3.1.4 QLB evolution of plane waves

It is instructive to analyze the effects of the QLB algorithm on plane waves of a single wave number k and compare with the theoretical evolution by the Dirac equation to see how the plane waves are modified in the QLB scheme, and how the plane waves change when crossing the potential step. We will use the previously derived eigenvalues and eigenvectors of the evolution matrices $\mathsf{E}_{\mathrm{QLB}}$ and E given in (2.18) and (2.19) to compose the theoretical and QLB plane waves for our form of the Dirac equation, transformed into u and d components.

Substituting $u(z,t) = \hat{u}\,(t)\,e^{ikz}$ and $d(z,t) = \hat{d}\,(t)\,e^{ikz}$ for fixed k into the QLB scheme (2.42), we obtain plane waves $\hat{u}$ and $\hat{d}$ that are evolved by

$$\begin{pmatrix} \hat{u}(t+\Delta t) \\ \hat{d}(t+\Delta t) \end{pmatrix} = \mathsf{E}_{\mathrm{QLB}} \begin{pmatrix} \hat{u}(t) \\ \hat{d}(t) \end{pmatrix}. \tag{3.29}$$

The $\mathsf{E}_{\mathrm{QLB}}$ matrix is given in equation (2.18) and is of the form

$$\begin{pmatrix} A & B \\ -B^* & A^* \end{pmatrix} \tag{3.30}$$

where A and B correspond to the shifting by one grid space and transformation by collision constants a and b given in (2.65), A^* is the complex conjugate of A. We have

switched the notation of matrix elements here to avoid confusion with the momentum of the plane waves. The eigenvectors of a matrix of this form are given by

$$\begin{pmatrix} B/\left(\lambda_{\pm} - A\right) \\ 1 \end{pmatrix}, \tag{3.31}$$

corresponding to positive (λ_{-}) and negative (λ_{+}) energy solutions. The eigenvalues of $\mathsf{E}_{\mathrm{QLB}}$ were derived in a previous section, and we repeat them here for convenience. They are given by

$$\tilde{\lambda}_{\pm} = \cos\left(k\Delta t\right)\left(\frac{1-\frac{1}{4}m^2\Delta t^2}{1+\frac{1}{4}m^2\Delta t^2}\right) \pm i\left(1-\cos^2\left(k\Delta t\right)\left(\frac{1-\frac{1}{4}m^2\Delta t^2}{1+\frac{1}{4}m^2\Delta t^2}\right)^2\right)^{\frac{1}{2}}. \tag{3.32}$$

We may rewrite them as $\lambda_{\pm} = \exp(\pm i\tilde{\Omega}\Delta t)$, where

$$\tilde{\Omega} = \frac{1}{\Delta t}\cos^{-1}\left\{\cos\left(k\Delta t\right)\left(\frac{1-\frac{1}{4}m^2\Delta t^2}{1+\frac{1}{4}m^2\Delta t^2}\right)\right\}, \tag{3.33}$$

The eigenvalues and eigenvectors of the exact evolution matrix E were also first given above and are equal to

$$\lambda_{\pm} = \exp(\pm i\Omega\Delta t) \qquad \mu_{\pm} = \begin{pmatrix} \frac{i}{m}\left(k \pm \Omega\right) \\ 1 \end{pmatrix}, \tag{3.34}$$

where $\Omega = \sqrt{k^2+m^2}$ is the corresponding particle energy. We can use the eigenvalues and eigenvectors of the QLB evolution matrices to express the QLB plane waves analytically, as they are represented in the algorithm, solve for the QLB reflection and transmission amplitudes, and explicitly show their convergence to the theoretical values. For a rectangular potential step at $z = 0$, as we are considering above, the wave function on the left of the barrier is given by

$$\psi_{z<0}\left(z,t\right) = e^{ikz}\begin{pmatrix} \frac{B(k)}{(\lambda_{-}-A(k))} \\ 1 \end{pmatrix} e^{-i\tilde{\Omega}\Delta t} + r_{QLB}e^{-ikz}\begin{pmatrix} \frac{B(-k)}{(\lambda_{-}-A(-k))} \\ 1 \end{pmatrix} e^{-i\tilde{\Omega}\Delta t}, \tag{3.35}$$

corresponding to the theoretical incident and reflected waves in (3.4). On the other side of the step we have a constant potential, the exact evolution matrix is $\mathsf{E}_g = e^{ig\Delta t}\mathsf{E}$, where E is the free particle evolution matrix (2.19), and the eigenvectors are

$$\begin{pmatrix} \frac{i}{m}\left(q \pm \Omega - V\right) \\ 1 \end{pmatrix}, \tag{3.36}$$

The QLB evolution matrix for a constant potential is given by (2.70) and can be represented in the form

$$\frac{|s|}{s}\begin{pmatrix} A_g & B_g \\ -B_g^* & A_g^* \end{pmatrix}, \tag{3.37}$$

where $s = 1 + \frac{1}{4}\Delta t^2(m^2 - g^2) - ig\Delta t$ and matrix terms A_g and B_g have $|s|$ in their denominators. Using (2.28) we expressed its eigenvalues as

$$\tilde{\lambda}_{\mathrm{g},\pm} = \exp(i(\tilde{g} \pm \tilde{\Omega}_g)\Delta t), \tag{3.38}$$

where

$$\tilde{g} = \frac{1}{\Delta t}\tan^{-1}\left(\frac{g\Delta t}{1 + \frac{1}{4}\Delta t^2\left(m^2 - g^2\right)}\right), \tag{3.39}$$

and

$$\tilde{\Omega}_g\left(k\right) = \frac{1}{\Delta t}\cos^{-1}\left(\mathrm{Re}\ A_g\right) = \cos^{-1}\left(\frac{\cos\left(k\Delta t\right)\left(1 - \frac{1}{4}\Delta t^2\left(m^2 - g^2\right)\right)}{|1 + \frac{1}{4}\Delta t^2(m^2 - g^2) - ig\Delta t|}\right). \tag{3.40}$$

Using the formula (3.31) for the eigenvectors of $\tilde{\mathsf{E}}_{\mathrm{g}}$, with the eigenvalue scaled by the inverse of the $|s|/s$ factor we took outside the evolution matrix in (3.37), we can then write down the QLB plane wave inside the potential

$$\psi_{z>0}\left(z,t\right) = \tau_{QLB}e^{iq_{QLB}z}\begin{pmatrix}\frac{B_g\left(q_{QLB}\right)}{\left(\frac{s}{|s|}\lambda_{g,-} - A_g\left(q_{QLB}\right)\right)}\\ 1\end{pmatrix}e^{i\left(\tilde{g} - \tilde{\Omega}_g\left(q_{QLB}\right)\right)\Delta t}. \tag{3.41}$$

The wave number q_{QLB} for the plane wave inside the potential is given by equating the energy levels of the states on both sides of the barrier,

$$-\tilde{\Omega}\left(k\right) = \tilde{g} - \tilde{\Omega}_g\left(q_{QLB}\right), \tag{3.42}$$

and taking the negative solution. It is given by

$$q_{QLB} = -\frac{1}{t}\cos^{-1}\left(\frac{4\left|1 - ig\Delta t + 0.25\Delta t^2\left(m^2 - g^2\right)\right|}{4 - m^2\Delta t^2 + g^2\Delta t^2}\cos\left(\Gamma\right)\right), \tag{3.43}$$

where

$$\Gamma = \cos^{-1}\left(\frac{\left(1 - 0.25m^2\Delta t^2\right)\cos\left(k\Delta t\right)}{1 + 0.25m^2\Delta t^2}\right) + \tan^{-1}\left(\frac{g\Delta t}{1 + 0.25\Delta t^2\left(m^2 - g^2\right)}\right), \tag{3.44}$$

and converges to the wave number q given by (3.5). The energy $\tilde{\Omega}_g\left(q_{QLB}\right)$ here corresponds to the negative energy states raised into the positive energy spectrum by the potential.

Unlike the infinitely steep potential step at $z = 0$ we are aiming to simulate, the discrete potential in the QLB algorithm has a finite slope and increases from $g(0) = 0$ to $g(\Delta z) = V_0$ over the length of one grid spacing. We can assume that to the left and to the right of the potential step the wave function is given by the QLB plane

waves (3.35) and (3.41) and evolved by a phase rotation $e^{-i\tilde{\Omega}\Delta t}$, but the values at the points $z = 0$ and $z = \Delta z$ have to accommodate the change in the potential and are unknown. We can solve for the wave function at those points and the amplitudes of the reflected and transmitted QLB plane waves by equating the wave function values at points near the potential, $z = -\Delta z, 0, \Delta z, 2\Delta z$, evolved by the QLB algorithm and by the uniform phase rotation. We get a set of six equations for the u and d components of the wave functions,

$$\begin{pmatrix} d\,(-\Delta z) \\ u\,(0) \\ d\,(0) \\ u\,(\Delta z) \\ d\,(\Delta z) \\ u\,(2\Delta z) \end{pmatrix} e^{-i\tilde{\Omega}\Delta t} = \begin{pmatrix} a\,d\,(0) - b\,u\,(0) \\ a\,u\,(-\Delta z) + b\,d\,(-\Delta z) \\ a\,d\,(\Delta z) - b\,u\,(\Delta z) \\ a\,u\,(0) + b\,d\,(0) \\ a\,d\,(2\Delta z) - b\,u\,(2\Delta z) \\ a\,u\,(\Delta z) + b\,d\,(\Delta z) \end{pmatrix}, \tag{3.45}$$

where a and b are the collision constants defined in (2.65), values of $u\,(-\Delta z)$, $d\,(-\Delta z)$, $u\,(2\Delta z)$, $d\,(2\Delta z)$ are given by the top and bottom components of the QLB plane waves (3.35) and (3.41), and $u\,(0)$, $d\,(0)$, $u\,(\Delta z)$, $d\,(\Delta z)$, r_{QLB}, τ_{QLB} are unknowns. Solving the system we obtain complex expressions for the unknowns, which we can use now to compare the values of the QLB amplitudes with the theoretical values of r and τ and show convergence of r_{QLB} and τ_{QLB} to the theory. The QLB reflection amplitude is given by

$$\begin{aligned} r_{QLB} = [e^{-2ik\Delta t}(-(a^2+b^2)(a_g^2+b_g^2)(b+aY_I)(a_g-b_gY_T)+(-a_gb(a_g^2+b_g(b+b_g+aY_I))+ \\ b_g(b(a^2+a_g^2+b^2+bb_g+b_g^2)+a(a^2+b(b+b_g))Y_I)Y_T)\lambda_-^2+ \\ (-a_gb_g+(b^2+b_g^2+b(b_g+aY_I))Y_T)\lambda_-^4+Y_T\lambda_-^6)]\times \\ [(a^2+b^2)(a_g^2+b_g^2)(b+aY_R)(a_g-b_gY_T)-(-a_gb(a_g^2+b_g(b+b_g+aY_R))+ \\ b_g(b(a^2+a_g^2+b^2+bb_g+b_g^2)+a(a^2+b(b+b_g))Y_R)Y_T)\lambda_-^2+ \\ (a_gb_g-(b^2+b_g^2+b(b_g+aY_R))Y_T)\lambda_-^4-Y_T\lambda_-^6]^{-1}, \end{aligned} \tag{3.46}$$

where a, b, a_g, b_g are the QLB collision constants for free particles and for particles in the presence of a potential, given by equations (2.65) and (2.60). The variables Y_I, Y_R and Y_T are the top components (the bottom component is equal to 1) of the QLB eigenvectors for incident, reflected and transmitted plane waves and are equal to

$$Y_I = \frac{B\,(k)}{\lambda_- - A\,(k)} \qquad Y_R = \frac{B\,(-k)}{\lambda_- - A\,(-k)} \qquad Y_T = \frac{B_g\,(q_{QLB})}{\frac{s}{|s|}\lambda_{g,-} - A_g\,(q_{QLB})}. \tag{3.47}$$

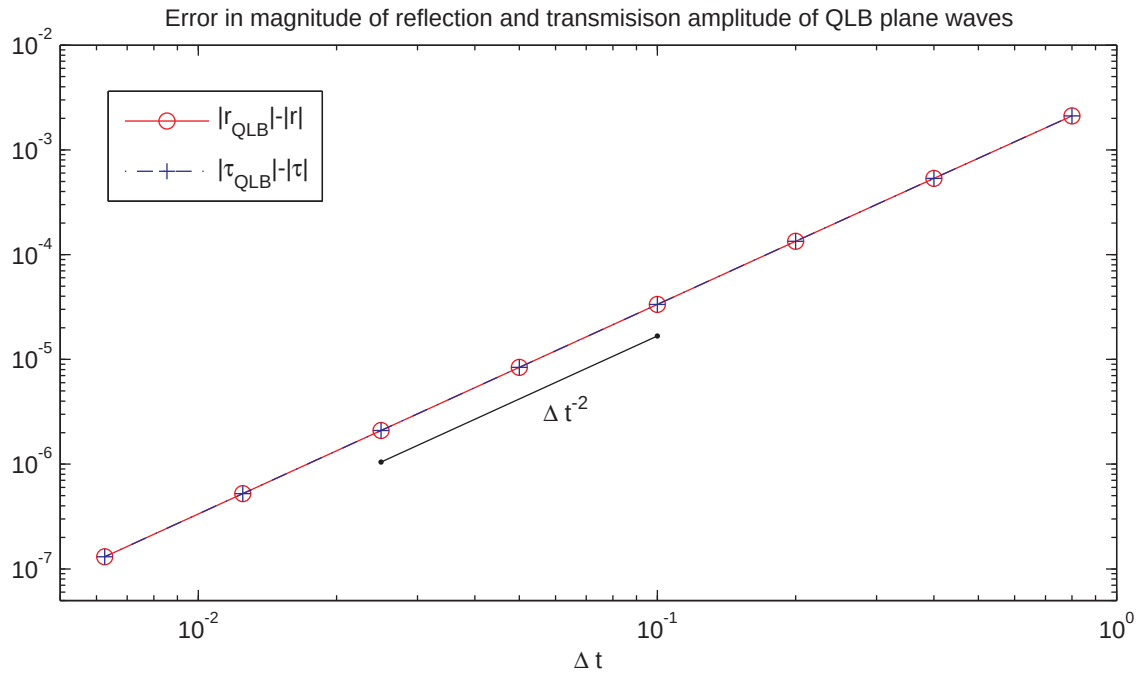

Figure 3.3: Errors in amplitudes of reflected and transmitted QLB plane waves, compared with the theoretical values, show second order convergence.

To confirm that the solutions we obtain in this way indeed give the complete QLB plane, we initialize a QLB algorithm with a plane wave over the domain and observe that each timestep of the QLB algorithm evolves the wave function at every grid point by an $e^{-i\tilde{\Omega}\Delta t}$ phase rotation.

Because the QLB plane waves are given in the form of the Dirac equation diagonalized along z-axis, and not in the standard form, the expressions for theoretical amplitudes of the incident, reflected, and transmitted waves we get are different from (3.10) and are obtained by equating theoretical plane waves given by eigenvectors (2.25) and (3.36) on both sides of the potential at $z = 0$ and solving for the amplitudes. They are equal to

$$r_z = -\frac{k - q + V}{k + q - V} \qquad \tau_z = 1 + r_z, \tag{3.48}$$

where $V = -\tilde{g}$ due to our sign convention in the QLB scheme. Using parameters of our simulations we now calculate the errors in r_{QLB} and τ_{QLB} and check their convergence, the results in Figure 3.3 show second order convergence.

In our simulations to study a particle moving towards the potential we initialize the QLB algorithm with a wave packet composed as a superposition of right going

plane waves, however because the QLB right going plane waves are different from the theoretical right going plane waves, given by (2.25) and (3.31) for the Dirac equation diagonalized along z-axis, each theoretical right going plane wave is composed of right going and left going QLB plane waves in the algorithm,

$$\begin{pmatrix} \frac{i}{m}(k+\Omega) \\ 1 \end{pmatrix} = \eta_1 \begin{pmatrix} \frac{B(k)}{(\lambda_- - A(k))} \\ 1 \end{pmatrix} + \eta_2 \begin{pmatrix} \frac{B(-k)}{(\lambda_- - A(-k))} \\ 1 \end{pmatrix}, \tag{3.49}$$

where $|\eta_2| < |\eta_1|$ for appropriately small Δt, and we can observe a very small amount of probability density moving away from the potential in the QLB simulations initialized in this way. Solving for η_1 and η_2 exactly they are given by,

$$\eta_1 = \frac{i\left(A\left(k\right) - \lambda_-\right)\left(iB\left(-k\right)m + \left(\Omega + k\right)\lambda_- - A\left(-k\right)\left(\Omega + k\right)\right)}{m\left(A\left(-k\right)B\left(k\right) - A\left(k\right)B\left(-k\right) + \left(B\left(-k\right) - B\left(k\right)\right)\lambda_-\right)} \tag{3.50}$$

$$\eta_2 = \frac{i\left(A\left(-k\right) - \lambda_-\right)\left(-iB\left(k\right)m - \left(\Omega + k\right)\lambda_- + A\left(k\right)\left(\Omega + k\right)\right)}{m\left(A\left(-k\right)B\left(k\right) - A\left(k\right)B\left(-k\right) + \left(B\left(-k\right) - B\left(k\right)\right)\lambda_-\right)}. \tag{3.51}$$

This effect is an additional source of error when calculating the transmitted probability density, for example, but the magnitude of the left going wave decreases with Δt and becomes negligible as we increase the grid size and reduce the timestep of the simulations. However, to obtain a pure right going wave packet in the QLB simulation we have to initialize with a wave packet composed of a mix of right going and left going plane waves,

$$\begin{pmatrix} \frac{B(k)}{(\lambda_- - A(k))} \\ 1 \end{pmatrix} = \mu_1 \begin{pmatrix} \frac{i}{m}(k+\Omega) \\ 1 \end{pmatrix} + \mu_2 \begin{pmatrix} \frac{i}{m}(-k+\Omega) \\ 1 \end{pmatrix}, \tag{3.52}$$

where the scaling parameters μ_1 and μ_2 are given by

$$\mu_1 = -\frac{A\left(k\right)\Omega - A\left(k\right)k - iB\left(k\right)m - \Omega\lambda_- + k\lambda_-}{2k\left(A\left(k\right) - \lambda_-\right)} \qquad \mu_2 = 1 - \mu_1. \tag{3.53}$$

Another important point we can learn from this analysis of the QLB plane waves is the correct alignment of the discrete potential with the step potential we are simulating. As mentioned before, the discrete potential slopes from $g(z) = 0$ to $g(z + \Delta z) = V_0$, and this can create a phase shift in r_{QLB} and τ_{QLB} depending on whether we are trying to simulate a step potential at z, $z + \Delta z/2$ or $z + \Delta z$. By studying the behaviour of QLB wave amplitudes we can say that to minimize the phase shift and additional error in the wave function output, the discrete potential should be placed such that the beginning of the slope coincides with the real step potential, $z = 0$ in our case – then the phase shift is on the order of round off error. Otherwise the phase shift is significant and converges at first order with grid spacing.

3.2 QLB simulation results

3.2.1 Tunnelling through a potential step

We aim to simulate a system of scattering from a potential step analogous to the one presented by Nitta, Kudo and Minowa [44] and compare our results with their solution of the time dependant one-dimensional Dirac equation, given in atomic units. The potential step is given by

$$V(z) = V_0 \, \Theta(z) \tag{3.54}$$

where $\Theta(z)$ is the Heaviside function, and V_0 is constant. We consider three values of V_0 which produce three qualitatively different systems with different results of the tunnelling. Based on Nitta, Kudo and Minowa's choice of parameters we use the following three values of V_0 relative to particle energy for our simulations,

$$V_0 = 0.05E, \qquad V_0 = E, \qquad V_0 = 5E. \tag{3.55}$$

They obey the following relationships between particle energy and potential height,

$$V_0 < E - mc^2 \qquad E - mc^2 < V_0 < E + mc^2 \qquad V_0 > E + mc^2, \tag{3.56}$$

and their qualitative differences are shown in Figure 3.1. In their work Nitta, Kudo and Minowa use atomic units with the speed of light equal to $c = 137 = \alpha^{-1}$, while the QLB convention is to use units in which $c = 1$, giving us the convenient $\Delta z = \Delta t$. To accomodate this difference we keep the atomic mass and length units but rescale time by the fine structure constant α. Rescaling time means we need to rescale mass to get the same mass parameter $m\Delta t$ in our simulations. We use $m = 137$ as the electron mass and rescale time such that $t_{atomic} = \alpha t_{QLB}$. We thus match the time scale of the scattering and can then compare the behaviour of our simulations with the results of Nitta, Kudo and Minowa. Following their values we set our parameters to wave number $k_0 = 50$, initial wave packet position $z_0 = -3.8$ and initial wave packet width $\Delta_0^2 = 0.55$ in atomic length units.

We initialize with the superposition of right-going plane waves (3.11) by using discrete Fourier Transforms,

$$\mathcal{F}\left[\Psi(z,t)\right] = \sum_{z \in L} \Psi(z,t) \, e^{-ikz} \qquad \mathcal{F}\left[{}^{-1}\hat{\Psi}(k,t)\right] = \frac{1}{N} \sum_{k \in K} \hat{\Psi}(k,t) \, e^{ikz}, \tag{3.57}$$

implemented with Fast Fourier Transforms as follows,

$$\Psi_0(z) = IFFT\left[FFT\left[\Phi_0^+\right]\left(\frac{1}{\frac{k}{\sqrt{k^2+m^2}+m}}\right)\right], \tag{3.58}$$

where we discretize our domain $L = [-20, 20]$ with $N = 16,384$ grid points. K is the reciprocal domain of wave numbers in Fourier space. In the first case of the potential heights given by (3.56) the energy of the incoming particle is greater than the height of the potential step and the incoming wave packet is scattered into a reflected component in the $z < 0$ region and a transmitted component that tunnels through the potential step in the $z > 0$ region. As shown in Figure 3.1, this corresponds to the positive energy continuums extending on both sides of the potential step, and qualitatively the result matches the evolution of the system according to the Schrödinger equation. The probability distribution function of this simulation is shown in Figure 3.4, with the incoming packet being split into a large transmitted and a smaller reflected component while conserving total probability.

In the second case, $V_0 = E$, the momentum of the transmitted component q becomes imaginary, producing an evanescent wave in the $z > 0$ region. The real part of the wave packet is then completely reflected, as shown in Figure 3.5. This also is the result predicted by the Schrödinger equation for $V_0 > E$ – the wave function decays exponentially inside the potential step.

However, as we increase the potential even further it reaches a critical point corresponding to the overlap of the positive and negative energy continuums in Figure 3.1 and is able to excite negative energy states inside the potential step. When the potential step height is greater than the total particle energy plus its rest mass, the momentum q inside the potential becomes real again, and there appears a non-zero transmission probability. As shown in Figure 3.6, the QLB simulation now allows a part of the incident wave packet to transmit through the strong repulsive potential. The transmitted probability density corresponds to the negative energy states excited by the interaction of the electron with the strong potential. Furthermore, as the potential is increased further to infinity, the transmission coefficient tends to a finite, non-zero limit.

Comparing our Figure 3.6 to Figure 3 in the Nitta, Kudo, Minowa paper [44] we can see the QLB simulation of the Klein paradox matches the results of the second numerical calculation performed by the authors, where the momentum inside the potential is negative, Klein paradox is interpreted as excitation of negative energy

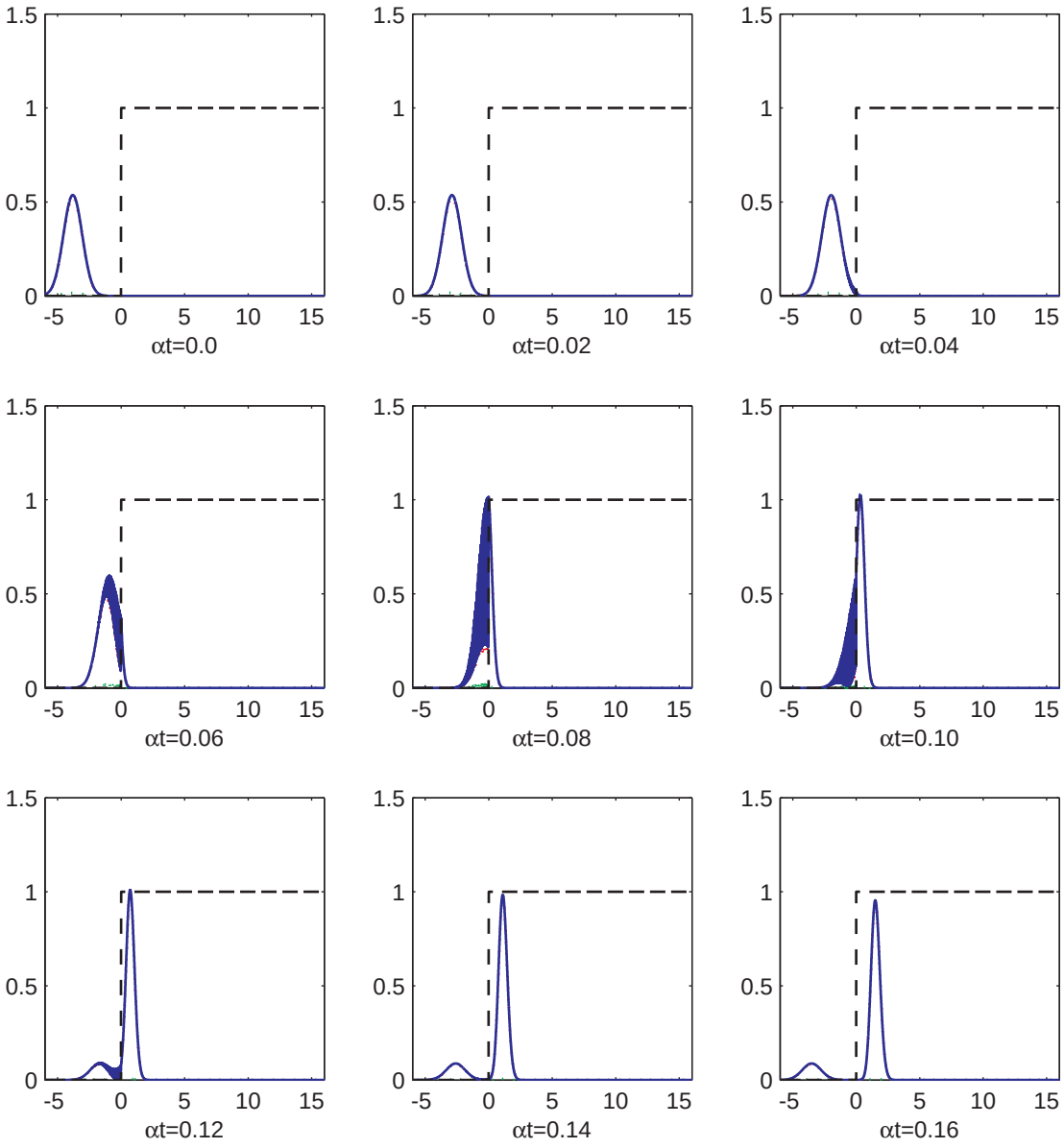

Figure 3.4: Simulation of wave packet with $V + m < E$. The incoming wave packet is partially reflected from the potential step, with the transmission coefficient decaying as the height of the potential step is increased. Time is scaled by the fine structure constant $\alpha = 1/137$ to match Nitta et. al. [44], αt – time in atomic units.

states inside the potential, and the total probability density is conserved. Note that the solid regions of our plots are closely packed Compton frequency oscillations of the scattering wave function near the potential step, and not defects of the QLB numerical method. Figure 3.7 shows a more detailed plot of these oscillations at the moment the wave packet tunnells into the barrier being resolved by the scheme. Similar oscillations near the potential barrier are also seen in the computer simulations of quantum

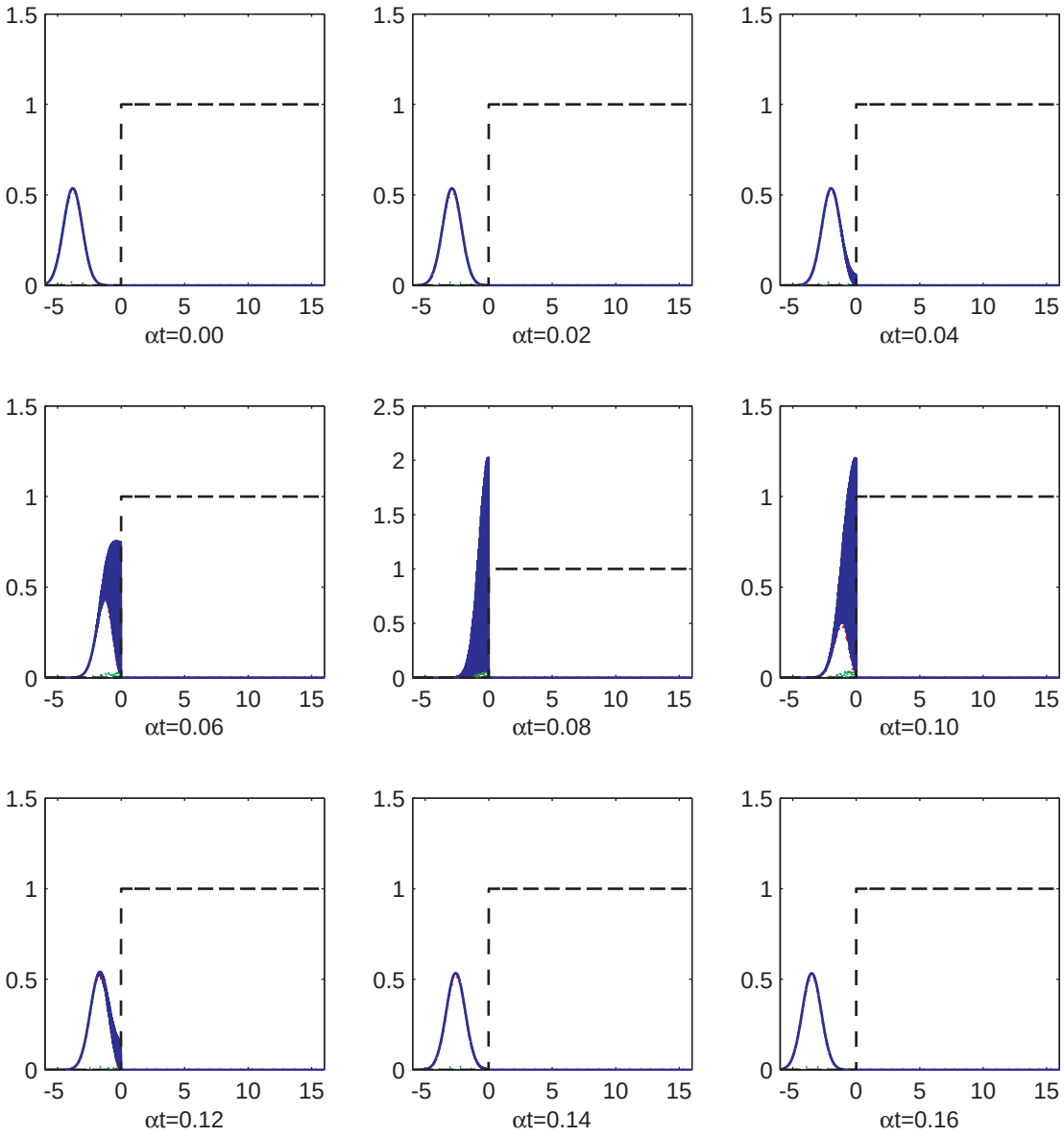

Figure 3.5: Simulation of wave packet with $V = E$. Increasing the height of the potential step causes the incoming wave packet to be reflected completely, the wave number of the tunnelling wave function inside the potential is imaginary. Time is scaled by the fine structure constant $\alpha = 1/137$ to match Nitta et. al. [44], αt – time in atomic units.

tunnelling performed by Huang et. al. in 1989 [51] to study the dependence of tunnelling time on the shape of the barrier. The QLB scheme producing a continuous evolution of the wave packet is also well suited to investigation of tunnelling times through a variety of potentials.

The total transmitted probability density in the QLB simulations is calculated as

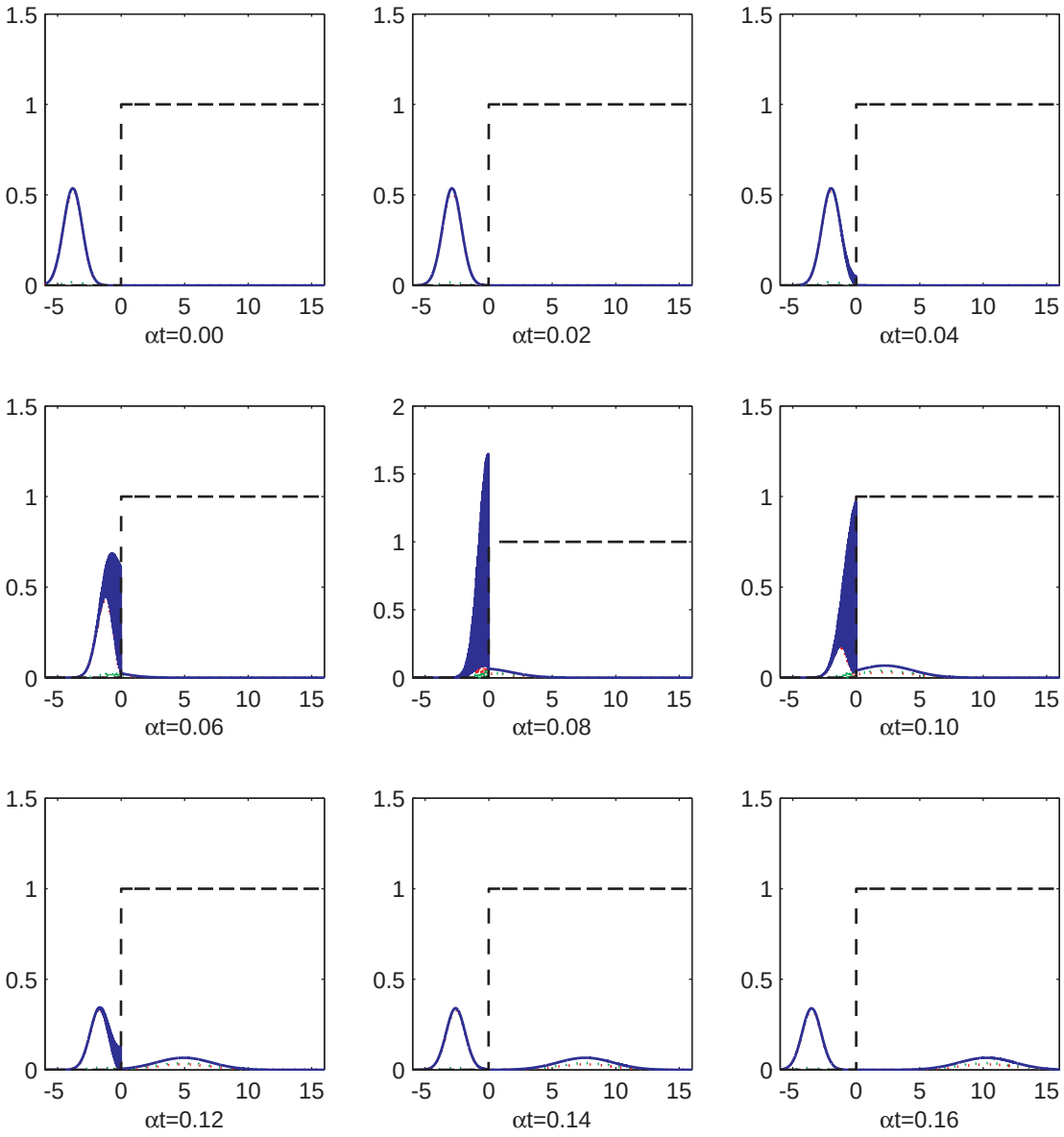

Figure 3.6: Simulation of wave packet with $V - mc^2 > E$. The potential step is raised once again and there appears a transmitted positron wave packet. Paradoxically, as the height of the potential step keeps growing, the transmission coefficient increases and approaches a non-zero limit. Time is scaled by the fine structure constant $\alpha = 1/137$ to match Nitta et. al. [44], αt – time in atomic units.

the sum of the discrete $|\Psi_{QLB}|^2$ values over the region to the right of the potential step at a time when the reflected and transmitted components have completely separated. Comparing that with the wave packet transmission coefficient given by (3.20) as we refine the grid, we observe second order convergence to the theoretical value, shown in Figure 3.9. As expected, the simulated wave function also converges to the $\Psi_R(z,t)$

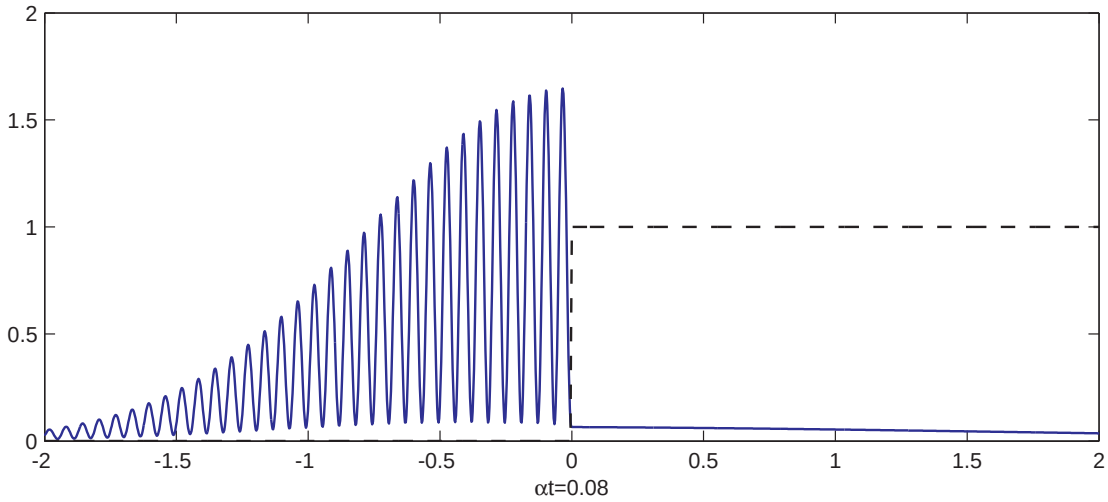

Figure 3.7: A close up of the Compton frequency oscillations of the wave function due to the scattering at the barrier during the tunnelling process.

and $\Psi_T(z,t)$ given by (3.15) and (3.16) at second order in our QLB scheme, shown in the bottom plot of Figure 3.9. On the same plot, the wave function simulated with the unmodified Succi-Benzi scheme converges at first order only.

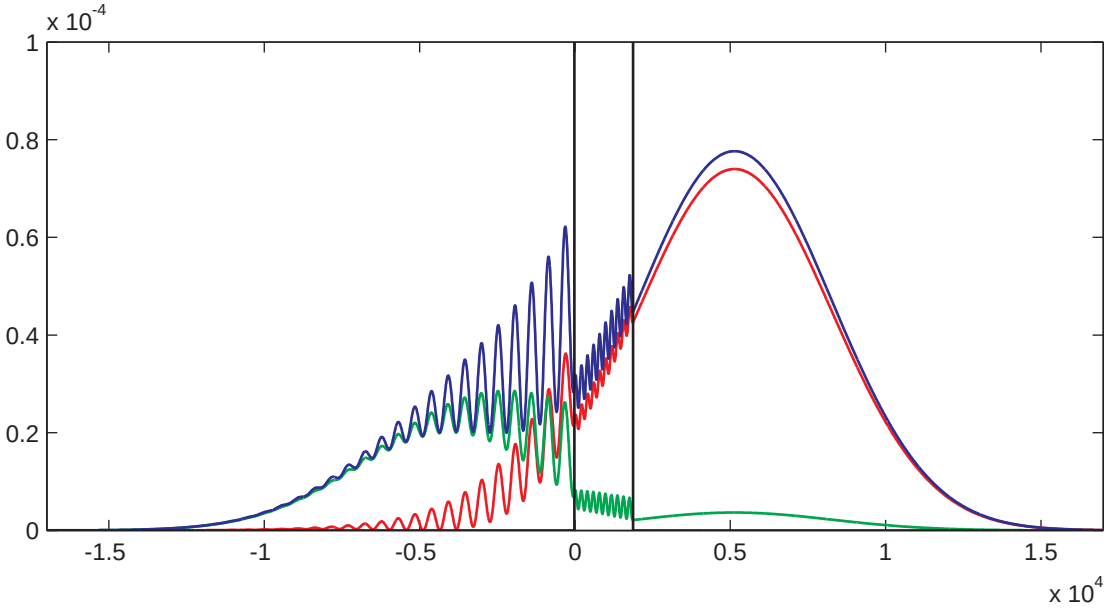

Figure 3.8: QLB simulation of a wave packet tunnelling through potential barrier in one dimension. Probability density $|\Psi|^2$ is plotted in blue, positive energy and negative energy components $|\psi^+|^2$ and $|\psi^-|^2$ making up the total probability density are plotted in red and green.

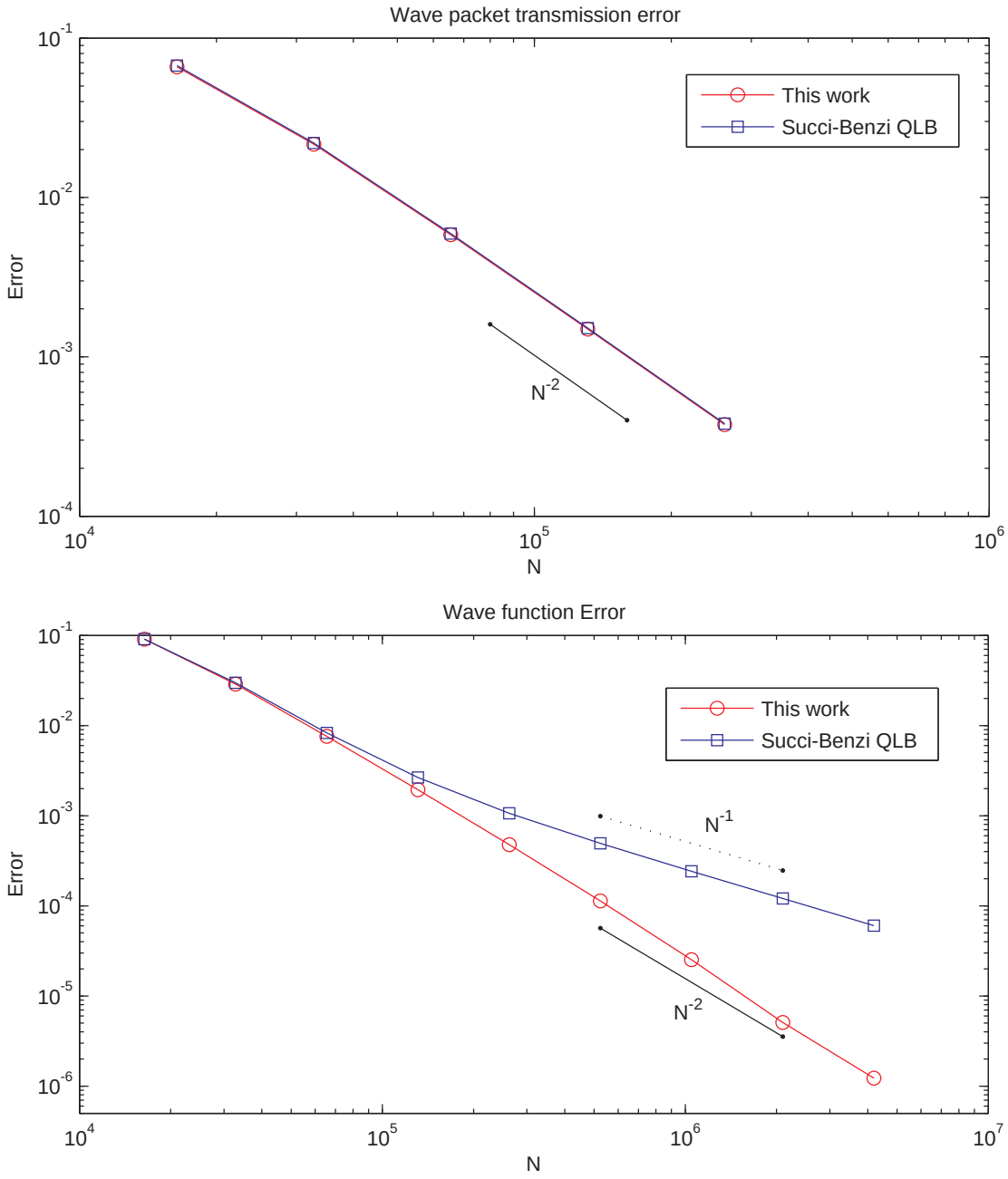

Figure 3.9: Second order convergence of the simulated wave packet transmission coefficient to the theoretical value $T_{Wavepacket}$ given by equation (3.20) (top panel). Second order convergence of the absolute value of the simulated reflected and transmitted wave function obtained with our QLB scheme to the theoretical wave function values given by equations (3.15) and (3.16) (bottom panel). The same plot shows first order convergence resulting from using the Succi-Benzi scheme to run the simulations. The results are plotted for increasing number of grid points N. [Data for bottom plot generated by P. Dellar]

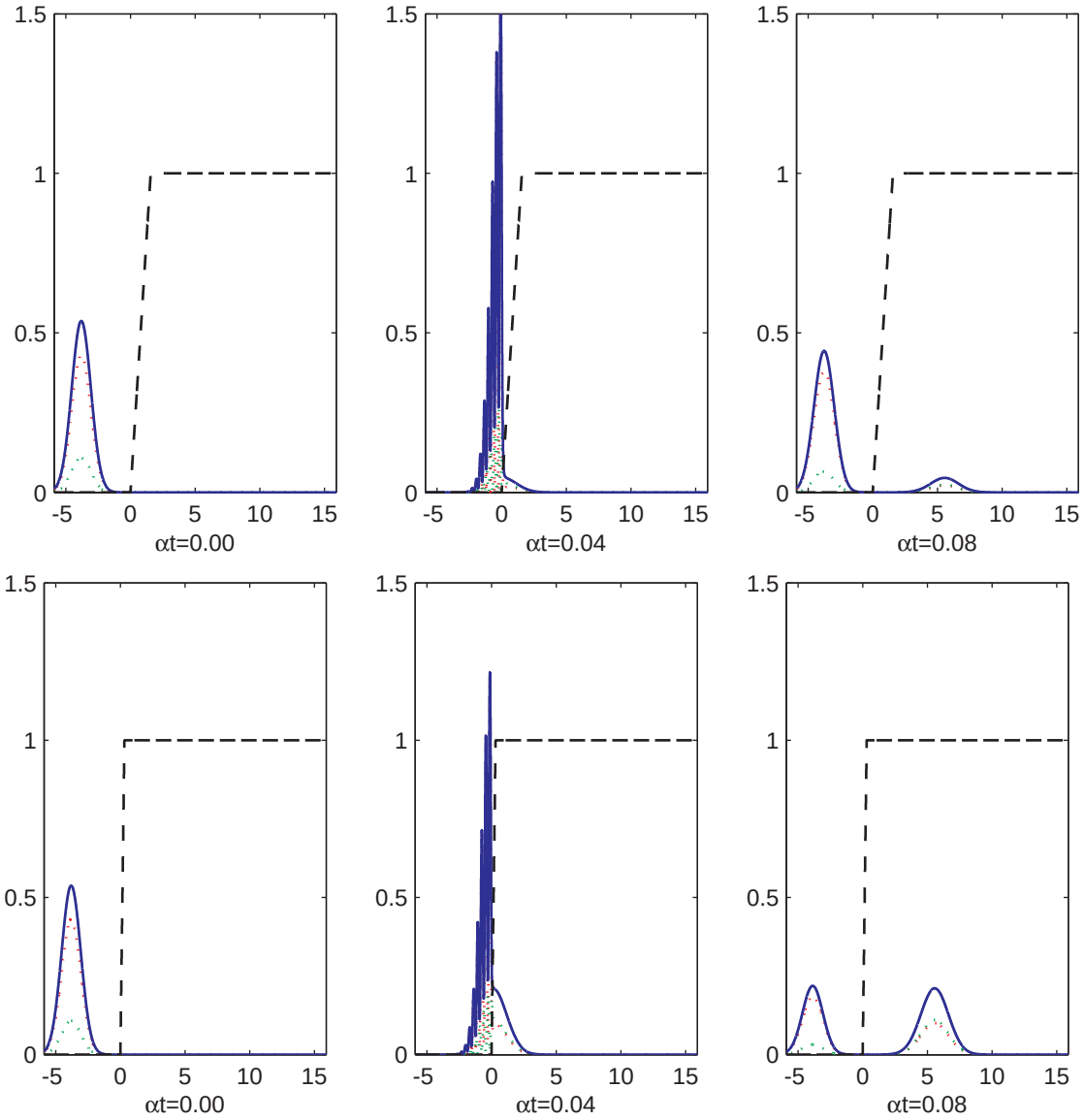

Figure 3.10: Simulation of the potential step with a finite slope. The transmission coefficient is exponentially damped (top). Steepening the slope causes the transmission coefficient to approach the limit of the vertical potential step, allowing a greater transmission probability (bottom). Time is scaled by the fine structure constant $\alpha = 1/137$ to match Nitta et. al. [44], αt – time in atomic units.

3.2.2 Tunnelling through sloping potential and barrier

We also simulate the more physically realistic case of a sloping potential over a region of length L that is given by

$$V(z) = 0 \quad z < 0; \quad V(z) = V_{slope} z \quad 0 \leq z \leq L; \quad V(z) = V_{slope} L \quad z > L. \tag{3.59}$$

This potential represents a constant electric field in a finite region of space, and the theoretical plane wave transmission coefficient for such a potential was calculated by Sauter [86],

$$T_{Slope} = e^{-\left(\pi m^2 L/\Delta V\right)}. \tag{3.60}$$

It is valid for potentials that are not strong enough to excite the negative energy states over a length scale on the order of the Compton wavelength of the electron, $V_{slope}L < 2m$, and the transmitted wave function becomes exponentially damped as it enters the region of the potential. However as the slope steepens and approaches a value of $|V_s| \approx \pi m^2$, we once again observe the Klein tunnelling effect, the transmission coefficient then is no longer governed by the exponential damping rule and approaches the T_{Step} limit given in (3.10) [1]. We set up simulations of a wave packet incident onto a sloping potential to observe this behaviour qualitatively, in Figure 3.10. The first plot shows a damped transmission of the wave packet, then decreasing L to increase the slope of the potential allows a greater part of the wave packet to be transmitted, as shown in the second part of the Figure. Instead of a piece-wise definition, a smooth sloping potential can be defined with a hyperbolic tangent function as follows,

$$V(z) = \frac{1}{2}V_0\left(1 + \tanh\left(z/w\right)\right), \tag{3.61}$$

where w is the width parameter that governs the distance across which the potential goes from $V = 0$ to $V = V_0$. For such a potential the transmission coefficient is equal to [55, 86],

$$T = \frac{\sinh\left(\pi k w\right)\sinh\left(\pi k w\right)}{\sinh\left(\pi\left(V_0/c + k + \kappa\right)w/2\right)\sinh\left(\pi\left(V_0/c - k - \kappa\right)w/2\right)}, \tag{3.62}$$

where the wave numbers are $k = \sqrt{\left(\left(E - V_0\right)^2 - c^4\right)/c}$ and $\kappa = -\sqrt{\left(E^2 - c^4\right)/c}$. In a later chapter we will use this definition of the potential slope to construct a potential barrier.

We also simulate the process of tunnelling through a rectangular potential barrier to observe the behaviour of the two wave function components. A plot of the wave function passing through the barrier is shown in Figure 3.8, where we can see the oscillations in the probability density inside the potential.

3.2.3 Zitterbewegung effect in one dimension

Zitterbewegung is an effect on the motion of the wave packet caused by the interference of the positive and negative energy components of the wave function when they overlap in momentum space, and materializes as oscillation and drift of the wave packet's average position [102, 47]. Zitterbewegung motion can be calculated from the expectation value of the standard position operator x,

$$\bar{x}\left(t\right)=\int_{-\infty}^{\infty}\Psi\left(x,t\right)^{\dagger}x\Psi\left(x,t\right)dx. \tag{3.63}$$

More generally, Zitterbewegung is given by the oscillating term in the explicit expression for the time evolution of the position of the wave packet $x\left(x\right)$, which can be obtained by integrating the standard velocity operator, given by the Heisenberg formula,

$$\frac{d}{dt}x\left(t\right)=\frac{i}{\hbar}[\boldsymbol{H}_{0},\bar{x}\left(t\right)]=e^{i\boldsymbol{H}_{0}t}i[\boldsymbol{H}_{0},\bar{x}]e^{-i\boldsymbol{H}_{0}t}=c\alpha_{x}, \tag{3.64}$$

where $\boldsymbol{H}_{0}$ is the Dirac Hamiltonian for a free particle, α_{x} is one of the Dirac matrices, and $c\alpha_{x}$ is the standard velocity operator in quantum electrodynamics, different from the classical space velocity of the particle. It has a purely discrete spectrum of eigenvalues, $+c$ and $-c$ as the only possible values of a velocity measurement at any moment. This unexpected result of quantum electrodynamics is different from the classical kinematic velocity relation $\boldsymbol{v}=c^{2}\boldsymbol{p}/E$, and we expect the quantum analog to be $\boldsymbol{v}=c^{2}\boldsymbol{p}\boldsymbol{H}_{0}^{-1}$, designated as the classical velocity operator, with a continuous spectrum of possible values in the $[-c,c]$ range [103]. Derivative of $x\left(t\right)$ implies

$$\boldsymbol{x}\left(t\right)=\boldsymbol{x}\left(0\right)+\int_{0}^{t}c\alpha\left(t\right)dt=\boldsymbol{x}+c^{2}\boldsymbol{p}\boldsymbol{H}_{0}^{-1}t+\frac{1}{2i}\boldsymbol{H}_{0}^{-1}\left(e^{2i\boldsymbol{H}_{0}t}-1\right)\boldsymbol{F}, \tag{3.65}$$

where $\boldsymbol{F}=c\alpha-c^{2}\boldsymbol{p}\boldsymbol{H}_{0}^{-1}$ is defined as the difference between the the standard and classical velocity operators. It is bounded and can be used to show that the velocity $c\alpha\left(t\right)$ oscillates around the conserved mean value of the classical velocity operator [103]. The first term in (3.65) is the initial position, the second term is the classical velocity due to initial momentum, and the third term is responsible for the Zitterbewegung oscillations. The observable particle position at time t is given by the expectation value of the position operator (3.65),

$$\bar{\boldsymbol{x}}\left(t\right)=\left\langle \boldsymbol{x}\right\rangle +\left\langle c^{2}\boldsymbol{p}\boldsymbol{H}_{0}^{-1}\right\rangle t+\left\langle \frac{1}{2i}\boldsymbol{H}_{0}^{-1}\left(e^{2i\boldsymbol{H}_{0}t}-1\right)\boldsymbol{F}\right\rangle , \tag{3.66}$$

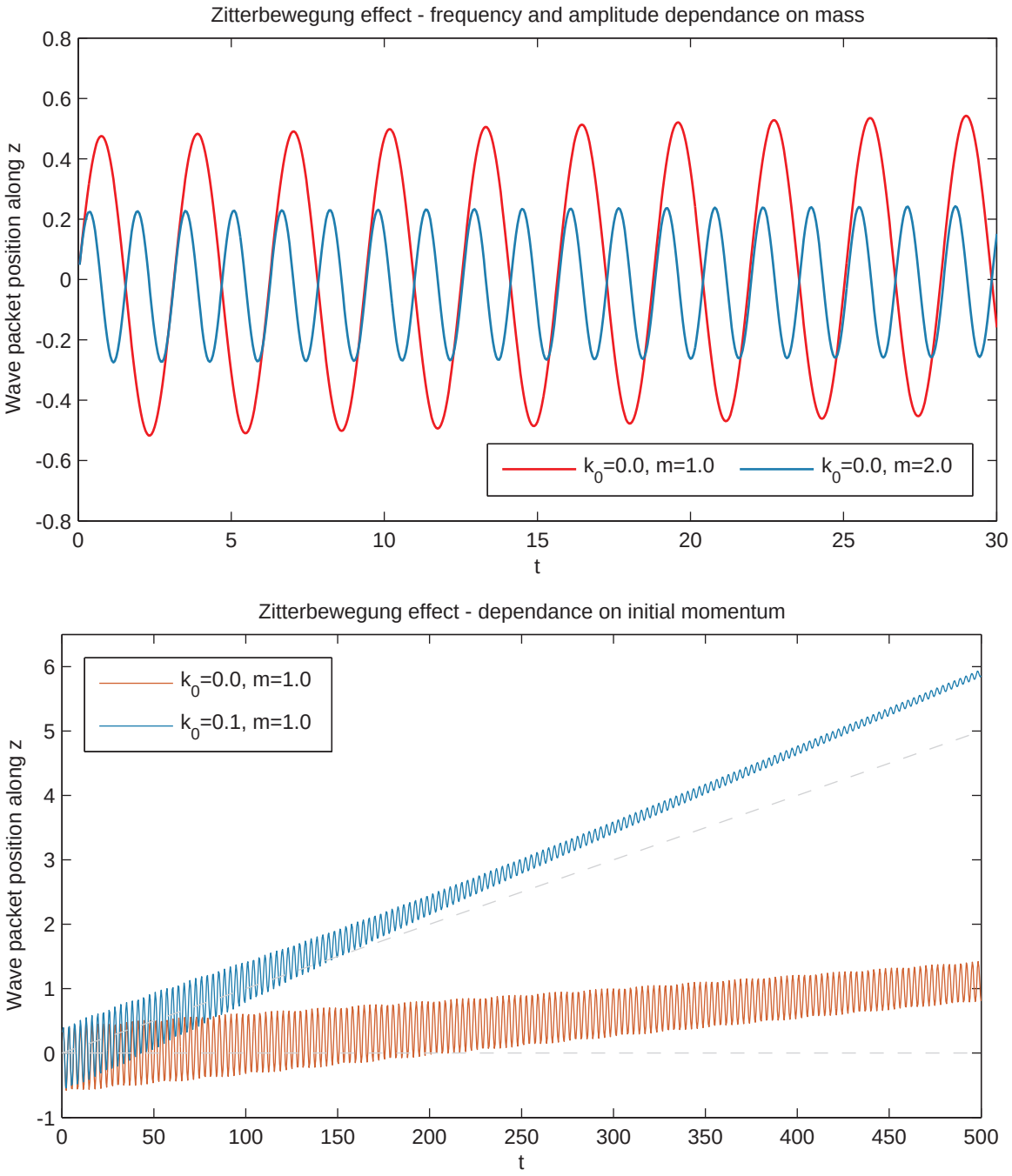

Figure 3.11: QLB Simulation of Zitterbewegung effect. First plot shows the oscillation of the average position of the wave packet (red curve). Doubling the mass (blue curve) halves the amplitude of the oscillations and doubles the frequency, confirming the reproduction of dependence of the Zitterbewegung effects on mass that was observed experimentally. Second plot shows evolution of the oscillations for a stationary particle (red curve) and a particle with non-zero momentum (blue curve). The oscillations of the free particle with zero initial momentum also generate a drift of the wave packet. The oscillations of the particle with non-zero momentum lose amplitude as the wave packet moves along its initial momentum and overlap of the positive and negative wave function components is decreased.

where the first term is the initial position of the wave packet, the second term is drift due to the classical velocity operator, and the last term is the Zitterbewegung oscillation. Because Zitterbewegung is caused by the interference of positive and negative energy states, wave packets composed entirely of positive or entirely negative states exhibit no Zitterbewegung motion. For more details we refer the reader to books on relativistic quantum mechanics [102, 103, 47].

Experimentally the Zitterbewegung effect has only recently been observed for the first time by Gerritsma et. al. [38], using a trapped Ca^+ ion to simulate this relativistic quantum effect. For free electrons the Zitterbewegung oscillations are predicted to have an amplitude on the order of the Compton wavelength. We set up QLB simulations to observe Zitterbewegung motion and reproduce the same effects in our solutions. As in the experiments [38], we observe in our simulations linear dependence of the frequency of the oscillations on the mass of the particle, and inverse relationship with the amplitude, as shown in the top panel Figure 3.11. As we can see on the same Figure, in our simulations the Zitterbewegung effect creates a non-zero drift velocity even for wave packets with zero average momentum, and the same drift was observed experimentally [38]. We calculate the theoretical drift velocity by calculating the expectation value of the classical velocity opearator in equation (3.66) for this case,

$$\langle \boldsymbol{v} \rangle = \int_{-\infty}^{\infty} \Psi^* c^2 \boldsymbol{p} \boldsymbol{H}_0^{-1} \Psi dx, \tag{3.67}$$

where

$$\Psi = \eta e^{-x^2/2} \begin{pmatrix} 1 \\ 1 \end{pmatrix}, \tag{3.68}$$

is a wave packet with zero initial momentum, centered at the origin, with equal magnitudes of the positive and negative components (equal to its conjugate Ψ^*), and η is a normalization constant. The free particle Hamiltonian $\boldsymbol{H}_0$ becomes a multiplication operator in momentum space [103],

$$\boldsymbol{h}_0(k) = \begin{pmatrix} mc^2 & ck \\ ck & -mc^2 \end{pmatrix}, \tag{3.69}$$

so that the classical velocity operator in momentum space is given by

$$\hat{\boldsymbol{v}} = ck^2 \boldsymbol{h}_0^{-1}(k) = \frac{ck^2}{-c^2k^2 - m^2c^4} \begin{pmatrix} -mc^2 & -ck \\ -ck & mc^2 \end{pmatrix}, \tag{3.70}$$

and we can calculate its expectation by integrating along k after transforming the wave function (3.68) into momentum space. The resulting integral

$$\langle \hat{\boldsymbol{v}} \rangle = \int_{-\infty}^{\infty} \frac{ck^2}{-c^2k^2 - m^2c^4} \left(\hat{\Psi}_1^* \left(-mc^2 \hat{\Psi}_1 - ck\hat{\Psi}_2 \right) + \hat{\Psi}_2^* \left(mc^2 \hat{\Psi}_2 - ck\hat{\Psi}_1 \right) \right) dk, \tag{3.71}$$

is simplified by the fact that for our wave function (3.68) we have $\hat{\Psi}_1^* = \hat{\Psi}_2^* = \hat{\Psi}_1 = \hat{\Psi}_2$, and is equal to

$$\langle \hat{\boldsymbol{v}} \rangle = 2\eta^2 c \left(\sqrt{\pi} - e^{m^2c^2} mc\pi \operatorname{erfc}(mc) \right). \tag{3.72}$$

If we let $c = 1$ and take the limit of the second term with increasing mass, we obtain,

$$\lim_{m \to \infty} e^{m^2} \pi m \operatorname{erfc}(m) = \sqrt{\pi}. \tag{3.73}$$

Setting the normalization constant to the appropriate value for our wave packet, $\eta = \left(\sqrt{2}\pi^{1/4}\right)^{-1}$ we write down

$$\langle \hat{\boldsymbol{v}} \rangle = c \left(1 - e^{m^2c^2} mc\sqrt{\pi} \operatorname{erfc}(mc) \right). \tag{3.74}$$

where the second term tends to 1 as mass of the particle is increased. We can thus see that the drift of the zero momentum wave packet composed equally of positive and negative energy wave function components tends to zero as mass is incresed, but is indeed non-zero for finite mass.

A wave packet initialized with only the top wave function component, with the second component set to zero, and non-zero momentum will split into a large positive energy component moving along the direction of the initial momentum (ϕ^+ in our notation), and a smaller negative energy component (ϕ^-) moving in the opposite direction. The magnitude of the negative energy component is negligible as long as the wave packet is not localized to a very narrow region of space. As the two components move apart, their interaction weakens and the amplitude of the Zitterbewegung oscillations gradually decreases until the effect disappears completely. We can see this in the second plot of Figure 3.11 – the oscillating motion of the wave packet with non-zero initial momentum loses amplitude with time. In the same Figure we see the non-zero drift of the wave packet for zero initial momentum. Looking at the magnitude of the drift, we note the final position of the wave packet with non-zero momentum is given by the sum of the drift due to Zitterbewegung and due to the classical velocity, as expected.

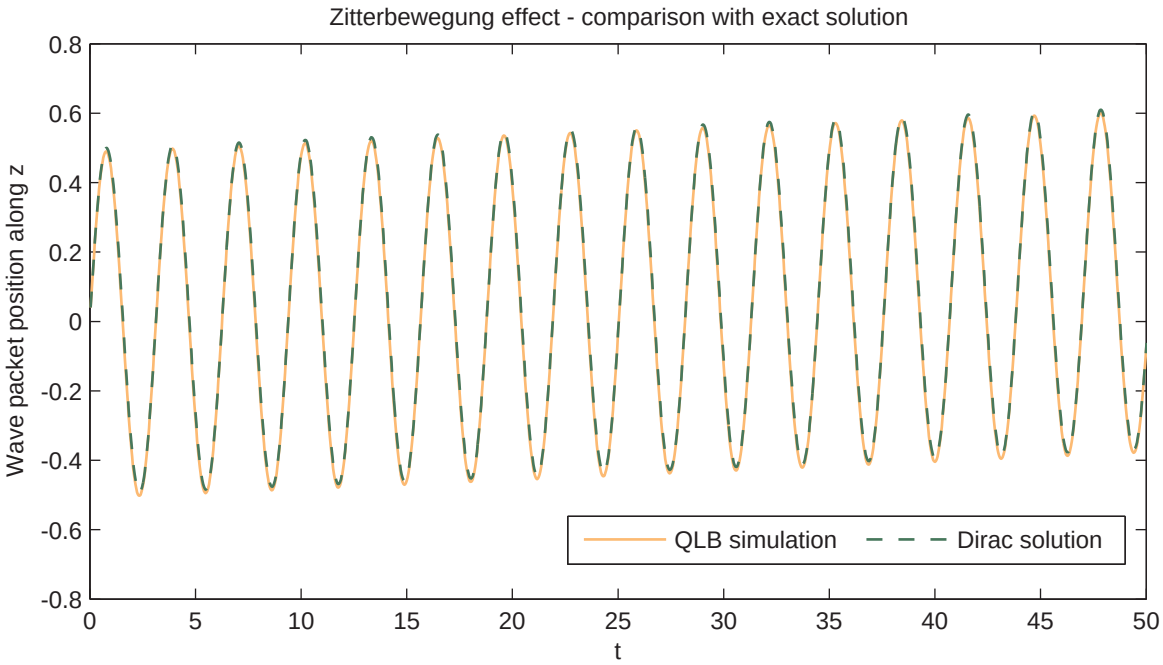

Figure 3.12: Comparison of QLB simulation of Zitterbewegung oscillations of a free particle in one dimension with the exact Dirac equation solution shows a good agreement and confirms the accuracy of the simulations.

To verify the Zitterbewegung observed in the QLB simulations we compare the oscillating motion of the free wave packet given by the scheme with the exact solution of the Dirac equation derived in section 2.1.2 and plot both in Figure 3.12. We observe good agreement with the exact solution and thus confirm that the QLB algorithm accurately reproduces the dynamics of the wave packets affected by Zitterbewegung oscillations.

Chapter 4

Multidimensional QLB

The work presented in section 4.1 is based on the three dimensional implementation described in Palpacelli and Succi (2007), shown later to be incorrect [unpublished notes]. These results on isotropy have appeared in Lapitski and Dellar (2010), and Dellar, Lapitski, Palpacelli and Succi (2011).

Although originally derived for the one-dimensional Dirac equation, the quantum lattice Boltzmann scheme can be expanded to simulate two and three dimensional systems and provide an alternative to the spectral split-operator method that is currently used for numerical solutions of the Dirac equation, which we described in section 1.2.

Because the Dirac streaming matrices cannot be diagonalized simultaneously, expansion of the QLB scheme is done through splitting the Dirac equation into separate one-dimension equations along each of the three axes, diagonalizing each equation's streaming matrix, and applying the one-dimensional QLB in turn along each direction to calculate evolution of a single timestep. Although Succi and colleagues had described and derived a QLB scheme in two and three dimensions [78], their scheme produced incorrect asymmetric evolution of spherical wave packets in three dimensions, and was thus unfinished in its development. In this chapter we find the source of the error and correct the multidimensional scheme, derive and test a second order multidimensional QLB scheme analogous to our approach in one dimension, clarify the correct transformation of the three-dimensional four-component wave function as compared with the two-component one-dimensional version, and introduce an alternative approach to extension of the QLB scheme to multiple dimensions that will be used in graphene simulation in the next chapter.

4.1 Isotropy of QLB in three dimensions

The extension of the QLB scheme to two and three dimensions proposed by Succi and Benzi [101] is based on the technique of operator splitting, which is done by dividing the three dimensional Dirac equation into three one-dimensional equations. Each one of them can be diagonalized by application of a so-called 'rotation matrix' that aligns the top two wave function components to stream toward the positive direction of the axis and the bottom two components stream in the negative direction of a given axis. The collisions and streaming along each direction are calculated with the one-dimensional QLB, then we move on to the second axis and repeat the rotation, collision and streaming steps, and the third axis in the same way. To show this in more detail we start with the Dirac equation in Majorana form, follow the set up used by Succi and co-workers [101, 78],

$$\left(\partial_t - c\alpha_x\partial_x + c\beta\partial_y - c\alpha_z\partial_z + i\omega_c\alpha_y - iqV/\hbar\right)\Psi' = 0, \tag{4.1}$$

where the Dirac matrices $\alpha_x, \alpha_y, \alpha_z, \beta$ are

$$\alpha_x = \begin{pmatrix} 0 & 0 & 0 & 1 \\ 0 & 0 & 1 & 0 \\ 0 & 1 & 0 & 0 \\ 1 & 0 & 0 & 0 \end{pmatrix} \qquad \alpha^y = \begin{pmatrix} 0 & 0 & 0 & -i \\ 0 & 0 & i & 0 \\ 0 & -i & 0 & 0 \\ i & 0 & 0 & 0 \end{pmatrix} \tag{4.2}$$

$$\alpha^z = \begin{pmatrix} 0 & 0 & 1 & 0 \\ 0 & 0 & 0 & -1 \\ 1 & 0 & 0 & 0 \\ 0 & -1 & 0 & 0 \end{pmatrix} \qquad \beta = \begin{pmatrix} 1 & 0 & 0 & 0 \\ 0 & 1 & 0 & 0 \\ 0 & 0 & -1 & 0 \\ 0 & 0 & 0 & -1 \end{pmatrix} \tag{4.3}$$

and the transformed wave function is given by $\Psi' = U\Psi$. The matrix $U = \frac{1}{\sqrt{2}}(\alpha^y + \beta)$ is applied to transform the standard representation of the Dirac equation (1.24) into Majorana form. This turns all the space derivatives that make up streaming along x, y, z directions real and is done for convenience. The next step is splitting of the equation in such a way that gives us three equations analogous to the one-dimensional equation,

$$\left(\partial_t - c\alpha_z\partial_z\right)\Psi^z = i\frac{1}{3}\left(Ig - \omega_c\alpha^y\right)\Psi^z \tag{4.4a}$$

$$\left(\partial_t + c\beta\partial_y\right)\Psi^{zy} = i\frac{1}{3}\left(Ig - \omega_c\alpha^y\right)\Psi^{zy} \tag{4.4b}$$

$$\left(\partial_t - c\alpha_x\partial_x\right)\Psi^{zyx} = i\frac{1}{3}\left(Ig - \omega_c\alpha^y\right)\Psi^{zyx} \tag{4.4c}$$

where $g = \frac{qV}{\hbar}$ and $\omega_c = \frac{mc^2}{\hbar}$. The wave function is evolved in a sequence of collision and streaming steps from Ψ^z to Ψ^{zy} to Ψ^{zyx} according the the above one dimensional equations [101], such that a complete timestep is given by

$$\Psi^z(x, y, z + \Delta z, t + \Delta t) = Q_z \Psi^z(x, y, z, t) \quad (4.5a)$$

$$\Psi^{zy}(x, y + \Delta y, z + \Delta z, t + \Delta t) = Q_y \Psi^{zy}(x, y, z + \Delta z, t + \Delta t) \quad (4.5b)$$

$$\Psi^{zyx}(x + \Delta x, y + \Delta y, z + \Delta z, t + \Delta t) = Q_x \Psi^{zyx}(x, y + \Delta y, z + \Delta z, t + \Delta t) \quad (4.5c)$$

where Ψ^z is the wave function aligned along the z-axis, Ψ^{zy} is the Ψ^z wave function aligned along y-axis, and Ψ^{zyx} is the Ψ^{zy} wave function alighned along the x-axis. We will detail the required diagonalization matrices and the derivation of the collision matrices Q_z, Q_y, Q_x below. Note that the collision matrix is multiplied by a factor of 1/3, effectively colliding for one third of a timestep along each axis. The matrices $-\alpha_x, -\alpha_z, \beta$ are streaming matrices for each one-dimensional Dirac equation, and before the one-dimensional QLB scheme can be applied along each direction, they need to be diagonalized by applying a rotation matrix to the Dirac equation. The one-dimensional QLB scheme is originally set up along the z direction, and we take that as the starting orientation of the three-dimensional Dirac equation.

We diagonalize $-\alpha_z$ with the rotation matrix Z,

$$\tilde{\alpha}_z = Z^{-1}(-\alpha^z) Z = \begin{pmatrix} 1 & 0 & 0 & 0 \\ 0 & 1 & 0 & 0 \\ 0 & 0 & -1 & 0 \\ 0 & 0 & 0 & -1 \end{pmatrix} \quad (4.6)$$

where

$$Z = \frac{1}{\sqrt{2}} \begin{pmatrix} 0 & -1 & 0 & 1 \\ 1 & 0 & -1 & 0 \\ 0 & 1 & 0 & 1 \\ 1 & 0 & 1 & 0 \end{pmatrix} \qquad Z^{-1} = \frac{1}{\sqrt{2}} \begin{pmatrix} 0 & 1 & 0 & 1 \\ -1 & 0 & 1 & 0 \\ 0 & -1 & 0 & 1 \\ 1 & 0 & 1 & 0 \end{pmatrix} \quad (4.7)$$

The rotation matrix Z is applied to the whole equation as follows,

$$Z^{-1}(\partial_t - c\alpha^x \partial_x + c\beta\partial_y - c\alpha^z \partial_z + i\omega_c \alpha^y - igI) Z Z^{-1} \Psi' = 0 \quad (4.8)$$

to give

$$(\partial_t + c\tilde{\alpha}_x \partial_x + c\tilde{\alpha}_y \partial_y + c\tilde{\alpha}_z \partial_z + i\omega_c C_z - igI) Z^{-1} \Psi' = 0 \quad (4.9)$$

where

$$\tilde{\alpha}_y = \begin{pmatrix} 0 & 0 & -1 & 0 \\ 0 & 0 & 0 & -1 \\ -1 & 0 & 0 & 0 \\ 0 & -1 & 0 & 0 \end{pmatrix} \qquad \tilde{\alpha}_x = \begin{pmatrix} 0 & 0 & 0 & -1 \\ 0 & 0 & 1 & 0 \\ 0 & 1 & 0 & 0 \\ -1 & 0 & 0 & 0 \end{pmatrix} \quad (4.10)$$

and $i\omega_c C_z - igI$ is the collision matrix that will turn into the QLB collision matrix Q_z when the Dirac equation is discretized,

$$Q_z = \begin{pmatrix} a & 0 & 0 & b \\ 0 & a & b & 0 \\ 0 & -b & a & 0 \\ -b & 0 & 0 & a \end{pmatrix}, \tag{4.11}$$

where a and b are collision constants given in (2.60).

Note that, together with the rotation of the streaming matrices, the wave function $\Psi' = [u_1, u_2, d_1, d_2]^T$ is transformed by application of Z^{-1}. In Succi's work the matrix Z, not Z^{-1}, is incorrectly applied to the wave function in the rotation transformations, as a result breaking the isotropy of the scheme. The lack of isotropy was noticed by Succi and Palpacelli when they ran larger scale three-dimensional simulations and observed a discrepancy in the dispersion of wave packet along the three directions – only along one axis it was following the expected theoretical evolution, and diverging along the other two [77]. In our investigation of the cause of this error we reproduced Succi's and Palpacelli's simulations and results for a harmonic potential, in Figure 4.1, and a free particle, in Figure 4.2. The Figures show the evolution of the standard deviation of the wave packets calculated from the numerical values of the probability density $|\Psi|^2$ on the lattice and compared with the theoretical dispersion according to the Schrödinger equation that is given by,

$$\Delta_{z,y,x}(t) = \left(\Delta_0^2 + \frac{t^2}{4m^2\Delta_0^2}\right)^{\frac{1}{2}}, \tag{4.12}$$

Correcting the ordering of the rotation matrices recovers the isotropy of the scheme and the wave packets disperse at the same rate in all directions, as we can see in the second plots of the same Figures.

A possible cause of the error is confusion with the Majorana transformation, where the application of the matrix U to the Dirac equation gives $\Psi' = U\Psi$. However in that transformation $U = U^{-1}$, which is not true for the rotation matrices. To reverse the rotation we then would apply Z to the wave function (and Z^{-1} was applied in Succi's case).

To simulate the streaming and collisions along y and x directions we apply rotation matrices Y and X to the Dirac equation aligned along z. This will give diagonalized streaming matrices $\tilde{\alpha}'_y = Y^{-1}\tilde{\alpha}_y Y$ and $\tilde{\alpha}'_x = X^{-1}\tilde{\alpha}_x X$, such that $\tilde{\alpha}'_y = \tilde{\alpha}'_x = \tilde{\alpha}_z$. The

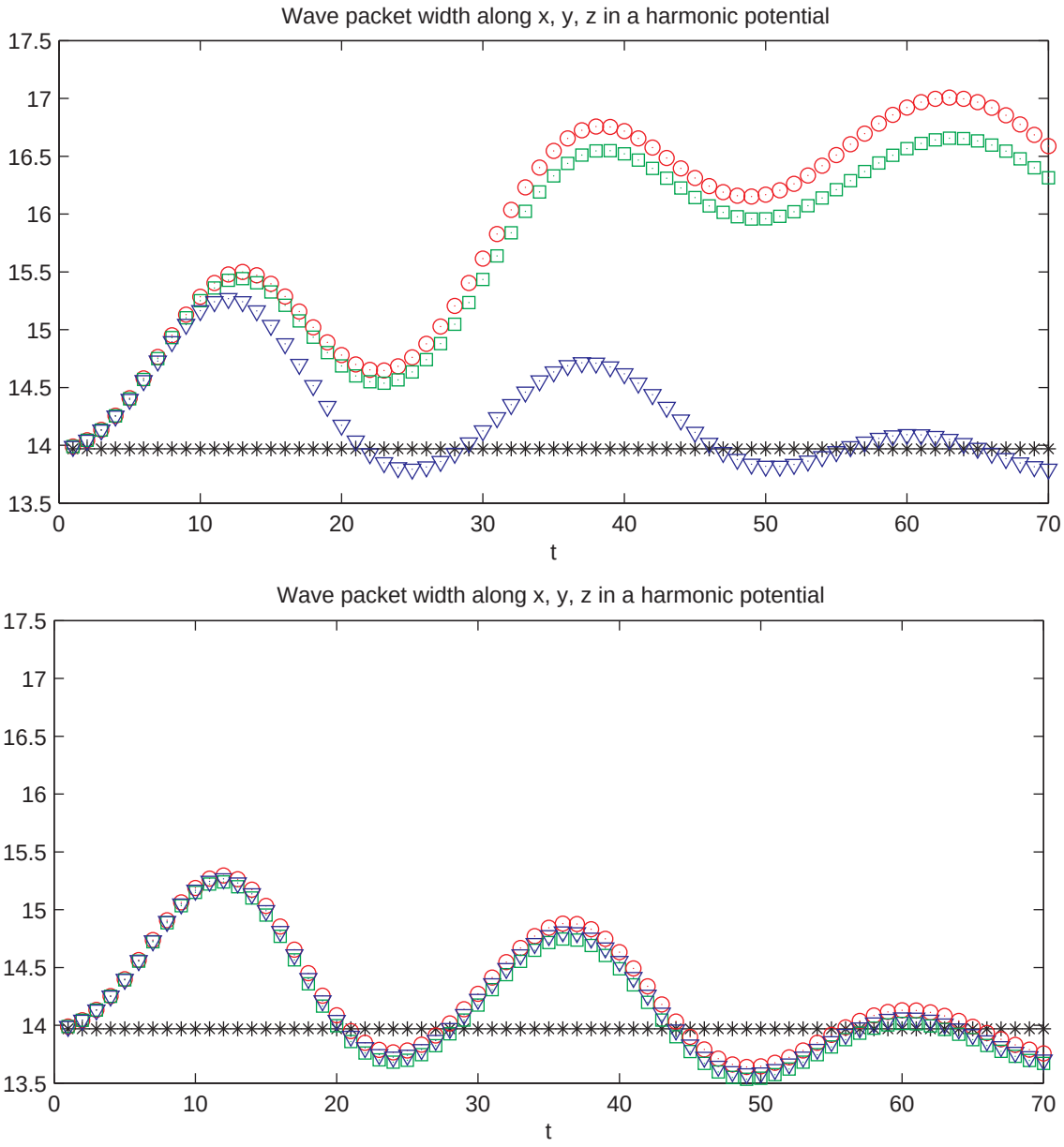

Figure 4.1: Evolution of wave packet widths along the three directions $\Delta_z, \Delta_y, \Delta_x$ with Succi's ordering of rotation matrices up to 1/4th of the period. Wave packet width along two of the three directions diverges from the expected $\Delta = 14$ maintained by the harmonic potential. The second plot shows evolution of wave packet widths along with corrected ordering of rotation matrices, following the same evolution along all three axes.

matrices Y and X are given by

$$Y = \frac{1}{\sqrt{2}} \begin{pmatrix} -1 & 0 & 0 & 1 \\ 0 & -1 & 1 & 0 \\ 1 & 0 & 0 & 1 \\ 0 & 1 & 1 & 0 \end{pmatrix} \qquad Y^{-1} = \frac{1}{\sqrt{2}} \begin{pmatrix} -1 & 0 & 1 & 0 \\ 0 & -1 & 0 & 1 \\ 0 & 1 & 0 & 1 \\ 1 & 0 & 1 & 0 \end{pmatrix} \tag{4.13}$$

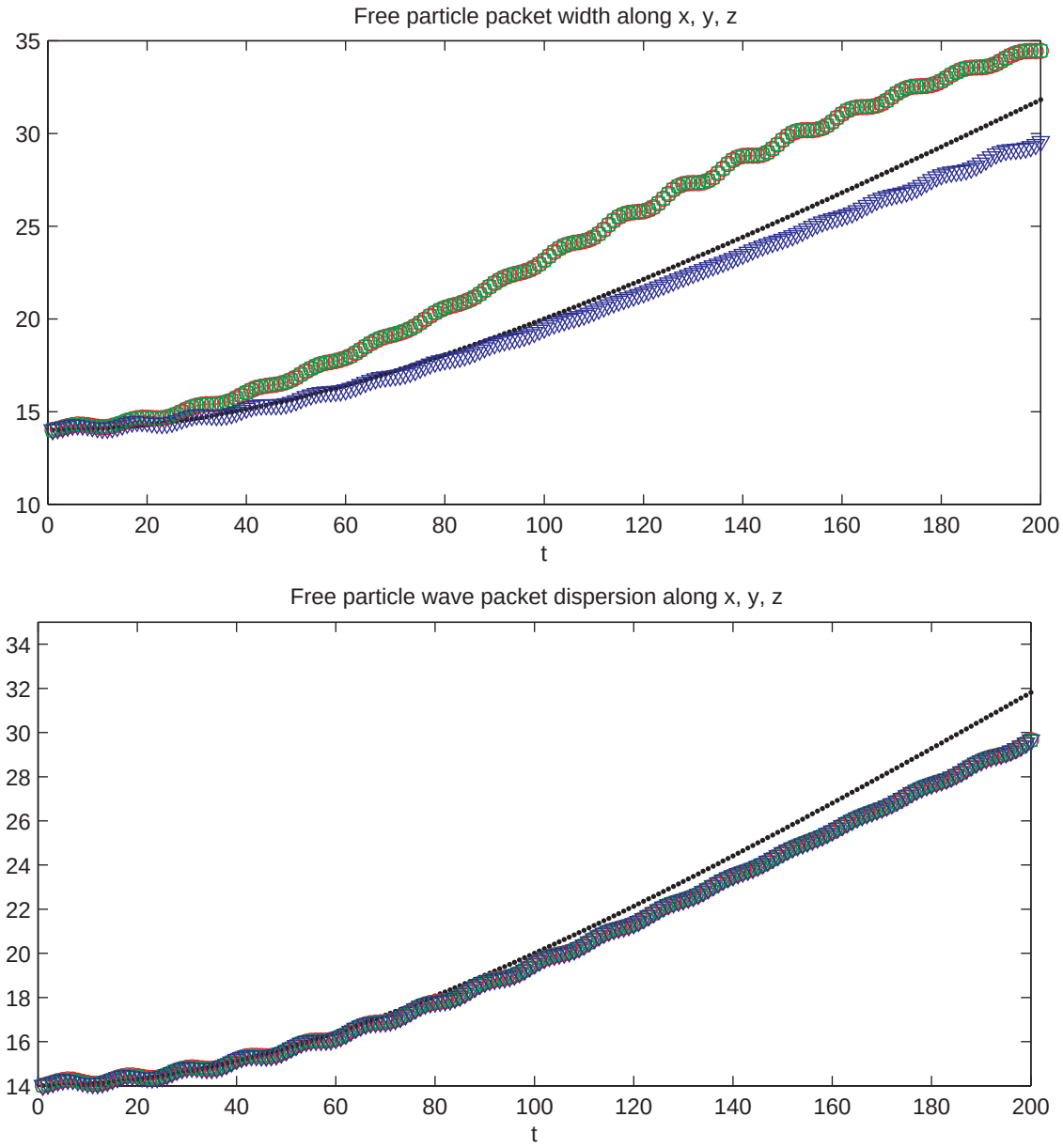

Figure 4.2: Evolution of wave packet width along three directions in the case of a zero potential with Succi's ordering of rotation matrices. As in the harmonic potential, wave packet dispersion along two of the three directions diverges from the expected analytic rate. The second plot shows evolution of wave packet width corrected ordering of rotation matrices, the dispersion is now approaching isotropy.

and

$$X = \frac{1}{\sqrt{2}} \begin{pmatrix} -1 & 0 & 0 & 1 \\ 0 & 1 & -1 & 0 \\ 0 & 1 & 1 & 0 \\ 1 & 0 & 0 & 1 \end{pmatrix} \qquad X^{-1} = \frac{1}{\sqrt{2}} \begin{pmatrix} -1 & 0 & 0 & 1 \\ 0 & 1 & 1 & 0 \\ 0 & -1 & 1 & 0 \\ 1 & 0 & 0 & 1 \end{pmatrix}. \tag{4.14}$$

The resulting QLB collision matrices are

$$Q_y = Y^{-1} Q_z Y = \begin{pmatrix} a & 0 & -b & 0 \\ 0 & a & 0 & -b \\ b & 0 & a & 0 \\ 0 & b & 0 & a \end{pmatrix} \tag{4.15}$$

and

$$Q_x = X^{-1} Q_z X = \begin{pmatrix} a & 0 & 0 & -b \\ 0 & a & b & 0 \\ 0 & -b & a & 0 \\ b & 0 & 0 & a \end{pmatrix}. \tag{4.16}$$

A single timestep of the three dimensional QLB simulation then consists of first performing the collisions and streaming along z direction, rotating the Dirac equation to align with y direction, performing collision and streaming along y direction, reverse rotation back to z and rotation to align with x direction (these two rotations can be combined into a single step), performing collision and streaming along x direction, and reverse rotation back to alignment with z direction, before the same is repeated for the next timestep. We can represent this as the following sequence of transformations,

$$\begin{pmatrix} u_1 \\ u_2 \\ d_1 \\ d_2 \end{pmatrix}_{[t=n\Delta t+\Delta t]} = X S_x Q_x X^{-1} Y S_y Q_y Y^{-1} S_z Q_z \begin{pmatrix} u_1 \\ u_2 \\ d_1 \\ d_2 \end{pmatrix}_{[t=n\Delta t]}, \tag{4.17}$$

where $Q_{z,y,x}$ are the collision and $S_{z,y,x}$ the streaming matrices. The order of directions along which the scheme is applied in each timestep can be alternated without modification to the rotation matrices. In Succi's case the sequence would be

$$\begin{pmatrix} u_1 \\ u_2 \\ d_1 \\ d_2 \end{pmatrix}_{[t=(n+1)\Delta t]} = X^{-1} S_x Q_x X Y^{-1} S_y Q_y Y S_z Q_z \begin{pmatrix} u_1 \\ u_2 \\ d_1 \\ d_2 \end{pmatrix}_{[t=n\Delta t]}. \tag{4.18}$$

Rewriting in terms of the Q_z collision matrix we can see that in that case the rotation matrices no longer cancel out,

$$\begin{pmatrix} u_1 \\ u_2 \\ d_1 \\ d_2 \end{pmatrix}_{[t=(n+1)\Delta t]} = X^{-1} S_x \left(X^{-1} Q_z X\right) X Y^{-1} S_y \left(Y^{-1} Q_z Y\right) Y S_z Q_z \begin{pmatrix} u_1 \\ u_2 \\ d_1 \\ d_2 \end{pmatrix}_{[t=n\Delta t]}, \tag{4.19}$$

leading to a broken spherical symmetry and inaccurate solutions.

4.1.1 Convergence analysis

Splitting the Dirac equations into three one-dimensional equations, with rotations between solution of each one, introduces an $\mathcal{O}(\Delta t)$ error, rendering the scheme first order accurate regardless of the discretization approach. To confirm first order convergence to isotropy we run simulations on a range of grid sizes for a free particle and a particle bound by a harmonic potential. Following Succi's parameters, the scheme is initialized with $u_{1,2} = \frac{1}{2}\phi$, $d_{1,2} = -iu_{1,2}$, where ϕ is a Gaussian wave packet given by

$$\phi = \left(2\pi\Delta_{0z}\Delta_{0y}\Delta_{0x}\right)^{-\frac{1}{2}} e^{-\frac{(z-z_0)^2}{4\Delta_{0z}^2}} e^{\frac{-(y-y_0)^2}{4\Delta_{0y}^2}} e^{\frac{-(x-x_0)^2}{4\Delta_{0x}^2}} e^{-i(k_{0z}z+k_{0y}y+k_{0x}x)}. \tag{4.20}$$

The spherically symmetric harmonic potential is given by

$$V = \frac{1}{2}m\omega_0^2\left((z-z_0)^2 + (y-y_0)^2 + (x-x_0)^2\right), \tag{4.21}$$

and the frequency ω_0 is set to preserve the wave packet's initial width,

$$\omega_0 = \left(2m\Delta_0^2\right)^{-1}, \tag{4.22}$$

where $\Delta_0 = \Delta_{0z} = \Delta_{0y} = \Delta_{0x}$. The parameters used are

initial packet width $\Delta_0 = 14$,
domain size $x, y, z \in [0, 100]$,
mass $m = 0.1$,

on a $100 \times 100 \times 100$ lattice [78], and we repeat the simulation on $200 \times 200 \times 200$ and $300 \times 300 \times 300$ grids. We check the convergence of $\Delta_z, \Delta_y, \Delta_x$ by plotting the average of $|\Delta_z - \Delta_y|$, $|\Delta_z - \Delta_x|$, and $|\Delta_x - \Delta_y|$. The results in Figure 4.3 show that the wave packet widths along the three directions do converge, and a plot of the same average difference scaled by the relative mesh size confirms first order of convergence.

For a stationary free particle we run further simulations to confirm spherical symmetry of solutions. We calculate the standard deviation of the probability density $|\phi^+|$ at all sets of points that are the same distance r from the center. In the case of a free particle the evolution of the wave packet width is given by

$$\Delta_{z,y,x}(t) = \left(\Delta_0^2 + \frac{t^2}{4m^2\Delta_0^2}\right)^{\frac{1}{2}}, \tag{4.23}$$

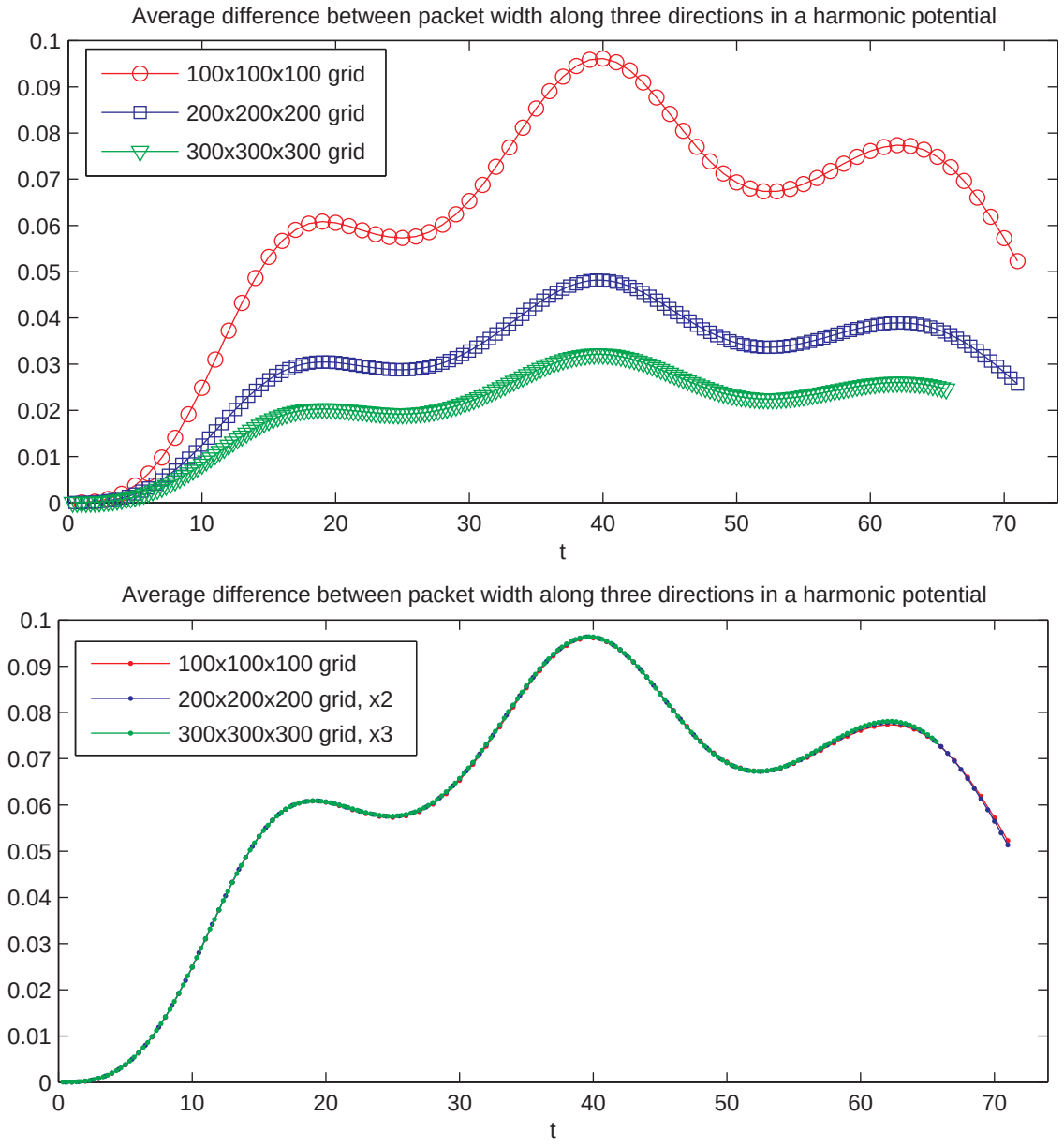

Figure 4.3: Evolution of the average of $|\Delta_z - \Delta_y|$, $|\Delta_z - \Delta_x|$, and $|\Delta_x - \Delta_y|$ in a harmonic potential, scaled by relative number of grid points in the second Figure, shows the expected first order convergence towards isotropy.

and $|\phi^+|$ should have the same values on such set of points in a perfectly spherically symmetric case. The results, in Figure 4.4, show first order convergence to spherical symmetry, as expected.

In Figure 4.2 the increasing width of the wave packet as simulated by the QLB scheme exhibits small oscillations around the monotonic dispersion according to the Schrödinger equation, eventually deviating from the value predicted by non-

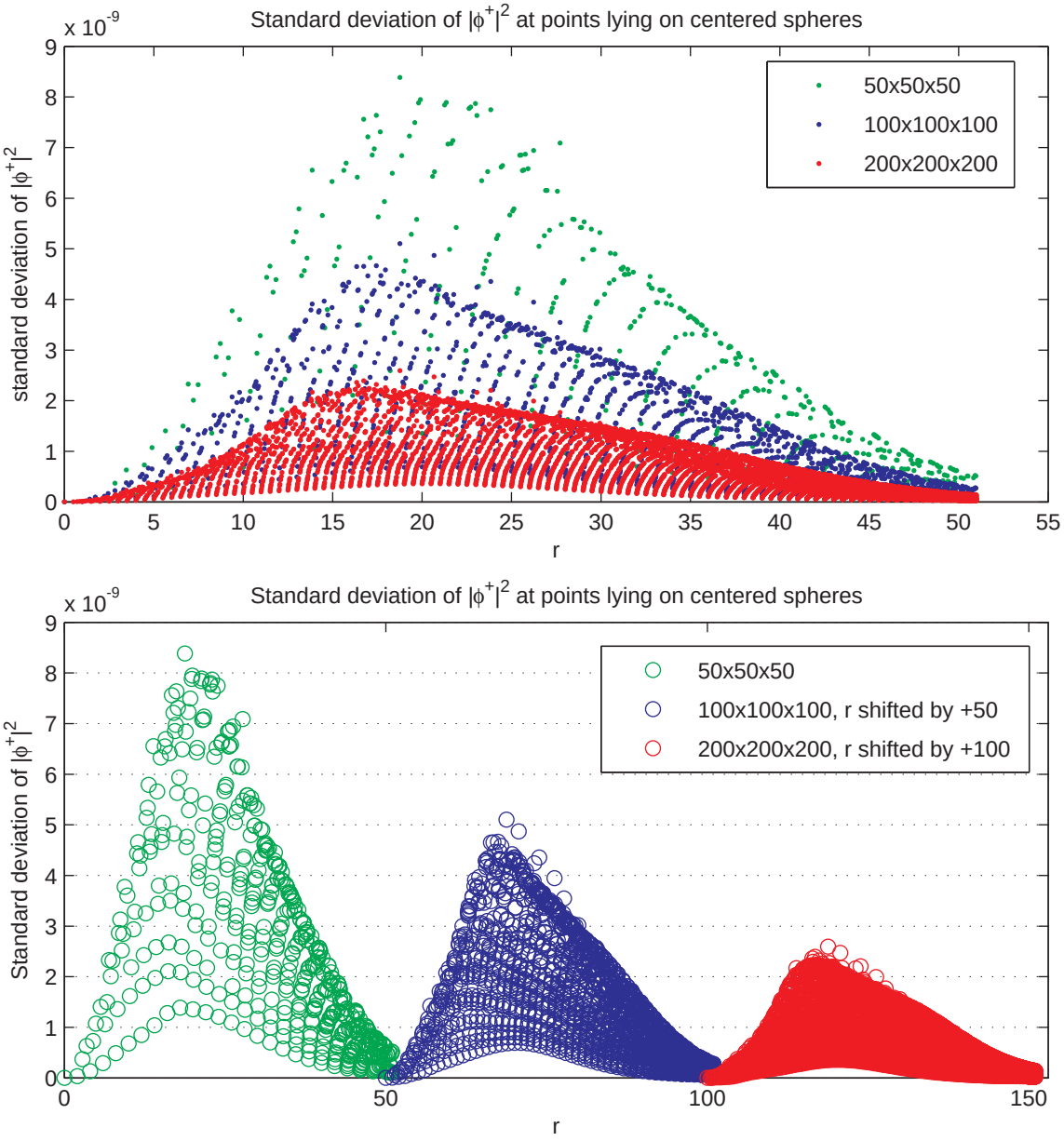

Figure 4.4: Standard deviation of $|\phi^+|^2$ on sets of points on a sphere centered at the initial position of the wave packet, shows first order convergence to spherical symmetry. The wave function amplitude is scaled to order of 10^{-6}.

relativistic quantum theory. To confirm that these oscillations are due to the relativistic description of our wave packet and not an artifact of the numerical solutions we can obtain an analytic solution of the Dirac equation in Fourier space for a free particle, and obtain exponentially accurate numerical approximations using Fast Fourier Transforms, as we did in the one-dimensional case in section 2.1.2.

We begin with the Majorana form of the Dirac equation aligned along the z-axis,

$$\left(\partial_t + c\tilde{\alpha}_x\partial_x + c\tilde{\alpha}_y\partial_y + c\tilde{\alpha}_z\partial_z + i\omega_c C_z\right)\left(Z^{-1}\Psi'\right) = 0, \tag{4.24}$$

and apply the Fourier transform defined by (2.1) and (2.2) to both sides. This turns the spatial derivatives into multiplication by the corresponding k_i and leaves only the first order time derivative. Rewriting in matrix form and solving the resulting ordinary differential equation, we can write down the evolution of the transformed wave function components in Fourier space as follows,

$$\begin{pmatrix} \hat{u}_{1,t} \\ \hat{u}_{2,t} \\ \hat{d}_{1,t} \\ \hat{d}_{2,t} \end{pmatrix} = \mathsf{E}_{3D} \begin{pmatrix} \hat{u}_{1,0} \\ \hat{u}_{2,0} \\ \hat{d}_{1,0} \\ \hat{d}_{2,0} \end{pmatrix}, \tag{4.25}$$

where

$$\mathsf{E}_{3D} = \begin{pmatrix} \frac{\Omega\cos(\Omega t) - ick_z\sin(\Omega t)}{\Omega} & 0 & \frac{ick_y\sin(\Omega t)}{\Omega} & \frac{(ick_x+\omega_c)\sin(\Omega t)}{\Omega} \\ 0 & \frac{\Omega\cos(\Omega t) - ick_z\sin(\Omega t)}{\Omega} & \frac{(-ick_x+\omega_c)\sin(\Omega t)}{\Omega} & \frac{ick_y\sin(\Omega t)}{\Omega} \\ \frac{ick_y\sin(\Omega t)}{\Omega} & \frac{-(ick_x+\omega_c)\sin(\Omega t)}{\Omega} & \frac{\Omega\cos(\Omega t)+ick_z\sin(\Omega t)}{\Omega} & 0 \\ \frac{(ick_x-\omega_c)\sin(\Omega t)}{\Omega} & \frac{ick_y\sin(\Omega t)}{\Omega} & 0 & \frac{\Omega\cos(\Omega t)+ick_z\sin(\Omega t)}{\Omega} \end{pmatrix} \tag{4.26}$$

is the evolution matrix and $\Omega^2 = c^2\left(k_x^2 + k_y^2 + k_z^2\right) + \omega_c^2$. Due to the properties of Pauli matrices that make up the 4×4 Dirac streaming matrices we can rewrite this in more compact form,

$$\mathsf{E}_{3D} = \cos(\Omega)\, I - i\frac{\sin(\Omega)}{\Omega}\left(\boldsymbol{k}\cdot\boldsymbol{\alpha}\right), \tag{4.27}$$

Re-running the simulations with the calculation of the Dirac solution included along with the QLB algorithm, in Figure 4.5 we plot the width of the wave packet given by the Dirac solution described above, calculated as the standard deviation of the probability density distribution on the grid, together with the previous QLB results and the Schrödinger evolution of the wave packet width. From the plot we confirm that the relativistic description of the wave packet is source of the oscillations that are correctly reproduced with the QLB scheme.

Comparing this Dirac solution with the simulation results will give a more accurate picture of the scheme's convergence in three dimensions, eliminating the extra error introduced by the non-relativistic limit. In Figure 4.6 we plot the error between the wave function probability density ($|\Psi|^2 = |\psi^+|^2 + |\psi^-|^2$) along the z axis as given

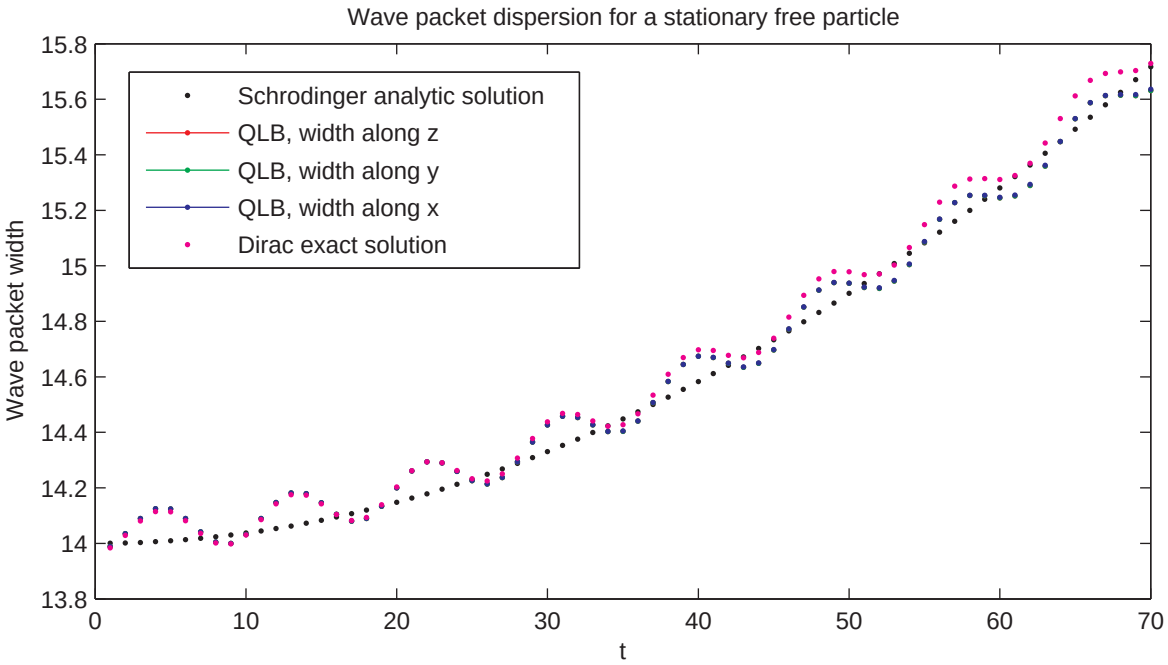

Figure 4.5: Evolution of the wave packet width along three axis as given by the QLB simulation, an exponentially accurate solution of the Dirac equation, and Schrödinger equation. The plot shows that oscillating evolution of the dispersion under the Dirac equation matches the QLB evolution, with discrepancies appearing at a later time due to accumulation of numerical error.

by the QLB simulation and the Dirac solution, and scale the error by the relative number of grid points. We can see that closer to the center of the domain the scheme is converging better than first order for these mesh sizes, with first order convergence at the edge of the domain. The average value of the error across the whole domain is

Grid size	Average $\|\Psi\|^2$ error	Reduction factor
$50 \times 50 \times 50$	3.38051×10^{-9}	–
$100 \times 100 \times 100$	1.71708×10^{-9}	1.969
$200 \times 200 \times 200$	8.48937×10^{-10}	2.023
$400 \times 400 \times 400$	4.21604×10^{-10}	2.014

we can see it reduced by a factor very close to 2 as the the size of the timestep is halved.

We plot $\frac{||\Psi_{3DQLB}|^2 - |\Psi_{Dirac}|^2|}{|\Psi_{Dirac}|^2}$ to get an idea of the relative error in Figure 4.7, the error drops to below 1% in most of the domain as the grid is refined to $200 \times 200 \times 200$ and beyond. In Figure 4.8 we plot the average difference between $|\Psi|^2$ along the three axes and see that converging to isotropy at second order for the given mesh sizes.

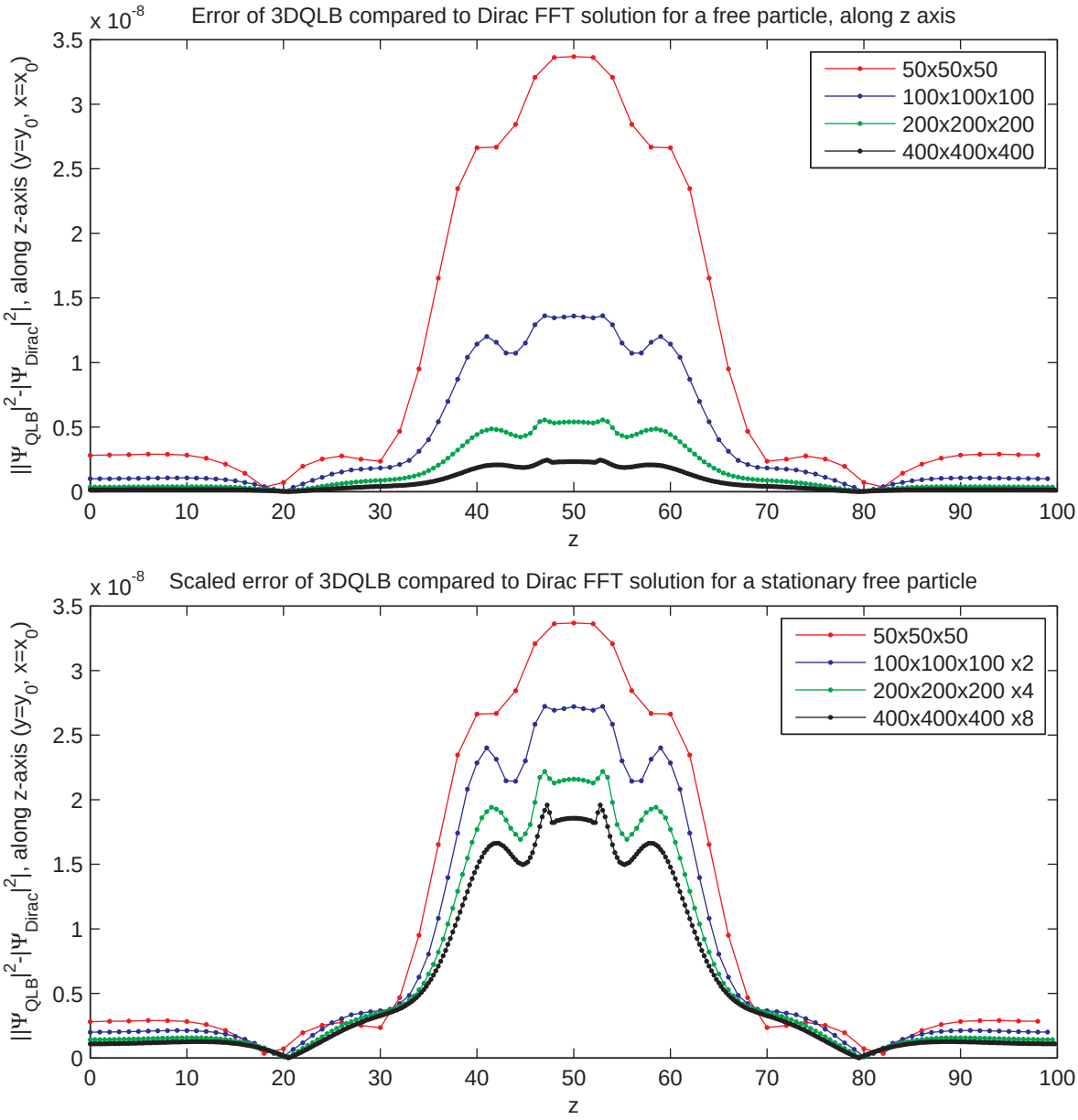

Figure 4.6: Total probability density error $||\Psi_{3DQLB}|^2 - |\Psi_{Dirac}|^2|$ along z-axis, scaled by the relative number of grid points in the second plot, shows general first order convergence.

As before, for a free particle we can derive the error between the 3DQLB scheme and the exact Dirac solution, after n timesteps it is given by

$$\begin{pmatrix} \Delta\hat{u}_1 \\ \Delta\hat{u}_2 \\ \Delta\hat{d}_1 \\ \Delta\hat{d}_2 \end{pmatrix} = [(\mathsf{E}_{3D})^n - (\mathsf{E}_{3DQLB})^n] \begin{pmatrix} \hat{u}_{1,0} \\ \hat{u}_{2,0} \\ \hat{d}_{1,0} \\ \hat{d}_{2,0} \end{pmatrix}. \tag{4.28}$$

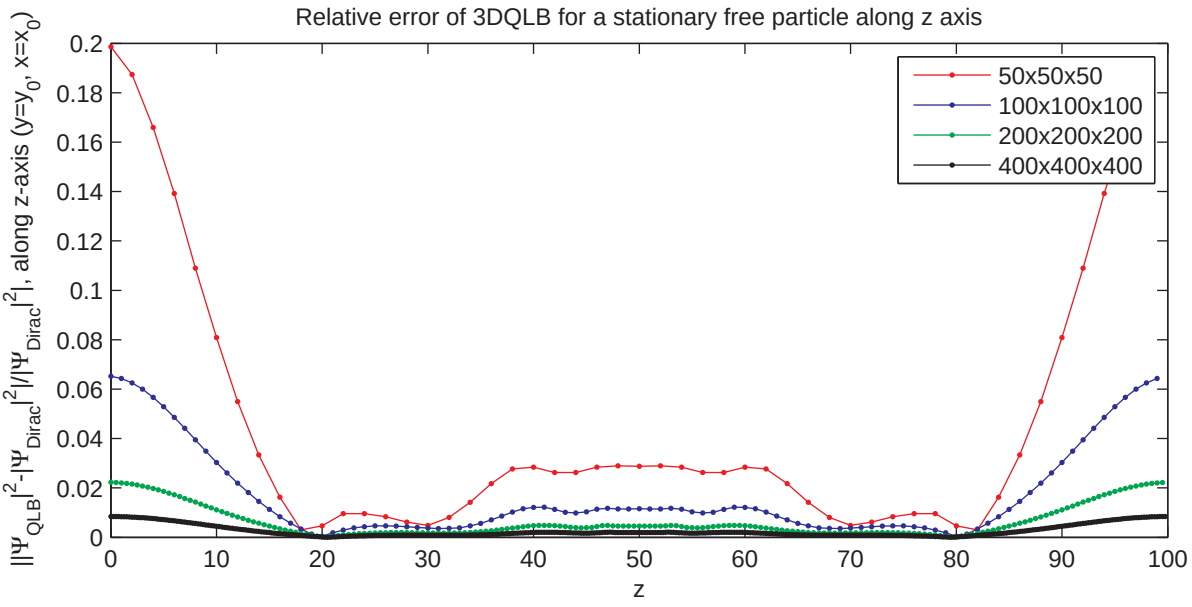

Figure 4.7: Relative 3DQLB error along z axis, given by $\frac{||\Psi_{3DQLB}|^2-|\Psi_{Dirac}|^2|}{|\Psi_{Dirac}|^2}$. The error falls below 1% for grid sizes $200 \times 200 \times 200$ and beyond.

Expanding for small Δt we get (for $c = 1$ and $\hbar = 1$)

$$\Delta \hat{u}_{1,t_{final}} = t_{final}[\hat{d}_{2,0}k_z \left(\frac{1}{3}im - k_x\right) -$$

$$\hat{u}_{2,0}k_y \left(\frac{1}{3}im + k_x\right) - \hat{d}_{1,0}k_y k_z - i\hat{u}_{1,0}k_x m]\Delta t + \mathcal{O}\left(\Delta t^2\right), \tag{4.29}$$

and similarly for $\Delta \hat{u}_2$, $\Delta \hat{d}_1$, and $\Delta \hat{d}_2$.

4.1.2 QLB in two dimensions

Two-dimensional QLB scheme is constructed by the same approach as the three-dimensional expansion. Operator splitting is applied to the Dirac equation, resulting this time in two one-dimensional equations to be diagonalized and solved using the one-dimensional QLB scheme in turn,

$$\left(\partial_t - c\alpha_z \partial_z\right) \Psi^z = i\frac{1}{2}\left(g - \omega_c \alpha_y\right) \Psi^z, \tag{4.30a}$$

$$\left(\partial_t + c\beta \partial_y\right) \Psi^{zy} = i\frac{1}{2}\left(g - \omega_c \alpha_y\right) \Psi^{zy}. \tag{4.30b}$$

The only difference to note is that the collision term is now multiplied by a factor of $\frac{1}{2}$ instead of $\frac{1}{3}$ as in the three dimensional case. Analogous with the three dimensional

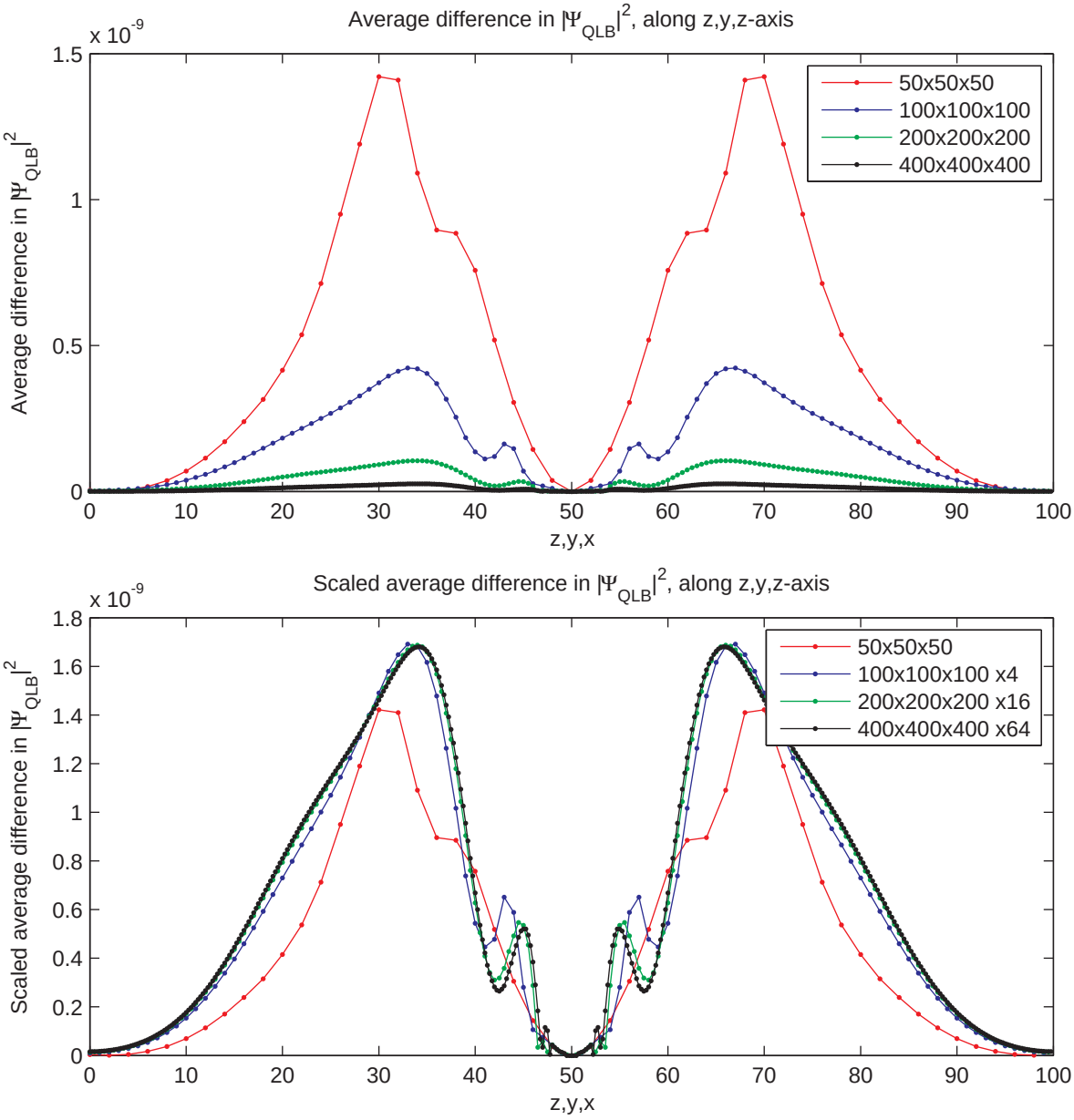

Figure 4.8: Average difference between $|\Psi_{3DQLB}|^2$ along z, y, z axis, scaled by twice the relative number of grid points to check second order of convergence to isotropy along axes.

case, the two-dimensional QLB requires rotation between collision and streaming along different axes so that evolution of a single timestep is given by the following

algorithm,

$$\begin{pmatrix} u_1 \\ u_2 \\ d_1 \\ d_2 \end{pmatrix}_{[t=(n+1)\Delta t]} = Y S_y Y^{-1} Q_z S_z Q_z \begin{pmatrix} u_1 \\ u_2 \\ d_1 \\ d_2 \end{pmatrix}_{[t=n\Delta t]} . \tag{4.31}$$

Due to quickly escalating computational costs in three dimensional simulations as the the complexity of the systems rises, more interesting simulations can be done in comfortable computational time in two dimensions. This will be the focus of our next chapter as we apply the QLB scheme to charge carriers in graphene monolayers, but now as a test we simulate a system of a wave packet incident onto a relativistic potential barrier, resulting in Klein tunnelling. The plots of the evolving probability density are shown in Figure 4.9, as well as transmission across the potential step, we can observe the dispersion of the wave packet and conservation of momentum along the y axis.

4.2 Second order multidimensional QLB

We have shown the original approach to multidimensional extension of the QLB scheme to be only first order accurate, and now will describe the modifications necessary, in addition to our 'barring' transformation, to make the multidimensional QLB scheme second order accurate. The operator splitting applied to the Dirac equation above is based on the following exponential splitting approximation

$$e^{\left(\tilde{Z}+\tilde{Y}\right)\Delta t} = e^{\tilde{Z}\Delta t} e^{\tilde{Y}\Delta t} + \mathcal{O}\left(\Delta t^2\right), \tag{4.32}$$

where $\tilde{Z}$ and $\tilde{Y}$ in our case are evolutions of the wave function (collision and streaming) along z and y axis for one timestep. Because the resulting wave function evolved along z and then along y does not equal the wave function evolved first along y and then along z, the matrices $\tilde{Z}$ and $\tilde{Y}$ do not commute, and by the BakerCampbell-Hausdorff formula,

$$e^{\left(\tilde{Z}+\tilde{Y}\right)\Delta t} = e^{\tilde{Z}\Delta t} e^{\tilde{Y}\Delta t} e^{-\frac{\Delta t^2}{2}[\tilde{Z},\tilde{Y}]} e^{\frac{\Delta t^3}{3}[\tilde{Y}[\tilde{Z},\tilde{Y}]]+[\tilde{Z},[\tilde{Z},\tilde{Y}]]} ..., \tag{4.33}$$

there is a second order error in each timestep, which accumulates to a larger error after many timesteps and gives overall first order convergence in the multidimensional QLB schemes, as we have shown above. In this case the global second order accuracy that the barring transformation gave in the one dimensional QLB is not possible.

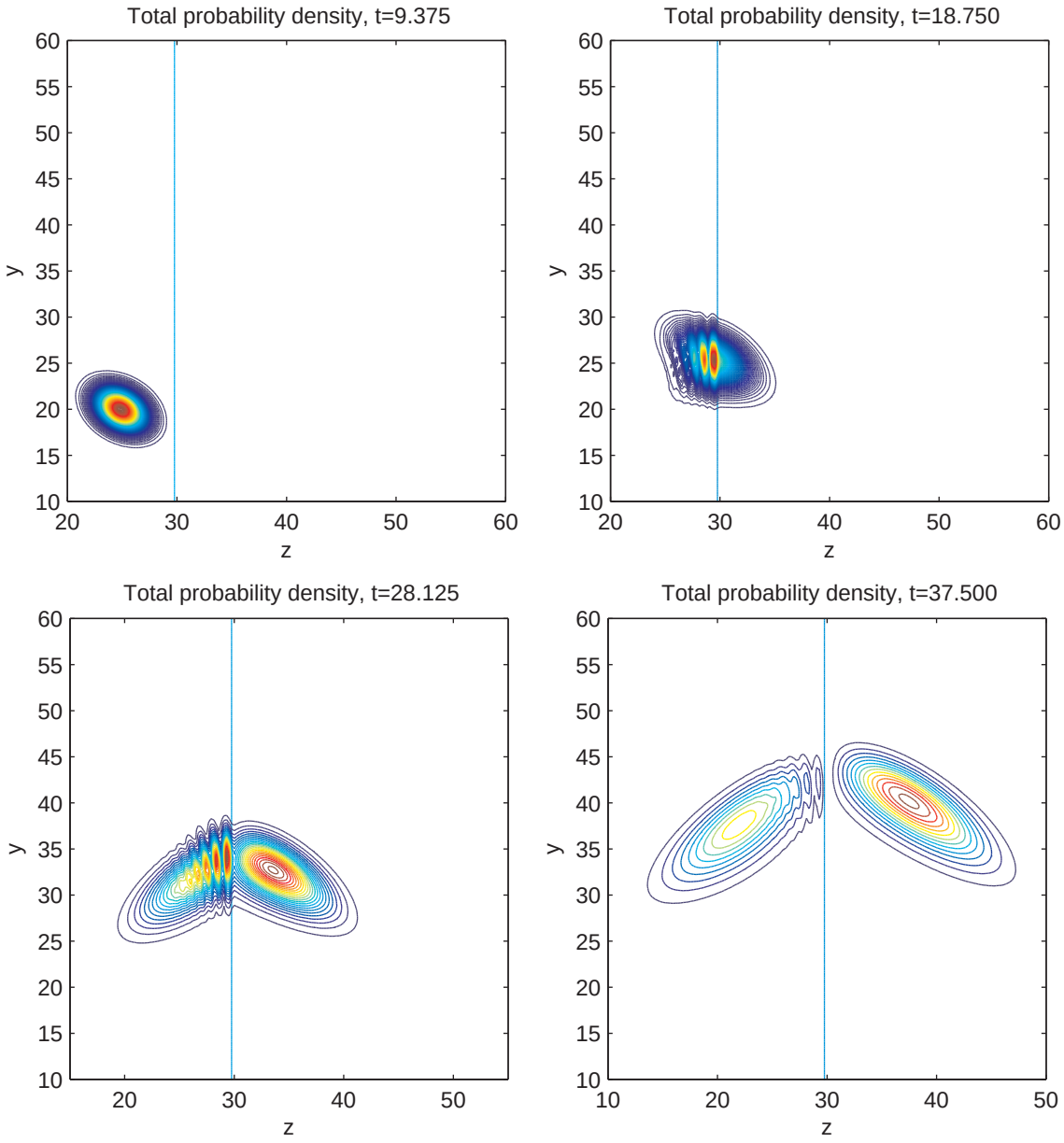

Figure 4.9: Evolution of a two dimensional wave packet incident onto a potential step at a 45 degree angle shows relativistic tunnelling and reflection. Simulated using first order two-dimensional QLB on a 256×256 lattice.

However we can improve the accuracy of operator splitting by employing second order exponential splitting approximation [92] – either generalized Strang's splitting [96],

$$e^{\left(\tilde{Z}+\tilde{Y}\right)\Delta t} = e^{\frac{1}{2}\tilde{Z}\Delta t}e^{\tilde{Y}\Delta t}e^{\frac{1}{2}\tilde{Z}\Delta t} + \mathcal{O}\left(\Delta t^3\right) \qquad 2D \qquad (4.34a)$$

$$e^{\left(\tilde{Z}+\tilde{Y}+\tilde{X}\right)\Delta t} = e^{\frac{1}{2}\tilde{Z}\Delta t}e^{\frac{1}{2}\tilde{Y}\Delta t}e^{\tilde{X}\Delta t}e^{\frac{1}{2}\tilde{Y}\Delta t}e^{\frac{1}{2}\tilde{Z}\Delta t} + \mathcal{O}\left(\Delta t^3\right) \qquad 3D \qquad (4.34b)$$

or parallel splitting

$$e^{(\tilde{Z}+\tilde{Y})\Delta t} = \frac{1}{2}\left(e^{\tilde{Z}\Delta t}e^{\tilde{Y}\Delta t} + e^{\tilde{Y}\Delta t}e^{\tilde{Z}\Delta t}\right) + \mathcal{O}\left(\Delta t^3\right) \qquad 2D \tag{4.35a}$$

$$e^{(\tilde{Z}+\tilde{Y}+\tilde{X})\Delta t} = \frac{1}{2}\left(e^{\tilde{Z}\Delta t}e^{\tilde{Y}\Delta t}e^{\tilde{X}\Delta t} + e^{\tilde{X}\Delta t}e^{\tilde{Y}\Delta t}e^{\tilde{Z}\Delta t}\right) + \mathcal{O}\left(\Delta t^3\right) \qquad 3D \tag{4.35b}$$

Once we use second order splitting of the Dirac equation, we can improve the global accuracy of the multidimensional QLB scheme to second order by applying the 'barring' transformation we derived for the one-dimensional version to the initial wave function and the inverse transformation to the final output. In two and three dimensions the barring matrix for the Dirac equation in Majorana form, aligned along z axis, is given by

$$\mathsf{B}_{\mathsf{ND}} = \frac{1}{\sqrt{1+\frac{m^2\Delta t^2}{4N^2}}}\begin{pmatrix} 1 & 0 & 0 & -\frac{m\Delta t}{2N} \\ 0 & 1 & -\frac{m\Delta t}{2N} & 0 \\ 0 & \frac{m\Delta t}{2N} & 1 & 0 \\ \frac{m\Delta t}{2N} & 0 & 0 & 1 \end{pmatrix}, \tag{4.36}$$

where N is the number of dimensions – as the Dirac equation is split into one dimensional equations, the mass term is split into equal parts, and the transformation to $\bar{u}_{1,2}$ and $\bar{d}_{1,2}$ is performed with reduced timestep size along each axis.

However second order splitting of the Dirac equation has some computational drawbacks – Strang's splitting requires doubling of the effective timestep Δt, since we cannot stream in the QLB algorithm for half a grid spacing we need to collide and stream twice along each axis to complete a timestep. Parallel splitting, on the other hand, requires doubling of computational time for a given timestep. The second order operator splitting in the three dimensional simulation is then given as the following ordering of operators, for the Strang's splitting,

$$\begin{pmatrix} u_1 \\ u_2 \\ d_1 \\ d_2 \end{pmatrix}_{[t=(n+2)\Delta t]} = S_z Q_z X S_x Q_x X^{-1} Y S_y Q_y S_y Q_y Y^{-1} X S_x Q_x X^{-1} S_z Q_z \begin{pmatrix} u_1 \\ u_2 \\ d_1 \\ d_2 \end{pmatrix}_{[t=n\Delta t]}, \tag{4.37}$$

and parallel splitting,

$$\begin{pmatrix} u_1 \\ u_2 \\ d_1 \\ d_2 \end{pmatrix}_{[t=(n+1)\Delta t]} = \frac{1}{2}(X S_x Q_x X^{-1} Y S_y Q_y Y^{-1} S_z Q_z +$$

$$S_z Q_z Y S_y Q_y Y^{-1} X S_x Q_x X^{-1}) \begin{pmatrix} u_1 \\ u_2 \\ d_1 \\ d_2 \end{pmatrix}_{[t=n\Delta t]} , \tag{4.38}$$

where S_i are streaming matrices, shifting the top two components to the right by one grid spacing and the bottom two components to the left by one grid spacing, and the rotation and collision matrices are the same as defined above for the first order multidimensional QLB scheme.

We run second order three-dimensional simulations simulations of a free particle with zero initial momentum using Strang's splitting and plot in Figure 4.10 the error in the first wave function component u_1, given as the absolute value of the difference between $u_{1,QLB}$ and $u_{1,Dirac}$. The average error over the whole domain is given by

Grid size	Average u_1 error	Reduction factor
$50 \times 50 \times 50$	1.40244×10^{-5}	–
$100 \times 100 \times 100$	3.64642×10^{-6}	3.846
$200 \times 200 \times 200$	1.03910×10^{-6}	3.509
$400 \times 400 \times 400$	3.26790×10^{-7}	3.180

We also plot the error in the total wave function's probability density $|\Psi|^2 = |\phi^+|^2 + |\phi^-|^2$ along the z axis in Figure 4.11. The average error in $|\Psi|^2$ across the whole domain in this case is

Grid size	Average $\|\Psi\|^2$ error	Reduction factor
$50 \times 50 \times 50$	4.03010×10^{-9}	–
$100 \times 100 \times 100$	1.20809×10^{-9}	3.336
$200 \times 200 \times 200$	3.70241×10^{-10}	3.263
$400 \times 400 \times 400$	1.25833×10^{-10}	2.942

We can see it reduced by a factor of only 3 to 3.3 in this case as the the size of the timestep is halved.

In Figure 4.12 we compare the error in first and second order three dimensional QLB schemes. We can see that the error for three-dimensional QLB on a $50 \times 50 \times 50$ grid is similar to the error of the second order scheme on a $100 \times 100 \times 100$ grid, because the effective timestep of the second order scheme is doubled compared to the first order QLB. However as the grid size is doubled for both cases, the magnitude of the error for the second order scheme becomes smaller than the first order three-dimensional QLB error.

The multidimensional QLB algorithm can be streamlined by colliding each time in the same form of the Dirac equation, and only applying the rotation transformations

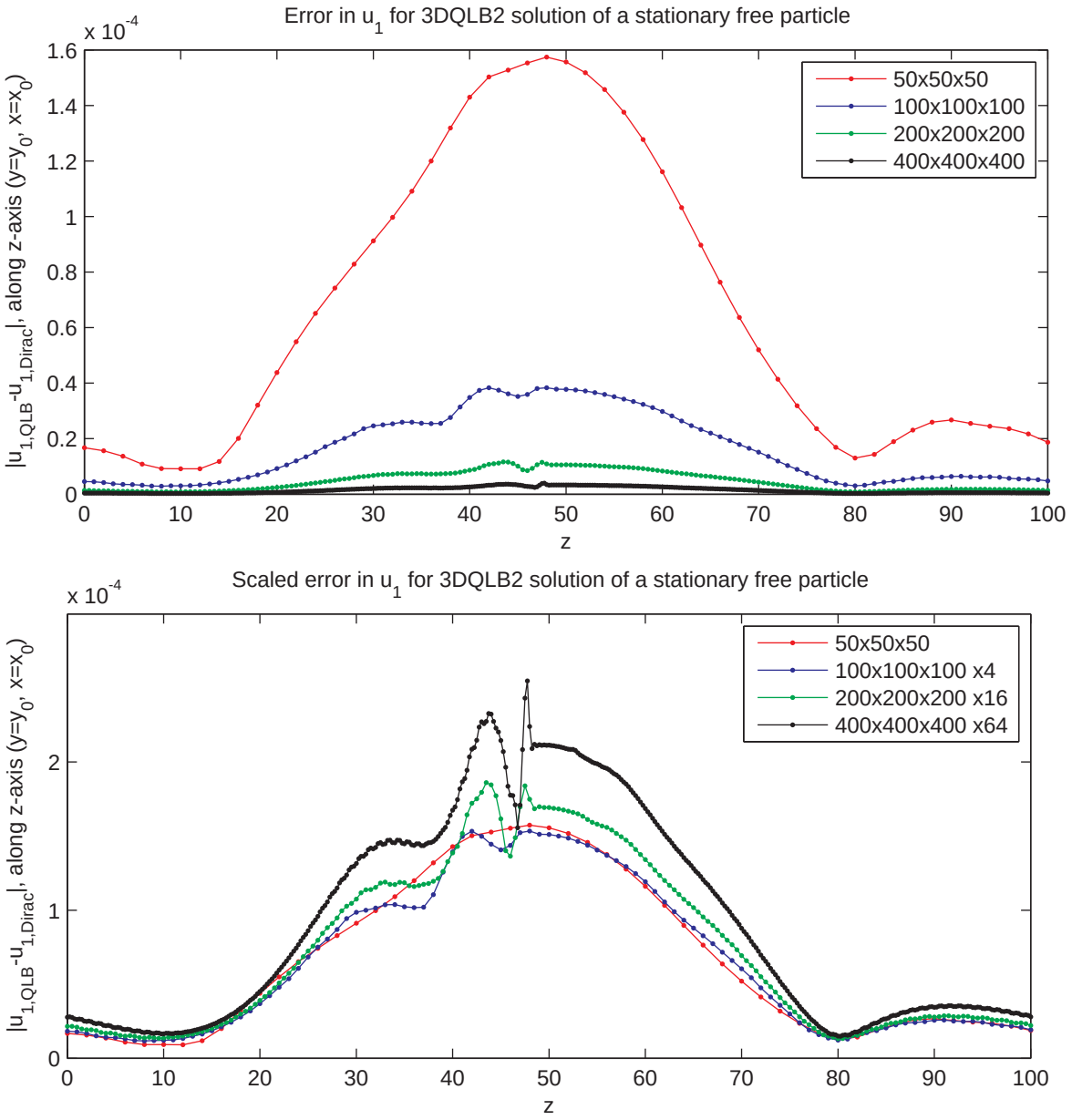

Figure 4.10: Wave function error in u_1 along z-axis, scaled by the relative number of grid points in the second plot, shows nearly second order convergence.

before and after the streaming steps along the three directions. We can see that this is possible by once again looking at the following representation of a single timestep in the scheme,

$$\begin{pmatrix} u_1 \\ u_2 \\ d_1 \\ d_2 \end{pmatrix}_{[t=(n+1)\Delta t]} = X S_x Q_x X^{-1} Y S_y Q_y Y^{-1} S_z Q_z \begin{pmatrix} u_1 \\ u_2 \\ d_1 \\ d_2 \end{pmatrix}_{[t=n\Delta t]} . \tag{4.39}$$

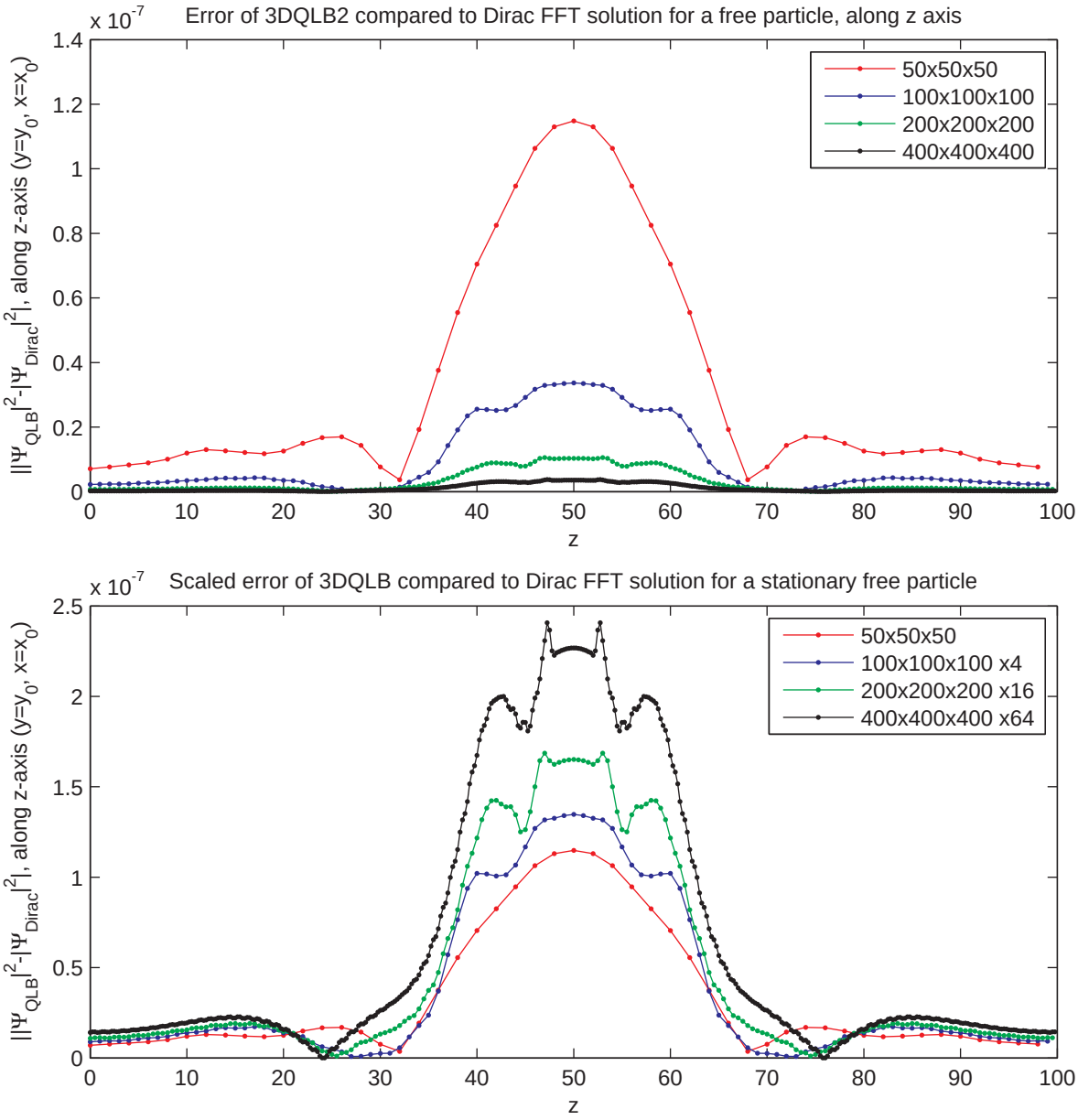

Figure 4.11: Total probability density error $||\Psi_{3DQLB}|^2 - |\Psi_{Dirac}|^2|$ along z-axis, scaled by the relative number of grid points in the second plot, shows better than first order convergence, however not exactly second order, possibly due to additional sources of error.

The collision matrices in the rotated forms of the Dirac equation are given by application of the rotation matrices to the collision matrix for the Dirac equation aligned along the z-axis,

$$Q_y = Y^{-1} Q_z Y \qquad Q_x = X^{-1} Q_z X. \tag{4.40}$$

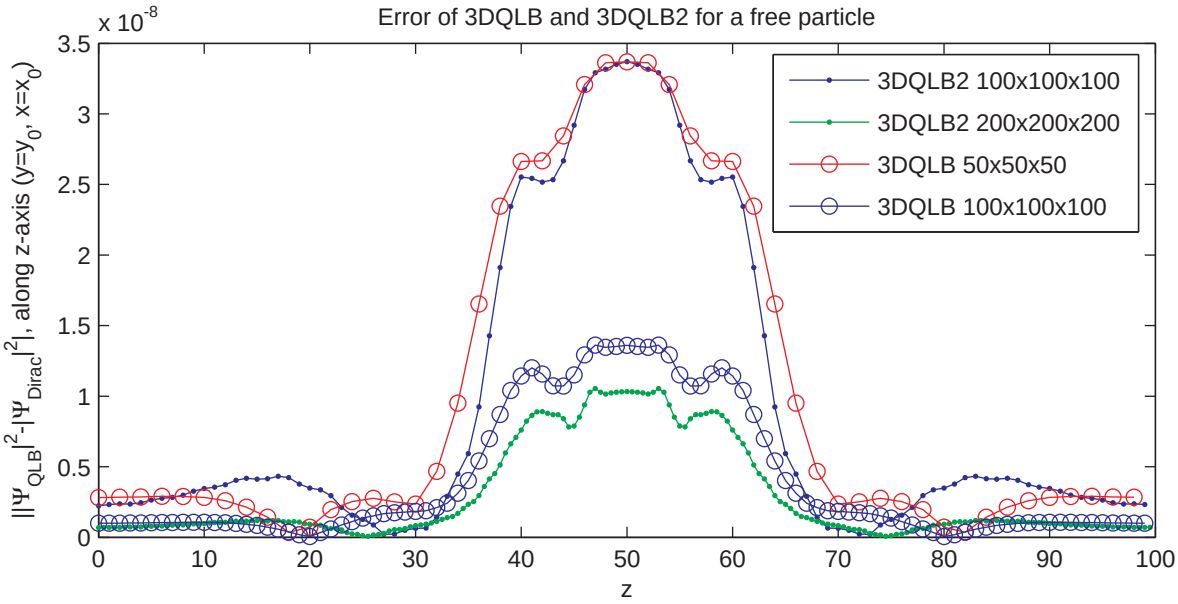

Figure 4.12: Comparison of error magnitude between first order (3DQLB) and second order (3DQLB2) three dimensional schemes – the error in total wave function probability density $|\Psi|^2$ of the first order scheme on a $50 \times 50 \times 50$ grid are about equal to the error of the second order scheme on a $100 \times 100 \times 100$ gird. Upon doubling the grid size for both schemes the error of the second order becomes comparatively smaller in magnitude.

The rotation matrices for the collisions will cancel out with those rotating the wave function, resulting in the same collision matrix being used throughout the split timestep and the wave function being rotated only before the streaming of the components,

$$\begin{pmatrix} u_1 \\ u_2 \\ d_1 \\ d_2 \end{pmatrix}_{[t=(n+1)\Delta t]} = X S_x X^{-1} Q_z Y S_y Y^{-1} Q_z S_z Q_z \begin{pmatrix} u_1 \\ u_2 \\ d_1 \\ d_2 \end{pmatrix}_{[t=n\Delta t]} . \tag{4.41}$$

The complete second order three-dimensional QLB scheme is then given by the following sequence of transformations,

$$\begin{pmatrix} u_1 \\ u_2 \\ d_1 \\ d_2 \end{pmatrix}_{[t=n\Delta t]} = \mathsf{B}_{3\mathsf{D}}^{-1} \left[S_z Q_z X S_x X^{-1} Q_z Y S_y^2 Y^{-1} Q_z^2 X S_x X^{-1} Q_z S_z Q_z \right]^n \mathsf{B}_{3\mathsf{D}} \begin{pmatrix} u_1 \\ u_2 \\ d_1 \\ d_2 \end{pmatrix}_{[t=0]} , \tag{4.42}$$

We have thus completely defined a second-order QLB scheme for three dimensions. The correction to the three dimensional scheme was published together with Succi

and Palpacelli [26], and allowed confirmation of convergence of the three dimensional scheme to the solution of Dirac equation [58]. Given the memory and CPU time requirements of such three dimensional calculations, it is impractical to run accurate simulations of complex three-dimensional systems on current generation of desktop machines, or machines not especially designed for large-scale calculations. Our further work will focus on two-dimensional systems that can be simulated more readily, and interestingly, are relevant to possible improvements in computational power of future machines that would allow much more reasonable simulation of complex three-dimensional systems.

4.2.1 Standard form of the Dirac equation

As we previously described, the QLB scheme is originally based on the Majorana form of the Dirac equation, with all the streaming matrices made real by applying matrix U to the Dirac equation in standard representation, and then applying a rotation matrix to diagonalize the streaming matrix along z, resulting in a wave function made up of $u_{1,2}$ and $d_{1,2}$ components. However, we are interested in the wave function components $\phi^+_{1,2}$ and $\phi^-_{1,2}$ that correspond to positive and negative energy solutions. The $\phi^+_{1,2}$ components approximate evolution according to the Schrödinger equation in the non-relativistic system and magnitude of $\phi^-_{1,2}$ accounts for the relativistic effects, going to zero in the non-relativistic limit. In the one-dimensional case the relationship between the two sets of components as given by equation (1.33), and in the three dimensional case this becomes

$$\phi^+_{1,2} = \frac{1}{\sqrt{2}}\left(u_{1,2} + id_{2,1}\right) \qquad \phi^-_{1,2} = \frac{1}{\sqrt{2}}\left(u_{1,2} - id_{2,1}\right), \tag{4.43}$$

with

$$|\phi^+|^2 = |\phi^+_1|^2 + |\phi^+_2|^2 \qquad |\phi^-|^2 = |\phi^-_1|^2 + |\phi^-_2|^2. \tag{4.44}$$

Therefore the multidimensional QLB implies transformation of the final output into $\phi^+_{1,2}$ and $\phi^-_{1,2}$. In the standard representation of the Dirac equation (1.27), the wave function Ψ is in the form that does not require any transformations to obtain ϕ^+ and ϕ^-,

$$\Psi = \begin{pmatrix} \psi_1 \\ \psi_2 \\ \psi_3 \\ \psi_4 \end{pmatrix} = \begin{pmatrix} \phi^+_1 \\ \phi^+_2 \\ \phi^-_1 \\ \phi^-_2 \end{pmatrix}. \tag{4.45}$$

The derivation of the non-relativistic limit is then more straight forward, as the energy shift represented by plugging in $\psi e^{-i\omega_c t}$ for the wave function components gives

$$\partial_t \begin{pmatrix} \psi_1^+ \\ \psi_2^+ \end{pmatrix} + \sigma_k \cdot \partial_k \begin{pmatrix} \psi_1^- \\ \psi_2^- \end{pmatrix} = 0 \qquad \partial_t \begin{pmatrix} \psi_1^- \\ \psi_2^- \end{pmatrix} - \frac{2imc^2}{\hbar} \begin{pmatrix} \psi_1^- \\ \psi_2^- \end{pmatrix} + \sigma_k \cdot \partial_k \begin{pmatrix} \psi_1^+ \\ \psi_2^+ \end{pmatrix} = 0, \quad (4.46)$$

and we assume the kinetic energy of $\psi_{1,2}^-$ is negligible compared to the rest mass to get the Schrödinger equation. We would then expect the ϕ^+ and ϕ^- given by (4.43) to match the ϕ^+ and ϕ^- components of the Ψ in the standard Dirac equation, however we find that is not the case. The formulae (4.43) used by Succi and co-workers are incorrect for the four component wave function, to be equal the components of the standard Dirac equation (4.45), $\phi_{1,2}^+$ and $\phi_{1,2}^-$ have to be composed from the u_1, u_2, d_1, d_2 components in the following way,

$$\phi_1^+ = \frac{1}{2}\left(-iu_1 - u_2 - id_1 + d_2\right) \qquad \phi_2^+ = \frac{1}{2}\left(u_1 + iu_2 - d_1 + id_2\right) \quad (4.47a)$$

$$\phi_1^- = \frac{1}{2}\left(-iu_1 - u_2 + id_1 - d_2\right) \qquad \phi_2^- = \frac{1}{2}\left(-u_1 - iu_2 - d_1 + id_2\right), \quad (4.47b)$$

that is given by the inverse of the transformation matrices U and Z. Expressions (4.47) and (4.47a) give the same values for the probability densities $|\phi^+|^2$ and $|\phi^-|^2$ as (4.43) when $u_1 = u_2$ and $d_1 = d_2$, but are not equal under more general conditions.

Since ϕ^+ and ϕ^- have more clear physical meaning, it is more sensible to initialize with given expressions for these components instead of $u_{1,2}$ and $d_{1,2}$, and transform into $u_{1,2}$ and $d_{1,2}$ before starting the QLB algorithm. This should be done according to the following transformations,

$$u_{1,0} = \frac{1}{2}\left(i\phi_1^+ + \phi_2^+ + i\phi_1^- - \phi_2^-\right) \qquad u_{2,0} = \frac{1}{2}\left(-\phi_1^+ - i\phi_2^+ - \phi_1^- + i\phi_2^-\right) \quad (4.48a)$$

$$d_{1,0} = \frac{1}{2}\left(i\phi_1^+ - \phi_2^+ - i\phi_1^- - \phi_2^-\right) \qquad d_{2,0} = \frac{1}{2}\left(\phi_1^+ - i\phi_2^+ - \phi_1^- - i\phi_2^-\right). \quad (4.48b)$$

Another way to correct this inconsistency in the original multidimensional QLB would be to derive a version of the QLB scheme based on the standard form of the Dirac equation instead of the Majorana form, and avoid the additional transformations [58]. Such an approach has an additional advantage of the collision matrix being diagonal, and using the streamlining of the algorithm described above, the same diagonal collision matrix can be used to evolve the wave function for all three sets of collisions.

4.2.2 Alternative approach to multidimensional QLB

Splitting the multidimensional Dirac equation into one-dimensional equations allows us to look at the second order one-dimensional scheme from a different point of view [25]. Going back to the one dimensional Dirac equation

$$\partial_t \Psi + \sigma_z \partial_z \Psi = -i\sigma_y \omega_c \Psi + ig\Psi, \tag{4.49}$$

we can split it into advection and collision equations and, by abuse of notation, write in the following way,

$$\partial_t \Psi + \sigma_z \partial_z \Psi = 0, \tag{4.50}$$

$$\partial_t \Psi = -i\sigma_y \omega_c \Psi + ig\Psi, \tag{4.51}$$

where Ψ is a two component wave function with u and d as the top and bottom component. Solving these equations in sequence, as in (4.4)-(4.5) is analogous to the collision and streaming steps of the one dimensional QLB algorithm. If we call the collision transformation Q and the streaming transformation S, the original first order accurate QLB algorithm evolving the wave function for n timesteps can be expressed as

$$\Psi(n\Delta t) = (SQ)^n \Psi(0). \tag{4.52}$$

Analogous to the approach used above, Strang splitting can be used to improve the accuracy of the scheme to second order. The wave function evolved in this way is given by

$$\Psi(n\Delta t) = \left(Q^{\frac{1}{2}} S Q^{\frac{1}{2}}\right)^n \Psi(0) = Q^{\frac{1}{2}} (SQ)^n Q^{-\frac{1}{2}} \Psi(0). \tag{4.53}$$

where, we remind from a previous chapter, the matrix Q is given by a and b evolution constants derived from discretized Dirac equation,

$$a = \frac{1 - \frac{1}{4}m^2\Delta t^2}{1 + \frac{1}{4}m^2\Delta t^2}, \qquad b = \frac{m\Delta t}{1 + \frac{1}{4}m^2\Delta t^2}. \tag{4.54}$$

$$Q = \frac{1}{1 + \frac{1}{4}m^2\Delta t^2} \begin{pmatrix} 1 - \frac{1}{4}m^2\Delta t^2 & e^{-ik\Delta t} m\Delta t \\ m\Delta t & 1 - \frac{1}{4}m^2\Delta t^2 \end{pmatrix}. \tag{4.55}$$

In deriving a second order QLB scheme in chapter 2, we came up with a 'barring' transformation of the initial conditions, and 'unbarring' of the evolved wave function component to produce the final output. These matrices are repeated below,

$$\mathsf{B} = \left(1 + \tfrac{1}{4}m^2\Delta t^2\right)^{-\frac{1}{2}} \begin{pmatrix} 1 & -\frac{1}{2}m\Delta t \\ \frac{1}{2}m\Delta t & 1 \end{pmatrix} \qquad \mathsf{B}^{-1} = \mathsf{B}^T, \tag{4.56}$$

and we note that squaring these 'barring' and 'unbarring' matrices gives the QLB collision matrix and its inverse, $\left(\mathsf{B}^{-1}\right)^2 = Q$ and $\left(\mathsf{B}\right)^2 = Q^{-1}$. This means that the second order scheme we derived in one dimension by re-discretizing the Dirac equation along the same direction on both sides of the each equation is exactly equal to the second order scheme that can be derived by Strang splitting of the collision and streaming steps,

$$\Psi\left(n\Delta t\right) = Q^{\frac{1}{2}}\left(SQ\right)^n Q^{-\frac{1}{2}}\Psi\left(0\right) = \mathsf{B}^{-1}\left(SQ\right)^n \mathsf{B}\Psi\left(0\right). \tag{4.57}$$

The initial 'barring' transformation therefore serves to compensate for the extra half of the collision that will be made in the first timestep, and the final 'unbarring' transformation is the final half collision of the simulation. Such a splitting can used to derive an alternative three-dimensional second order QLB scheme, without an explicit 'barring' transformation. The standard Dirac equation

$$\left(\partial_t + c\boldsymbol{\alpha}^x\partial_x + c\boldsymbol{\alpha}^y\partial_y + c\boldsymbol{\alpha}^z\partial_z\right)\Psi = -i\left(\omega_c\boldsymbol{\beta} + g\right)\Psi, \tag{4.58}$$

is split into three streaming and one collision equation, by abuse of notation as above,

$$\partial_t\Psi + c\alpha_x\partial_x\Psi = 0, \tag{4.59}$$

$$\partial_t\Psi + c\alpha_y\partial_y\Psi = 0, \tag{4.60}$$

$$\partial_t\Psi + c\alpha_z\partial_z\Psi = 0, \tag{4.61}$$

$$\partial_t\Psi = -i\left(\omega_c\beta + g\right)\Psi. \tag{4.62}$$

Applying Strang's splitting to the solutions of these four equations this will produce the following second order QLB algorithm,

$$\Psi\left(n\Delta t\right) = \left[S_z^{\frac{1}{2}}S_y^{\frac{1}{2}}S_x^{\frac{1}{2}}QS_x^{\frac{1}{2}}S_y^{\frac{1}{2}}S_z^{\frac{1}{2}}\right]^n\Psi\left(0\right) \tag{4.63}$$

with the added advantage that we mentioned in the previous section - the collision matrix is diagonal, and collisions can be done by exact solution of (4.62) as well as by second order discretization. In the next chapter we will use this approach in deriving a two-dimensional QLB scheme for charge carriers in graphene that are governed by a Dirac-like equation.

Chapter 5

QLB simulation of graphene

We have shown in the previous chapters that the quantum lattice Boltzmann scheme has several issues in simulation of the Schrödinger equation, such as additional approximation error, oscillation of the total probability density in $|\phi^+|^2$, and a choice of initialization that implies relativistic effects in non-zero ϕ^- components, and it became clear that is much more suited to accurate simulation of quantum systems governed by the Dirac equation. One example of such a system is graphene, whose charge carriers exhibit behaviour of relativistic particles, and we find a natural application of the QLB scheme in their simulation.

Graphene is a one-atom-thick material made up of a hexagonal lattice of carbon atoms, the first free-standing truly two-dimensional material. Layers of graphene stacked on top of each other make up graphite, graphene sheets rolled up into balls or tubes make up fullerenes and nanotubes. The theoretical physical properties and electronic band structure of graphene were known and analysed several decades ago [107], but only recently, in 2004, has a single layer of graphene been isolated in a table-top experiment [75]. Graphene has a long list of remarkable properties – it is the stiffest and strongest material, most stretchable and pliable crystal, has the highest thermal conductivity and current density, is completely impermeable to other atoms and nearly completely transparent to light. With its discovery graphene has quickly become the subject of widespread interest and intensive research due to its suitability for experimentation and potential for application in modern technology [37, 14].

At low energies, up to about 1 eV, the charge carriers in graphene are governed by a Dirac-like equation that implies zero effective mass, analogous to the Weyl equations for massless particles that allow decoupling of the four component Dirac equation

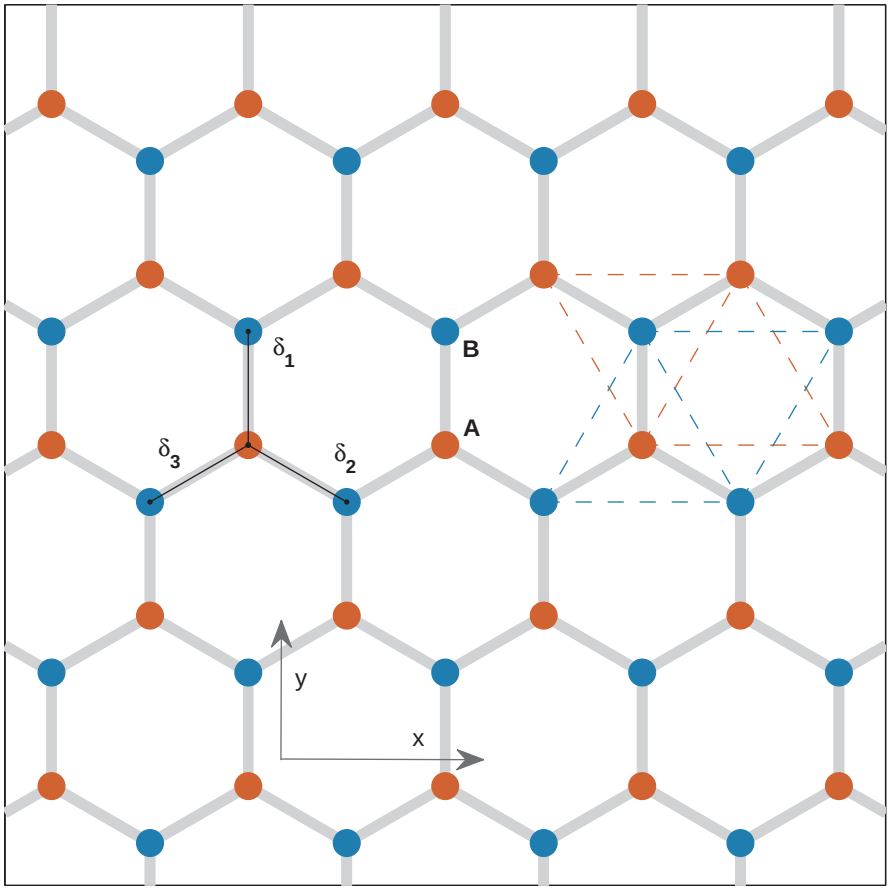

Figure 5.1: Structure of the hexagonal graphene atomic lattice, made up of two triangular sublattices (shown by red and blue coloured atoms and dashed lines) with a carbon-carbon distance is 0.142 nm^{-1}, and two carbon atoms per unit cell. Nearest-neighbour hopping of the tight-binding approach is shown by directions δ_1, δ_2, and δ_3.

into two equations for two components [76]. The massless nature of graphene's quasi-particles allows them to pass through electrostatic potentials by the way of Klein tunnelling much easier than massive particles, and shortly after its prediction [63], the Klein tunnelling effect was observed experimentally in graphene for the first time using a gate induced potential [95, 111].

The hexagonal lattice of graphene is made up of two overlapping triangular sub-lattices A and B with a distance of $a_0 = 0.142$ nm between the neighbouring carbon atoms [14], seen in Figure 5.1. The electronic band structure of graphene in the tight-binding model assumes electrons can hop to nearest (from one sublattice to the other)

and next-nearest (within the same sublattice) neighbours in the hexagonal structure of carbon atoms, and is given by

$$E_{\pm}\left(\boldsymbol{k}\right)=\pm\gamma\sqrt{3+f\left(\boldsymbol{k}\right)}-\gamma' f\left(\boldsymbol{k}\right), \tag{5.1}$$

$$f\left(\boldsymbol{k}\right)=2\cos\left(\sqrt{3}k_y a_0\right)+4\cos\left(\frac{\sqrt{3}}{2}k_y a_0\right)\cos\left(\frac{3}{2}k_x a_0\right), \tag{5.2}$$

where $\boldsymbol{k}$ is the wave number vector, $\gamma\approx 2.8$ eV and $\gamma'\approx 0.1$ eV are the nearest and next-nearest neighbour hopping energies and the $\pm$ signs correspond to the conduction (upper) and valence (lower) energy bands [14, 63]. The band structure (5.1)-(5.2) is derived as a solution to the the Schrödinger equation

$$H\Psi\left(k,r\right)=\left(\frac{p^2}{2m}+V\left(r\right)\right)\Psi\left(k,r\right)=E\left(k\right)\Psi\left(k,r\right), \tag{5.3}$$

where the wave function of graphene's valence electrons Ψ_j is written in terms of the Bloch functions Φ_j, such that

$$\Psi_j\left(k,r\right)=C_{j,A}\Phi_A\left(k,r\right)+C_{j,B}\Phi_B\left(k,r\right), \tag{5.4}$$

$$\Phi_j\left(k,r\right)=\frac{1}{\sqrt{N}}\sum_{R_j}^{N}e^{ik\cdot R_j}\phi_j\left(r-R_j\right), \tag{5.5}$$

where R_j are the coordinates of the atomic sites, ϕ_j is the atomic wave function, A and B are the two sublattices in one unit cell, and N is the number of unit cells [65]. The energy in terms of Bloch functions is given by

$$E_j\left(k\right)=\frac{\langle\Psi_j|H|\Psi_j\rangle}{\langle\Psi_j|\Psi_j\rangle}=\frac{\sum\limits_{i,l}C^*_{j,i}C_{j,l}\langle\Phi_i|H|\Psi_l\rangle}{\sum\limits_{i,l}C^*_{j,i}C_{j,l}\langle\Phi_i|\Psi_l\rangle}, \tag{5.6}$$

and is determined by minimizing the expression (5.6) with respect to variations of $C^*_{j,m}$. Setting $\partial E_j/\partial C^*_{j,m}=0$ gives

$$\sum_{l=1}^{2}H_{m,l}C_{j,l}=E_j\sum_{l=1}^{2}S_{m,l}C_{j,l},\quad H_{m,l}=\langle\Phi_m|H|\Phi_l\rangle,\quad S_{m,l}=\langle\Phi_m|\Phi_l\rangle, \tag{5.7}$$

which can be rewritten as a matrix equation for graphene,

$$H\begin{pmatrix}C_{j,1}\\C_{j,2}\end{pmatrix}=E_j S\begin{pmatrix}C_{j,1}\\C_{j,2}\end{pmatrix},\quad H=\begin{pmatrix}H_{AA}&H_{AB}\\H_{BA}&H_{BB}\end{pmatrix},\quad S=\begin{pmatrix}S_{AA}&S_{AB}\\S_{BA}&S_{BB}\end{pmatrix}. \tag{5.8}$$

The components of the transfer integral matrix H and overlap integral matrix S are given by substituting the wave function equation (5.4) into (5.7) and result in the following values,

$$H_{AA} = H_{BB} \approx \epsilon_{2p}, \qquad S_{AA} = S_{BB} \approx 1, \tag{5.9}$$

$$H_{AB} \approx -\gamma f(k), \quad S_{AB} \approx s_0 f(k), \quad f(k) = \sum_{\delta_j=1}^{3} e^{ik\cdot\delta_j}, \tag{5.10}$$

where domination of the same site contributions in the diagonal matrix elements and domination from nearest neighbor hopping in the off-diagonal matrix elements are assumed. The parameters γ and s_0 are given by,

$$\gamma = -\langle \phi_A(r - R_{A,i}) | H | \phi_B(r - R_{B,l}) \rangle \tag{5.11}$$

$$s_0 = \langle \phi_A(r - R_{A,i}) | \phi_B(r - R_{B,l}) \rangle \tag{5.12}$$

and δ_j is the position vector of sublattice point B_j relative to point A_i, equal in magitude to the carbon-carbon distance in graphene,

$$\delta_1 = \left(0, \frac{a}{\sqrt{3}}\right), \quad \delta_2 = \left(\frac{a}{2}, -\frac{a}{2\sqrt{3}}\right), \quad \delta_3 = \left(-\frac{a}{2}, -\frac{a}{2\sqrt{3}}\right). \tag{5.13}$$

The eigenvalues E_j are found by solving the secular equation,

$$det\left[\begin{pmatrix} \epsilon_{2p} & -\gamma f(k) \\ -\gamma f^*(k) & \epsilon_{2p} \end{pmatrix} - E\begin{pmatrix} 1 & s_0 f(k) \\ s_0 f^*(k) & 1 \end{pmatrix}\right] = 0, \tag{5.14}$$

and give the band structure in equations (5.1)-(5.2) above.

Omitting the next-nearest neighbour hopping effects we get a dispersion relation that is symmetric around zero energy. The Brillouin zone of graphene in momentum (reciprocal) space is also hexagonal, with the so called Dirac points located at the corners of the hexagon, labelled $\boldsymbol{K}$ and $\boldsymbol{K'}$. At these points the conduction and valence bands of the graphene electronic band structure touch each other with no gap between them, forming the so-called Dirac cones. The coordinates of the Dirac points in momentum space are given by

$$\boldsymbol{K} = \left(\frac{2\pi}{3a_0}, \frac{2\pi}{3\sqrt{3}a_0}\right) \qquad \boldsymbol{K'} = \left(\frac{2\pi}{3a_0}, -\frac{2\pi}{3\sqrt{3}a_0}\right). \tag{5.15}$$

At low energies, around the $\boldsymbol{K}$ and $\boldsymbol{K'}$ points, the dispersion relation (5.1) can be approximated by a linear function,

$$E_{\pm} = \pm\hbar v_F k_{tot} \qquad k_{tot} = \sqrt{k_x^2 + k_y^2}, \tag{5.16}$$

where $v_F \equiv \sqrt{3}\gamma a_0/(2\hbar) \approx 10^6$ m/s is the Fermi velocity, in place of the speed of light for these quasiparticles. It is important to keep in mind that the momentum values k_x and k_y in the graphene's Hamiltonian are relative to the Dirac point $\boldsymbol{K}$ ($\boldsymbol{K'}$) at the corners of the Brilouin zone and have momentum coordinates (5.15) as their origin. The dispersion relation (5.16) holds for $|k_{tot}| \ll |\boldsymbol{K}|$, which corresponds to particle energies less than 1 eV. At energies much higher than 1 eV the Dirac cones of (5.1) become affected by the trigonal warping effects, they no longer have a circular cross-section and the dispersion relation of charge carriers is no longer linear. For a more detailed account of graphene's electronic properties we refer the reader to recent reviews [14, 22]. The graphene charge carrier wave function $\tilde{\Psi}$ at low energies is described by a Dirac-like Hamiltonian governing the charge carriers in graphene under low energy approximation [63],

$$i\hbar\partial_t\tilde{\Psi} = \left[-i\hbar v_F\left(\sigma_x\partial_x + \sigma_y\partial_y\right) + qV\right]\tilde{\Psi}, \tag{5.17}$$

where V is the external scalar potential and q is the modulus of the pseudo-particle charge. The Pauli spin matrices σ_x, σ_y,

$$\sigma_x = \begin{pmatrix} 0 & 1 \\ 1 & 0 \end{pmatrix} \qquad \sigma_y = \begin{pmatrix} 0 & -i \\ i & 0 \end{pmatrix} \qquad \sigma_z = \begin{pmatrix} 1 & 0 \\ 0 & -1 \end{pmatrix}, \tag{5.18}$$

satisfy the commutation relation $[\sigma_i, \sigma_j] = 2i\epsilon_{ijk}\sigma_k$, where ϵ_{ijk} is the alternating Levi-Civita tensor [5]. The two wave function components in this case represent the amplitude of the envelop wave function on the A and B sublattices, a so called pseudo-spin of graphene's charge carriers that is separate from the intrinsic electron spin. For the full details of the derivation we refer the reader to the literature [65, 107]. The appearance of such linear 'Dirac cones' in the dispersion relation is not unique to graphene, and has been proved to be present in any periodic potential with honeycomb symmetry [31].

Simulation of charge carriers governed by the Dirac-like equation in graphene is a natural and topical application for the quantum lattice Boltzmann scheme designed for solution of the Dirac equation, given the surge in research on graphene and interest in simulation and experimental observation of quantum electrodynamical effects. We will begin by adapting the two-dimensional massless Dirac equation to the one-dimensional QLB scheme in the first section, and simulate transmission of charge carriers through a potential barrier. We will then derive a two-dimensional quantum lattice Boltzmann scheme for graphene as a tool for simulation of charge carriers and

apply it to this quantum system. In this work we study bulk region of a sheet of graphene and will neglect the complex effects of boundaries of graphene.

5.1 Klein Paradox in graphene - simulations in one dimension

In graphene the Klein paradox takes place as charge carriers are matched with holes in the valence band in the region inside the potential step, where the Dirac point is shifted by the potential. As we can see from the diagram in Figure 5.2, the lack of a band gap between the valence and conduction bands due to the massless nature of charge carriers allows even the weakest potential to create an energy range where Klein tunnelling can take place. This is in contrast with high minimum requirements for the potential strength in the case of Klein tunnelling by massive particles governed by the standard Dirac equation, as shown in Figure 3.1. The massless nature of graphene's charge carriers is also what allows us to represent motion of wave packets and Klein tunnelling in two-dimensional sheets of graphene in one dimension by using the conserved component of the momentum parallel to the barrier as the effective mass of the particle [95], allowing us to use the one dimensional QLB simulations to model relativistic quantum tunnelling in graphene.

To start we write down the plane waves in two dimensional graphene [63], similar to the plane wave description of tunnelling through a barrier in one dimension and equations (3.21)-(3.23),

$$\psi_I(x,y) = e^{ik_x x + ik_y y}\begin{pmatrix}1\\ e^{i\theta_1}\end{pmatrix} \quad \psi_R(x,y) = re^{-ik_x x + ik_y y}\begin{pmatrix}1\\ -e^{i\theta_1}\end{pmatrix} \tag{5.19}$$

$$\psi_B(x,y) = b_1 e^{iqx + ik_y y}\begin{pmatrix}1\\ e^{i\theta_2}\end{pmatrix} + b_2 e^{-iqx + ik_y y}\begin{pmatrix}1\\ -e^{i\theta_2}\end{pmatrix} \tag{5.20}$$

$$\psi_T(x,y) = \tau e^{ik_x x + ik_y y}\begin{pmatrix}1\\ e^{i\theta_1}\end{pmatrix} \qquad q = \pm\sqrt{(E-V)^2/\hbar^2 v_F^2 - k_y^2}. \tag{5.21}$$

Where ψ_I, ψ_R, ψ_T and ψ_B are the incident, reflected, transmitted and inside the barrier plane waves. The angle of incidence of the wave packet onto the potential barrier that is aligned along the y-axis is $\theta_1 = \tan^{-1}(k_y/k_x)$ and $\theta_2 = \tan^{-1}(k_y/q)$ is the refraction angle [63, 14]. From the continuity of the wave function at the edges of the barrier we can find the amplitude of the reflected plane wave [63]

$$r = -2ie^{i\theta_1}\sin(qd)\,\frac{\sin\theta_1 + \sin\theta_2}{e^{-iqd}\cos(\theta_1+\theta_2) + e^{iqd}\cos(\theta_1-\theta_2) + 2i\sin(qd)}, \tag{5.22}$$

and the amplitude of the transmitted plane wave,

$$\tau = 2e^{-ik_x d}\frac{\cos\theta_1\cos\theta_2}{e^{-iqd}\cos(\theta_1+\theta_2)+e^{iqd}\cos(\theta_2-\theta_1)+2i\sin(qd)}. \tag{5.23}$$

The corresponding transmission coefficient for Klein tunnelling through a potential barrier in two-dimensional planes of graphene is given by $T = 1-|r|^2 = |\tau|^2$ and is equal to

$$T_{Graphene2D} = \frac{\cos^2\theta_1\cos^2\theta_2}{(\cos(qd)\cos\theta_1\cos\theta_2)^2+\sin^2(qd)(1+\sin\theta_1\sin\theta_2)^2}. \tag{5.24}$$

For a potential barrier parallel to the y axis, the transverse component of the momentum k_y is constant inside and outside the barrier, so if we begin with a y-momentum eigenstate we can write $\tilde{\Psi}$ as

$$\tilde{\Psi}(x,y,t) = \Psi(x,t)\,e^{-ik_y y}. \tag{5.25}$$

Substituting this expression into (5.17) and simplifying gives,

$$\partial_t\Psi + v_F\begin{pmatrix}0&1\\1&0\end{pmatrix}\partial_x\Psi = \left[k_y v_F\begin{pmatrix}0&1\\-1&0\end{pmatrix}+ig\right]\Psi. \tag{5.26}$$

We now have a one dimensional Dirac equation with the constant $k_y v_F$ playing the role of particle mass. It is analogous to the standard Dirac equation (2.55) that we started with, but with a different collision matrix on the right hand side. To match the exact form of the standard Dirac equation (2.55) we apply the unitary matrix Λ to (5.26),

$$\Lambda = \frac{1}{2}\begin{pmatrix}1+i&1-i\\1-i&1+i\end{pmatrix} \qquad \Lambda^{-1} = \frac{1}{2}\begin{pmatrix}1-i&1+i\\1+i&1-i\end{pmatrix}. \tag{5.27}$$

to get the desired result

$$\partial_t\Psi' + v_F\begin{pmatrix}0&1\\1&0\end{pmatrix}\partial_x\Psi' = \left[k_y v_F\begin{pmatrix}-i&0\\0&i\end{pmatrix}+ig\right]\Psi'. \tag{5.28}$$

The components of the wave function described by the graphene Hamiltonian are related to the wave function components described by the standard Dirac equation form by the same transformation,

$$\Psi' = \begin{pmatrix}\Phi^+\\\Phi^-\end{pmatrix} = \Lambda^{-1}\begin{pmatrix}\Phi_A\\\Phi_B\end{pmatrix}. \tag{5.29}$$

We now have a transformation of the graphene Dirac-like equation to the standard Dirac equation (2.55), and from that, as before, we can transform to equations (2.53a)

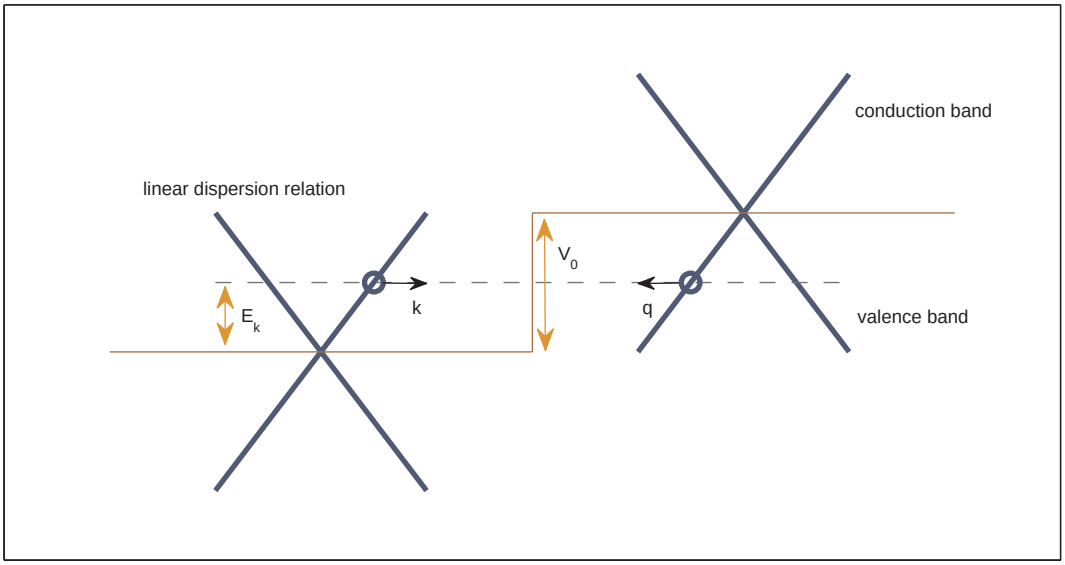

Figure 5.2: A diagram of Klein tunnelling through a potential step in graphene shows the shifting of the Dirac point by the potential so that incident particles are matched with holes in the valence band as they are transmitted across the potential step. The momentum of the holes q is opposite to the momentum of the incident charge carriers k, but they travel in the same direction, analogous to anti-particles in the relativistic tunnelling governed by the standard Dirac equation.

in terms of u and d to set up the QLB simulations. The effective mass is now a function of the angle of incidence relative to the x axis,

$$k_y v_F = k_{tot} \sin(\theta_1) v_F = \frac{E}{\hbar} \sin(\theta_1), \tag{5.30}$$

and effective wave number is given by $k_x = k_{tot} \cos(\theta_1)$. The total relativistic energy of this one dimensional massive particle analog, calculated from the sum of the effective rest energy and momentum, matches the energy of the quasiparticle in graphene,

$$E = \sqrt{\hbar^2 k_{tot}^2 \cos^2(\theta_1) v_F^2 + \hbar^2 k_{tot}^2 \sin^2(\theta_1) v_F^2} = \hbar k_{tot} v_F, \tag{5.31}$$

as defined by the approximation to the tight binding dispersion relation near the Dirac points (5.16). For our representation of graphene tunnelling in one dimension the formula for $T_{Graphene2D}$ (5.24) simplifies to $T_{Barrier1D}$ (3.28) when mass is given by the transverse momentum as described above.

5.1.1 Potential barrier simulation results

We aim to qualitatively study the dependence of the wave packet transmission coefficient on the angle of incidence using QLB simulations, confirm that the QLB scheme

correctly reproduces these relativistic effects, observe the differences between wave packet and plane wave transmission, and observe Fabry-Perot resonance effects that we mentioned in chapter 3. Our parameter choice is guided by the Figures given by Katsnelson, Novoselov and Geim in their paper on the theoretical possibility of Klein tunnelling in graphene [63],

barrier width $d = 98.3$ nm,
particle energy/wavenumber $E = 0.1215$ nm^{-1} (80 meV),
potential height $V_1 = 0.3037$ nm^{-1} (200 meV),
potential height $V_2 = 0.4328$ nm^{-1} (285 meV),
and Fermi velocity $v_F = 10^6$ m/s.

For convenience we have transformed the energies into wave numbers by multiplying $E = \hbar v_F k_{tot}$ by $1/\hbar v_F$. Although the Fermi velocity v_F slightly changes with charge concentration due to renormalization effects created by electron-electron interactions [28], we use the commonly accepted Figure of $v_F = 10^{15}$ nm/s, and $\hbar = 1.055 \times 10^{-34}$ $kg \cdot m^2/s$ for our simulations. Our domain of $z = [-5291, 5291]$ nm is discretized with $N = 20000$ grid points. We run two sets of simulations with different values of the initial wave packet width, $\Delta_0^2 = 529101$ nm^2 and $\Delta_0^2 = 2 \times 529101$ nm^2 to also observe the effects of wave packet width on the transmission probability. The widths are set high to make the wave packet narrow enough in momentum space to have the resonance effects more noticeable. Note that, as required for the presence of Klein tunnelling effects, the potential heights V_1 and V_2 are more that twice the particle energy.

We run a series of simulations with a range incidence angles and calculate the resulting transmission coefficient by taking the sum of the probability density values in the region beyond the potential step once the tunnelling process is concluded and the wave packet has split into clearly separated reflected and transmitted parts. The plots of the theoretical and simulated transmission probabilities are shown in Figure 5.3. These simulations correspond to the one-dimensional simulations of the standard Dirac equation we described in section 3.2, and can be run with the same 1DQLB code if the wave function is modified by Λ as we described above. Adjusting the effective mass parameter is used to model incidence of the wave packet onto the barrier at different angles. We can see that both the calculated theoretical and the

simulated transmission coefficients for a wave packet never quite reach the plane wave transmission coefficient of 1 at resonance peaks. This is due to only a fraction of the wave numbers composing the wave packets resonating at that particular angle of incidence, and the rest are split into reflected and transmitted components. Comparing the wave packets of different widths, we see that as we make the wave packet wider in position space (therefore narrower in momentum space), the transmission probability reaches closer to the plane wave values.

Thus we conclude that the one dimensional QLB is a suitable tool for quick qualitative simulation of wave packet dynamics in graphene. We should note, however, that such a representation of graphene's massless charge carriers in one dimension is of limited accuracy. While the effective mass is set by a single value of the transverse momentum of the plane wave k_y, a real wave packet in two dimensions has its transverse momentum also as a range of k_y values, a range of the plane waves that make up the wave packet. To represent this range of k_y we need to run multiple one dimensional simulations with a corresponding range of effective mass values, but this is impractical. To simulate the behaviour of two dimensional wave packets in graphene more accurately we can use multidimensional QLB. In the next section we will derive a two-dimensional QLB scheme for graphene and study this problem in more detail.

5.2 QLB method for graphene

To derive a two-dimensional quantum lattice Boltzmann scheme for graphene we once again go back to the Dirac-like equation (5.17) and start by dividing through by $i\hbar$,

$$\partial_t \Psi + v_F \left(\sigma_x \partial_x + \sigma_y \partial_y\right) \Psi = -\frac{iqV}{\hbar} \Psi. \tag{5.32}$$

To simplify implementation of the QLB it is customary to use units in which the speed of light is set $c = 1$ and $\Delta x = \Delta t$. In graphene the Fermi velocity v_F takes the place of the speed of light and we can reach the same $\Delta x = \Delta t$ relation by dividing (5.32) by v_F and rescaling time by v_F,

$$\partial_t \Psi + \left(\sigma_x \partial_x + \sigma_y \partial_y\right) \Psi = ig\Psi, \tag{5.33}$$

where $g = -qV/\hbar$ and $t = v_F t_{physical}$ are now in units of length. We use the alternative splitting of the Dirac equation that we described in the last section of the previous

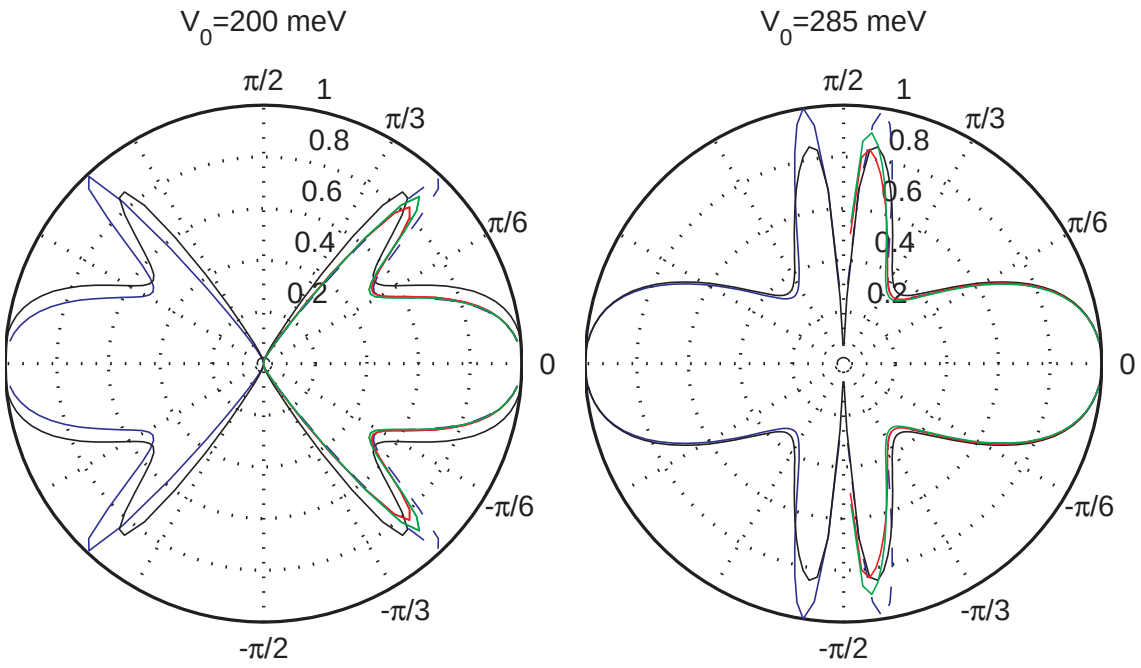

Figure 5.3: Plots of the theoretical plane wave transmission coefficient (blue), theoretical wave packet transmission coefficient (black) and simulated wave packet transmission coefficient (red, green) as a function of the angle of incidence of the incoming wave packet. When the plane wave transmission coefficient (blue) reaches perfect transmission due to resonance effect for the particular wave number, the corresponding peak in simulated the wave packet transmission probability (red) does not reach perfect transmission due to the presence of other wave numbers in the wave packet that have limited transmission. However if we make the simulated wave packet narrower in momentum space (green), it is able to reach a higher transmission coefficient due to resonance effects, as shown on the plot. Simulations were run on a $10,582$ nm domain, discretized with $N = 20,000$ points.

chapter to separate advection in each spatial dimension from the collision and, by abuse of notation, we get the following set of equations,

$$\partial_t \Psi + \sigma_x \partial_x \Psi = 0, \tag{5.34}$$

$$\partial_t \Psi + \sigma_y \partial_x \Psi = 0, \tag{5.35}$$

$$\partial_t \Psi = ig\Psi, \tag{5.36}$$

where for one timestep the wave function Ψ is evolved in sequence according to each equation, as in (**??**)-(4.5). We can diagonalize σ_x and σ_y by applying unitary

transformations to equations (5.34) and (5.35),

$$X^{-1}\sigma_x X = Y^{-1}\sigma_y Y = \begin{pmatrix} 1 & 0 \\ 0 & -1 \end{pmatrix}. \tag{5.37}$$

The unitary transformation matrices we use are

$$X^{-1} = \frac{1}{\sqrt{2}}\begin{pmatrix} 1 & 1 \\ -1 & 1 \end{pmatrix} \qquad X = \frac{1}{\sqrt{2}}\begin{pmatrix} 1 & -1 \\ 1 & 1 \end{pmatrix}, \tag{5.38}$$

$$Y^{-1} = \frac{1}{\sqrt{2}}\begin{pmatrix} i & 1 \\ -i & 1 \end{pmatrix} \qquad Y = \frac{1}{\sqrt{2}}\begin{pmatrix} -i & i \\ 1 & 1 \end{pmatrix}. \tag{5.39}$$

Application of these transformations decouples the two components of the wave function, one streaming in the positive direction and one in the negative direction,

$$\partial_t \Psi + \begin{pmatrix} 1 & 0 \\ 0 & -1 \end{pmatrix} \partial_x \Psi = 0 \qquad \partial_t \Psi + \begin{pmatrix} 1 & 0 \\ 0 & -1 \end{pmatrix} \partial_y \Psi = 0, \tag{5.40}$$

and the resulting equations can be solved by integration along characteristics as we have done for the one-dimensional QLB in section 2.2.1. The wave functions after one timestep Δt are given by

$$\psi_1(x, t+\Delta t) = \psi_1(x-\Delta t, t) \qquad \psi_2(x, t+\Delta t) = \psi_2(x+\Delta t, t), \tag{5.41}$$

$$\psi_1(y, t+\Delta t) = \psi_1(y-\Delta t, t) \qquad \psi_2(y, t+\Delta t) = \psi_2(y+\Delta t, t), \tag{5.42}$$

and these are exact solutions of streaming equations (5.40). We can also solve equation (5.36) governing collisions exactly,

$$\Psi(x, t+\Delta t) = e^{ig\Delta t}\Psi(x, t), \tag{5.43}$$

or with second order accuracy using Crank-Nicolson approximation as before,

$$\Psi(x, t+\Delta t) = \frac{1 + ig(x)\Delta t/2}{1 - ig(x)\Delta t/2}\Psi(x, t). \tag{5.44}$$

It is important to note that although we have exact solutions for the streaming and collisions, sequential evolution of the wave function by these steps will generate a second order error in the wave function, so using a second order discrete approximation for the collisions will not degrade the global accuracy of the scheme.

We represent a single timestep in the QLB algorithm as application of a series of matrices to the initial two-component wave function,

$$\Psi(t+\Delta t) = YS^y Y^{-1} QXS^x X^{-1}\Psi(t), \tag{5.45}$$

where S^x and S^y represent streaming of the wave function components. The first component ψ_1 is streamed in the positive direction the second component ψ_2 in the negative direction. The collision matrix Q is equal to,

$$Q = \begin{pmatrix} e^{ig\Delta t} & 0 \\ 0 & e^{ig\Delta t} \end{pmatrix} \quad or \quad Q = \begin{pmatrix} \frac{1+ig(x)\Delta t/2}{1-ig(x)\Delta t/2} & 0 \\ 0 & \frac{1+ig(x)\Delta t/2}{1-ig(x)\Delta t/2} \end{pmatrix}. \tag{5.46}$$

As mentioned above, such operator splitting generates a $\mathcal{O}(\Delta t^2)$ error at each timestep due to non-commutation of the steps, the errors accumulate into a $\mathcal{O}(\Delta t)$ being introduced into the scheme by the splitting. We can reduce the overall error to $\mathcal{O}(\Delta t^2)$ by using Strang's splitting method at every timestep [92, 96],

$$e^{(A+B)\Delta t} = e^{A\Delta t/2} e^{B\Delta t} e^{A\Delta t/2} + \mathcal{O}\left(\Delta t^3\right). \tag{5.47}$$

Exponential factors here represent shifting and collisions done in turn instead of simultaneously. As mentioned in chapter 4, Strang splitting requires us to run at an effectively double the grid size, because the shifting for 'half a grid space' by the equations (5.41)-(5.41) implies collisions for a double timestep and shifts by a single grid space. This is equivalent to running simulations on two interlapping grids and results in a jagged solution profile and reduced accuracy. However, in the case of two dimensions we can remove these undesirable effects by performing the half-shifts through action on the discrete Fourier transforms of the wave function. We designate the transformation and shifting along x and y as

$$\bar{X} = XS^xX^{-1} \qquad \bar{Y} = YS^yY^{-1}, \tag{5.48}$$

and therefore have $\bar{X}^{\frac{1}{2}}$ and $\bar{Y}^{\frac{1}{2}}$ as shifts by half a timestep. Using (5.45) we can express a complete Strang splitting QLB simulation of n timesteps up to a final time t_f as follows,

$$\Psi(t_f) = \left[\bar{Y}^{\frac{1}{2}} Q^{\frac{1}{2}} \bar{X} Q^{\frac{1}{2}} \bar{Y}^{\frac{1}{2}}\right]^n \Psi(0) = \bar{Y}^{-\frac{1}{2}} \left[\bar{Y} Q^{\frac{1}{2}} \bar{X} Q^{\frac{1}{2}}\right]^n \bar{Y}^{\frac{1}{2}} \Psi(0), \tag{5.49}$$

We see that representing the QLB algorithm in this way we do not suffer increased running times due to the greater computational cost of performing the half-step shifting by actions in Fourier space at each timestep. We only have to shift by half a grid space once in the beginning and once at the end of the simulation, which is important if we wish to perform the half-shifts in momentum space, and use simple shifting of the wave function arrays over the grid for the bulk of the simulation. Collisions for

half a timestep $Q^{\frac{1}{2}}$ are done by using $\Delta t/2$ in place of Δt in (5.46). The half-shifts in Fourier space are defined as a unitary transformation,

$$\bar{Y}^{\pm\frac{1}{2}}\Psi\left(x,y,t\right)=\mathcal{F}^{-1}\left[e^{\pm ik_y\Delta t/2}\hat{\Psi}\left(k_x,k_y,t\right)\right], \tag{5.50}$$

where $\hat{\Psi}=\mathcal{F}\left[\Psi\right]$ is a discrete Fourier transform of the wave function Ψ and $\mathcal{F}^{-1}$ is the inverse discrete Fourier transform operator. They are defined by

$$\hat{\Psi}\left(k_x,k_y,t\right)=\sum_{x,y\in L}\Psi\left(x,y,t\right)e^{-ik_xx-ik_yy}, \tag{5.51}$$

$$\Psi\left(x,y,t\right)=\frac{1}{N}\sum_{k_x,k_y\in K}\hat{\Psi}\left(k_x,k_y,t\right)e^{ik_xx+ik_yy}, \tag{5.52}$$

where L is the domain in real space, K is the wave number domain in momentum space, and N is the number of grid points. Thus with equation (5.49) we have completely defined a second order accurate unitary QLB algorithm for graphene.

5.3 Free wave packets in graphene

To test the scheme's ability to correctly simulate the evolution of wave functions in graphene we run simulations of free wave packets in graphene and compare with the analytical solutions of Maksimova et. al. [64], as well as spectral solutions of the Dirac equation. We initialize the system with a Gaussian wave packet, centred at (x_0,y_0), given by

$$\Psi\left(x,y,0\right)=\frac{1}{\sigma\sqrt{\pi}\sqrt{\left|c_1\right|^2+\left|c_2\right|^2}}e^{-\frac{(x-x_0)^2+(y-y_0)^2}{2\sigma^2}+ik_yy}\begin{pmatrix}c_1\\c_2\end{pmatrix}, \tag{5.53}$$

where c_1 and c_2 are the relative amplitudes of the wave function on sublattices A and B. To match the results of Maksimova et. al. [64] we simulate over the same 40×40 nm domain and use the following parameters

wavenumber $k_y=1.5$ nm^{-1},
wave packet width $\sigma=2$ nm,
wave packet initial position $x_0=20$ nm, $y_0=20$ nm.

As before, we have converted energy and potential values from eV to nm^{-1} by scaling with $\frac{1}{\hbar v_F}$, where $v_F=10^{15}$ nm/s and $\hbar=6.582\times10^{-16}$ eVs. Our simulations are run on a 2000×2000 grid point lattice, using round numbers here instead of the traditional powers of two to be able to exactly match the final time of $t_f=14\times10^{-15}$ s

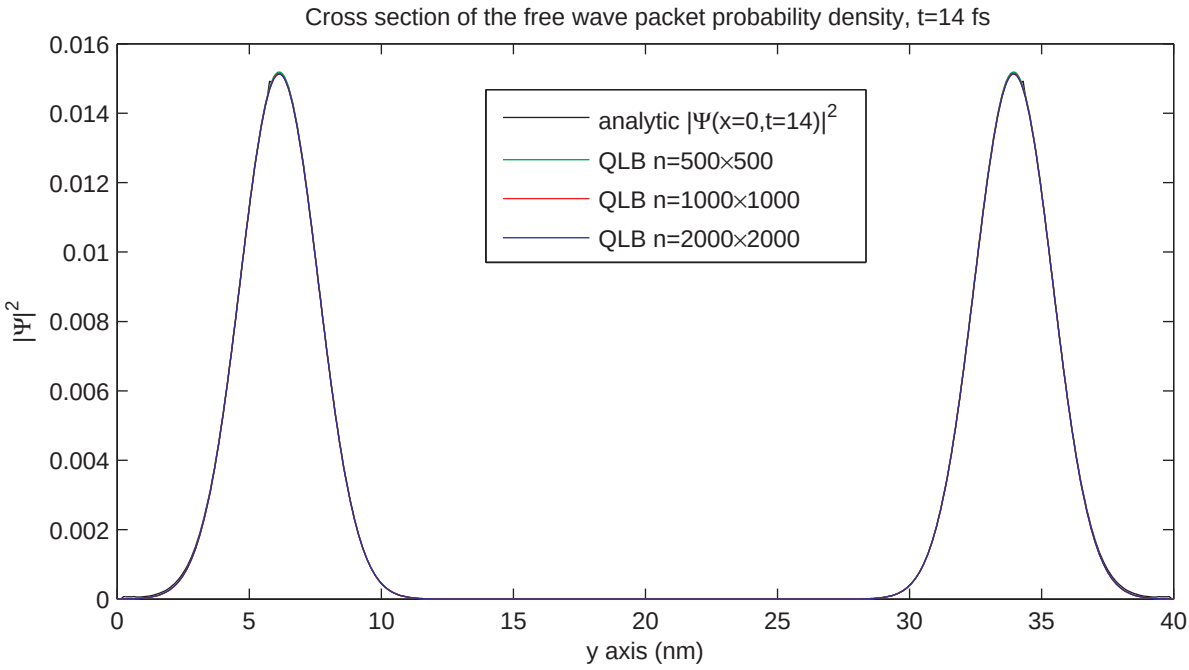

Figure 5.4: A cross section of the free wave packet probability density at $t = 14$ fs, comparing analytical solution with the QLB simulation results.

with the calculations of Maksimova et. al. [64]. The results show that our simulations qualitatively match the evolution of the wave packet for all sets of initial amplitudes of the wave function components,

$$c_1 = 1,\ c_2 = 0,$$
$$c_1 = 1,\ c_2 = 1,$$
$$c_1 = 1,\ c_2 = i,$$
$$c_1 = 1,\ c_2 = e^{i\pi/4},$$

with an evolution plot of the $c_1 = 1$, $c_2 = e^{i\pi/4}$ case shown in Figure 5.5. We can see $\theta_1 = \pi/4$ phase difference between the two wave function components distorting dispersion and breaking up of the wave packet into two parts. Note that due to the massless nature of quasiparticles in graphene, the QLB simulation in the absence of a scalar potential involves only streaming of the wave function components along the x and y axis, with no collisions taking place. A comparison of the simulated wave function probability density $|\Psi|^2 = |\psi_1|^2 + |\psi_2|^2$ with the analytical expressions given in [64] is shown in Figure 5.4 - the simulated results all lie on top of the analytical solution, with the difference being less than 1×10^{-4}, or 0.06%. A calculation of the

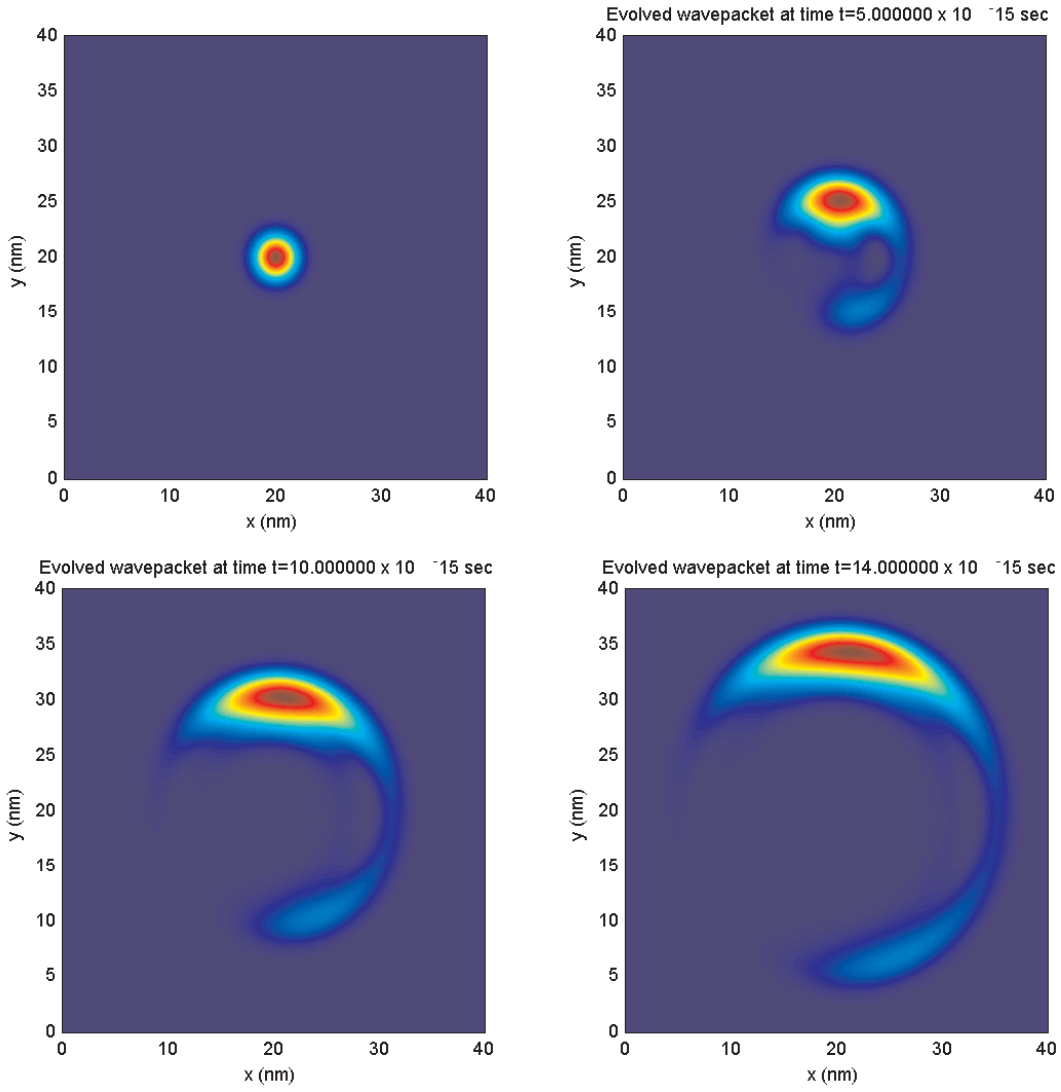

Figure 5.5: Evolution of a free wave packet in graphene in a 40×40 nm domain with $c_1 = 1$, $c_2 = e^{i\pi/4}$ and initial momentum directed along the y-axis.

differences in $|\Psi|^2$ between the QLB simulations, averaged over the whole domain shows second order convergence of the results,

$$
\begin{aligned}
a_1 &= N^{-1} \sum \left(|\Psi_{n=2000^2}|^2 - |\Psi_{n=4000^2}|^2 \right) = 1.27637 \times 10^{-7}, \\
a_2 &= N^{-1} \sum \left(|\Psi_{n=1000^2}|^2 - |\Psi_{n=2000^2}|^2 \right) = 5.10877 \times 10^{-7} = 4.00 a_1, \\
a_3 &= N^{-1} \sum \left(|\Psi_{n=500^2}|^2 - |\Psi_{n=1000^2}|^2 \right) = 2.04881 \times 10^{-6} = 4.01 a_2.
\end{aligned}
$$

We also calculate the QLB simulation of the Zitterbewegung effect that we discussed in Chapter 2, and compare with the analytical solution. In graphene the Zitterbewe-

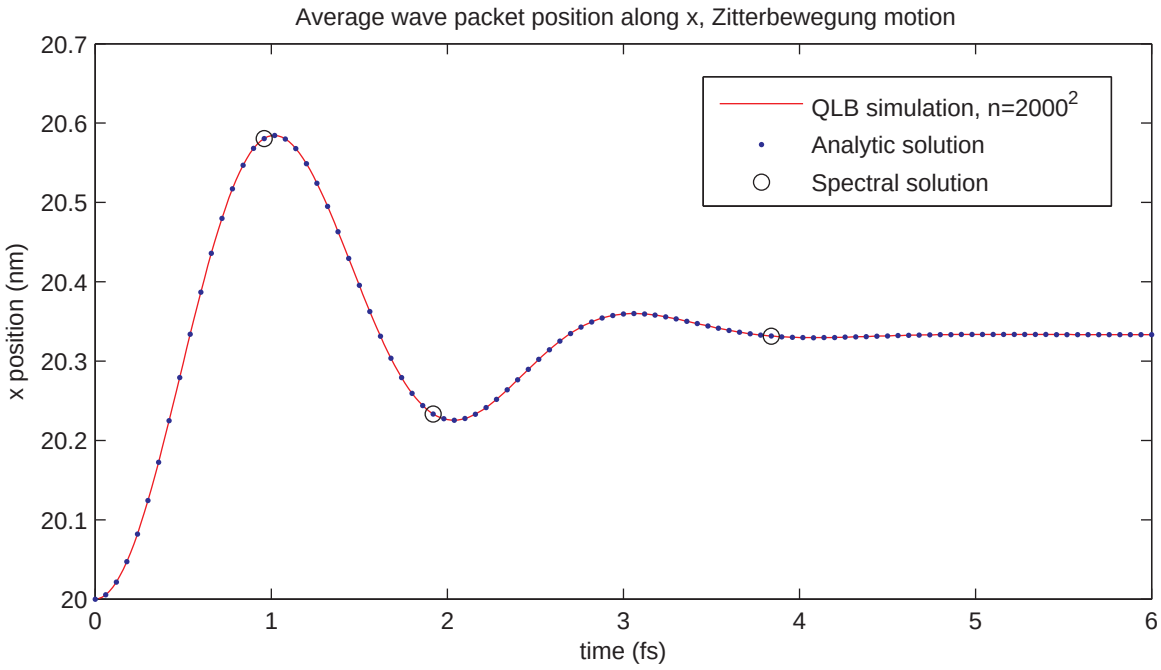

Figure 5.6: Zitterbewegung motion of a free wave packet in graphene, initialized with $c_1 = 1$ and $c_2 = 0$, shows good agreement between the analytical solution, the spectral solution and the simulated motion.

gung oscillation occurs due to interaction of the two components of the quasiparticle wave function in the same way as it does for massive particles. The theoretical description of the oscillating motion is calculated by Maksimova et. al. [64] by finding the expectation of the position operator in momentum space, where it becomes $i\hbar\frac{d}{dk}$, analogous to the calculation for the standard Dirac equation (3.63). For initial amplitudes of the wave function $c_1 = 1$ and $c_2 = 0$ the position of the wave packet along the x-axis is given by [64]

$$\bar{x}\,(t) = \frac{1 - e^{-a^2}}{2a} - e^{-a^2} \int_0^\infty e^{-\rho^2} \cos\left(2\rho t\right) I_1\left(2a\rho\right) d\rho, \tag{5.54}$$

where I_1 is a modified Bessel function of the first order, and a is a dimensionless parameter given by $a = k_y\sigma$ that dictates the general shape of the Zitterbewegung motion, with its amplitude and evolution in time scaled by wave packet width σ. We compare (5.54) with our simulation result and observe good agreement with the analytical expression, shown in Figure 5.6.

We run the same simulation with $c_1 = 1$ and $c_2 = 0$ at a range of grid point resolutions, from $n = 500 \times 500$ to $n = 4000 \times 4000$, and compare the difference

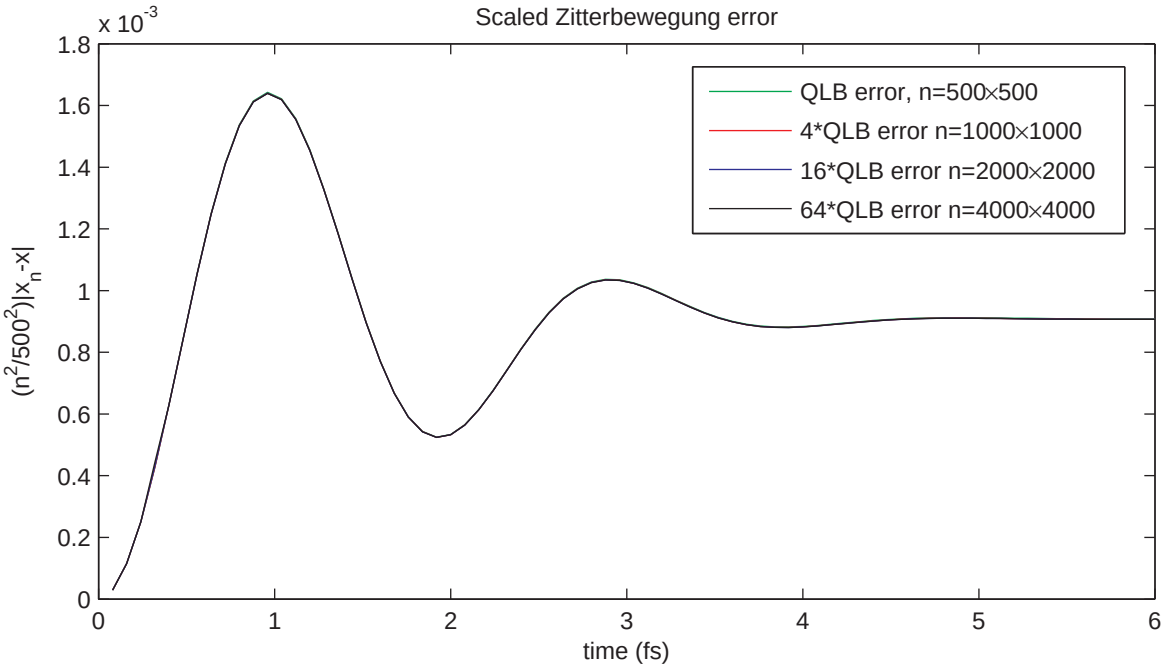

Figure 5.7: Comparison of the error in the Zitterbewegung motion of the wave packet for different grid resolutions shows second order convergence in the average wave packet position, with no noticeable growth of error with time.

between the QLB average position calculations and the analytical result, scaled by the ratio of grid resolutions, to check the rate of convergence. The plot of the results in Figure 5.7 confirms second order of convergence.

As another confirmation of the scheme's second order convergence with grid refinement we use an exponentially accurate spectral solution for free particles that we described in the one-dimensional error analysis in section 2.1.3, and look at the evolution with time of the error in probability density taken across the whole simulated domain, in the left panel of Figure 5.8. This shows clear second order convergence of the probability density over the whole domain. Noticing in Figure 5.7 the lack of apparent growth of error in wave packet position with time, we look at the evolution of error in probability density with time in the right panel of Figure 5.8. After the initial drop in the magnitude of the error at $t = 1.92$, corresponding to a similar drop in the average position error (see Figure 5.7), the error in $|\Psi|^2$ grows linearly with time as expected as the position stabilizes.

In addition to the probability density comparisons, we also use the spectral solution to demonstrate second order convergence of the amplitude and phase of wave

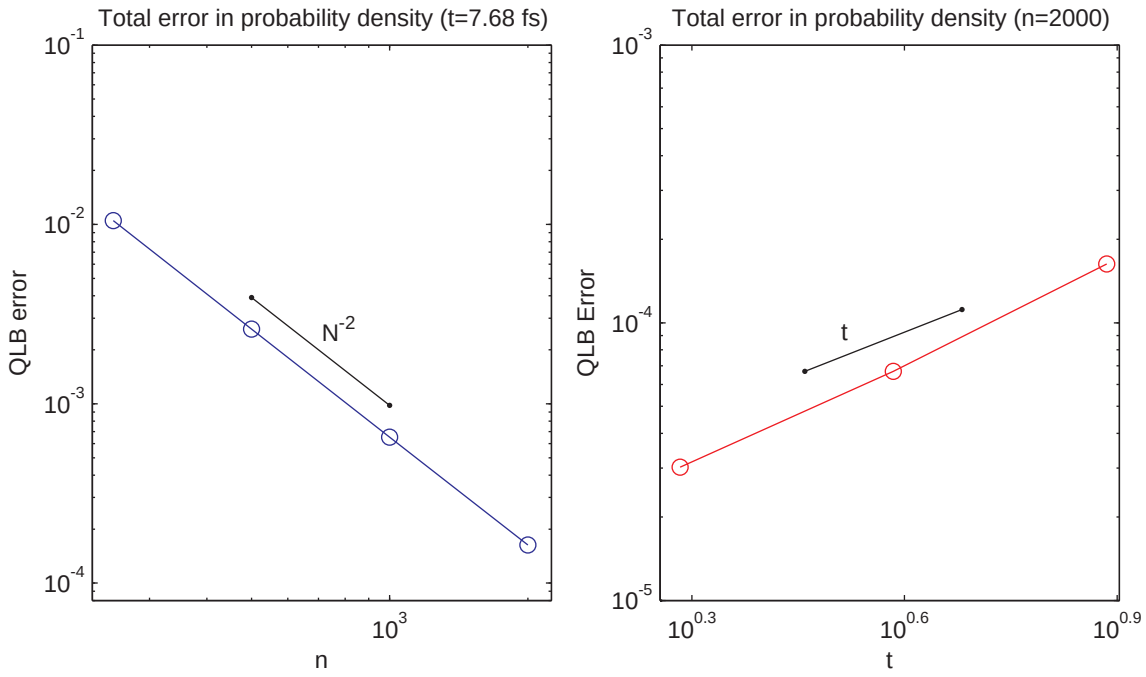

Figure 5.8: Total error in the probability density across the simulated domain, $\sum_{x,y}(|\Psi_{spectral}|^2 - |\Psi_{QLB}|^2)$, shows second order convergence with increasingly fine grid (left), and linear increase of the error with time (right).

function itself, which is hidden in calculations of $|\Psi|^2$. We do this by looking at values of the wave fuction along a cross section of the domain, with the results shown in Figure 5.9.

5.4 Wave packet transmission

Before applying the QLB method to simulation of complex potentials in graphene to study transmission effects, we run simulations of simple sharp potential barriers, with wave packets approaching from the left at a range of incidence angles to confirm the accuracy of the QLB scheme and demonstrate the dependence of transmission on angle of incidence. Investigation of the transmission properties of wave packets as opposed to plane waves can serve as a basis for the simulations to try to predict charge flow carried by graphene's quasiparticles across a potential barrier in a graphene transistor to define on/off states, which we will investigate in Chapter 6. Pereira et. al. [82] have done simulations of wave packets incident onto barriers in graphene to demonstrate negative refraction properties of potential in graphene and investigate

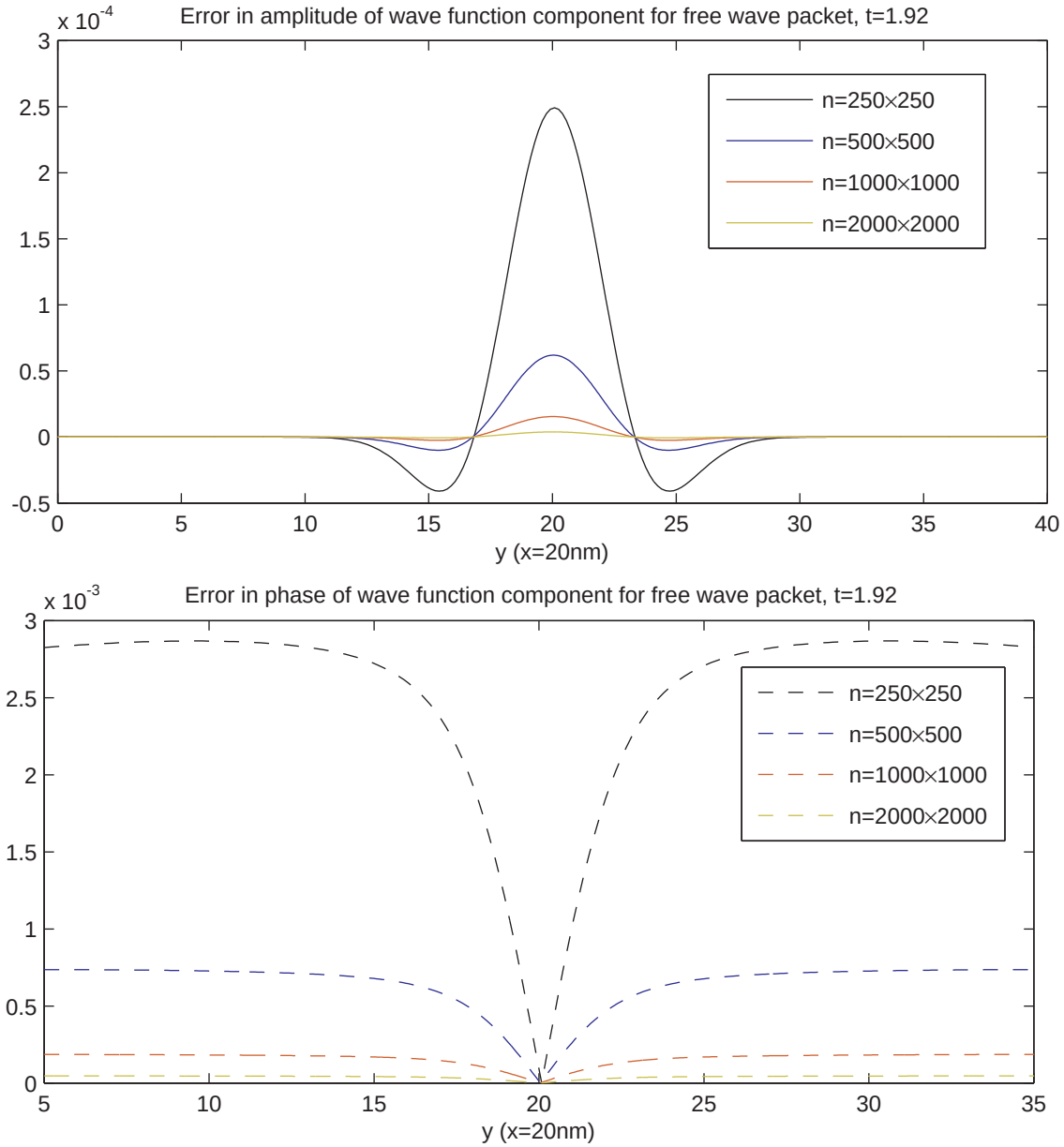

Figure 5.9: Second order convergence of errors in the phase and amplitude of the cross section of the wave function Ψ along the $x = 20$ nm line, relative to the exact spectral solution.

tunnelling through multiple barriers, using spectral split-operator solutions.

We look at a rectangular potential barrier positioned along the y-axis, with $g = V$ for $x \in [0, d]$ and $g = 0$ otherwise, where d is the width of the barrier in nanometers. Assuming the regime with $V > E$ in which Klein tunnelling effects become relevant,

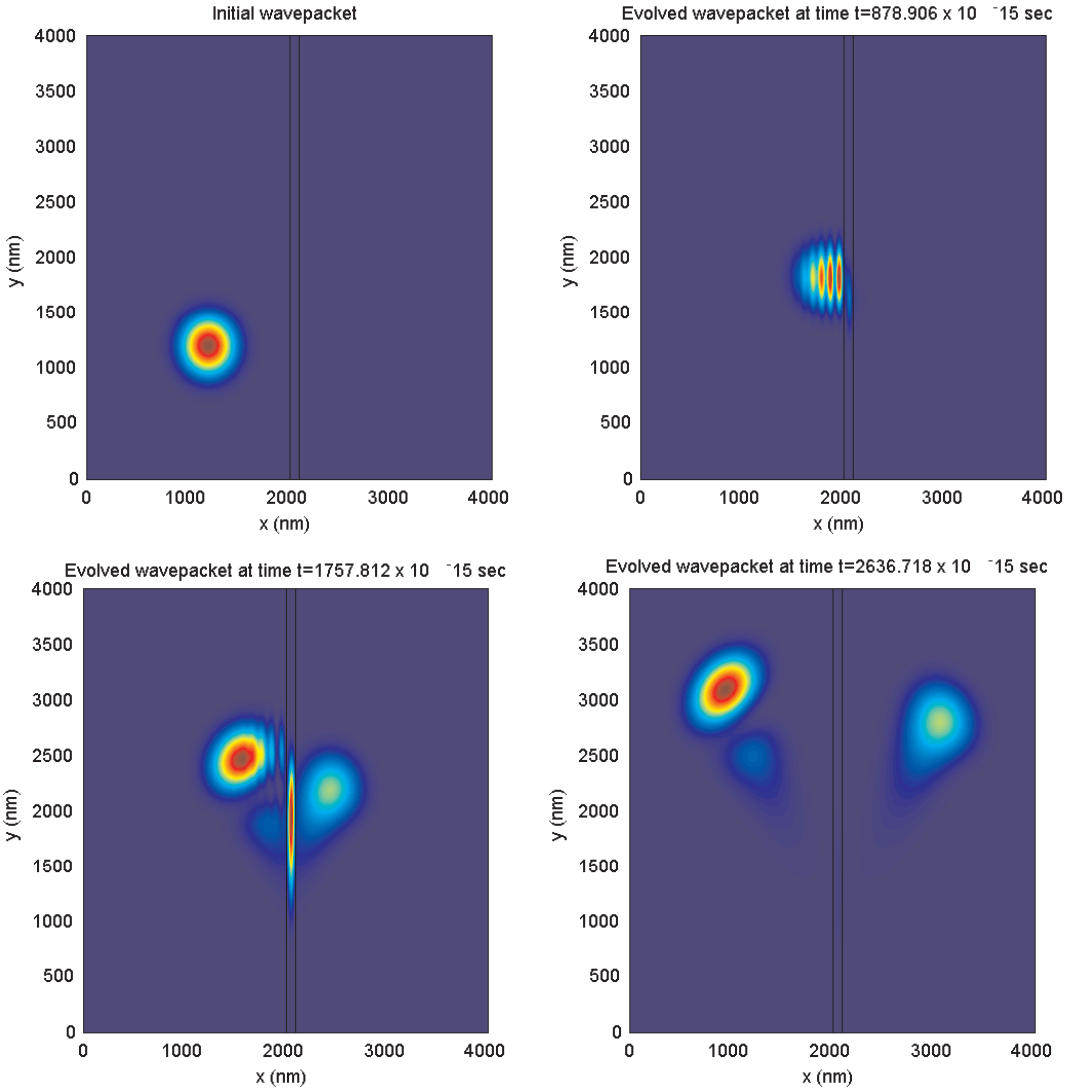

Figure 5.10: Evolution of the probability density shows transmission of a wave packet through a rectangular potential barrier of width 100 nm and 0.100 nm^{-1} height, angle of incidence $\theta = \pi/4$. We observe deformation of the wave packet during tunnelling, reflection of the greater part of probability density due to a large incidence angle, and conservation of wave number along y.

the plane wave solutions in the three regions are given by

$$\Psi_1 = \left[e^{ik_x x} \begin{pmatrix} 1 \\ e^{i\theta_1} \end{pmatrix} + r e^{-ik_x x} \begin{pmatrix} 1 \\ -e^{-i\theta_1} \end{pmatrix} \right] e^{ik_y y}, \qquad x \leq 0, \tag{5.55}$$

$$\Psi_2 = \left[A e^{iq_x x} \begin{pmatrix} 1 \\ -e^{i\theta_2} \end{pmatrix} + B e^{-iq_x x} \begin{pmatrix} 1 \\ e^{-i\theta_2} \end{pmatrix} \right] e^{ik_y y}, \qquad x \in [0, d], \tag{5.56}$$

$$\Psi_3 = \tau e^{ik_x x} e^{ik_y y} \begin{pmatrix} 1 \\ e^{i\theta_1} \end{pmatrix}, \qquad x \geq d, \tag{5.57}$$

where the angle of incidence $\theta_1 = \tan^{-1}(k_y/k_x)$ and the refraction angle $\theta_2 = \tan^{-1}(k_y/q)$ are measured counterclockwise from the positive x axis [63, 3]. The wave numbers are given by,

$$k_x = E\cos(\theta_1) \qquad k_y = E\sin(\theta_1) \qquad q_x = \sqrt{(E-V)^2 - k_y^2}. \tag{5.58}$$

The wave number inside the barrier q_x is anti-parallel to the direction of motion due to being an excited negative energy state [89, 59]. From equations of continuity of the wave function at $x = 0$ and $x = d$,

$$1 + r = A + B \qquad e^{i\theta_1} - re^{-i\theta_1} = -Ae^{i\theta_2} + Be^{-i\theta_2}, \tag{5.59}$$

$$\tau e^{ik_x d} = Ae^{iq_x d} + Be^{-iq_x d} \qquad \tau e^{i\theta_1 + ik_x d} = -Ae^{i\theta_2 + iq_x d} + Be^{-i\theta_2 - iq_x d}, \tag{5.60}$$

we can solve for the amplitudes of the reflected and transmitted waves,

$$r = -2ie^{i\theta_1}\frac{\sin(q_x d)(\sin\theta_1 + \sin\theta_2)}{e^{-iq_x d}\cos(\theta_1+\theta_2) + e^{iq_x d}\cos(\theta_1-\theta_2) + 2i\sin(q_x d)}, \tag{5.61}$$

$$\tau = 2e^{-ik_x d}\frac{\cos(\theta_1)\cos(\theta_2)}{e^{-iq_x d}\cos(\theta_1+\theta_2) + e^{iq_x d}\cos(\theta_1-\theta_2) + 2i\sin(q_x d)}. \tag{5.62}$$

The transmission and reflection coefficients are given by the ratio of the probability currents,

$$R = \left|\frac{j_{reflected}}{j_{incident}}\right| \qquad T = \left|\frac{j_{transmitted}}{j_{incident}}\right|. \tag{5.63}$$

From conservation of probability $\nabla\cdot\boldsymbol{j} = -\partial_t|\Psi|^2$, the probability currents are defined as the following,

$$j_x = \Psi^\dagger\sigma_x\Psi \qquad j_y = \Psi^\dagger\sigma_y\Psi, \tag{5.64}$$

where $\Psi^\dagger$ is the Hermitian transpose of Ψ. The momentum in the y direction is constant so that the probability current j_y is independent of the region inside or outside the potential and we can calculate the incident, reflected and transmitted currents from j_x alone using plane waves (5.55)-(5.57),

$$j_{incident} = 2\cos(\theta_1) \qquad j_{reflected} = 2|r|^2\cos(\theta_1) \qquad j_{transmitted} = 2|\tau|^2\cos(\theta_1). \tag{5.65}$$

We can then write down the reflection and transmission probabilities,

$$R = |r|^2 \qquad T = |\tau|^2, \qquad R + T = 1, \tag{5.66}$$

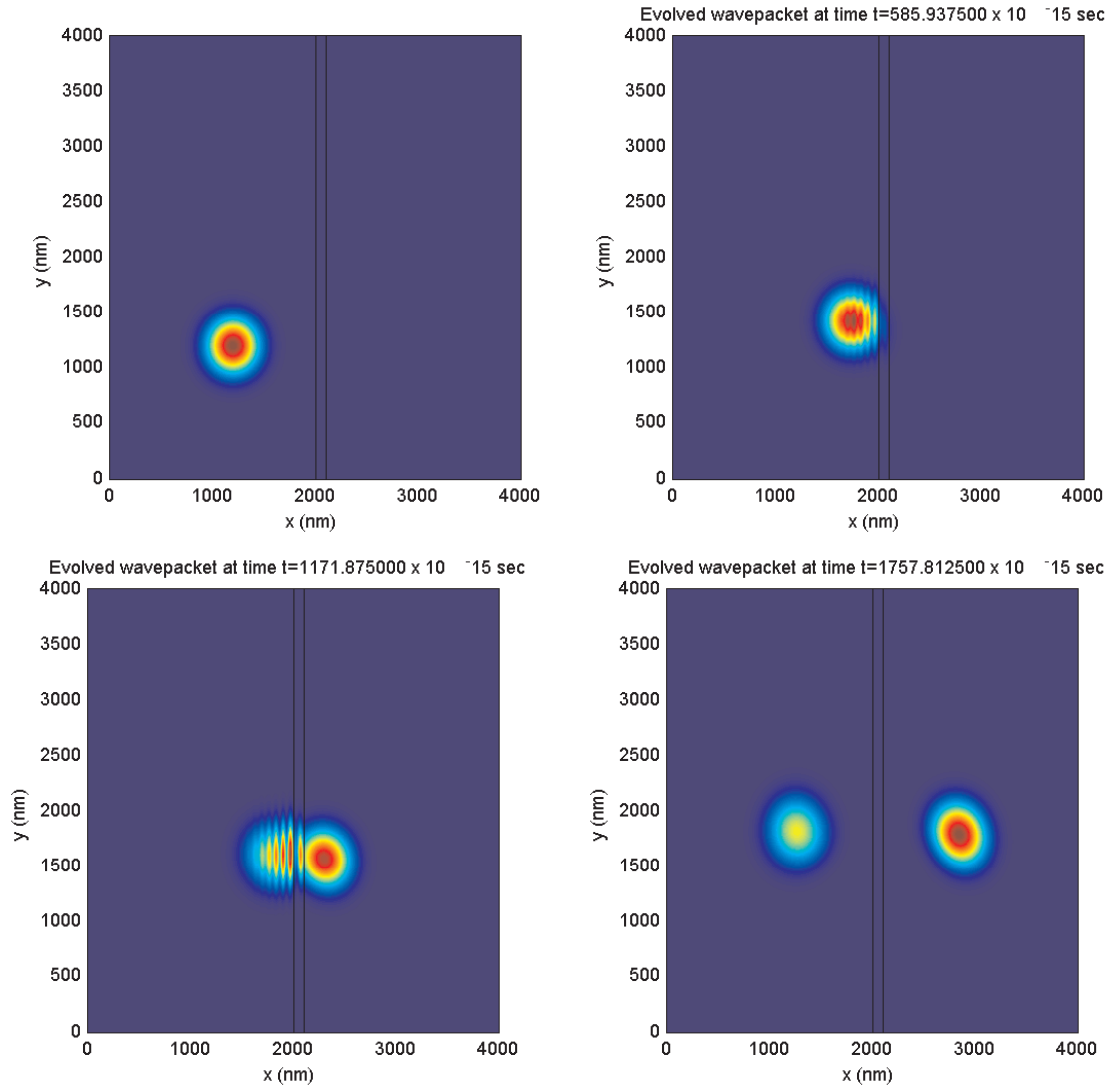

Figure 5.11: Evolution of the probability density showns transmission of a wave packet through a rectangular potential barrier of width 100 nm and 0.100 nm^{-1} height, angle of incidence $\theta = \pi/8$. Lower angle of incidence allows a larger fraction of the wave packet to be transmitted across the barrier than for a wave packet incident at $\theta = \pi/4$.

and the plane wave transmission coefficient [14],

$$T(\theta_1, \theta_2, E, V_0, d) = \frac{\cos^2(\theta_1)\cos^2(\theta_2)}{\cos^2(\theta_1)\cos^2(\theta_2)\cos^2(q_x d) + \sin^2(q_x d)\left(1 + \sin(\theta_1)\sin(\theta_2)\right)^2}. \tag{5.67}$$

As in the one-dimensional case, there will be resonant incidence angles which will cause high transmission probability peaks - when $qd = n\pi$ we have $\sin(q_x d) = 0$ and the transmission coefficient is equal to 1 [1, 3].

The transmitted wave function is given by the superposition of plane waves,

$$\Psi_T(x,y,t) = \int\int \hat{\Psi}(k_x,k_y,0)\,\tau \begin{pmatrix} 1 \\ e^{i\theta} \end{pmatrix} e^{ik_x x + ik_y y} e^{-iEt} dk_x dk_y. \tag{5.68}$$

Then using Plancharel's Theorem,

$$\int_{-\infty}^{\infty}\int_{-\infty}^{\infty} |\Psi(x,y)|^2 dxdy = \int_{-\infty}^{\infty}\int_{-\infty}^{\infty} |\hat{\Psi}(k_x,k_y)|^2 dk_x dk_y, \tag{5.69}$$

and analogous to the calculation we did for the one-dimensional potential step in section 3.1.2, we can calculate the transmission (and reflection) coefficients for wave packets by integrating the probability distribution $|\Psi|^2$ of the reflected and transmitted wave packets Ψ_T and Ψ_R in momentum space as follows,

$$T_{wavepacket} = \int_{-\infty}^{\infty}\int_{-\infty}^{\infty} |\Psi_T|^2 dxdy = \int_{-\infty}^{\infty}\int_{-\infty}^{\infty} \left|\hat{\Psi}_0(k_x,k_y)\right|^2 T dk_x dk_y, \tag{5.70}$$

$$R_{wavepacket} = \int_{-\infty}^{\infty}\int_{-\infty}^{\infty} |\Psi_R|^2 dxdy = \int_{-\infty}^{\infty}\int_{-\infty}^{\infty} \left|\hat{\Psi}_0(k_x,k_y)\right|^2 R dk_x dk_y, \tag{5.71}$$

where T, given by (5.67) has to be expressed as a function of k_x and k_y through definitions of θ_1, θ_2, E and q_x, acting as a weighting function across the momentum space.

An important point to keep in mind is the possibility of the incident wave numbers turning into evanescent waves inside the barrier, which will decay exponentially inside the barrier. An evanescent wave is generated when the wave number inside the potential $q_x = \sqrt{(E-V)^2 - k_y^2}$ turns out to be imaginary, and will only tunnel through if the barrier is very narrow. This is the case of quantum tunnelling in the traditional sense, as opposed to Klein tunnelling where the incident positive energy wave number is matched with a negative energy wave number inside the potential (in the case of graphene this corresponds to a conduction band charge carrier matched with a valence band charge carrier). In that case the transmission probability is not given by equation (5.67), and when calculating the wave packet transmission probability using equation (5.70), those regions of momentum space that will generate evanescent waves should be left out of the integration. Evanescent waves will occur only for wave numbers k_{tot} that are greater than half of the potential height $V_0/2$, and are dependent on the incidence angle, being much more prevalent at oblique incidence [3]. For wave packets intended to transmit through the barrier only by the process of Klein tunnelling the effect of evanescent waves on the transmission can be minimized by making sure the bulk of the wave packet in momentum space is completely inside

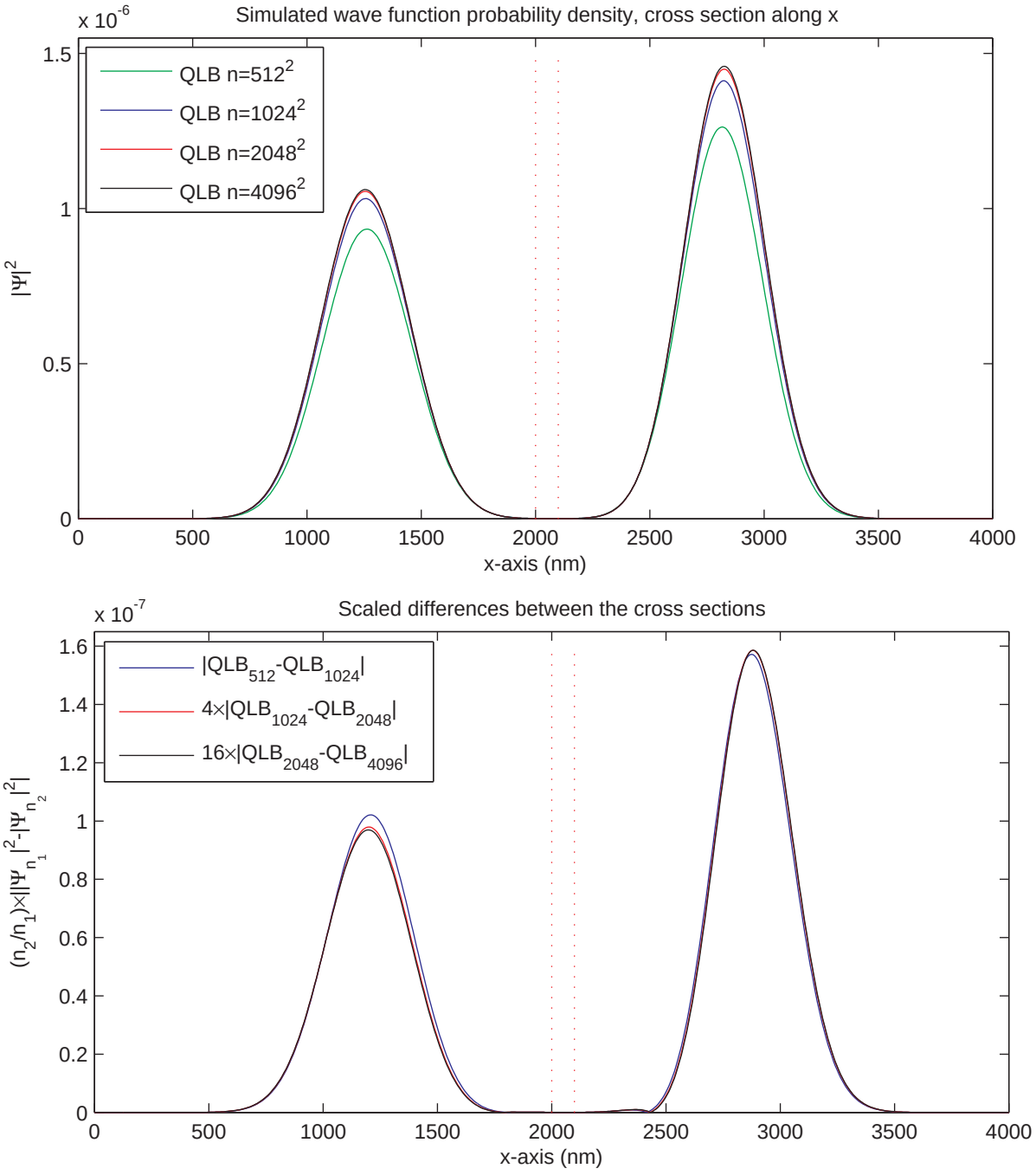

Figure 5.12: Converging cross sections of probability density $|\Psi^2|$ along x-axis for a wave packet incident onto a barrier along the y axis at $\theta_1 = \pi/8$, showing a second order rate of convergence in the second plot of scaled differences between the results.

the $\sqrt{k_x^2 + k_y^2} = V_0/2$ curve so that any wave number combinations that will result in evanescent waves have minimal amplitude.

The Gaussian wave packets we used for simulation of free dispersion in graphene

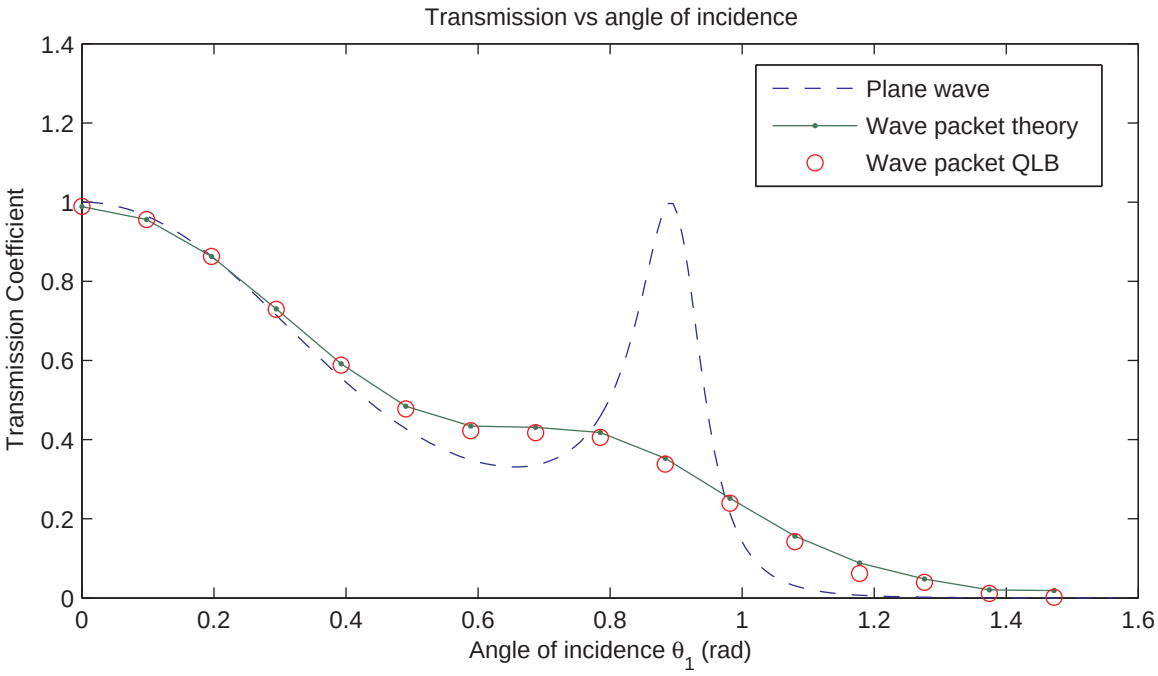

Figure 5.13: Transmission coefficient for plane waves and wave packets vs angle of incidence θ_1. $V_0 = 0.1$ nm^{-1} nm $d = 100$ nm, comparing the QLB simulation with the theoretical wave packet transmission coefficient calculated from FFT decomposition.

had the second component equal to the first component multiplied by a single phase $e^{i\theta}$. If θ is aligned along the angle formed by the initial wave numbers $k_{y,0}$ and $k_{x,0}$, the wave packet is mostly electron-like, representing electrons in the conduction band, but does contain hole-like components from the valence band with negative energies and wave numbers that are anti-parallel to the initial wave numbers. For the simulation of transmission at different incidence angles we want to construct a wave packet that is completely electron-like, and form our initial wave packet such that the angle θ in the phase difference between the second and first components of each plane wave making up the wave packet ($c_2 = e^{i\theta}$ for $c_1 = 1$) is given exactly by the angle of the total wave number k_{tot} formed by each combination of k_x and k_y. To construct such a wave packet we define the top wave function component with a Gaussian wave packet,

$$\Psi(x, y, 0) = \frac{1}{d\sqrt{\pi}} e^{-\frac{(x-x_0)^2+(y-y_0)^2}{2d^2} + ik_{y,0}y + ik_{x,0}x}, \tag{5.72}$$

where the angle formed by $k_{y,0}$ and $k_{x,0}$ will be the direction of motion of the initial wave packet relative to the positive x axis, $\theta_1 = \tan^{-1}(k_{x,0}/k_{y,0})$, and therefore also the angle of incidence onto the potential barrier placed along the y axis. The second

component of the wave function is given by a superposition of plane waves of the decomposed Gaussian of the first component in momentum space that are individually modified by a phase factor $e^{i\theta} = e^{i\tan^{-1}(k_x/k_y)}$ for each k_x and k_y pair. The decomposition of the first component and superposition of the second component are calculated using Fast Fourier Transforms.

For a wave packet constructed in this way we can also use the discrete Fourier transformed version of the initial wave packet to calculate the wave packet transmission probability by multiplying the plane waves in momentum space by the amplitude of the transmitted plane wave (5.23), filtering out any plane waves that will result in evanescent waves, and adding up the resulting probability density. By Plancharel's Theorem we used above the total probability density of the resulting wave function in Fourier space will be equal to the probability density of the wave function in real space.

The rectangular potential barrier is given by

$$g(x,y) = 0 \quad \forall \quad x \in (-\infty, d_i) \cup (d_{ii}, \infty) \qquad g(x,y) = V_0 \quad \forall \quad x \in [d_i, d_{ii}], \quad (5.73)$$

where d_i and d_{ii} are the start and end points of the barrier, $d = d_{ii} - d_i$ is the barrier width, and V_0 is the barrier height. We simulate a 4000×4000 nm domain and use the following parameters

wave packet initial position $x_0 = 1200$ nm, $y_0 = 1200$ nm,
barrier position $d_1 = 2000$ nm, $d_2 = 2100$ nm,
barrier width $d = 100$ nm,
wave packet width $\sigma = 250$ nm,
particle wavenumber $k_{tot} = 0.05$ nm^{-1} (33 meV),
potential height $V_0 = 0.100$ nm^{-1} (66 meV),

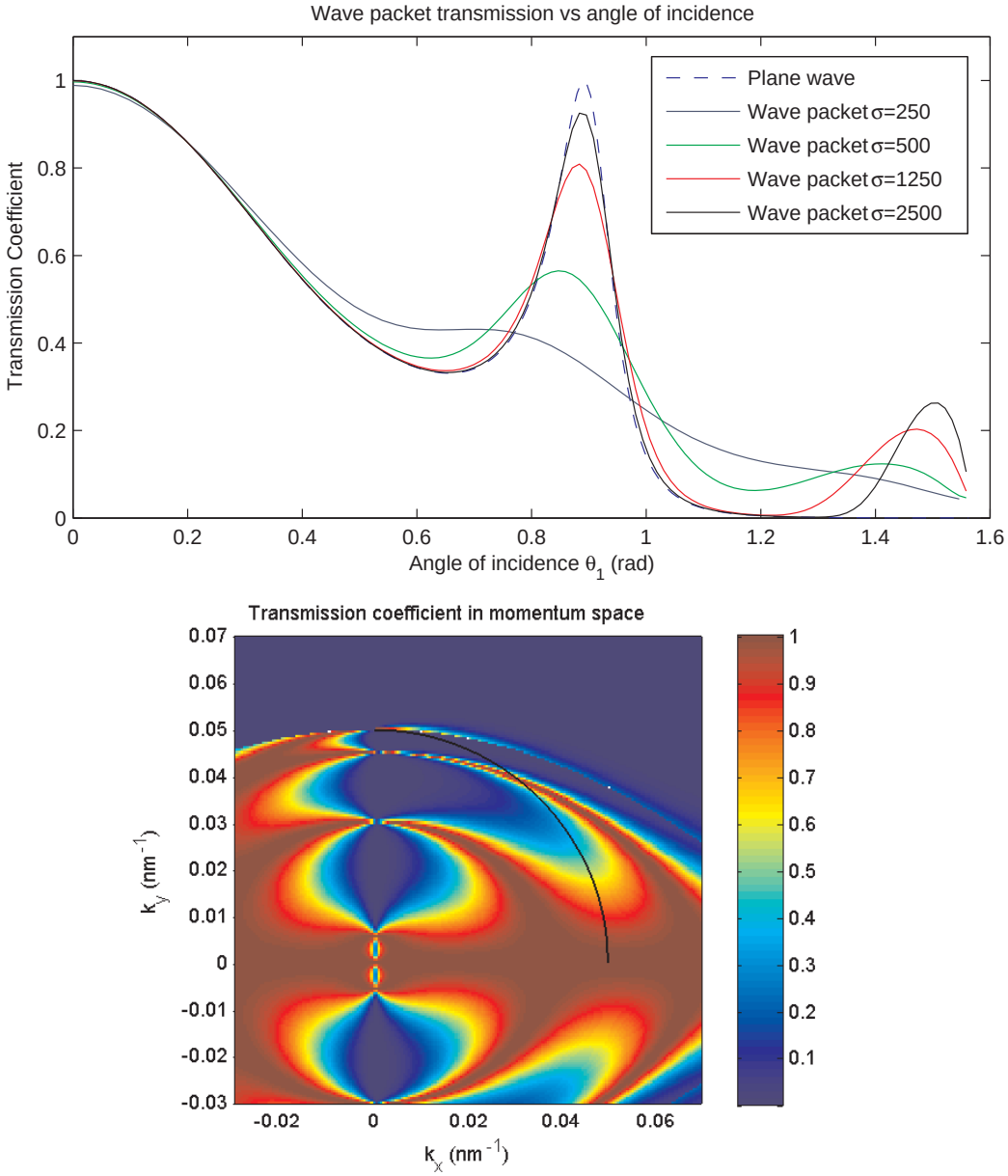

Figure 5.14: Dependence of the wave packet transmission probability on the incidence angle shows sharper transmission resonance peaks as the width of the wave packet σ is increased (top panel). A secondary resonance peak that is not present in the plane wave transmission coefficient (dashed line) appears at high angle of incidence. Bottom panel shows the plane wave transmission coefficient over the momentum domain of k_x, k_y. The center of the wave packet with $k_{tot} = 0.05$ nm^{-1} (black line) is near a thin area of high transmission at high incidence angles. Because the line of the wave packet center does not cross the resonance area, the second peak is not present in the plane wave transmission, but the finite width of the wave packet does overlap the area of resonance and allows an increased overall transmission probability for oblique incidence. As σ increases, the width of the wave packet in momentum space ranges from ≈ 0.02 nm^{-1} at $\sigma = 250$ nm to ≈ 0.002 nm^{-1} at $\sigma = 2500$, and a greater proportion of it is affected by the resonance, evidence of which we observe in the top panel.

where everything is in terms of wavenumbers as for the free wave packet. We run QLB simulations up to a point in time when the transmission of the wave packet across the barrier is complete, for a range of incidence angles from $\theta_1 = 0$ to $\theta_1 = 15\pi/32$, in increments of $\pi/32$, and for each one calculate the transmission coefficient by adding up the probability density to the right of the barrier and dividing by the total probability density,

$$T_{QLB} = \frac{\sum_{y=0}^{4000} \sum_{x=2100}^{4000} \Delta x \Delta y |\Psi_{QLB}(x,y)|^2}{\sum_{y=0}^{4000} \sum_{x=0}^{4000} \Delta x \Delta y |\Psi_{QLB}(x,y)|^2}. \tag{5.74}$$

An example of evolution of a wave packet incident onto a rectangular barrier at $\theta_1 = \pi/4$ can be seen in Figure 5.10. We can see the two parts of the reflected wave packet, one from reflection off each side of the barrier, move away from the barrier at the same angle. The transmitted component continues at the $\theta_1 = \pi/4$ angle with the x axis. The velocity along the y axis is unaltered by the interaction with the barrier, as expected from the conservation of k_y. In our simulations we also observe the negative refraction of the wave packet inside the barrier, as reported by Pereira et. al in their simulations [82]. Although it is easier to see with potential step simulations instead of a narrow potential barrier, we can see the consequence of this effect in the lagging of the transmitted component in its vertical motion compared to the reflected component, due to it emerging from the barrier at a lower point along the y axis. Theoretical work of Cheianov et. al. predicts the negative refraction property to allow the ability to focus electron flow in graphene-based devices using a Veselago lens type of potential [17].

The complete set of wave packet transmission results is plotted in Figure 5.13, together with the theoretical wave packet transmission coefficient given by (5.70) and the corresponding plane wave transmission. The wave packet transmission coefficient is dependent on the plane wave transmission for the center of the wave packet in momentum space - the monotone decrease of the transmission coefficient with increasing angle of incidence is slowed down as the wave packet approaches and passes a point of resonance in momentum space and some of the plane waves making up our wave packet are able to pass the barrier with perfect or very high probability. We observe good agreement between the simulation and the analytical calculation for most of the incidence angles, however as they increase we are able to measure significantly less transmitted probability density than expected. One reason for this effect in the simulation is that at large angles of incidence the momentum k_x, and therefore the

group velocity of the wave packet, becomes very low and it takes a lot longer for parts of the wave packet to escape the barrier. They become trapped for some time before emerging on the transmitted or reflected side, and by that time the main reflected body of the wave packet will already move outside our simulated domain, possibly wrapping around to the other side to the right of the barrier, making it more difficult to accurately calculate the transmission coefficient. This can be remedied by using a larger domain to run the simulations and running them for a greater number of timesteps.

The other, more significantly contributing reason for lower than expected transmission at high incidence angles is that although we aim to simulate a perfectly rectangular barrier, the sharpness of our potential is limited by the grid point resolution and our barrier will always have a finite slope. Whether a particular slope is considered 'sharp' or 'smooth' depends on the value of the dimensionless quantity $k_{tot}\omega$, where ω is the lengthscale along which the potential jump takes place. If ω is large enough the potential will behave as 'smooth' at larger incidence angles, with transmission being exponentially damped [3]. We have qualitatively observed this effect of the slope of the potential in one-dimensional simulations in section 3.2.2. Running simulations of wave packets incident onto the barrier at grazing angles on larger grid sizes will increase the slope of the effective potential and remedy this effect. We can see that accurate simulation of the behaviour of wave packets incident at angles close to $\pi/2$ has greater computational time and memory requirements, care should be taken to ensure sufficient evolution running time to allow the tunnelling process to complete, and a domain large enough not to allow reflected probability density to approach the periodic boundaries, maintaining negligible wave function values at the edges of the domain.

To check the rate of convergence of the simulated probability density and the transmission coefficient we have to set up our potential barrier to have the same finite slope, independent of the grid spacing, and chose an angle of incidence that is not far from normal so that the results are not distorted at low grid resolution. We run simulations with $\theta_1 = \pi/8$, at a range of grid resolutions from $n = 512 \times 512$ to $n = 4096 \times 4096$, with the slope of the barrier given by the smallest resolution - $V_0/\Delta x_{512} = 0.10/7.8125$, the evolution of the wave packet is shown in Figure 5.11. We plot the cross sections of the probability density and their differences scaled by the ratio of grid sizes in Figure 5.12, showing second order convergence. Similarly,

second order of convergence is also displayed by the transmission coefficients,

$$
\begin{aligned}
b_1 &= |T_{4096} - T_{2048}| = 1.88340 \times 10^{-4}, \\
b_2 &= |T_{2096} - T_{1024}| = 7.72583 \times 10^{-4} = 4.10 b_1, \\
b_3 &= |T_{1024} - T_{512}| = 3.71498 \times 10^{-3} = 4.80 b_2.
\end{aligned}
$$

As a note on the computational performance of the QLB scheme we give CPU time values for our FORTRAN implementation of the graphene QLB alorithm, run on a single core of a desktop machine with the AMD Phenom II X3 720 2.8GHz processor,

Grid size	Timesteps	CPU time	Seconds per timestep
512×512	225	21.4 sec	0.0951 sec
1024×1024	450	246.7 sec	0.548 sec
2048×2048	900	2010.5 sec	2.234 sec
4096×4096	1800	17414.6 sec	9.675 sec

As expected, we observe a near four-fold increase in computational time per timestep as we double the grid size. We also use a dedicated computational machine with a sufficiently large amount of memory and 2.3GHz cores to run a 3600 timestep simulation on a 8192×8192 grid, with a resulting CPU time of 275118.2 sec and 76.42 sec per timestep.

It is interesting to look at how the wave packet transmission changes with the initial width of the wave packet, and at what point it begins to resemble the plane wave transmission, to see whether the behaviour of quasiparticles strongly localized in momentum space can be approximated with the simpler plane wave expressions. We calculate the wave packet transmission coefficients across the full range of incidence angles for several values of σ and plot the results in Figure 5.14. As expected, the wave packet transmission coefficient approaches the plane wave curve, forming the same resonance peak. However we also see a second peak developing at very high incidence angles as the wave packet becomes more delocalized.

To explain the cause of the second peak that is not present in the plane wave transmission profile we look at a plot of $T\left(k_x, k_y, V_0, \sigma, \right)$ across the full region of momentum space we are considering, shown in the second panel of Figure 5.14. The plane wave with $k_{tot} = 0.05\ \mathrm{nm}^{-1}$ comes across only one resonance as it moves through the range of incidence angles, shown in black, however it comes close to a second area of resonant wave numbers at high incidence angle. Although under our parameters the plane wave misses the second resonance peak, a wave packet centered on the black

line will capture it, as well as the high transmission coefficients in the negative k_x plane, and a part of its wave numbers will be transmitted perfectly. The narrower is the wave packet in momentum space (and therefore wider in real space), the greater will be the proportion of the plane waves making it up that is transmitted perfectly - that is the reason for a growing second peak in Figure 5.14 as we increase the width of the wave packet σ.

We also investigate the sensitivity of the wave packet transmission coefficient to changes in potential height, wave packet energy, and initial wave packet width by differentiating our expression for the transmission coefficient,

$$\frac{\partial}{\partial \alpha_i} \int \int \left| \hat{\Psi}_0 \left(k_x, k_y \right) \right|^2 T \left(k_{tot}, V_0, \sigma, \theta_1 \right) dk_x dk_y, \tag{5.75}$$

where α_i's are k_{tot}, σ, or V_0. The results are plotted altogether in top panel of Figure 5.15, scaled to the $(-1, 1)$ range, and show the direct or inverse proportionality of the transmission coefficient to system's parameters. It shows the transmission coefficient is directly proportional to wave packet width for all incidence angles, with greater sensitivity at normal incidence and around the resonance peak - higher wave packet width implies a greater part of the wave packet's wave numbers will be in the high transmission configuration of k_x and k_y, and as the wave packet gets narrower its transmission probability averages over a greater region of the k_x-k_y plane. The dependence of wave packet transmission on particle energy k_{tot} and barrier height V are similar to each other and will decrease or increase the transmission probability depending on the incidence angle. They are governed by the changes the resonant incidence angles which are very sensitive to changes in the relationship between particle energy and potential height. For a more informative look at the dependance of wave packet transmission on the potential height we calculate the values of (5.75) for $\alpha_i = V_0$ across a whole region of the momentum domain and plot the results in the bottom panel of Figure 5.15. The effect of increasing potential alternates between increasing and decreasing the transmission probability as the particle energy increases and wave packet moves across resonance regions. Changes in incidence angle, on the other hand, have a smaller impact on the sensitivity of the transmission probability to fluctuation of potential height, especially near normal incidence.

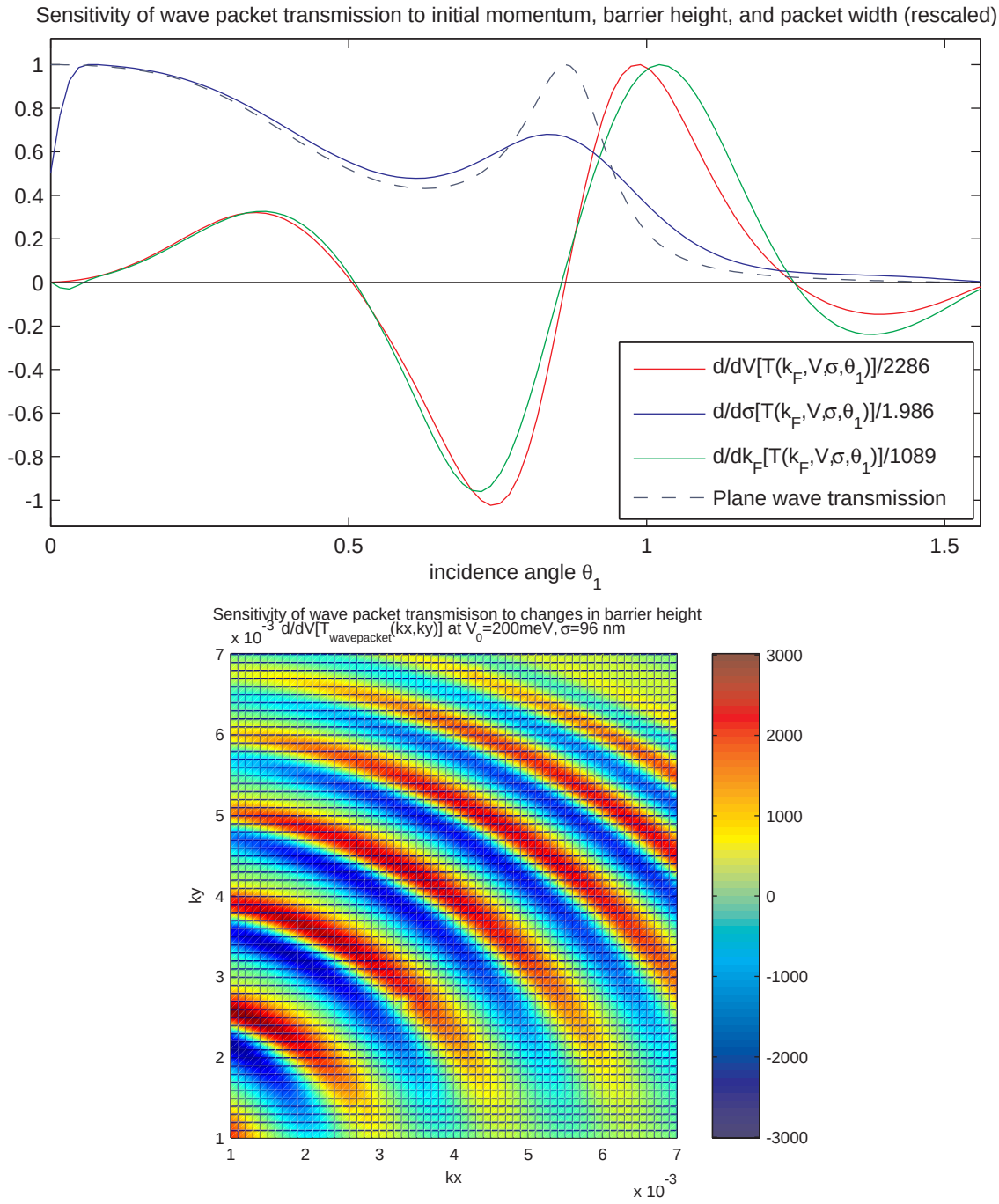

Figure 5.15: Sensitivity of the wave packet transmission coefficient to changes in initial momentum, potential barrier height and wave packet width (rescaled), with the corresponding plane wave transmission coefficient for reference (top panel). Parameters are $k_{tot} = 0.1215$ nm^{-1}, $V_0 = 0.30375$ nm^{-1}, $\sigma = 384$ nm. Bottom panel shows sensitivity of the wave packet transmission coefficient to potential barrier height across the momentum domain, demonstrating alternating positive and negative impact of increasing potential height on the transmission coefficient as the energy of wave packet moves across areas of resonance. Incidence angle adjusts the magnitude of the derivative, but does not change the overall effect of potential height increases.

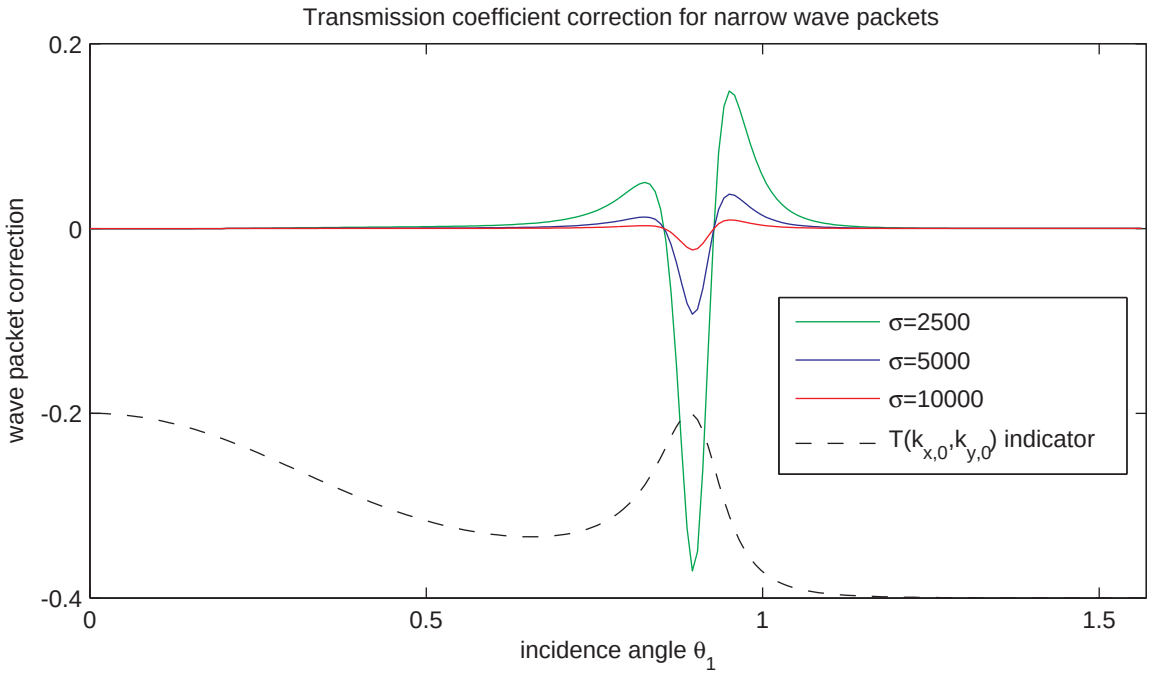

Figure 5.16: Transmission coefficient correction for wave packets narrow in momentum space for $k_{tot} = 0.05$ nm^{-1}, $V_0 = 0.10$ nm^{-1}, and $d = 100$ nm. An indicator of the corresponding plane wave transmission coefficient is plotted for reference at the bottom.

5.4.1 Plane wave approximation for narrow wave packets

Looking at wave packets that are narrow in momentum space, we want to see how large a correction is required to the plane wave transmission coefficient to calculate the wave packet transmission coefficient, and whether an accurate approximation can be made for the wave packet transmission formula. Inside the integral (5.70) we expand the transmission coefficient (5.67), rewritten as a function of k_x and k_y, around the wave packet's center $(k_{x,0}, k_{y,0})$, and let

$$\kappa_x = k_x - k_{x,0} \qquad \kappa_y = k_y - k_{y,0}. \tag{5.76}$$

We then get

$$T(\kappa_x, \kappa_y) = T(k_{x,0}, k_{y,0}) + \frac{\partial T}{\partial k_x}\kappa_x + \frac{\partial T}{\partial k_y}\kappa_y + \frac{\partial T}{\partial k_x \partial k_y}\kappa_x\kappa_y + \frac{\partial^2 T}{\partial k_x^2}\kappa_x^2 + \frac{\partial^2 T}{\partial k_y^2}\kappa_y^2 + \mathcal{O}\left(\kappa_x^3\right), \tag{5.77}$$

where κ_x and κ_y are small and the derivatives of T are evaluated at $(k_{x,0}, k_{y,0})$. We

make the substitution (5.76) in the wave packet $\left|\hat{\Psi}_0\left(k_x,k_y\right)\right|^2$,

$$\left|\hat{\Psi}_0\left(k_x,k_y\right)\right|^2 = 2\left(\frac{\sigma^2}{2\pi}e^{-\left(\kappa_x^2+\kappa_y^2\right)\sigma^2}\right), \tag{5.78}$$

and rewrite our expression for the wave packet transmission coefficient (5.70)

$$T_{narrow} = \int\int \frac{\sigma^2}{\pi}e^{-\left(\kappa_x^2+\kappa_y^2\right)\sigma^2}\left[T\left(k_{x,0},k_{y,0}\right)+\frac{\partial^2 T}{\partial k_x^2}\kappa_x^2+\frac{\partial^2 T}{\partial k_y^2}\kappa_y^2\right]d\kappa_x d\kappa_y, \tag{5.79}$$

where we dropped the odd terms that integrate to zero and neglected the remaining $\mathcal{O}\left(\kappa_x^4\right)$ terms. Integrating from $-\infty$ to ∞ we finally obtain,

$$T_{narrow} = T\left(k_{x,0},k_{y,0}\right)+\frac{1}{2\sigma^2}\left(\frac{\partial^2 T}{\partial k_x^2}\left(k_{x,0},k_{y,0}\right)+\frac{\partial^2 T}{\partial k_y^2}\left(k_{x,0},k_{y,0}\right)\right), \tag{5.80}$$

where $T\left(k_{x,0},k_{y,0}\right)$ is the plane wave transmission coefficient. To get an idea of the magnitude, we calculate the correction to the plane wave coefficient for our initial wave packet with a range of σ values and show the results in Figure 5.16. As expected, we see the corrections decrease as wave packets become narrower in momentum space, and corrections being most significant near the resonance peak. However our approximation does not capture the second resonance peak that we found in the exact calculations above. Higher order expansions can be derived in a similar way using formulas for $\int x^n e^{-px^2}dx$ for $n>2$ and may resolve this feature.

5.5 Vector potentials and pseudo-magnetic fields in graphene

Another unusual property of graphene is that strain on the material affects the hopping energy of charge carriers in the same way as a vector potential would, shifting the Dirac cones located at the K and K' corners of the Brillouin zone in the opposite directions, and therefore manifests itself as a pseudo-magnetic field [14]. A magnetic field applied to graphene can be used to direct charges within graphene with the Lorentz force [30], improve the transmission through fiber-optical guiding in graphene [109], open a band gap between the valence and conduction bands [42, 62], and separate charges of different chirality that are in K and K' valleys [16]. It has been predicted that uniform strain cannot be used to generate a uniform pseudo-magnetic field perpendicular to the plane of graphene, instead strain should be triangularly symmetrical, alternating pulling along the directions of three out of six vertices in a

carbon hexagon and pushing along the other three [42]. Such a strain would open band gaps greater than 0.1 eV in bulk graphene and can be achieved by depositing a graphene sheet onto a surface with a triangular landscape.

In the original derivation and in our development of the QLB scheme only systems with zero magnetic field were considered. However we can adapt the QLB scheme to include vector potentials to simulate non-zero time-dependent magnetic fields as well as the pseudo-magnetic fields created by strain on the two-dimensional graphene structures. In this section we expand the QLB scheme in this way and run simulations of a wave packet in constant magnetic field to observe qualitative behaviour and test the accuracy of the scheme by comparison with a spectral solution of the Dirac equation.

5.5.1 Expanded QLB with vector potential

We begin by including the vector potential terms in the two dimensional Dirac-like equation governing charge carriers in graphene,

$$i\hbar\partial_t\Psi = \left[\sigma_x v_F\left(-i\hbar\partial_x + qA_x\right) + \sigma_y v_F\left(-i\hbar\partial_y + qA_y\right) + qV\right]\Psi, \tag{5.81}$$

where V is the external scalar potential, q is the modulus of the charge as before, A_x and A_y are the components of the vector potential $\boldsymbol{A}$ that is associated with by the external magnetic or pseudo-magnetic field, $\boldsymbol{B} = \nabla \times \boldsymbol{A}$. The Pauli spin matrices,

$$\sigma_x = \begin{pmatrix} 0 & 1 \\ 1 & 0 \end{pmatrix} \qquad \sigma_y = \begin{pmatrix} 0 & -i \\ i & 0 \end{pmatrix} \qquad \sigma_z = \begin{pmatrix} 1 & 0 \\ 0 & -1 \end{pmatrix}, \tag{5.82}$$

satisfy the commutation relation $[\sigma_i, \sigma_j] = 2i\epsilon_{ijk}\sigma_k$, where ϵ_{ijk} is the alternating Levi-Civita tensor [5]. Dividing through by $i\hbar v_F$ and rescaling the potentials as before, we get

$$\partial_t\Psi + \left(\sigma_x\partial_x + \sigma_y\partial_y\right)\Psi = i\left(g - \sigma_x A_x - \sigma_y A_y\right)\Psi, \tag{5.83}$$

where $g = -qV/\hbar v_F$ is the scalar potential, the vector potential terms A_x and A_y absorbed a factor of $\frac{q}{\hbar}$, and everything is now in units of length. Separating advection in each spatial dimension and the collision term that now includes the vector potentials we get the following set of equations,

$$\partial_t\Psi + \sigma_x\partial_x\Psi = 0, \tag{5.84}$$

$$\partial_t\Psi + \sigma_y\partial_x\Psi = 0, \tag{5.85}$$

$$\partial_t \Psi = i \left(g - \sigma_x A_x - \sigma_y A_y \right) \Psi. \tag{5.86}$$

Advection equations (5.84) and (5.85) produce streaming of the wave function along x and y axes, and we designate these operators by S^x and S^y as before. We write down the exact solution to the collision equation (5.86)

$$\Psi \left(x, t + \Delta t \right) = e^{i(g - \sigma_x A_x - \sigma_y A_y)\Delta t} \Psi \left(x, t \right), \tag{5.87}$$

where we use a property of the Pauli matrices [81, 16],

$$e^{-i\boldsymbol{M}\cdot\boldsymbol{\sigma}} = \cos\left(|M| \right) \boldsymbol{I} - i \frac{\sin\left(|M| \right)}{|M|} \left(\boldsymbol{M} \cdot \boldsymbol{\sigma} \right), \tag{5.88}$$

to write down the collision matrix as

$$C\left(\Delta t \right) = e^{ig\Delta t} \begin{pmatrix} \cos\left(A\Delta t \right) & -i \sin\left(A\Delta t \right) \left(A_x - iA_y \right) / A \\ -i \sin\left(A\Delta t \right) \left(A_x + iA_y \right) / A & \cos\left(A\Delta t \right) \end{pmatrix}, \tag{5.89}$$

where $A = \sqrt{A_x^2 + A_y^2}$. Because we are using Strang splitting in application of the steaming and collision operators, our effective collision operator is $C^{1/2} = C\left(\Delta t / 2 \right)$.

The QLB for the standard Dirac equation for massive particles in two and three dimensions can be expanded to include magnetic fields in a similar way.

5.5.2 Reference spectral solution

To test the accuracy of the expanded QLB scheme we compare the simulated solutions against a spectral solution of the Dirac equation that is calculated by splitting the Hamiltonian into two parts and applying them in turn to evolve the wave function. The evolution of the wave function is governed by the Dirac Hamiltonian, and the solution can be written down,

$$i\hbar \frac{\partial}{\partial t} \Psi \left(t \right) = H \Psi \left(t \right) \qquad \Psi \left(t \right) = e^{-iHt/\hbar} \Psi \left(0 \right). \tag{5.90}$$

An exact solution is not possible due to the coupling of Fourier modes by the spatially varying scalar and vector potentials, but we can obtain an accurate approximation by applying Strang splitting to the wave number dependent and the space dependent parts of the Hamiltonian,

$$H = H_k + H_r = \left(\boldsymbol{\sigma} \cdot \boldsymbol{k} \right) + \left(\boldsymbol{\sigma} \cdot \boldsymbol{A} + gI \right), \tag{5.91}$$

so that the evolution for one time step is given by

$$\Psi \left(t + \Delta t \right) = \exp\left(-i \frac{1}{2} \Delta t H_r \right) \mathcal{F}^{-1} \exp\left(-i \Delta t H_k \right) \mathcal{F} \exp\left(-i \frac{1}{2} \Delta t H_r \right) \Psi \left(\Delta t \right) + \mathcal{O}\left(\Delta t^3 \right), \tag{5.92}$$

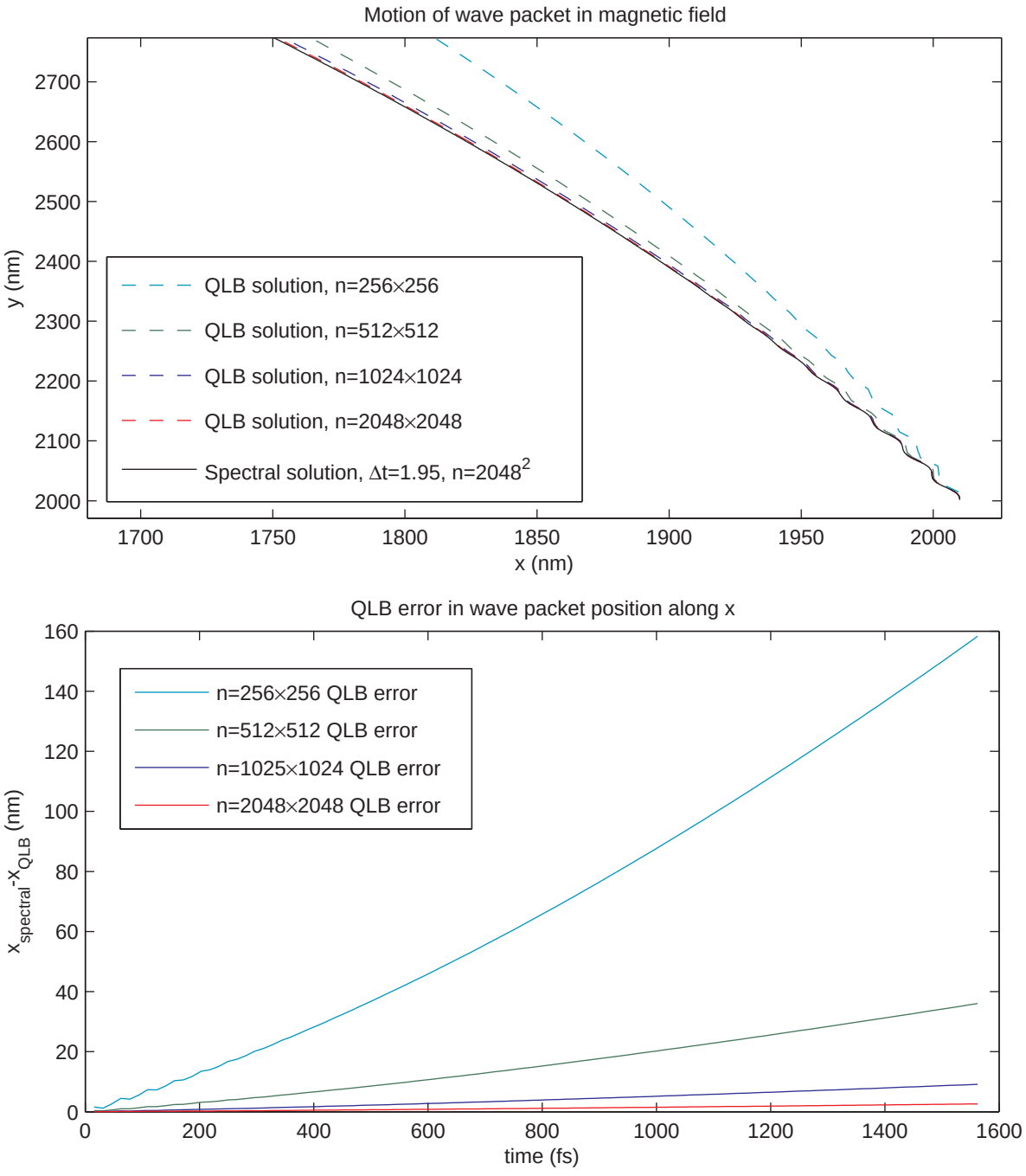

Figure 5.17: Average position of the wave packet moving under effects of a constant magnetic field perpendicular to the x-y plane, QLB simulations compared with a spectral solution. Second order convergence of QLB error of the average position of the wave packet along x, moving under effects of a constant magnetic field perpendicular to the x-y plane. The error is calculated as the difference between the QLB results and a spectral reference solution (bottom).

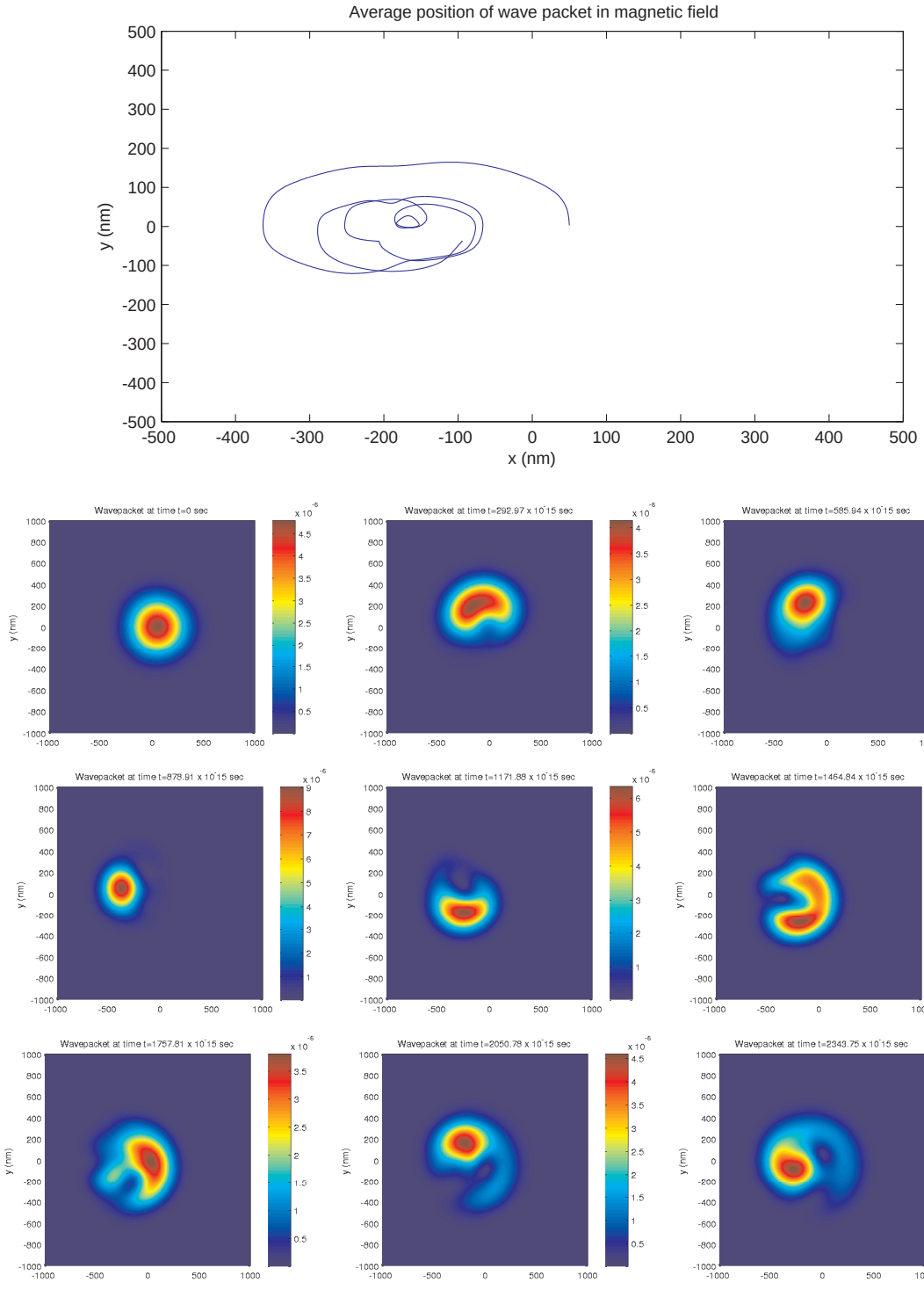

Figure 5.18: Average position of a wave packet with initial momentum $k_{tot} = 0.01$ nm^{-1} along the y-axis under the effects of a magnetic field perpendicular to the graphene sheet (top). Evolution of a wave packet with initial momentum along the y-axis under the effects of a magnetic field perpendicular to the graphene sheet (bottom).

where we apply a Fourier transform before and an inverse Fourier transform after the wave number dependent evolution. The discrete Fourier transforms are defined in (5.51) and performed using FFT algorithms. The space dependent evolution matrix $\exp(-i\Delta t H_r/2)$ is the same as the collision matrix derived for the QLB scheme above, given by (5.89) with Δt replaced by $\Delta t/2$, and the wave number dependent matrix can be written down using formula (5.88). It is equal to

$$e^{-i\Delta t H_k} = \begin{pmatrix} \cos(k\Delta t) & -i\sin(k\Delta t)(k_x - ik_y)/k \\ -i\sin(k\Delta t)(k_x + ik_y)/k & \cos(k\Delta t) \end{pmatrix}, \tag{5.93}$$

where $k = \sqrt{k_x^2 + k_y^2}$. Each time step generates an $\mathcal{O}(\Delta t^3)$ error, accumulating after many timesteps to second order error accuracy of the spectral scheme. However, unlike the QLB scheme, we can adjust the timestep independently of the grid size.

5.5.3 QLB simulation of vector potential

To test the scheme with the addition of the vector potential we create a system of constant magnetic field perpendicular to the plane of graphene, $\boldsymbol{B} = (0, 0, B)$, so that the Lorentz force on the charge is directed in-plane. The vector potential for such a magnetic field in the symmetric gauge is given by

$$\boldsymbol{A} = \frac{B}{2}(-y, x, 0) \tag{5.94}$$

where B is the magnitude of the resulting uniform magnetic field. The initial wave packet is the same configuration that we used for for previous tunnelling simulations, given by equation (5.72), with initial velocity directed along the y-axis ($k_{tot} = 0.05$ nm^{-1} and $\theta_1 = \pi/2$). In selecting the size of the simulated domain and grid size we need to remember that although our magnetic field B is constant, the vector potential $\boldsymbol{A}$ is a function of the space coordinates, and the combination of domain and grid sizes should result in a step size that will satisfy the QLB simulation accuracy requirement of $|\boldsymbol{A}(x, y)|\Delta t < 1$ everywhere on the domain. We run our vector potential simulations on a 4000 nm $\times$ 4000 nm domain with a 2048 $\times$ 2048 grid, which results in a timestep of $\Delta t = 1.953$ fs and satisfies the accuracy requirement even at the edges of the domain for our magnetic field $B = 0.000015$ nm^{-1} in our units (equation scaled by $\frac{1}{\hbar v_F}$) that will force the moving wave packet to deviate from its vertical path through the Lorentz force. We plot the average position of the wave packet as the system evolves for a range of grid resolutions and the spectral

solution in the first part of Figure 5.17. The results show the expected deviation of the wave packet trajectory away from vertical and a transient oscillation due to the Zitterbewegung effect, with the QLB solutions approaching the spectral results as the grid is refined. The difference in position along x between the QLB and the spectral solution is shown in the second plot of the same Figure, where we can see that the errors grow with time, and decrease by a factor of four as we double the grid size.

Further evidence of second order convergence is seen from the ratios of the total errors in position along x and y for the whole duration of the simulation for a range of grid resolutions,

Grid size	$\sum_t \lvert x\,(t)_{spec} - x\,(t)_{QLB} \rvert$	Reduction factor
256×256	6.9729×10^3	–
512×512	1.6047×10^3	4.35
1024×1024	0.4092×10^3	3.92
2048×2048	0.1186×10^3	3.45

Grid size	$\sum_t \lvert y\,(t)_{spec} - y\,(t)_{QLB} \rvert$	Reduction factor
256×256	2.6983×10^3	–
512×512	0.5762×10^3	4.68
1024×1024	0.1375×10^3	4.19
2048×2048	0.0327×10^3	4.20

They show second order convergence, as expected.

We also simulate a system with a stronger magnetic field ($B = 0.00005$ nm^{-1}) to force the wave packet to move in a smaller radius and rotate inside our 3000 nm $\times$ 3000 nm domain. The simulation are run up to $t = 2343.75 \times 10^{-15}$ sec, with initial wave number $k_{tot} = 0.01$ nm^{-1} directed along the y-axis, and the results are plotted in Figure 5.18.

The evolution of the wave packet position is similar to the results of motion of a wave packet subject to a magnetic field in graphene that were obtained from numerical calculations by Schliemann [88] and Rusin et. al [85] and is determined by a combination of circular and Zitterbewegung motion. The probability density at equal periods of the simulation is plotted in the second part of Figure 5.18 and shows the rotational motion of the wave packet more clearly. These results are similar to the 'revivals' of wave packets in graphene obtained by Krueckl and Kramer [56], referring to the oscillation of probability density as it is split and moves in a clockwise and counterclockwise circular motion around the initial position. In our case the wave packet is not split into two counter-rotating parts and moves all in one direction

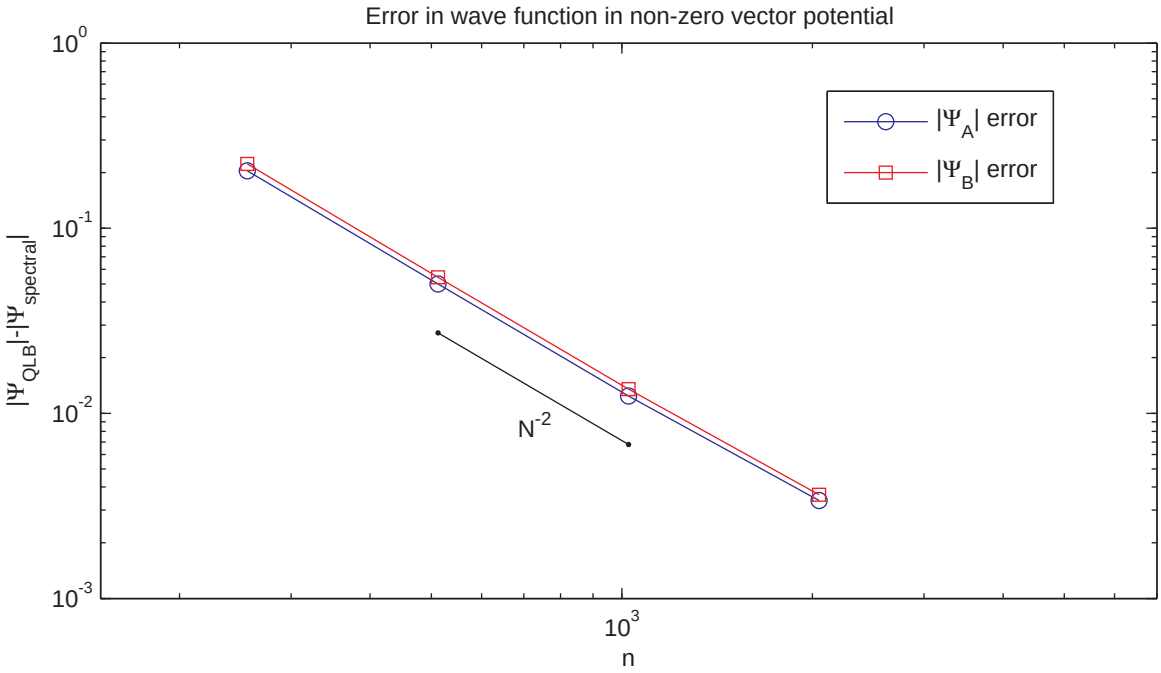

Figure 5.19: The total QLB error in absolute value of the wave function components for a wave packet in a magnetic field perpendicular to the plane of graphene at $t = 937.5$ fs shows clear second order convergence. Reference is a spectral solution on a 1024×1024 grid with a timestep of $\Delta t = 0.37$.

because of the way we built the initial wave packet, as a superposition of plane waves with the phase angle of the second component aligned along the direction given by the combination of each $k_{x,i}$ and $k_{y,i}$ plane wave pair.

In this case we want to confirm convergence of the resulting wave function, not only of the average position, and rerun the QLB simulations on a range of grid sizes up to $t = 937.5$ fs. Our reference spectral solution is calculated on a 1024×1024 grid with $\Delta t = 0.37$. Its timestep is selected such that the solution is indistinguishable for the purposes of error analysis from a more accurate one with a twice reduced timestep. The total errors in the absolute values of both wave function components, given by

$$\sum_{j=1}^{j=n} \sum_{i=1}^{j=n} |\Phi_{QLB}(x_i, y_j)| - |\Phi_{spectral}(x_i, y_j)|, \tag{5.95}$$

are plotted in Figure 5.19, and show clear second order convergence.

We have now defined a complete QLB scheme for simulation of massless charge carriers in monolayer graphene, and will apply it directly to study properties of com-

plex potential configurations in the next chapter.

5.6 Bilayer graphene

Bilayer graphene is an intermediate material between bulk graphite and monolayer graphene, it is made up of two coupled hexagonal lattices aligned on top of each other according to Bernal stacking, in the same manner as in 3D graphite [37, 66, 73, 14], with lattice sites A1, B1 in the bottom layer and sites A2, B2 in the top layer positioned such that B1 sites lie exactly below the A2 sites, and sites A1 and B2 do not have a corresponding site directly above or below them in the bilayer structure. Unlike monolayer graphene, the bilayer energy dispersion relation is parabolic at low energies, indicating a non-zero effective mass of charge carriers, equal to somewhere between $0.03m_e$ and $0.05m_e$ [66, 22]. The other important property different from monolayer graphene is the ability to open a band gap between the valence and conduction bands in the bilayer graphene by applying a scalar potential across the graphene sheet [67].

Similarly to the monolayer graphene, the tight-binding approach to bilayer graphene is used to derive its Hamiltonian for low energies at the corners of the Brillouin zone [67],

$$i\hbar\partial_t \begin{pmatrix} \Psi_{A1} \\ \Psi_{B2} \\ \Psi_{A2} \\ \Psi_{B1} \end{pmatrix} = \begin{pmatrix} -\frac{1}{2}\Delta & v_3\left(p_x + ip_y\right) & 0 & v\left(p_x - ip_y\right) \\ v_3\left(p_x - ip_y\right) & \frac{1}{2}\Delta & v\left(p_x + ip_y\right) & 0 \\ 0 & v\left(p_x - ip_y\right) & \frac{1}{2}\Delta & \xi\gamma_1 \\ v\left(p_x + ip_y\right) & 0 & \xi\gamma_1 & -\frac{1}{2}\Delta \end{pmatrix} \begin{pmatrix} \Psi_{A1} \\ \Psi_{B2} \\ \Psi_{A2} \\ \Psi_{B1} \end{pmatrix}, \tag{5.96}$$

where v and v_3 are the electron velocities

$$v = \frac{\sqrt{3}}{2}a\gamma_0/\hbar \qquad v_3 = \frac{\sqrt{3}}{2}a\gamma_3/\hbar. \tag{5.97}$$

They are given by the in-plane hopping energy $\gamma_0 \approx 2.5$ eV that describes hopping between lattice sites in the same graphene layer, and the weak interlayer hopping energy γ_3 that describes the hopping between lattice sites A1 and B2 that do not lie directly above and below each other. The hopping between the aligned sites A2 and B1 is described by the hopping energy $\gamma_1 \approx 0.4$ eV. The parameter $\xi = \pm 1$ labels the K and $\tilde{K}$ corners of the Brillouin zone, and Δ is the potential created by an external electric field perpendicular to the two layers that would form a band gap in the electronic structure of bilayer graphene. The relative position and orientation of

the two layers is the same as in bulk graphite, with one layer shifted by the carbon-carbon distance relative to the other layer along one of the faces of the hexagon [67], producing the asymmetry of hopping energies in the Hamiltonian.

The A1-B2 γ_3 interlayer hopping causes trigonal warping effects in the dispersion relation at low energies [67, 14], similar to those of monolayer graphene, where the dispersion relation no longer has circular symmetry around the Dirac point and deforms the isoenergetic lines as the energy gets higher than 1 eV. But unlike the monolayer graphene, the trigonal warping due to interlayer A1-B2 hopping develops at low energies, $E_{BLG} < \frac{1}{4}\gamma_1 \left(v_3/v\right)^2 \approx 1$ meV [66].

Bilayer graphene as described by the Hamiltonian (5.96) has a complex dispersion relation, that can be approximated [67] as follows,

$$E_{BLG}^2 \approx \frac{\gamma_1^2}{2} + \frac{\Delta^2}{4} + v^2p^2 \pm \sqrt{\frac{\gamma_1^4}{4} + v^2p^2\left(\gamma_1^2 + \Delta^2\right)}, \tag{5.98}$$

where the γ_3 interlayer coupling is neglected, but the characteristic band structure of bilayer graphene is preserved. In the intermediate energy range $\frac{1}{4}\gamma_1 \left(v_3/v\right)^2 < |E_\pm| < \gamma_1$ and the absence of layer asymmetry Δ, the disperion relation becomes [67],

$$E_\pm \approx \pm\frac{1}{2}\gamma_1 \left(\sqrt{1 + 4v^2k^2/\gamma_1^2} - 1\right). \tag{5.99}$$

At low energies $\hbar v_F k \ll \gamma_1$ it is further approximated by a parabolic dispersion relation,

$$E_{BLG} \approx \pm\frac{\hbar^2k^2}{2m} \qquad m = \frac{\gamma_1}{2v^2}, \tag{5.100}$$

and at higher moments $\hbar v_F k \gg \gamma_1$ turns into a linear relationship $E_{BLG} \approx \pm\hbar vk$, analogous to monolayer graphene [67, 22]. For $m \approx 0.03m_e$ the characteristic momentum far above (below) which the dispersion relation is linear (parabolic) is $k_0 = 0.3nm^{-1}$ [22].

5.6.1 QLB scheme for bilayer graphene

The full Hamiltonian of bilayer graphene (5.96) has streaming matrices that cannot be diagonalized, and therefore it cannot be simulated with the QLB scheme in its complete form. If we neglect the γ_3 interlayer hopping terms because they are much smaller than γ_1 and γ_0 hopping energies [22], we can derive a QLB scheme for the bilayer Hamiltonian in the same way as for monolayer graphene – by breaking up the equation into streaming along x, streaming along y, and collision equations, solving

each one numerically, and applying the evolutions one by one using Strang splitting. Rewriting (5.96) in this way we get

$$\partial_t \begin{pmatrix} \Psi_{A1} \\ \Psi_{B2} \\ \Psi_{A2} \\ \Psi_{B1} \end{pmatrix} + v \begin{pmatrix} 0 & 0 & 0 & 1 \\ 0 & 0 & 1 & 0 \\ 0 & 1 & 0 & 0 \\ 1 & 0 & 0 & 0 \end{pmatrix} \partial_x \begin{pmatrix} \Psi_{A1} \\ \Psi_{B2} \\ \Psi_{A2} \\ \Psi_{B1} \end{pmatrix} = 0 \tag{5.101}$$

$$\partial_t \begin{pmatrix} \Psi_{A1} \\ \Psi_{B2} \\ \Psi_{A2} \\ \Psi_{B1} \end{pmatrix} + v \begin{pmatrix} 0 & 0 & 0 & -i \\ 0 & 0 & i & 0 \\ 0 & -i & 0 & 0 \\ i & 0 & 0 & 0 \end{pmatrix} \partial_y \begin{pmatrix} \Psi_{A1} \\ \Psi_{B2} \\ \Psi_{A2} \\ \Psi_{B1} \end{pmatrix} = 0, \tag{5.102}$$

$$\partial_t \begin{pmatrix} \Psi_{A1} \\ \Psi_{B2} \\ \Psi_{A2} \\ \Psi_{B1} \end{pmatrix} = -i \begin{pmatrix} -\frac{1}{2}\Delta + g & 0 & 0 & 0 \\ 0 & \frac{1}{2}\Delta + g & 0 & 0 \\ 0 & 0 & \frac{1}{2}\Delta + g & \xi\gamma_1 \\ 0 & 0 & \xi\gamma_1 & -\frac{1}{2}\Delta + g \end{pmatrix} \begin{pmatrix} \Psi_{A1} \\ \Psi_{B2} \\ \Psi_{A2} \\ \Psi_{B1} \end{pmatrix}. \tag{5.103}$$

We solve the streaming equations (5.101) and (5.102) by first diagonalizing the matrices as follows,

$$X_B^{-1} M_x X_B = Y_B^{-1} M_y Y_B = \begin{pmatrix} 1 & 0 & 0 & 0 \\ 0 & 1 & 0 & 0 \\ 0 & 0 & -1 & 0 \\ 0 & 0 & 0 & -1 \end{pmatrix}, \tag{5.104}$$

where the required diagonalization matrices are as follows,

$$X_B^{-1} = \frac{1}{\sqrt{2}} \begin{pmatrix} 1 & 0 & 0 & 1 \\ 0 & 1 & 1 & 0 \\ -1 & 0 & 0 & 1 \\ 0 & -1 & 1 & 0 \end{pmatrix} \qquad X_B = \frac{1}{\sqrt{2}} \begin{pmatrix} 1 & 0 & -1 & 0 \\ 0 & 1 & 0 & -1 \\ 0 & 1 & 0 & 1 \\ 1 & 0 & 1 & 0 \end{pmatrix} \tag{5.105}$$

$$Y_B^{-1} = \frac{1}{\sqrt{2}} \begin{pmatrix} i & 0 & 0 & 1 \\ 0 & -i & 1 & 0 \\ -i & 0 & 0 & 1 \\ 0 & i & 1 & 0 \end{pmatrix} \qquad Y_B = \frac{1}{\sqrt{2}} \begin{pmatrix} -i & 0 & i & 0 \\ 0 & i & 0 & -i \\ 0 & 1 & 0 & 1 \\ 1 & 0 & 1 & 0 \end{pmatrix}. \tag{5.106}$$

This allows to perform evolution of the wave function by the streaming through shifting the top two components of the transformed wave function towards the positive direction by one grid spacing, the bottom two components towards the negative direction by one grid spacing, and transforming the wave function back to its original form. The collision equation (5.103) can be solved to second order accuracy using

Crank-Nicolson discretization and generates the following collision matrix to multiply the wave vector,

$$Q_B = \begin{pmatrix} \frac{4i+\Delta t(2g-\boldsymbol{D})}{4i-\Delta t(2g-\boldsymbol{D})} & 0 & 0 & 0 \\ 0 & \frac{4i+\Delta t(2g+\boldsymbol{D})}{4i-\Delta t(2g+\boldsymbol{D})} & 0 & 0 \\ 0 & 0 & -\frac{16+\Delta t^2\left((2g+\boldsymbol{D})^2-4\xi^2\gamma_1^2\right)}{(-4i+\Delta t(2g+\boldsymbol{D}))^2-4\Delta t^2\xi^2\gamma_1^2} & \frac{16i\xi\gamma_1\Delta t}{(-4i+\Delta t(2g+\boldsymbol{D}))^2-4\Delta t^2\xi^2\gamma_1^2} \\ 0 & 0 & \frac{16i\xi\gamma_1\Delta t}{(-4i+\Delta t(2g+\boldsymbol{D}))^2-4\Delta t^2\xi^2\gamma_1^2} & -\frac{16+\Delta t^2\left((2g+\boldsymbol{D})^2-4\xi^2\gamma_1^2\right)}{(-4i+\Delta t(2g+\boldsymbol{D}))^2-4\Delta t^2\xi^2\gamma_1^2} \end{pmatrix} \tag{5.107}$$

where we have replaced the layer asymmetry Δ with $\boldsymbol{D}$ to avoid confusion with Δt. As for monolayer graphene, we can thus write down the second order QLB algorithm of n timesteps up to a final time $t_f = n\Delta t$ using Strang splitting,

$$\Psi\left(t_f\right) = \bar{Y}_B^{-\frac{1}{2}}\left[\bar{Y}_B Q_B^{\frac{1}{2}} \bar{X}_B Q_B^{\frac{1}{2}}\right]^n \bar{Y}_B^{\frac{1}{2}} \Psi\left(0\right), \tag{5.108}$$

where

$$\bar{X}_B = X_B S^x X_B^{-1} \qquad \bar{Y}_B = Y_B S^y Y_B^{-1}. \tag{5.109}$$

Therefore, if we ignore the effects of the weak interlayer hopping energy γ_3, the QLB scheme can also be used to simulate charge carriers in bilayer graphene.

Chapter 6

Charge confinement in graphene

As silicon-based transistors become smaller and smaller to improve performance of processors, they approach the limits of size that are dictated by the properties of silicon. Soon a new material will have to be found to be able to continue the growth of processing speed that has so far been following Moore's law, and graphene is a material uniquely suitable to replace thin layers of silicon in the construction of field effect transistors due to its high carrier mobility that allows high frequency of operation, remarkable durability and low production costs [90, 37, 61]. The first graphene field effect transistors were created soon after the discovery of graphene in 2007 [60] and sparked a lot of research in this area of potential application. However the problem with graphene transistors is that they cannot be switched off – the charge carriers in large-area monolayer graphene cannot be completely confined electrostatically due to zero effective mass and zero band gap between the conductance and valence bands, current cannot be stopped from flowing. Early graphene transistors reported on/off current ratios of $2 - 20$, while digital devices require an on/off current ratio of $I_{on}/I_{off} = 10^4 - 10^7$ [90], and that is difficult to achieve with graphene's massless charge carriers and zero band gap.

There are several ways to create a band gap in graphene that have been explored theoretically and experimentally, such as confining electrons by cutting graphene into narrow nanoribbons of only $10 - 100$ nm wide, where the energy gap is inversely proportional to the width [108, 36, 33]; strain engineering to create an effective magnetic field that will also open a band gap to generate non-zero effective mass [42], as we mentioned in section 5.5; creating graphene nanomesh - a graphene sheet with holes; and hydrogenation - incorporating hydrogen atoms into the graphene surface [87, 29, 53]. Each approach, however, has its technical production difficulties - for

example it is difficult to create graphene nanoribbons of a certain width and regular edges at this time. In addition, the non-zero effective mass of charge carriers that results from opening a band gap also has a negative effect on carrier mobility, thus negating some of the advantage of using graphene over silicon. The advantage provided by graphene's extreme thinness, however, is more important as it allows scaling transistors to shorter gate length and achieving higher speed in this way [90].

6.1 Smooth potential barriers

We, on the other hand, propose to obtain charge confinement in unmodified monolayer graphene, with zero band gap and a linear dispersion relation, using a configuration of multiple scalar potential barriers positioned at angles to each other. In a graphene field effect transistor (FET) the energy of the charge carriers is controlled by the back gate voltage and the height of the potential barrier is controlled by the top gate voltage, with the distance between the top gate and back gate governing the distance over which the potential grows, therefore governing the slope of the potential [3]. For a sloping potential barrier only wave numbers near normal incidence have a significant probability of transmission, with the rest being filtered out and reflected back [15]. We can use this collimation effect to achieve very low transmission coefficients using multiple barriers created by metallic top gates on graphene positioned at an angle relative to each other that are turned on and off.

As noted in section 3.2.2 on one dimensional simulations of a sloping potential step, realistic electric fields generate potentials with non-zero slope, and realistic potential barriers are also smooth, not rectangular or 'top-hat' shaped. In section 5.4 we described the tunnelling through sloping potentials, as the distance over which the potential changes increases (decreasing the slope), the barrier switches from 'sharp' to 'smooth', the transmission process switches from Klein tunnelling to traditional quantum tunnelling by evanescent waves, resulting in a drastically reduced transmission coefficient. In general terms a potential is considered 'smooth' when the wavelength of the incident particle is smaller than the distance over which the potential changes its height. A sloping potential step in graphene was considered by Cheianov and Falko [30], for a strictly symmetrical case where the incident particle energy is exactly half of the barrier height. The expression for the transmission across the potential step,

$$T(\phi) \approx e^{-\pi k_{tot} \omega \sin^2(\phi)}, \tag{6.1}$$

is valid for angles of incidence near zero and less than 45°. It shows near perfect transmission for near-normal incidence, that quickly decays as the angle of incidence grows. More specifically, the smoothness criterion is given by

$$k_{tot}\omega \sin^2(\phi) \gg 1, \tag{6.2}$$

where ω is half the distance over which the potential grows and ϕ is the angle of incidence [3]. This means that for configurations where $k_{tot}\omega > 1$, the barrier is 'sharp' and the transmission probability is high as long as the angle of incidence is close to normal. As ϕ grows and the angle of incidence deviates from normal, the barrier becomes 'smooth' and the transmission coefficient rapidly falls to zero. This results in a collimation effect – only plane waves that are very close to normal incidence are transmitted through smooth potential barriers, while those falling onto the barrier at an angle are reflected. Due to this a wave packet incident onto a smooth barrier will have a complex interaction with the barrier - part of the wave numbers making up the wave packet will see the barrier as 'sharp' and have a near perfect transmission probability, and part of the wave numbers will see the barrier as smooth and be reflected from it. We begin by testing this effect using our two-dimensional QLB method for graphene.

Plane wave tunnelling through trapezoidal shaped potential barriers in graphene was analysed by Sonin [94] and confirmed the evidence of Klein tunnelling effects in experimental results obtained with graphene devices [95, 111]. The research of Shytov et. al. [93] suggests using a parabolic potential to approximate the potentials created in top-gate graphene devices, like the ones used to observe Klein tunnelling [95]. Our smooth potentials are defined using hyperbolic tangent functions, based on the definition of the smooth potential step (3.61), to replace the piece-wise definition of the potential and eliminate the sharp corners with smooth transitions that are more realistic. Each barrier is given by,

$$g_i(x,y) = \frac{V_0}{2}\tanh\left(\frac{x - x_{0,i} - y\tan(\theta_i)}{s_i}\right) - \frac{V_0}{2}\tanh\left(\frac{x - x_{0,i} - w_i - y\tan(\theta_i)}{s_i}\right), \tag{6.3}$$

where $x_{0,i}$ is the position of the left end of the barrier, w_i is the width of the barrier, and θ_i is the angle of the barrier in the $x-y$ plane ($\theta_i = 0$ for a barrier parallel to the y-axis). The distance over which the potential grows and decays on either side of the potential barrier is controlled by the 'smoothness' parameter s_i, we will

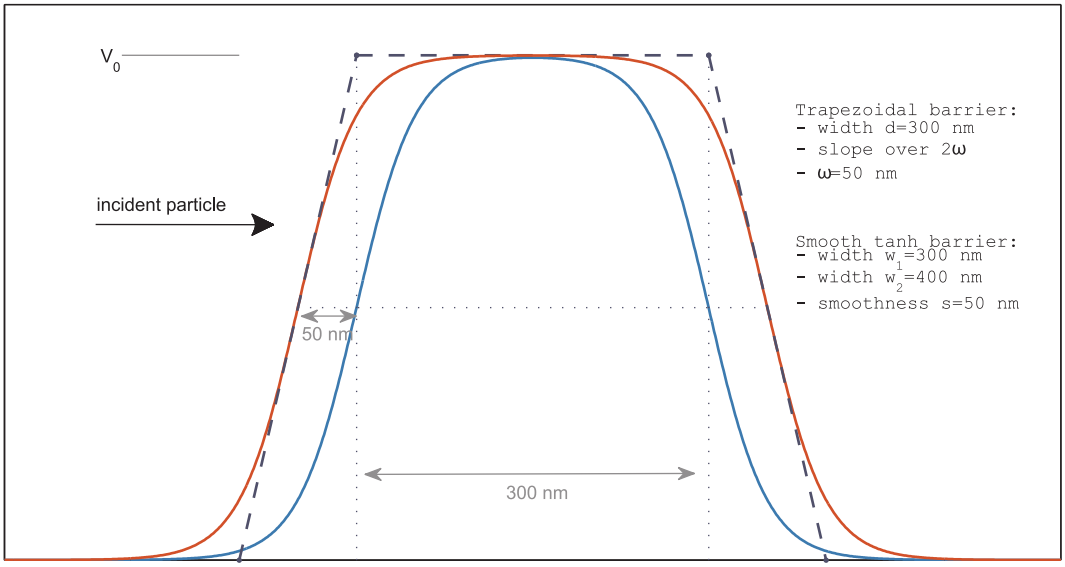

Figure 6.1: A comparison of a smooth barrier defined with hyperbolic tangent functions and a piece-wise defined trapezoidal barrier. All barriers are defined with same height V_0, and same smoothness parameter $s = \omega = 50$ nm. The hyperbolic tangent function produces a barrier with a matching slope that is narrower by approximately $2s = 100$ nm if we set width equal to $d = w = 300$ nm, or same width if we set $w = d + 2\omega = 400$ nm.

call it slope width, for an ideal rectangular barrier it is equal to zero. The index $i = 1, 2, 3, ...$ designates the number of the barrier, as we will require multiple barriers for our potential configurations. The relationship between the smooth hyperbolic tangent potential and the trapezoidal barrier is such that our smoothness parameter s_i closely matches the distance ω that determines the slope of the trapezoidal barrier and is compared with the incident particle's wavelength (equation (6.1)) to determine whether the barrier is seen as smooth or sharp. The Figure 6.1 shows that for $s = \omega$ the two potentials have comparable slope. We also see that using $w = 300$ nm barrier width parameter equal to width trapezoidal barrier at the top, $d = 300$ nm, produces a narrower smooth barrier. To match the widths of the trapezoidal and smooth barrier, the width parameter w should be set to the width of the trapezoidal barrier in the middle of the potential, $w = d + 2\omega = 400$ nm.

We form the complete potential system by adding all the required barriers onto the domain one by one such that at any point in the domain the magnitude of the potential is given by the maximum of all the barriers and not their sum.

A voltage V_t applied to the top gate placed across the graphene device creates a

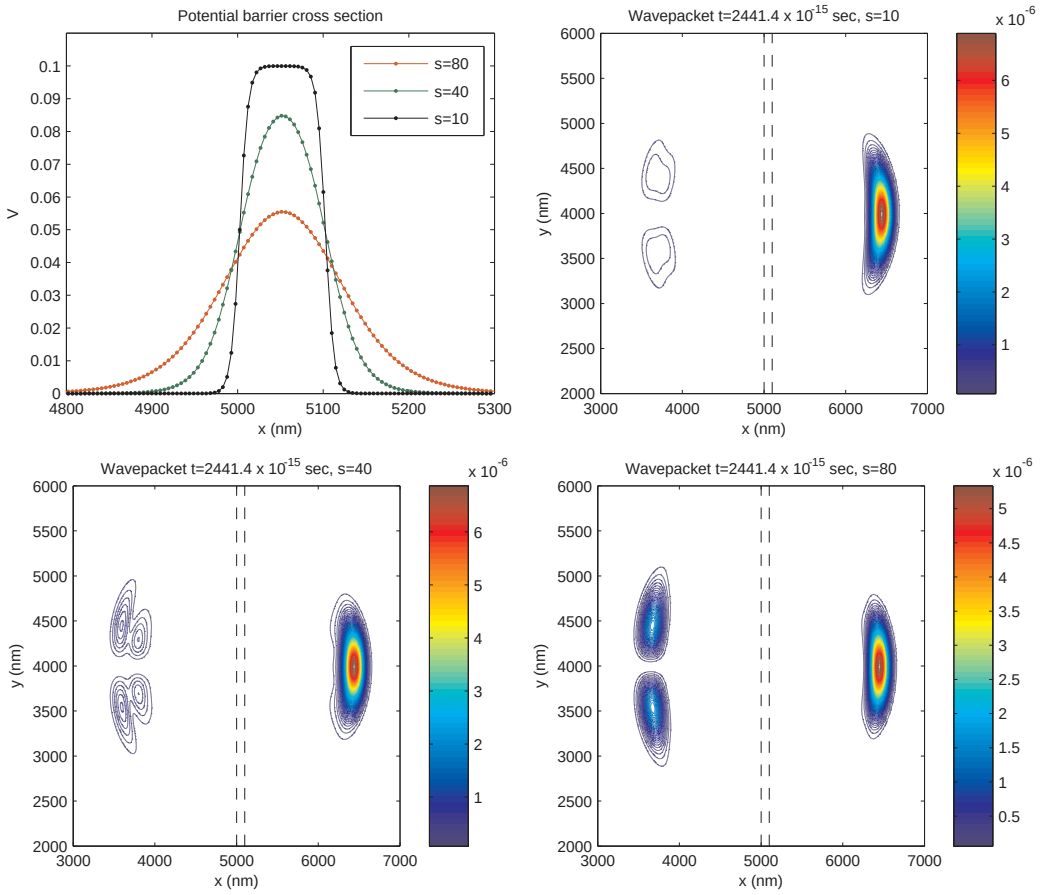

Figure 6.2: Profiles of smooth potential barriers for a range of s_i values (top left). Transmission of wave packet normally incident onto a sloping potential barrier for $s_i = 10$ (top right), $s_i = 40$ (bottom left), and $s_i = 80$ (bottom right). The reflection coefficient increases as the barrier becomes more smooth the reflection coefficient increases, reflecting parts of the wave packet that are composed of wave numbers with angles of incidence far from normal.

potential barrier in the path of the current by shifting the Dirac cones of the charge carriers in that region, that shift corresponds to the potential barriers we simulate. The magnitude of the voltage determines the height of the barrier and the distance between the top gate and the back gate determines the smoothness of the potential barrier. The Fermi energy of charge carriers is controlled by a voltage applied to the back gate, V_b, and determines k_{tot}. Therefore controlling V_t will control the conducting channel and the switching between the on and off states of the transistor, as fast as possible. Fast operation of the transistor requires fast charge carriers, and graphene has highest current density at room temperature, million times that of copper, its carriers can travel ballistically over submicron distances [14]. Graphene carrier mo-

bility at room temperature (300K) is about $15,000\ cm^2/Vs$, up to $20,000\ cm^2/Vs$ in suspended graphene, and $150,000\ cm^2/Vs$ in stretched graphene, where the effect of scattering by flexural phonons is diminished [28, 72]. A theoretical mobility limit of $200,000\ cm^2/Vs$ is predicted, more than double of Indium antimonide (InSb) - a semiconductor with the highest known carrier mobility of $77,000\ cm^2/Vs$ [18].

6.1.1 Simulation of smooth barriers

We run a set of simulations with a wave packet normally incident onto increasingly smooth potentials and observe the transmission and reflection behaviour. The simulations are run on a 10000 nm $\times$ 10000 nm domain with a 2048×2048 grid, with the wave packet initialized with the same configuration as for the rectangular barrier tunnelling simulation before, given by equation (5.72). The wave packet has an energy of 33 meV, corresponding to $k_{tot} = 0.05$ nm^{-1}, and the potential strength is given by $V_0 = 0.10$ nm^{-1}. Wave number $k_{tot} = 0.05$ nm^{-1} corresponds to a typical experimental Fermi wavelength of 20 nm, even smaller k_{tot} values are difficult to achieve currently due to inhomogeneities present in graphene sheets. We choose a potential barrier width of $w_i = 100$ nm for all barriers, equal to average mean free path of a good graphene sample, and a typical value for experimental devices [3]. Experiments measuring resistance across a tunable potential barrier in graphene and comparing with diffusive and ballistic theories have shown that ballistic transport is able to explain the transmission results better [52, 41], and therefore in our simulations we assume a graphene sheet without impurities on the scale of our barrier widths and a ballistic regime of charge transport.

We start with a narrower wave packet than in rectangular barrier simulations, with $\sigma = 100$, to cover a larger section of the possible momentum space with our wave packet and observe the complexity of interactions with the barrier more clearly. The simulations results are shown in Figure 6.2. The profiles of the barriers are shown in the first part of the Figure and the probability density plots for each barrier in the other three parts. We see that the shape of the barrier generated by our function (6.3) closely resembles the shape of a barrier generated by a narrow top gate in a graphene device [111]. Note that given the width of our barrier, the maximum height of the barrier for high s_i is lower than V_0 due to overlap of the two sloping sides of the barrier. We see that for each barrier the transmission probability is quite large due to normal incidence, but the reflected part grows as s_i increases and the barrier gets

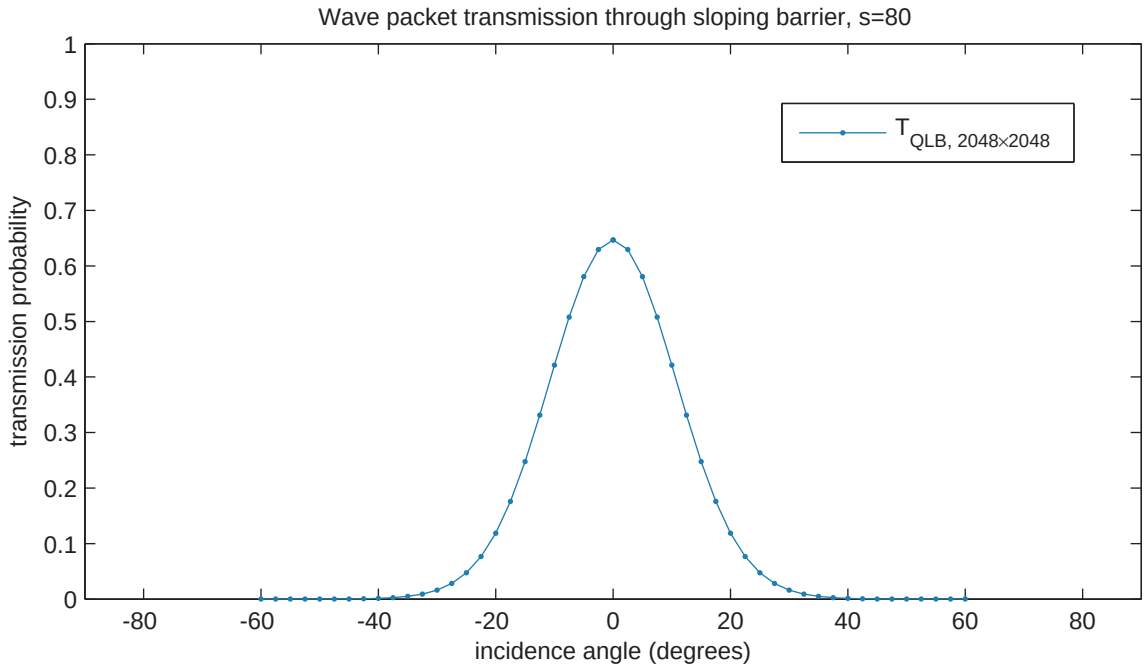

Figure 6.3: Simulated transmission coefficient for a smooth barrier for a range of incidence angles shows rapid decay of the transmission probability as the angle of incidence onto the barrier deviates from normal.

more smooth. The reflected parts are not moving directly backwards, as we would expect for reflection off a sharp rectangular barrier, but instead appear on either side of normal incidence. This is exactly due to the collimation effect - the parts of the wave packet made up of plane wave combinations with k_x and k_y that give an incidence angle far enough from zero on either side of normal are reflected off the barrier and only the portion of the wave packet composed of wave numbers of near normal incidence is transmitted. The smoother the barrier, the closer to normal do the wave numbers have to be to have a high probability of transmission.

We next simulate wave packets incident at non-zero angles onto a smooth barrier and plot the evolved probability densities, see Figure 6.4. For a wave packet incident at 22.5° we see most of the probability being reflected, while the transmitted part does not continue moving at the same angle on the other side of the barrier as it would for a rectangular potential (see Figures 5.10 and 5.11). Instead the transmitted component travels nearly perpendicular to the barrier, due to the fact that only wave numbers with near normal incidence onto the barrier have a high transmission probability. Since our initial wave packet is made especially wide in momentum space, a portion of

it does lie in the region of the (k_x, k_y) plane that contains wave numbers perpendicular to the barrier despite the non-zero average incidence angle, and is able to tunnel through the barrier. In the second part of the plot we show a wave packet incident at 45°, and see that at this angle there is no significant transmission through the barrier, a wave packet with such a large deviation from normal incidence will contain a very small proportion of wave numbers that will have a high transmission probability. For a more quantitative description of the tunnelling through a smooth barrier we run a series of simulations with wave packets incident onto the barrier at a range of angles and calculate the transmitted probability density. We continue to use $s_i = 80$ as a realistic parameter for the smoothness of the potential, based on an $\omega = 80$ nm step size of the potential generated in a graphene top gate device created by Huard et. al. for transport measurements [52]. A plot of the resulting transmission coefficient versus incidence angle is shown in Figure 6.3. It displays the effect of deviating from normal incidence more clearly and has the same general shape that was predicted in plane wave analysis of smooth barriers in graphene by Cayssol et. al. [15]. There are no resonant incidence angles with high transmission probabilities like we observed for a rectangular barrier (see Figure 5.14) due to the appearance of classically forbidden regions for wave numbers with non-zero incidence angles and tunnelling taking place only through evanescent waves when the barrier is 'smooth' for the given incident wave packet.

Although our potential barriers are based on the hyperbolic tangent barrier definition for which there is an analytic expression for the transmission coefficient (3.62), it does not apply to our potential barriers when the barrier is too narrow to treat the two sides as separate potential steps. Having thoroughly confirmed the accuracy of the QLB scheme in the previous chapters, in this part of the work we apply the scheme directly and base our conclusions solely on the results of the simulations. To make sure the simulations do converge to a solution, we run simulation of a wave packet incident at an angle of 11.25° onto a smooth barrier ($s_i = 80$) at a range of grid resolutions and compare the resulting transmission coefficient. We use Richardson extrapolation to calculate an accurate value of the transmission coefficient from the last two simulation results with larger grid sizes and calculate the errors as an absolute value of the difference from the extrapolated value - these show a clear second order convergence, as we expect.

Grid size	Transmitted $\|\Psi\|^2$	Error ratio
256×256	0.34606833336092652	–
512×512	0.37115886974747159	5.7509
1024×1024	0.37521141600631897	4.2982
2048×2048	0.37613819743468530	4.0696
4096×4096	0.37636496536463637	4.0173
8192×8192	0.37642136783840480	4.0075
16384×16384	0.37643543311286976	4.0000
Richardson extrapolation	0.37644012153769140	–

6.2 Charge confinement using multiple barriers

Given these properties of smooth potential barriers we can use multiple barriers to obtain charge confinement by drastically reducing the transmission profile for all possible incidence angles if we place barriers at an angle to each other to force the wave packet to tunnel through them one after another. If we have two smooth barriers positioned at an angle $\gamma = |\theta_1 - \theta_2|$ to each other, the wave packet incident onto the first barrier at some non-zero angle ϕ will be split into reflected and transmitted components by the first barrier. The transmitted component will be normal to the first barrier and will therefore fall onto the second barrier with the incidence angle equal to γ. If the angle between the barriers is large enough and the barriers are smooth enough, the second barrier will almost completely block the transmission of the part of the wave packet that went through the first barrier. Transmission of plane waves through a superlattice of rectangular barriers was studied by Guo et. al. [43], and transmission of wave packets through multiple barriers was touched upon in the work on simulations of wave packet tunnelling in graphene by Pereira et. al. [82], however they were concerned with rectangular barriers that are parallel to each other, and the additional transmission resonances such a double barrier configuration will cause.

After testing several angles between barriers we chose $\gamma = 45°$ to provide a high enough angle of incidence onto the second barrier. We set up our potential configuration out of four smooth barriers ($s_i = 80$ for all) – first one aligned along the y-axis ($\theta_1 = 0°$), second barrier at an angle of $\theta_2 = 45°$, third barrier at an angle of $\theta_3 = -45°$ and the fourth barrier is parallel to the first one. The second and third barriers are placed in such a way that they intersect with each other behind the first barrier, and the vertical fourth barrier is placed on top of their intersection. The resulting potential is shown in the first plot of Figure 6.5. We are assuming the

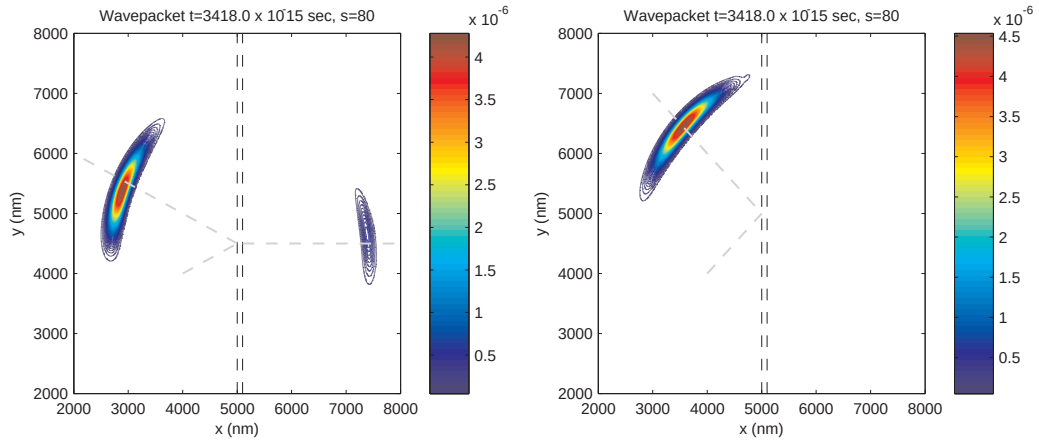

Figure 6.4: Transmission of wave packet incident onto a smooth potential barrier ($s_i = 80$) at angles of 22.5° (left) and 45° (right). The simulations are run on a 10000 nm × 10000 nm domain with a 2048×2048 grid, with initial wave number $k_{tot} = 0.05$ nm^{-1} and wave packet width $\sigma = 100$.

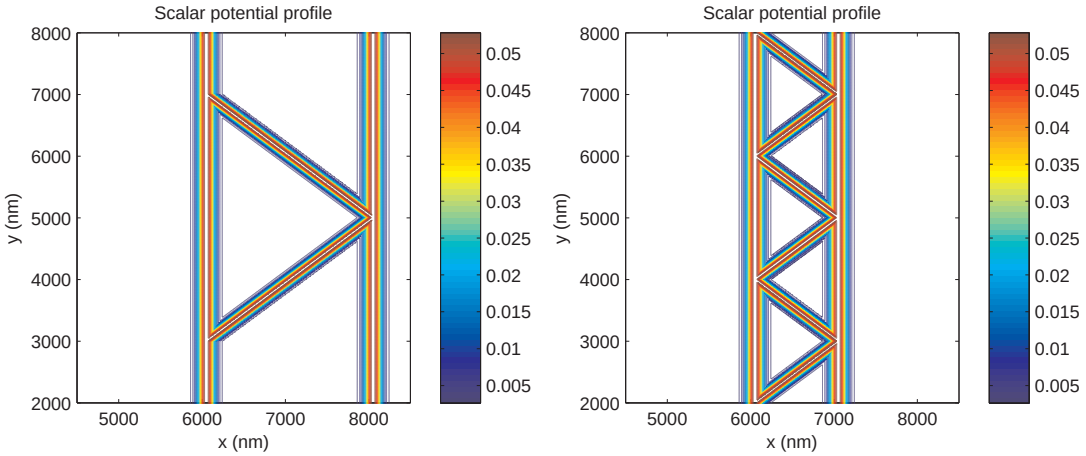

Figure 6.5: Contour plots of the potential barrier structures designed to confine massless charge carriers in graphene. On the left a configuration with two angled barriers at 45° to the two vertical barrier, with edges of the graphene sheet assumed at $y = 3000$ nm and $y = 7000$ nm. On the right a narrower configuration independent of the width of graphene sheet, with successive barriers placed at an angle of 45° to the two bounding vertical barriers. All the barriers have the same profile, given by equation (6.3) with $s_i = 80$.

possible channel of horizontal motion of charge carriers from the left to right passes between the points of intersection of the angled barriers with the vertical first barrier, at $y = 3000$ nm and $y = 7000$ nm (if the edges of the graphene sheet are located there, for example), and in this way our potential configuration presents two barriers for charge carriers incident at any point along the first barrier. The fourth barrier

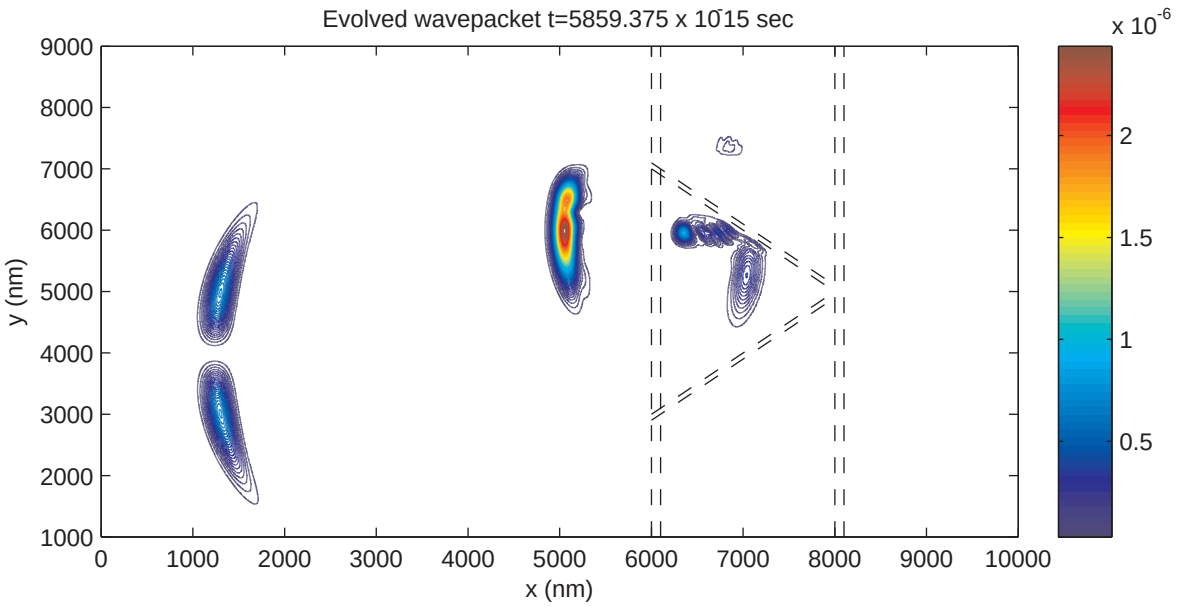

Figure 6.6: Transmission of wave packet through multiple barriers at 45° to each other. The plot shows no significant transmission through the complete potential configuration, and the greater part of the probability density will be reflected back out of the barrier towards the initial position of the wave packet. Wave number $k_{tot} = 0.05$ nm^{-1}, wave packet width $\sigma = 100$, normally incident at $y = 4000$ nm.

will meet at 45° any probability density that may be transmitted through the first pair of barriers, serving as an additional way to suppress transmission and to make the overall barrier configuration a more symmetric shape for easier calculation of the transmission probability.

The total transmission through the complete potential configuration can be represented as a product of transmission probabilities through each of the three barriers that the wave packet needs to tunnel through. For our potentials it is equal to $T_{total} = T_1(\phi)\, T_2(45°)\, T_3(45°)$ where ϕ is the angle of incidence onto the first barrier and an example of $T_i(\phi)$ for our wave packet is plotted in Figure 6.3. Because the wave packet transmitted through the first barrier will continue to move almost perpendicular to it regardless of the incidence angle, the transmission coefficients through the second and third barriers are not dependant on ϕ and we would expect to obtain the greatest T_{total} when $\phi = 0°$. Since we aim to obtain a transmission coefficient through the complete potential configuration that is as low as possible for a charge carrier incident at any angle, we can treat the system with $\phi = 0°$ as a 'worst case scenario' and can assume the total transmission probability T_{total} for a stream

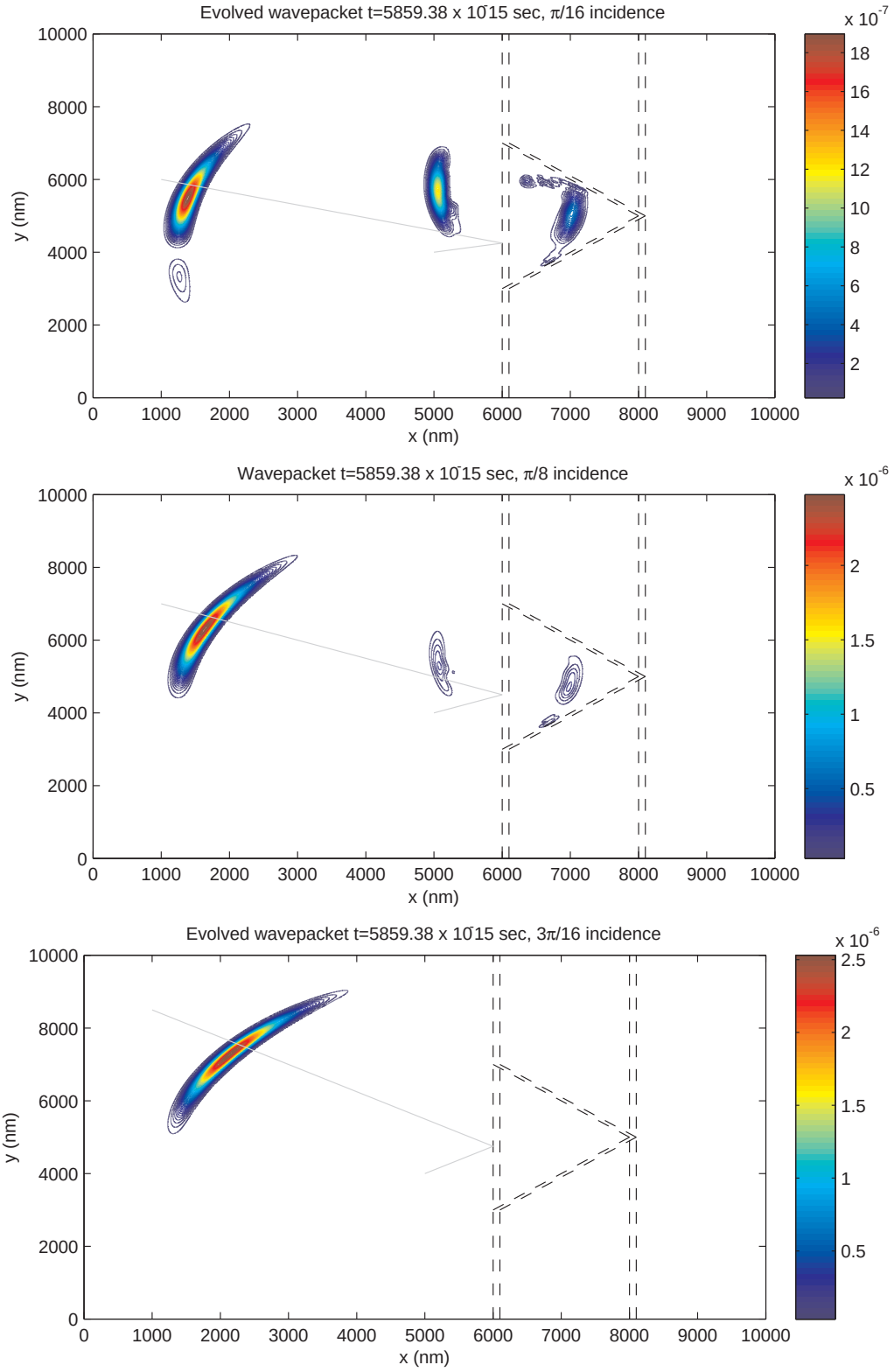

Figure 6.7: Transmission of wave packet incident at 11.25° (top), 22.5° (middle), 33.75° (bottom) onto multiple barriers at 45° to each other shows decreasing transmission as the incidence angle is increased. Wave number $k_{tot} = 0.05$ nm^{-1}, wave packet width $\sigma = 100$.

of charge carriers incident onto our potential configuration at all angles will be less than the T_{total} we can obtain from our simulations of normal incidence.

Having set up the potential profile we run simulations of a wave packet normally incident onto the first barrier, initialized with the same parameters as above on the same 10000 nm $\times$ 10000 nm domain. The evolved probability density is shown in Figure 6.6. The wave packet meets the barrier at the $y = 4000$ nm level, and a large part of the probability density is reflected on initial contact with the barrier. Having travelled leftward away from the barrier, it is on the far left side of the domain. The transmitted component is reflected by the angled barrier and moves vertically towards the second angled barrier, where it is reflected back towards the first vertical barrier and is transmitted through it back towards the left at the $y = 6000$ nm level. This transmitted component is the largest amount of probability density on the plot, which we see to the left of the potential, and is moving away from the potential. The small amount of probability density that remains confined between the potential barriers will move down towards the first angled barrier and be transmitted back out at the same point where the initial wave packet made contact with the barrier. We see that there is no probability density that shows up transmitted through the complete potential configuration, beyond the $x = 8000$ nm line, and if we calculate the total probability density present in the region of the domain beyond the barrier it adds up to the order of $T_{total} \approx 10^{-5}$.

To make sure that normal incidence is the 'worst case' scenario, and there are no unusual transmission probability spikes through the pair of barriers for wave packets incident at non-zero angles, we run simulations for $\phi > 0$. Plots of the evolved probability density for $\phi = 11.25°, 22.5°, 33.75°$ are shown in Figure 6.7. We can see that as the angle of incidence grows, there is a monotonic and rapid decrease of transmission through the first smooth barrier, and in each case the transmitted wave packet travels perpendicular to the first barrier, reflects between the two angled barriers and is transmitted back out through the first vertical barrier. At $\phi = 33.75°$ there is already complete reflection off the first barrier and we do not expect any additional transmission effects at even greater angles of incidence.

To explore the possibility of a confining potential that is more narrow relative to the width of the graphene sheet, we test a potential configuration with multiple angled barrier forming a zig-zag pattern between two vertical barriers that are 1000 nm apart, still 100 nm wide and at 45° angle to vertical. It is shown in second plot of

Figure 6.5. We initialize normally incident wave packets at two positions ($y = 4000$ nm and $y = 5000$ nm) to test interaction of the wave packet with the intersection of the angled barriers at the first and second vertical barriers, and plot the results in Figure 6.8. As we can see, in both cases there is significant transmission through the complete potential configuration at the position of the intersection of the angled barriers, as shown by the probability density on right side of the potential configuration, with an initial transmitted component followed by a secondary portion of probability density travelling beyond the barrier. On the first plot we see secondary transmission through the potential configuration at $y = 3000$ and $y = 5000$ levels, possibly due to probability density that travels inside the angled potential barriers across the potential configuration. On the second plot we see two pairs of additional packets of probability density that are transmitted back out through the first vertical barrier by continuously reflecting between the two angled barriers, as we described above. In both cases there is some probability density that slowly propagates vertically inside the potential configuration between the two vertical barriers towards the assumed edges of the graphene sheet.

To investigate the behaviour of the wave packet incident onto the intersection of the angled barriers we go back to the wide barrier configuration, shown in the left panel of Figure 6.5, initializing the same wave packet as before at $y = 5000$ nm level and observing the evolution of the probability density function at different times. A plot of the results at two successive times in the simulations is shown in Figure 6.9. We observe that the probability density that is transmitted through the first vertical barrier forms a large peak upon meeting the intersection of the angled barriers. This results in the majority of the probability density being reflected back toward the first vertical barrier, and a small part of the probability density is transmitted through the second vertical barrier and continues moving horizontally beyond the potential barrier configuration. The amount of probability density transmitted in this case is $T_{Total} = 0.0381$ - not a significant amount, but not enough to conclude the barrier does completely block wave packets incident at the level of the intersection of angled barriers. Similarly, we run simulations with the potential configuration reversed to observe the behaviour of a wave packet incident onto the intersection of the angled barriers at the first vertical barrier, with the results plotted in Figure 6.10. We see that the probability density transmitted through the first vertical barrier is split by the angled barriers into three regions, the probability density does not travel inside

the potential along the barriers, and a portion of the probability density is transmitted through the complete potential configuration, $T_{Total} = 0.0717$ in this case.

To avoid the transmission resulting from wave packets incident onto the intersection of angled barriers we can construct a confining potential with a single angled barrier across the width of the graphene sheet, shown in the left panel of Figure 6.11. This will direct the incoming wave packets vertically inside the potential configuration, into the edges of the graphene sheet. We initialize the normally incident wave packet with a width of $\sigma = 250$, and the results of the simulation are shown in Figure 6.12. The transmission coefficient in this case is only $T_{total} = 2.186 \times 10^{-4}$, and assuming the edges of the graphene sheet will reflect the wave packet, the greater part of the probability density will be transmitted back towards the left.

Alternatively, given the results of the above simulations, we can construct a narrow confining potential that is independent of the width of the graphene sheet from two consecutive barriers made of multiple short angled barriers forming a zig-zag pattern, as before, with the second barrier shifted vertically by half of the distance between the first and second vertical barriers. This way the portions of the wave packet transmitted through the intersections of the first set of angled barriers will fall onto the sloped section of the second set of angled barriers that will reflect and direct the incoming probability density leftward. A plot of this configuration is show in the second part of Figure 6.11, with the barrier width $w_i = 100$ nm as before, the distance between the vertical barriers set at 1000 nm, and the second set of angled barriers shifted downward by 500 nm. We test this potential configuration in three sets of simulations, with wave packets falling onto both intersections of angled barriers at $y = 4000$ nm and $y = 5000$ nm levels, and onto the smooth part of the angled barriers at $y = 4500$ nm. The initial wave packets are wider than in original simulations, $\sigma = 250$, to exclude more of the wave numbers with non-zero incidence angles from the wave packet and observe the effects of normal incidence more clearly. The results of the simulations are shown in Figure 6.13, we see that such a potential configuration does not allow any significant transmission for any incidence level, with the following resulting transmission probabilities,

Incidence level	T_{total}
4000 nm	9.9236×10^{-4}
4500 nm	1.1005×10^{-4}
5000 nm	1.1877×10^{-4}

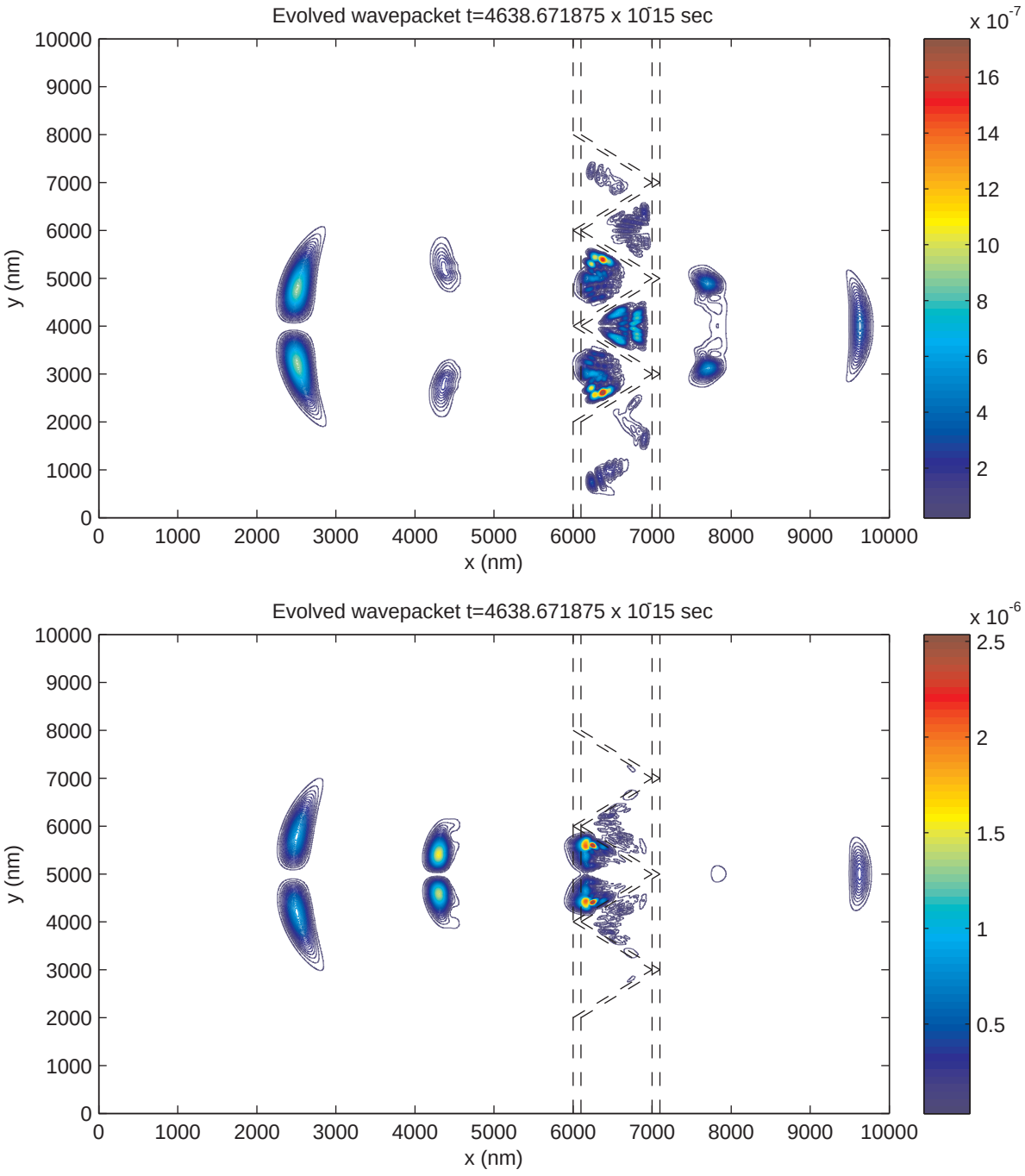

Figure 6.8: Transmission of wave packet through a complex barrier, normally incident at $y = 4000$ nm and $y = 5000$ nm levels, shows a significant amount of probability density transported across the barrier at points of intersection of angled barriers. The transmission Wave number $k_{tot} = 0.05$ nm^{-1}, wave packet width $\sigma = 100$.

We conclude that the given potential barrier configuration is able to effectively confine charge carriers in unmodified monolayer graphene.

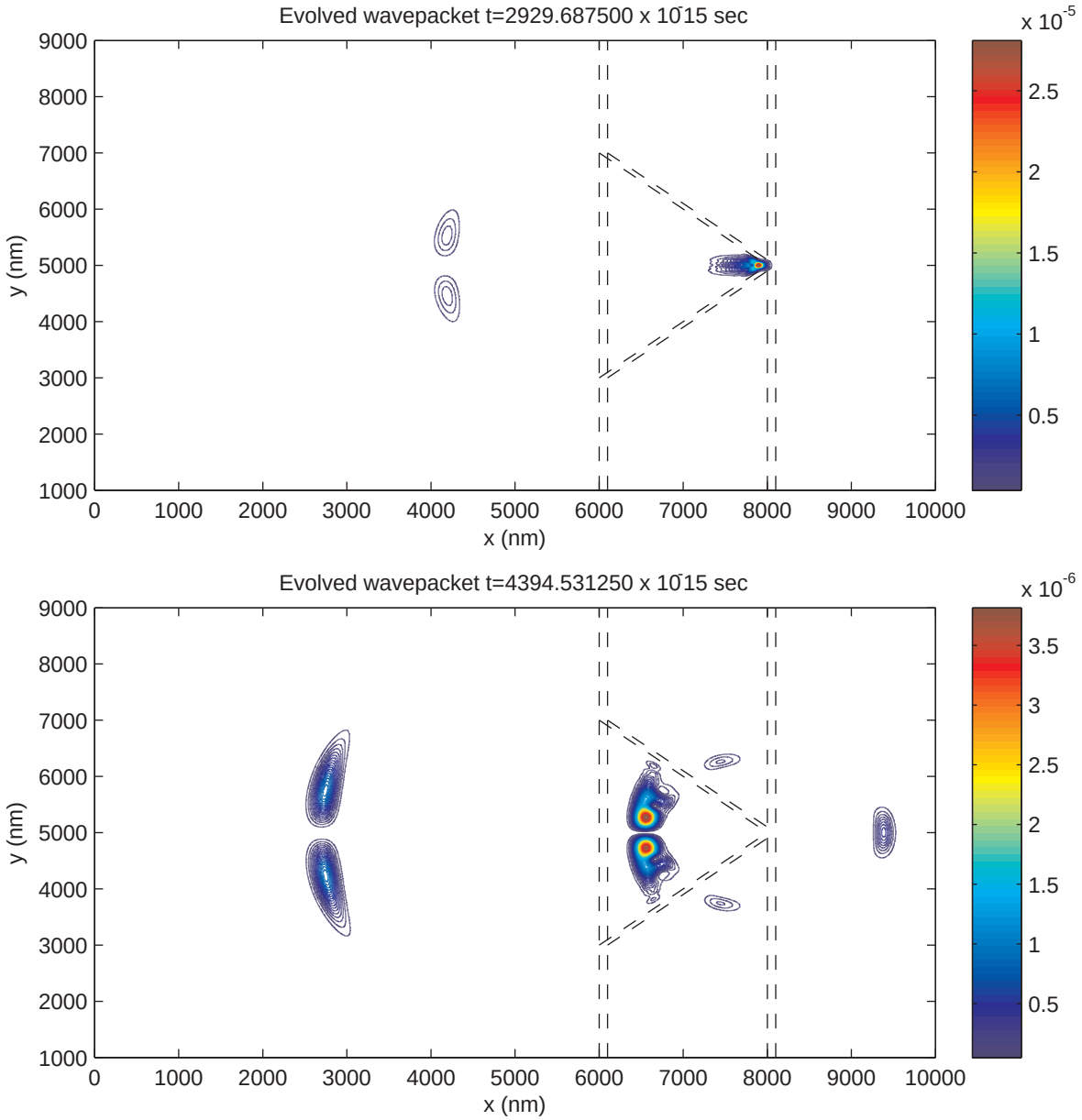

Figure 6.9: Transmission of wave packet through multiple barriers at 45° to each other, incident at the intersection of the angled barriers and the second vertical barrier, shown at two successive moments. The second plot shows a significant portion of probability density transmitted through the complete barrier configuration. Wave number $k_{tot} = 0.05$ nm^{-1}, wave packet width $\sigma = 100$.

In the beginning of the chapter we quoted a $10^4 - 10^7$ ratio of on/off current required for logic operation of field effect transistors and low enough power consumption. Using the transmission probabilities we can estimate the current that would flow through our potential configuration. The current is proportional to the conductance

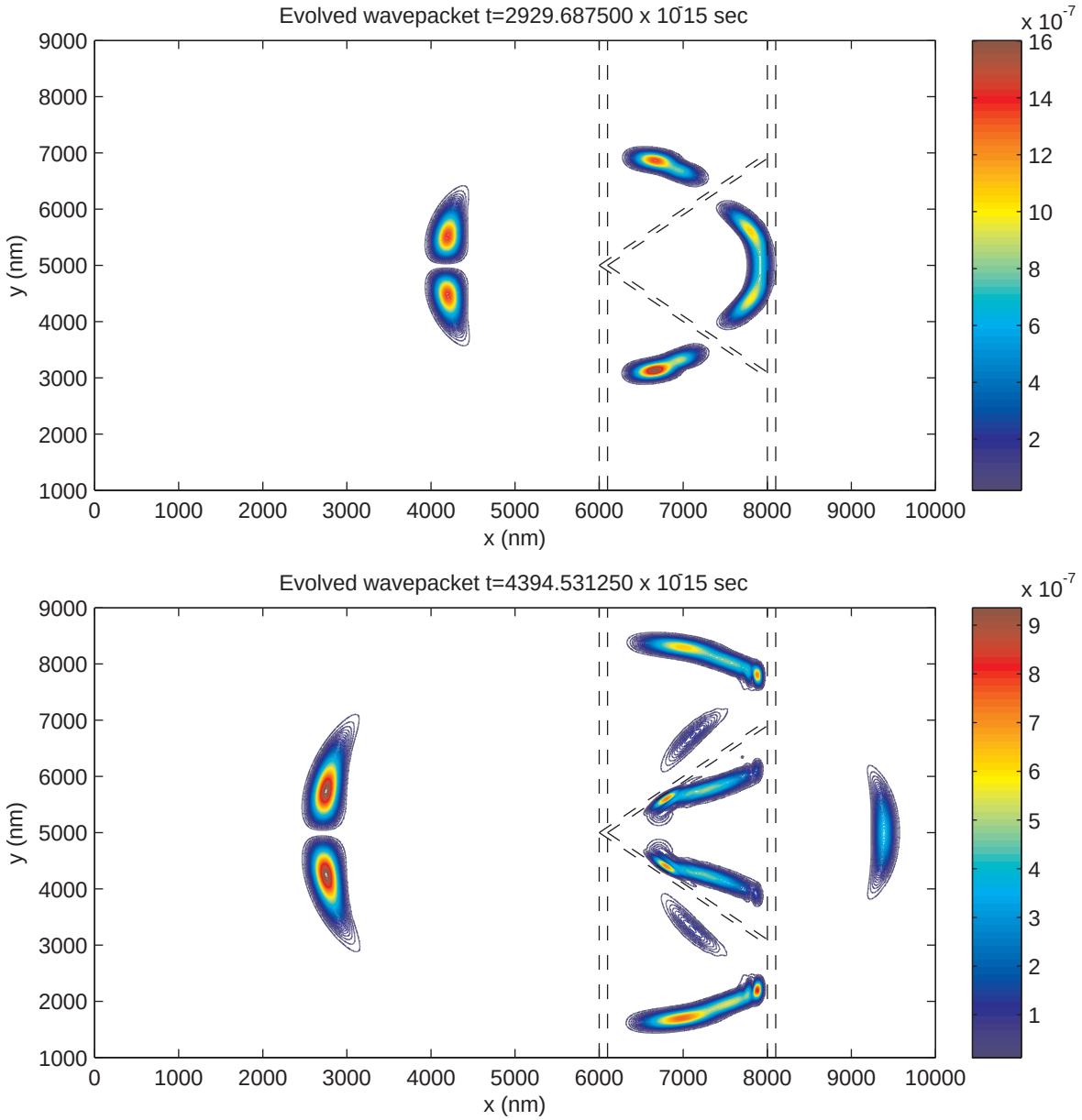

Figure 6.10: Transmission of wave packet through multiple barriers at 45° to each other, incident at the intersection of the angled barriers and the first vertical barrier, shown at two successive moments. The second plot shows a significant portion of probability density transmitted through the complete barrier configuration. Wave number $k_{tot} = 0.05$ nm^{-1}, wave packet width $\sigma = 100$.

$G = I/V$, where V is the voltage applied across the transistor that causes the current to flow through the conducting channel. Conductance per unit length is calculated from the transmission coefficient, and is given by the Landauer formula [30, 57],

$$g_{np} = \frac{4e^2}{h} \int_{-\pi/2}^{\pi/2} \frac{k_{tot} T(\theta)}{2\pi} d\theta, \tag{6.4}$$

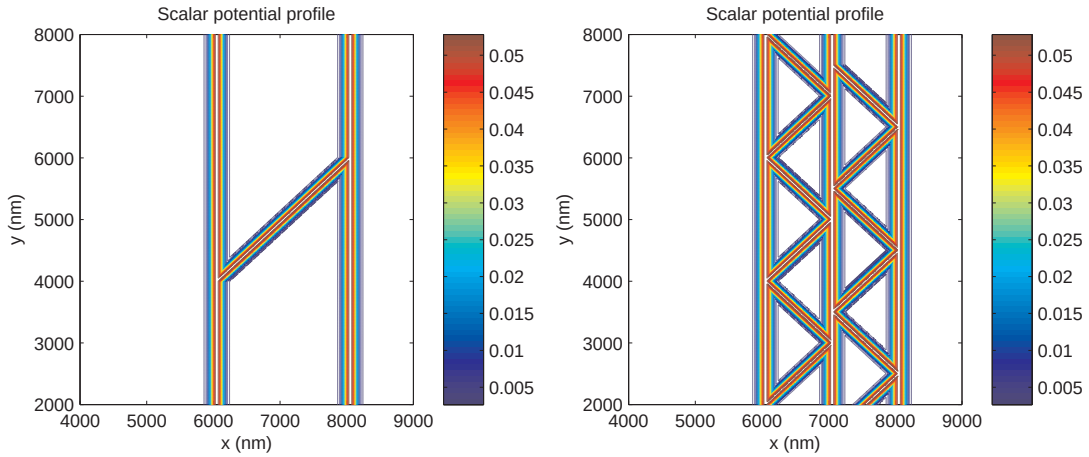

Figure 6.11: Contour plots of the potential barrier structures to block the transmission of charge carriers in graphene. On the left, a single angled barrier, at 45° to the bounding vertical barriers across the width of the graphene sheet, with edges assumed at $y = 4000$ nm and $y = 6000$ nm. On the right, a pair of potential configurations made up of successive barriers placed at an angle of 45° to each other, with the second part vertically shifted by half of the width, in our case 500 nm.

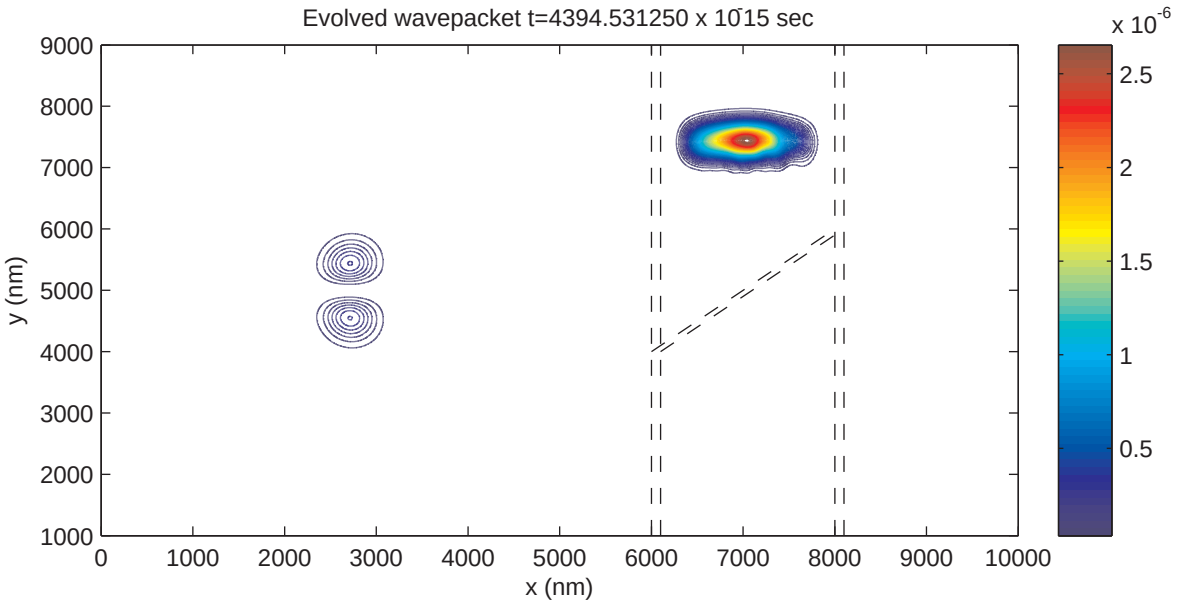

Figure 6.12: Transmission of a wave packet normally incident onto a potential configuration with a single angled barrier, at 45° to the bounding vertical barriers. No transmission through the potential configuration takes place, and assuming the edges of graphene (at $y = 4000$ nm and $y = 6000$ nm) reflect the wave packet, the probability density will be sent back towards the initial position. Wave packet width $\sigma = 250$, wave number $k_{tot} = 0.05$ nm^{-1}.

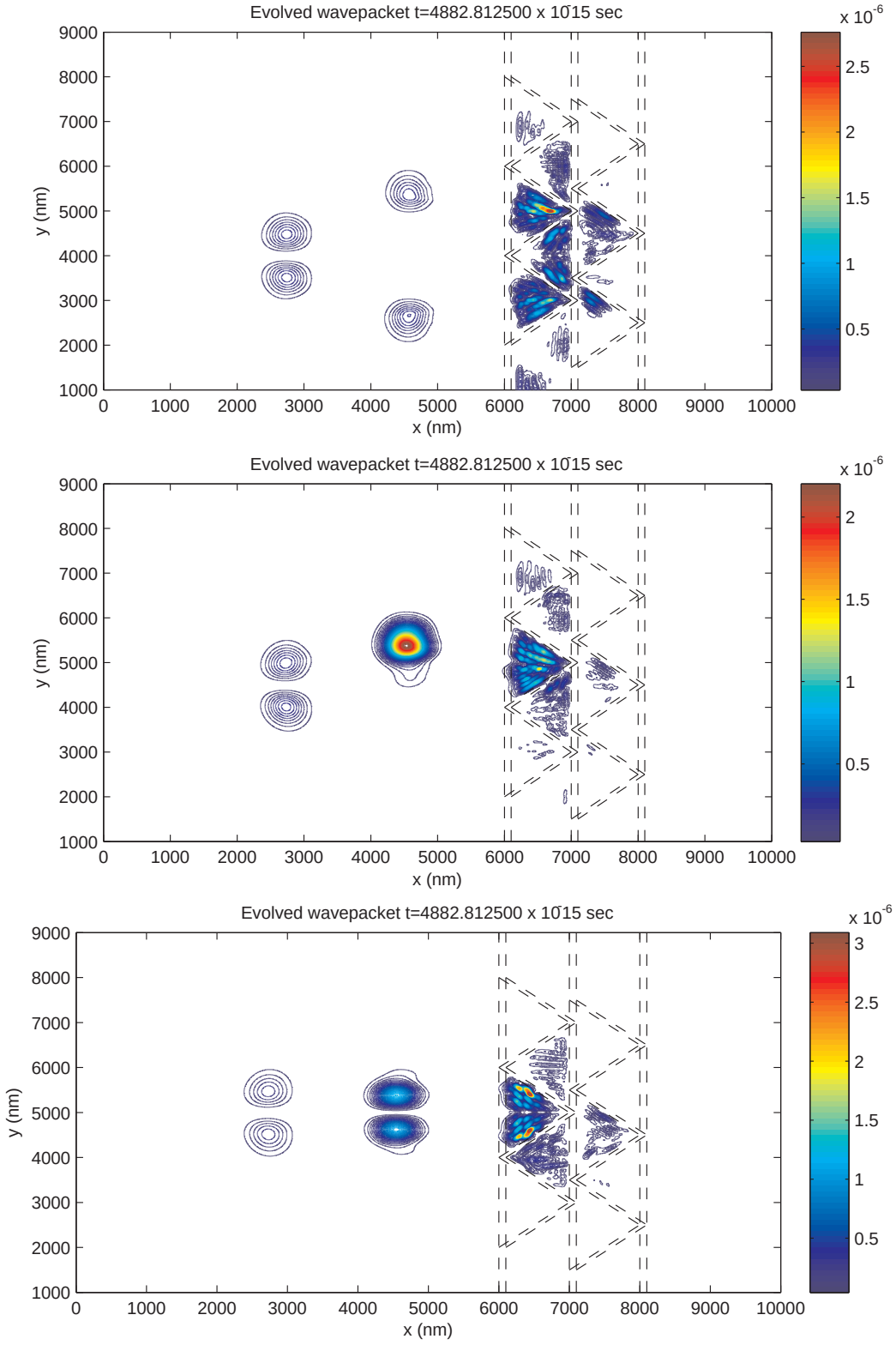

Figure 6.13: Transmission of wave packet normally incident at $y = 4000$ nm (top), $y = 4500$ nm (middle), and $y = 5000$ nm (bottom) onto a potential barrier configuration with multiple barriers at 45° to each other. Results show no significant transmission in all three cases. Wave packet width $\sigma = 250$, wave number $k_{tot} = 0.05$ nm^{-1}.

where the factor of 4 is due to the valley and spin degeneracy of charge carriers in graphene. The total conductance of a junction is given by $G = g_{np}W$, where W is the width of the current carrying graphene piece. In our simulations this is equal to about $2000 - 3000$ nm - the distance along the y-axis between the assumed edges of the graphene sheet.

Above we have shown that normal incidence onto a pair of smooth barriers positioned at an angle of 45° to each other will generate the highest transmission coefficient. The transmission coefficient in that case was found to be on the order of 10^{-4}, and if we assume that wave packets incident at all angles will generate equally high transmission, we can say that the ratio of on/off currents will be at least on the order of 10^4, assuming perfect transmission for all incidence angles in the absence of the barrier. This is the 'worst case scenario' for the ability of the potential configuration to confine charge carriers. However we know that at non-zero incidence angles the transmission is depressed significantly. To obtain more quantitative results for our particular system we simulate wave packets incident onto the last potential configuration (given in the second plot of Figure 6.11) and calculate $T_{total}(\phi)$. The results are given in the first plot of Figure 6.14, and show the expected decay of the transmission probability, reaching $T_{total} \approx 10^{-10}$ at 45° incidence. To give an approximate Figure for the ratio of on/off current generated by the randomly directed incident charge carriers according to the Landauer formula (6.4), we integrate the transmission results in Figure 6.14 by adding up the areas of the rectangular regions given by the product of the transmission coefficient at each incidence angle and the difference in angles and divide the conductance for perfect transmission by the result to get

$$\frac{I_{on}}{I_{off}} = 3.7598 \times 10^4. \tag{6.5}$$

This is an approximate measure, due to the finite end time of our simulations (although running the simulations for longer periods did not show significant growth of the transmitted probability density beyond the barrier), ignoring the possible complex interactions at the edges of the conducting channel, and discretization errors (which can be reduced by running on a larger grid). However, it does show charge confinement, and tuning the potential height and shape will allow us to decrease the transmission coefficients even further.

We also demonstrate the effect of a lower Fermi energy on the transmission coefficient by running simulations of wave packets with smaller wave numbers normally

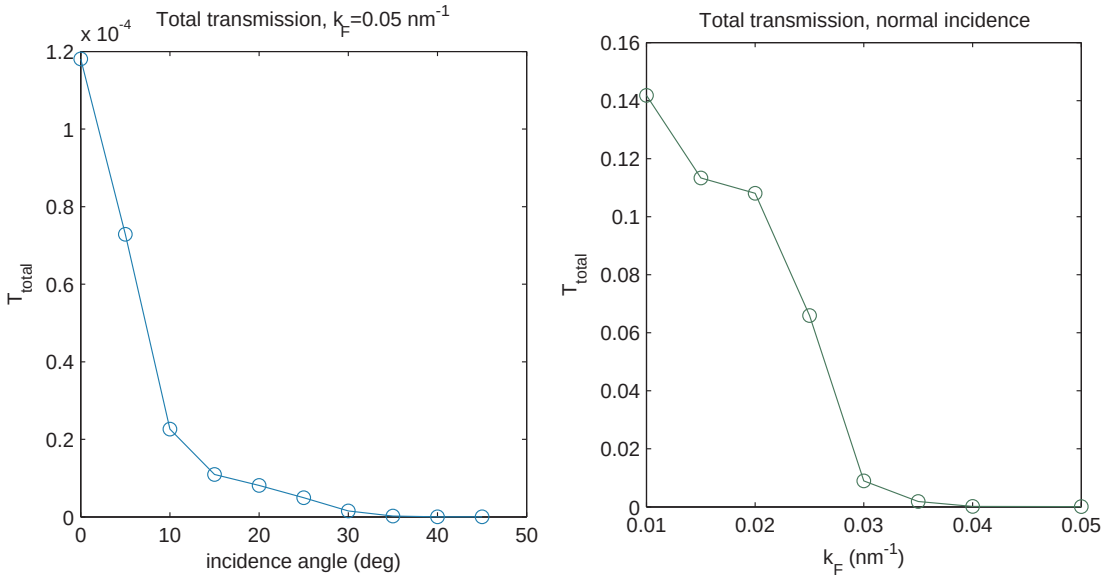

Figure 6.14: Total transmission of a wave packet through a potential configuration for a range of incidence angles (left). The plot shows rapidly decaying transmission probability through the complex potential structure for non-normal incidence, as expected. Total transmission of a wave packet through a potential configuration for a normally incident wave packet for a range of particle energies (right). As the wave number decreases and the wave length becomes comparable to the distance over which the potential increases, the barrier becomes 'sharp' for the incident wave packet and allows greater transmission. Both sets of simulations are run with a wave packet width $\sigma = 250nm$, incident at $y = 4500$ nm level.

incident onto the same potential as above. The resulting transmission coefficients are shown in the second plot of Figure 6.14 and display a switch in the way the wave packet sees our sloping potential. As the mean wave length of the wave packet increases, a greater part of the wave numbers making up the wave packet switch from seeing the potential as smooth to seeing it as a sharp barrier, thus allowing greater transmission. The transmission begins to increase at $k_{tot} = 0.03$ nm^{-1} when the tails of the wave packet begin to see the barrier as sharp, and when the wave length reaches 66 nm ($k_{tot} = 0.015$ nm^{-1}), the barrier becomes sharp for most of the wave packet and the transmission probability surpasses 0.10. To avoid excessive transmission through a confining potential the Fermi energy should be balanced against the height of the potential and the distance between the top gate and the back gate that will determine the distance over which the barrier reaches its maximum height. For example, increasing the potential height of our barrier configuration from $V_0 = 0.10$ nm^{-1} to $V_0 = 0.12$ nm^{-1} will reduce the transmission of a normally incident wave packet from

$T_{total} = 1.18076 \times 10^{-4}$ to $T_{total} = 4.38109 \times 10^{-5}$, as the barrier becomes significantly larger than the energy of the incident wave packet. However increasing the potential height further, up to $V_0 = 0.15$ nm^{-1}, while keeping the potential smoothness parameter s and the particle energy constant, causes the transmission coefficient to grow to $T_{total} = 7.5897 \times 10^{-4}$, due to the barrier becoming sharper and the system moving from a mode of tunnelling by evanescent waves, where higher potential dampens the transmission, to a mode of Klein tunnelling, where a higher potential may increase transmission. To better understand these complex effects we run a set of simulations of a wave packet normally incident onto single smooth barrier with the same parameters for wave packet and barrier width as before, adjusting the potential height and smoothness. We see that increasing the potential height increases the transmission coefficient, as the barrier becomes sharper for the incoming wave packet. However, if we increase the smoothness parameter along with the potential height to preserve the effective slope of the barrier, the transmission coefficient decreases

It is important to note that the above results are not intended to provide an exact specification for graphene device design, with well defined parameters of barrier width, height, slope and angle between them, particle energy or charge densities. Instead we demonstrate the viability of the idea to confine the flow of charge carriers in unmodified monolayer graphene with a configuration of potential barriers, and this research can be continued with experimental verification of the simulated effects in simple graphene devices.

Chapter 7

Non-linear Dirac equation

Optical lattices can be used to create artificial systems of ultra-cold atoms for study of quantum effects. In particular a hexagonal 'honeycomb' lattice of fermions could produce an analog of the electronic structure of graphene [45]. Bosons in a hexagonal optical lattice, however, can be used to create a Bose-Einstein condensate that is described by a massless Dirac-like equation similar to graphene with the addition of a non-linear term [45]. In this short chapter we investigate whether the QLB scheme can be expanded to solve this non-linear Dirac equation and, as a result, become a tool for simulation of these systems. The original QLB scheme has been applied to simulation of Bose-Einstein condensates governed by the Gross-Pitaevskii equation - a non-linear form of the Schrödinger equation - by Succi and Palpacelli [79, 80], and application of the QLB scheme to a Bose-Einstein condensate in an optical lattices governed by a non-linear Dirac equation would form a logical step, as we use it to solve the governing non-linear equation directly instead of approaching the solution with half of the wave function components generated by the simulation.

An optical lattice is constructed with counter-propagating interfering lasers that create a regular grid of standing waves based on their wavelengths and power, serving as a lattice of potential wells that is occupied by atoms as they are cooled and trapped in by radiation-induced forces [8]. To generate a hexagonal lattice the direction of the laser beams should be separated by 120 degrees, and to obtain the desired non-linear Dirac equation structure the particles are first cooled into the lowest energy state and then translated to the Dirac point corresponding to the Dirac cone by tuning the relative phases of the laser beams [46].

The non-linear Dirac equation describing the wave function on a hexagonal optical lattice is derived by Haddad and Carr [45], starting with the second quantized

Hamiltonian for a bosonic gas in two dimensions,

$$\hat{H} = \int d^2 r \hat{\psi}^* H_0 \hat{\psi} + \frac{g}{2} \int d^2 r \hat{\psi}^* \hat{\psi}^* \hat{\psi} \hat{\psi}, \qquad H_0 = -\frac{\hbar^2}{2m} \bigtriangledown^2 + V(r) \tag{7.1}$$

with the wave function $\hat{\psi} = \hat{\psi}_A + \hat{\psi}_B$ expanded in terms of Bloch states,

$$\hat{\psi}_A = \sum_A \hat{a} e^{ik\cdot(r-r_A)} u(r - r_A), \qquad \hat{\psi}_B = \sum_B \hat{b} e^{ik\cdot(r-r_B)} u(r - r_B), \tag{7.2}$$

where r_A and r_B are the positions of the A and B lattice sites, $\hat{a}$ ($\hat{a}^*$) and $\hat{b}$ ($\hat{b}^*$) are destruction (creation) operators at those sites, and $g = 4\pi\hbar^2 a_s/m$ is the coupling strength for binary contact interactions. Substituting equation (7.2) into (7.1) and simplifying to include only nearest neighbor hopping between lattice sites allows the elimination of negligible terms of same-site transitions in the integral over H_0, and elimination of terms composed of different sites in the interaction integral [45]. The resulting tight-binding approximation equation is

$$\hat{H} = -t_h \sum_{A,B} \left[\hat{a}^* \hat{b} e^{ik\cdot(r_A - r_B)} + \hat{b}^* \hat{a} e^{-ik\cdot(r_a - r_b)} \right] + \frac{U}{2} \sum_A \hat{a}^* \hat{a}^* \hat{a} \hat{a} + \frac{U}{2} \sum_B \hat{b}^* \hat{b}^* \hat{b} \hat{b}, \tag{7.3}$$

where t_h is the hopping energy, U is the interaction energy, and constant terms proportional to $\hat{a}^*\hat{a}$ and $\hat{b}^*\hat{b}$ have also been dropped because they amount to an overall constant. The time evolution of $\hat{a}$ and $\hat{b}$ operators required to obtain the non-linear Dirac equation is calculated from the Heisenberg equation of motion,

$$i\hbar \partial_t a_j = \left[\hat{a}_j, \hat{H} \right], \tag{7.4}$$

and the bosonic commutator relation satisfied by $\hat{a}_j$ and $\hat{a}_j^*$,

$$\left[\hat{a}_j, \hat{a}_{j'}^* \right] = \delta_{jj'}, \tag{7.5}$$

to obtain a pair of equations

$$i\hbar \partial_t a = -t_h \left(b_j e^{ik\cdot\delta_3} + b_{j-n_1} e^{ik\cdot\delta_1} + b_{j-n_2} e^{ik\cdot\delta_2} \right) + U a_j^* a_j a_j, \tag{7.6}$$

$$i\hbar \partial_t b = -t_h \left(a_j e^{-ik\cdot\delta_3} + a_{j+n_1} e^{-ik\cdot\delta_1} + a_{j+n_2} e^{-ik\cdot\delta_2} \right) + U b_j^* b_j b_j, \tag{7.7}$$

where a_j and b_j are expectations of the correponding operators, and δ_1, δ_2, δ_3 are the nearest neighbor vectors in the hexagonal lattice, as in graphene's lattice. In the long wavelength limit, near the corners of the Brillouin zone, the quantities a_j

and b_j can be replaced with continuous wave functions Ψ_A and Ψ_B and, after further manipulation, the equations take the form of a massless non-linear Dirac equation,

$$\left[i\partial_t + ic_s \begin{pmatrix} 0 & \partial_x - i\partial_y & 0 & 0 \\ \partial_x + i\partial_y & 0 & 0 & 0 \\ 0 & 0 & 0 & -\partial_x + i\partial_y \\ 0 & 0 & -\partial_x - i\partial_y & 0 \end{pmatrix} \right] \Psi_{NLDE} = U \begin{pmatrix} \Psi^*_{A+}\Psi_{A+}\Psi_{A+} \\ \Psi^*_{B+}\Psi_{B+}\Psi_{B+} \\ \Psi^*_{B-}\Psi_{B-}\Psi_{B-} \\ \Psi^*_{A-}\Psi_{A-}\Psi_{A-} \end{pmatrix} \tag{7.8}$$

where $\Psi_{NLDE} = [\Psi_{A+}, \Psi_{B+}, \Psi_{B-}, \Psi_{A-}]^T$ is the four component wavefunction, with subscripts A and B referring to the two sublattices, as in graphene's structure. As before, $\boldsymbol{\sigma}$ represents the x and y Pauli matrices, and $c_s = \sqrt{3}t_h a/2\hbar$ is the effective speed of sound in the lattice, on the order of cm/s in Bose-Einstein condensates. This is the complete four component version of the non-linear Dirac equation (NLDE) that takes into account wave functions at both corners of the Brillouin zone, designated by plus and minus subscripts. The top two and bottom two components describe the wave function at the inequivalent points $\boldsymbol{K}$ and $-\boldsymbol{K}$, and are coupled only to each other. We thus can separate the equation in two and write the two component wave equation,

$$\left[i\partial_t + ic_s \begin{pmatrix} 0 & \partial_x - i\partial_y \\ \partial_x + i\partial_y & 0 \end{pmatrix} \right] \begin{pmatrix} \Psi_{A+} \\ \Psi_{B+} \end{pmatrix} = U \begin{pmatrix} \Psi^*_{A+}\Psi_{A+}\Psi_{A+} \\ \Psi^*_{B+}\Psi_{B+}\Psi_{B+} \end{pmatrix}. \tag{7.9}$$

It is of the same form as the two-component Dirac-like equation for free charge carriers in graphene, with the addition of a non-linear term. The streaming matrices are diagonalizable, so that we can stream the components along each axis after transforming the wave function, and can solve the equation using the QLB approach. The details of this derivation are described in the next section.

7.1 QLB scheme for non-linear Dirac equation

To derive a QLB scheme for the NLDE we follow the same approach as we did for graphene in section 5.2, breaking up (7.9) into streaming along x, streaming along y, and collision equations,

$$\partial_t \begin{pmatrix} \Psi_{A+} \\ \Psi_{B+} \end{pmatrix} + c_s \begin{pmatrix} 0 & 1 \\ 1 & 0 \end{pmatrix} \partial_x \begin{pmatrix} \Psi_{A+} \\ \Psi_{B+} \end{pmatrix} = 0 \tag{7.10}$$

$$\partial_t \begin{pmatrix} \Psi_{A+} \\ \Psi_{B+} \end{pmatrix} + c_s \begin{pmatrix} 0 & -i \\ i & 0 \end{pmatrix} \partial_y \begin{pmatrix} \Psi_{A+} \\ \Psi_{B+} \end{pmatrix} = 0, \tag{7.11}$$

$$\partial_t \begin{pmatrix} \Psi_{A+} \\ \Psi_{B+} \end{pmatrix} = -iU \begin{pmatrix} \Psi^*_{A+}\Psi_{A+}\Psi_{A+} \\ \Psi^*_{B+}\Psi_{B+}\Psi_{B+} \end{pmatrix}. \tag{7.12}$$

We can solve the streaming equations (7.10) and (7.11) exactly by diagonalizing them and presenting as shifts of the wave function along the x and y axis, as before,

$$X^{-1}_{NL} M_x X_{NL} = Y^{-1}_{NL} M_y Y_{NL} = \begin{pmatrix} 1 & 0 \\ 0 & -1 \end{pmatrix}, \tag{7.13}$$

where the required diagonalization matrices are the same as for monolayer graphene in equations (5.38) and (5.39).

We can solve the non-linear collision equation (7.12) exactly in polar coordinates. Expressing the complex wave function values as $\Psi_{A+} = r_{A+}e^{i\theta_{A+}}$, and similarly for the other three components, each of the components of equation (7.12) becomes

$$e^{i\theta_{A+}}\partial_t r_{A+} + i r_{A+} e^{i\theta_{A+}} \partial_t \theta_{A+} = -iU r^3_{A+} e^{i\theta_{A+}} \tag{7.14}$$

$$\partial_t r_{A+} = 0 \qquad r_{A+}\partial_t \theta_{A+} = -U r^3_{A+} \tag{7.15}$$

The solutions for r_{A+} and θ_{A+} are equal to

$$r_{A+}(t) = C_1 \qquad \theta_{A+}(t) = C_2 - UC_1^2 t, \tag{7.16}$$

and similarly for the other component. The collision evolution for each wave function component is then given by

$$\Psi_i(x,y,t+\Delta t) = |\Psi_i(x,y,t)| \cos\left[\tan^{-1}\left(\frac{Im[\Psi_i(x,y,t)]}{Re[\Psi_i(x,y,t)]}\right) - U|\Psi_i(x,y,t)|^2 \Delta t\right] +$$

$$i|\Psi_i(x,y,t)| \sin\left[\tan^{-1}\left(\frac{Im[\Psi_i(x,y,t)]}{Re[\Psi_i(x,y,t)]}\right) - U|\Psi_i(x,y,t)|^2 \Delta t\right], \tag{7.17}$$

for $i = A_+, B_+$. Because the phase change with each timestep is given by the absolute value of the wave function, and the absolute value is constant, this evolution is equivalent to multiplication by a collision matrix

$$Q_{NL} = \begin{pmatrix} e^{-iU|\Psi_{A+}(t)|^2\Delta t} & 0 \\ 0 & e^{-iU|\Psi_{B+}(t)|^2\Delta t} \end{pmatrix} \tag{7.18}$$

Therefore, each of the equations (7.10), (7.11), (7.12) is solved exactly and the only source of error is due to the splitting and sequential application of each evolution. We use the same second order accurate Strang splitting coupled with half-step shifting that we derived for graphene in section 5.2,

$$\Psi\left(t_f\right) = \bar{Y}_{NL}^{-\frac{1}{2}} \left[\bar{Y}_{NL} Q_{NL}^{\frac{1}{2}} \bar{X}_{NL} Q_{NL}^{\frac{1}{2}}\right]^n \bar{Y}_{NL}^{\frac{1}{2}} \Psi\left(0\right), \tag{7.19}$$

where $t_f = n\Delta t$ and

$$\bar{X}_{NL} = X_{NL} S^x X_{NL}^{-1} \qquad \bar{Y}_{NL} = Y_{NL} S^y Y_{NL}^{-1}. \tag{7.20}$$

The collision matrix $Q_{NL}^{1/2}$ is given by the set of equations (7.17) with $\Delta t/2$. However an exact solution of the non-linear collision equation (7.12) is not required generate a collision matrix for the QLB scheme, and may not be available for other equations. We can represent the non-linear term as an external potential, so that the collision equation (7.12) becomes

$$\partial_t \Psi_i = -iU g_i \Psi_i, \tag{7.21}$$

where the potential $g_i = \Psi_i^* \Psi_i$ is constant inside each timestep, but is recalculated for each timestep based on the values of the wave function components, as it would be in a standard QLB simulation with a time-dependant potential $g\left(t\right)$ that would be evaluated at discrete times. The evolution by collision matrix Q_{NL} for one timestep in this case is given by

with $\Delta t/2$ in case of $Q_{NL}^{1/2}$ collision for half a timestep.

To test the QLB algorithm for the non-linear Dirac equation we initialize with $\Psi_{A+}\left(0\right)$ given by a Gaussian wave packet and the rest of the wave function components set to zero, the other parameters are set to $U = 1$ and $c_s = 1$. We compare the cross sections of the probability density $|\Psi|^2$ across the center of the domain, along x and y axes run at a range of resolutions. The differences in the cross sections along x axis (top panel) and y axis (bottom panel) are plotted in Figure 7.1, and we see evidence of first order convergence one plot and second order convergence in the second plot. For more conclusive evidence of convergence we compare the total of the differences in the probability density across the whole domain,

Grid sizes	Difference	Reduction factor
$\sum_y \sum_x \|\Psi\|^2_{250} - \|\Psi\|^2_{500}$	0.05777129184	–
$\sum_y \sum_x \|\Psi\|^2_{500} - \|\Psi\|^2_{1000}$	0.01431934630	4.03
$\sum_y \sum_x \|\Psi\|^2_{1000} - \|\Psi\|^2_{2000}$	0.00357220550	4.01

and see clear second order convergence. This approach of using the non-linear term as an external potential is also applicable to the Gross-Pitaevskii equation - a non-linear form of the Schrödinger equation - where the non-linear term is also a function of the absolute value of the wave function [110].

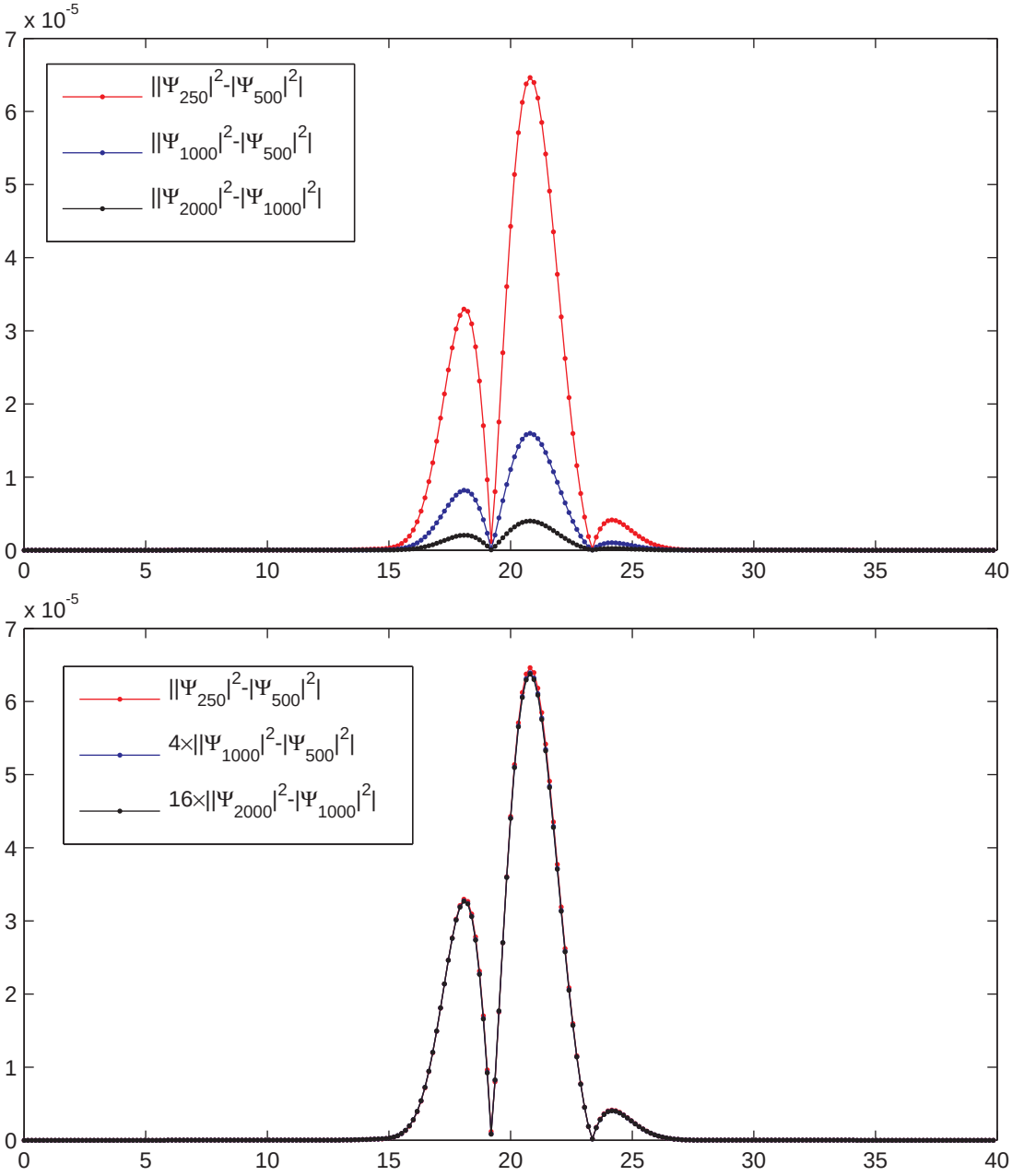

Figure 7.1: Difference in cross sections of probability density along the x axis given by simulation for a range of grid resolutions, from 250×250 to 2000×2000. The differences are scaled by the ratio of grid resolutions in the bottom panel, confirming second order convergence.

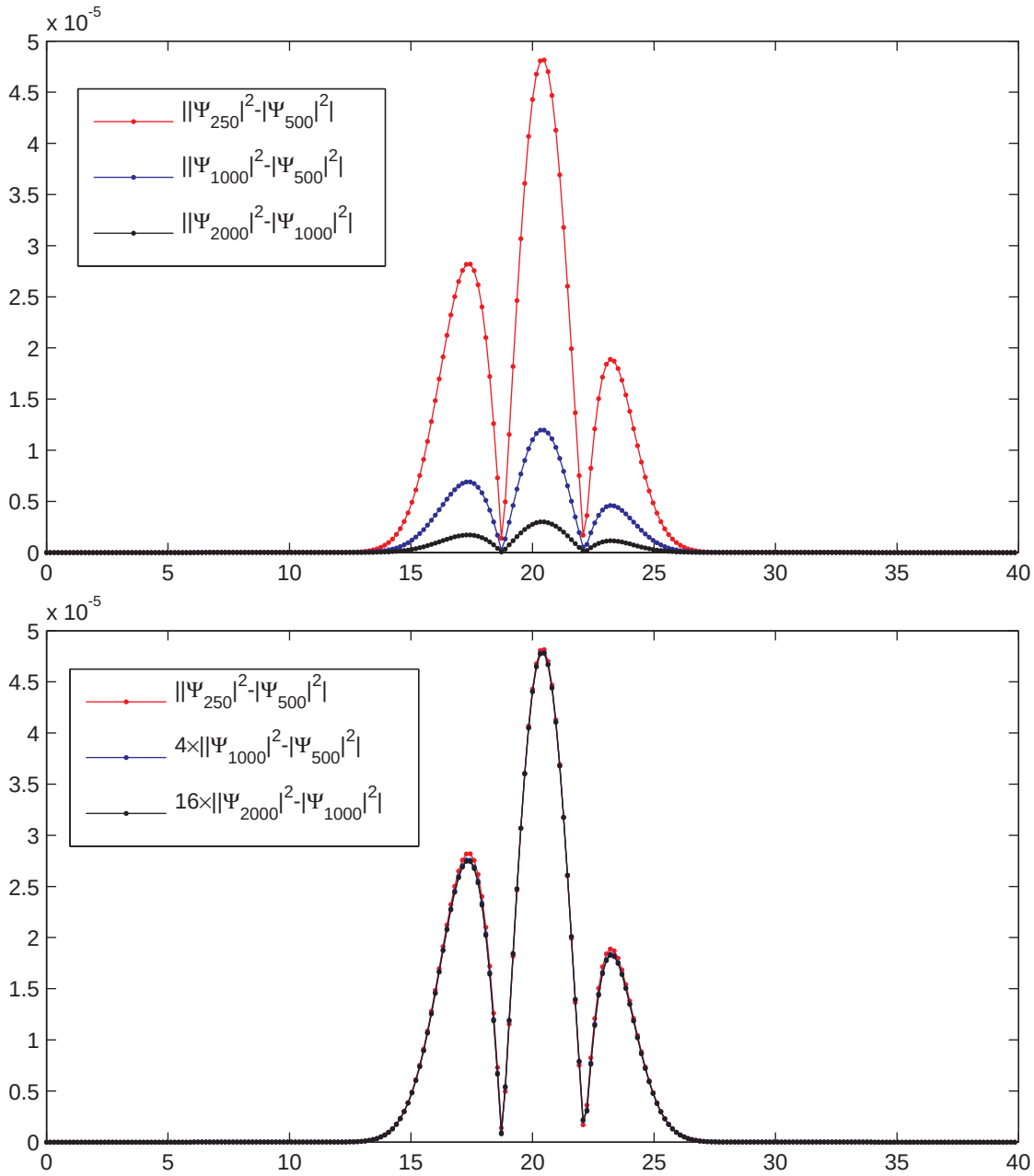

Figure 7.2: Difference in cross sections of probability density along the y axis given by simulation for a range of grid resolutions, from 250×250 to 2000×2000. The differences are scaled by the ratio of grid resolutions in the bottom panel, confirming second order convergence.

Chapter 8

Conclusion

8.1 Summary of completed research

We have investigated the derivation and convergence of the one dimensional Succi-Benzi QLB scheme for both a free particle and a particle in a spatially varying potential. To perform careful error analysis of the original QLB scheme we derived exact solutions for the behaviour of individual Fourier modes and compared with the corresponding evolution of a free particle under the QLB scheme. We found the scheme to be generally first order accurate, except the error in the ϕ^+ component, that follows evolution by the Schrödinger equation, under a special case initialized with $d_0 = -iu_0$.

However, initializing with $d_0 = -iu_0$ has the effect of setting the negative energy wave function ϕ^- to zero in the initial conditions, which is inconsistent with the adiabatic relation between ϕ^- and ϕ^+ that is a condition of the non-relativistic limit of the Dirac equation. As a result, initializing with $d_0 = -iu_0$ generates oscillations in the simulated solution around the analytic solution of the Schrödinger equation. A consistent choice of initial conditions reduces the high frequency component of the oscillations.

We show that the original QLB scheme may be derived as a discretisation of the one-dimensional Dirac equation by integrating along characteristics, using different characteristics for the streaming and collision terms, and this difference explains the generic first order accuracy of the QLB scheme. By consistently integrating along the same characteristic for both streaming and collision terms we derive an alternative, second order accurate, discretisation of the Dirac equation. Introducing new variables $\overline{u}$ and $\overline{d}$ by a transformation analagous to change of variables from f_i to $\overline{f}_i$ in

hydrodynamic lattice Boltzmann we transform the equations from an implicit into an explicit system.

The resulting second order accurate QLB scheme turns out to be identical in form to the original Succi-Benzi scheme, but expressed in terms of the "barred" variables $\overline{u}$ and $\overline{d}$ instead of the original variables u and d. After suitable scaling, the two sets of variables are related by a unitary "barring matrix" B, so we may readily invert the transformation to recover u and d from $\overline{u}$ and $\overline{d}$.

The same analysis extends to the Dirac equation with a scalar external potential. For the case of a constant potential we can find exact solutions for Fourier modes as before. For the case of spatially varying potentials, comparison between the original QLB scheme and highly accurate spectral solutions of the Dirac equation shows that the original QLB scheme reduces to first order accuracy even with the special initialisation of $d_0 = -iu_0$.

By integrating along characteristics, we again derive a second order accurate QLB scheme, which transforms into the original scheme expressed in terms of a set of "barred" variables $\overline{u}$ and $\overline{d}$. The barring matrix cannot now be exactly rescaled into a unitary matrix, but it may be approximated to second order in Δt by a unitary matrix. Numerical experiments confirm that the resulting scheme is second-order accurate even for spatially varying potentials for which the Fourier mode analysis becomes intractable due to the coupling between modes caused by the potential.

Having performed the error analysis of the QLB scheme, we isolated two sources of error when applied to simulation of the Schrödinger equation, identified the effects of incorrect initialization, and achieved second order convergence to the solution of the Dirac equation. Given these results, we find the QLB scheme to be more suitable for simulation of relativistic quantum systems governed by the Dirac equation. Therefore, further research focused on using the QLB scheme to simulate and study quantum electrodynamical effects in systems that are free from the limits of low particle energies and potentials in the non-relativistic approximation.

We have applied the second order quantum lattice Boltzmann simulation method to a system of electron scattering by a potential step, as governed by the Dirac equation, and compared the results with theoretical expectations and previous numerical results. Although previously only applied for simulation of the Schrödinger equation, the method was shown to correctly reproduce relativistic quantum tunneling effects, and the Klein paradox predicted by the Dirac equation in particular. The

transmission coefficient of the simulated wave packet was shown to converge to the theoretical wave packet transmission coefficient. Our second order QLB simulations also reproduced the same qualitative behaviour as that obtained by numerical solutions of Nitta, Kudo and Minowa [44], as well as the expected behaviour of Klein tunneling through a sloping potential. We have also run simulations to study the Zitterbewegung osicllations of wave packets due to interaction of positive and negative energy components, predicted by quantum electrodynamics, and were able to show the same dependance on particle mass and momentum as demonstrated in the recent first experimental observation of the Zitterbewegung effect.

Upon considernig the multidimensional QLB scheme, we found from Succi and co-workers that their extension of the QLB scheme to three dimensions suffered from assymetric evolution along the three coordinate axes. We identified the source of error to be incorrect application of the transformation matrices to the wave function when aligning the Dirac equation along each axis. We corrected the ordering of rotation matrices to recover isotropy of the multidimensional QLB scheme, showed its first order convergence to spherical symmetry and the error for the free particle case. We have improved the accuracy of the operator splitting by using a second order exponential splitting to evolve the wave function along each axis, and together with the four-component version of the "barring" transformation obtained a second order accurate multidimensional QLB scheme. Based on the standard form of the Dirac equation, we have also derived a more accurate initialization of u_1, u_2, d_1, d_2 components for given positive and negative energy wave functions $\phi^+_{1,2}$ and $\phi^-_{1,2}$. The QLB scheme can now be applied for accurate simulation of two and three dimensional quantum systems governed by the Dirac equation.

With the scheme now able to accurately simulate multidimensional systems, we applied it to graphene - a newly discovered two dimensional material made up of a single layer of carbon atoms. Its charge carriers are governed by a Dirac-like equation and exhibit properties of relativistic quantum systems in a 'table top' experimental enviroment, providing an exciting platform for study of quantum electronynamics. For graphene the first approach was using a unitary transformation to apply the one dimensional QLB scheme based on the Majorana form of the Dirac equation to simulation of massless charge carriers governed by the Dirac-like equation in two dimensions, and studied the transmission probability of wave packets due to Klein tunnelling across potential barriers in graphene. For more accurate simulation of wave

packets in graphene we derived a two dimensional second order QLB scheme based on the equation governing massless charge carriers at low energies, shown it to correctly simulate free wave packets and wave packet transmission coefficients, and analyzed the dependance of the wave packet transmission probability on the incidence angle, wave packet width and barrier height. We also expanded the QLB scheme for graphene to include non-zero vector potentials and confirmed its second order of convergence by comparing with spectral solutions, allowing the QLB scheme to simulate external magnetic fields and pseudo-magnetic fields caused by mechanical stress in graphene.

Once the QLB scheme was shown to give accurate evolution of wave packets in graphene, we used it to study the possibility of confining charges using configurations of multiple potential barriers in graphene devices, with potential application in graphen-based field-effect transistors. Electronic and material properties of graphene make it an excellent substitue for silicon in transistors, but due to the massless nature of graphene's charge carriers and relativistic Klein tunnelling effects it is very difficult to block the flow of current without complex modifications of the graphene sheet that give the charge carriers a non-zero effective mass. We wanted to try and block the flow of current using only scalar potentials in unmodified graphene monolayer, and, using multiple smooth barriers generated by top-gates placed at angles to each other, we were able to demonstrate transmission coefficients on the order of 10^{-4} in bulk graphene. This translates into a ratio of on and off currents that is enough for operation of field effect transistors in logic application, and it possible to reduce the transmission even further with careful parameter adjustement. Besides further simulations with different set of parameters, the next step in this direction of research would be experimental testing of charge transfer through smooth sloping barriers in simple graphene devices. We have discussed this approach to charge confinement with material scientists working with graphene at University of Oxford, and they agreed that it was an interesting set up for experimentation. To isolate the effects of the barriers the graphene samples should be of equally high quality with minimal deffects that may affect the direction of charges. Once the effects of a single smooth barrier placed at angle across the graphene sheet are confirmed, additional barriers can be added to the device to test the charge-confining ability of multiple barriers predicted by simulations. The distance between successive potential barriers should also be on the order of the mean free path of the charge carriers, determined by the quality of the graphene sample, to preserve the ballistic regime of the charge transfer.

To test the limits of the scope of quantum systems that can be solved with the quantum lattice Boltzmann scheme, we investigated the applicability of the QLB scheme to simulation of charge carriers in bilayer graphene and Bose-Einstein condensates in hexagonal optical lattices. The bilayer graphene is a more complex system, with a greater number of neighboring nodes available for the charge carriers to move across, and a complex Hamiltonian in the low energy approximation. Only by ignoring the small hopping energies, as frequently done in the literature, do we get a Dirac-like equation with diagonalizable streaming matrices that can be numerically solved using the QLB method. We also investigate the application of the QLB scheme for solution of the non-linear Dirac equation governing Bose Einstein condensates in hexagonal optical lattices and derive the scheme using an exact solution of the non-linear collisions that are represented as a time-dependant external potential. Implimenting the non-linear Dirac QLB algorithm we confirm its second order accuracy.

The result of our research is the development of a framework for a flexible numerical scheme, in the spirit of the Quantum Lattice Boltzmann method orginally proposed by Succi and Benzi, that is able to tackle a variety of problems to a high degree of accuracy without excessive computational times, and is a strong alternative to the traditional spectral schemes used for numerical solutions of systems governed by the Dirac equation.

8.2 Possibilities for further research

With the QLB scheme now generating correct solutions in multiple dimensions and converging more rapidly with the refinement of the grid, it would be interesting to compare its performance with other ways of simulating systems governed by the Dirac equation, extend it to simulate more complex quantum electrodynamical systems, and apply it to more physical cases. As a Dirac equation solver, the QLB scheme has many potential areas of application and with more work we hope the explicit, unitary, and unconditionally stable quantum lattice Boltzmann scheme can become a succesful method of simulating quantum systems in the same way that the hydrodynamic lattice Boltzmann has taken up its place as an alternative to traditional computational fluid dynamics. Below we outline possible directions of further research that will develop the scheme and allow us to gain new insight in these areas.

8.2.1 Investigation of QLB with time-dependant potentials

Although the scheme is derived for scalar and vector potentials that can be dependant on time, at each timestep they are approximated by constant values. All our simulations were done for constant potentials, and in the Strang splitting the collisions are done in two parts at each timestep with a streaming step between them. Given that set up, it would be useful to study whether the same constant potential value could be used in both collisions matrices of a single timestep, or whether a combination of multiple potential values should be used inside one timestep to maintain second order accuracy. Alternatively, use of parallel splitting in case of time dependant potentials can be investigated.

8.2.2 Simulation of massive charge carriers in graphene

Graphene research is very active and we think the QLB method is well suited for simulation of this material. As we noted before, electrons in single layer graphene are governed by a massless Dirac equation. However, the application of massive two dimensional QLB to graphene is also possible – as we have described in chapter 6, there are many efforts to induce a finite bandgap in graphene, making its dispersion relation no longer linear in momentum [91], instead the Hamiltonian they satisfy is given by

$$\boldsymbol{H} = -iv_F\boldsymbol{\sigma}\cdot\nabla \pm \Delta\sigma^z, \tag{8.1}$$

where Δ is equal to half of the induced gap in graphene spectrum, and the energy eigenvalues are then given by

$$E_k = \lambda\sqrt{v_F^2k^2 + \Delta^2} \tag{8.2}$$

and the charge carriers are no longer effectively massless. This is an even more natural application for the QLB scheme than unmodified monolayer graphene, as it was originally developed for the Dirac equation with non-zero mass.

8.2.3 Application to high-energy laser particle acceleration

One particular field where a numerical solution of the Dirac equation is necessary is acceleration of electrons and other particles by intense laser fields. For weak lasers of today, or most powerful lasers several years back, the behaviour of electrons could be treated with the Schrödinger equation [71]. In this mode several effects of laser could

be neglected - the magnetic component of the electromagnetic field generated by the laser, the spin of the particle, and relativistic kinematic effects [21]. Non-relativistic treatment stops being reliable as laser intensity approaches $10^{17} - 10^{18}\ W/cm^2$ and resulting velocity of the electrons approaches the order of the speed of light [12], and today much higher intensities are possible. Magnetic field effects become relevant as the strength of the external electromagnetic field becomes very high and the Dirac equation, accounting for relativistic effects, is required to study the behaviour of such systems. We have expanded the QLB scheme to include non-zero vector potentials so that it can be used to study these effects.

Bibliography

[1] N. Dombey A. Calogeracos. History and physics of the Klein paradox. *Contemp. Physics*, **40**:313–321, 1999.

[2] Takashi Abe. Derivation of the lattice Boltzmann method by means of the discrete ordinate method for the Boltzmann equation. *J. Comput. Phys.*, **131**(1):241–246, 1997.

[3] P. E. Allain and J-N. Fuchs. Klein tunnelling in graphene: optics with massless electrons. *The European Physical Journal B*, **83**:301–317, 2011.

[4] U. Becker, N. Grün, W. Scheid, and G. Soff. Nonperturbative treatment of excitation and ionization in $u^{92+} + u^{91+}$ collisions at 1 GeV/amu. *Phys. Rev. Lett.*, **56**:2016–2019, May 1986.

[5] V. B Berestetskii, E. M. Lifshitz, and L. P. Pitaevskii. *Quantum Electrodynamics. Landau and Lifshitz course of theoretical physics.* Elsevier, Oxford, 2008.

[6] P. L. Bhatnagar, E. P. Gross, and M. Krook. A model for collision processes in gases. I. small amplitude processes in charged and neutral one-component systems. *Physical Review*, **94**:511–525, May 1954.

[7] I. Bialynicki-Birula. Weyl, Dirac, and Maxwell equations on a lattice as unitary cellular automata. *Phys. Rev. D*, **49**:6920–6927, Jun 1994.

[8] I. Bloch. Ultracold quantum gases in optical lattices. *Nat. Phys.*, **1**:23–30, 2005.

[9] B. M. Boghosian and W. Taylor. Quantum lattice-gas model for the many-particle Schrödinger equation in d dimensions. *Phys. Rev. E*, **57**:54–66, Jan 1998.

[10] C. Bottcher and M. R. Strayer. Relativistic theory of fermions and classical fields on a collocation lattice. *Ann. Phys.*, **175**(1):64–111, 1987.

[11] C. Bottcher, M. R. Strayer, A. S. Umar, and P.-G. Reinhard. Damped relaxation techniques to calculate relativistic bound states. *Phys. Rev. A*, **40**:4182–4189, Oct 1989.

[12] J. W. Braun, Q. Su, and R. Grobe. Numerical approach to solve the time-dependent Dirac equation. *Phys. Rev. A*, **59**(1):604–612, Jan 1999.

[13] O. Busic, N. Grun, and W. Scheid. A new treatment of the fermion doubling problem. *Phys. Lett. A*, **254**(6):337–340, 1999.

[14] A. H Castro Neto, F. Guinea, N. M. R. Peres, K. S. Novoselov, and A. K. Geim. The electronic properties of graphene. *Rev. Mod. Phys*, **81**:109–162, 2009.

[15] J. Cayssol, B. Huard, and D. Goldhaber-Gordon. Contact resistance and shot noise in graphene transistors. *Phys. Rev. B*, **79**:075428, Feb 2009.

[16] A. Chaves, L. Covaci, Kh. Yu. Rakhimov, G. A. Farias, and F. M. Peeters. Wave-packet dynamics and valley filter in strained graphene. *Phys. Rev. B*, **82**:205430, 2010.

[17] V. V. Cheianov, V. Fal'ko, and B. L. Altshuler. The focusing of electron flow and a veselago lens in graphene p-n junctions. *Science*, **315**(5816):1252–1255, 2007.

[18] J. H. Chen, C. Jang, S. Xiao, M. Ishigami, and M. S. Fuhrer. Intrinsic and extrinsic performance limits of graphene devices on sio2. *Nature Nano*, **3**:206–209, April 2008.

[19] S. Chen and G. D. Doolen. Lattice Boltzmann method for fluid flows. *Annu. Rev. Fluid Mech.*, **30**:329–364, 1998.

[20] S. Chen, Z. Wang, X. Shan, and G. D. Doolen. Lattice Boltzmann computational fluid dynamics in three dimensions. *J. Stat. Phys.*, **68**(3/4):379–400, 1992.

[21] J. C. Csesznegi, Q. Su. Rutheford, and R. Grobe. Dynamics of wave packets in inhomogeneous and homogeneous magnetic fields. *Laser Physics*, **9**(1):41–47, 1999.

[22] S. Das Sarma, A. Shaffique, E. H. Hwang, and E. Rossi. Electronic transport in two-dimensional graphene. *Rev. Mod. Phys.*, **83**:407–470, May 2011.

[23] P. J. Dellar. Macroscopic descriptions of rarefied gases from the elimination of fast variables. *Phys. Fluids*, **19**:107101–14, 2007.

[24] P. J. Dellar. An introduction to the lattice Boltzmann method. *Presentation given at LBM Workshop in Cardiff*, September 2009.

[25] P. J. Dellar. An interpretation and derivation of the lattice Boltzmann method using Strang splitting. *Comput. Math. Applic.*, **65**:129–141, 2013.

[26] P. J. Dellar, D. Lapitski, S. Palpacelli, and S. Succi. Isotropy of three-dimensional quantum lattice boltzmann schemes. *Phys. Rev. E*, **83**:046706, Apr 2011.

[27] P. A. M. Dirac. The quantum theory of the electron. *Proceedings of the Royal Society of London. Series A*, **117**(778):610–624, 1928.

[28] D. C. Elias, R. V. Gorbachev, A. S. Mayorov, S. V. Morozov, A. A. Zhukov, P. Blake, L. A. Ponomarenko, I. V. Grigorieva, K. S. Novoselov, F. Guinea, and A. K. Geim. Dirac cones reshaped by interaction effect in suspended graphene. *Nature Physics*, **7**:701704, 2011.

[29] D. C. Elias, R. R. Nair, T. M. G. Mohiuddin, S. V. Morozov, P. Blake, M. P. Halsall, A. C. Ferrari, D. W. Boukhvalov, M. I. Katsnelson, A. K. Geim, and K. S. Novoselov. Control of graphenes properties by reversible hydrogenation: Evidence for graphane. *Science*, **323**(5914):610–613, 2009.

[30] V. I. Falko and V. V. Cheianov. Selective transmission of Dirac electrons and ballistic magnetoresistance of n-p junctions in graphene. *Phys. Rev. B*, **74**:041403, 2006.

[31] C. L. Fefferman and M. I. Weinstein. Honeycomb lattice potentials and Dirac points. *J. Amer. Math. Soc.*, **25**:1169–1220, 2012.

[32] M. D. Feit, J. A. Fleck, and A. Steiger. Solution of the Schrödinger equation by a spectral method. *J. Comp. Phys.*, **47**, 1982.

[33] G. Fiori, S. Lebegue, A. Betti, P. Michetti, M. Klintenberg, O. Eriksson, and G. Iannaccone. Simulation of hydrogenated graphene field-effect transistors through a multiscale approach. *Phys. Rev. B*, **82**, 2010.

[34] J. A. Fleck, J. R. Morris, and M. D. Feit. Time-dependent propagation of high energy laser beams through the atmosphere. *Appl. Phys.*, **10**(2):129–160, June 1976.

[35] U. Frisch, B. Hasslacher, and Y. Pomeau. Lattice-gas automata for the Navier-Stokes equation. *Phys. Rev. Lett.*, **56**(14):1505–1508, Apr 1986.

[36] M. S. Fuhrer. Graphene: ribbons piece-by-piece. *Nat. Mater.*, **9**:611–612, 2010.

[37] A. K. Geim. Graphene: Status and Prospects. *Science*, **324**(5934):1530–1534, 2009.

[38] R. Gerritsma, G. Kirchmair, F. Zahringer, E. Solano, R. Blatt, and C.F. Roos. Quantum simulation of the Dirac equation. *Nature*, **463**:pp. 68–71, Jan 2010.

[39] R. Gerritsma, B. P. Lanyon, G. Kirchmair, F. Zahringer, C. Hempel, J. Casanova, J. J. Garcia-Ripoll, E. Solano, R. Blatt, and C. F. Roos. Quantum simulation of the Klein paradox with trapped ions. *Phys. Rev. Lett.*, **106**, Feb 2011.

[40] S. J. Glass and H. Mendlowitz. Spin-flips in dirac scattering by a one-dimensional barrier. *Am. J. Phys.*, **57**:466–467, May 1988.

[41] R. V. Gorbachev, A. S. Mayorov, A. K. Savchenko, D. W. Horsell, and F. Guinea. Conductance of p-n-p graphene structures with air-bridge top gates. *Nano Letters*, **8**(7):1995–1999, 2008. PMID: 18543979.

[42] F. Guinea, M. I. Katsnelson, and A. K. Geim. Energy gaps and a zero-field quantum Hall effect in graphene by strain engineering. *Nature Physics*, **6**:30 – 33, 2009.

[43] X-X. Guo, D. Liu, and Y-X. Li. Conductance and shot noise in graphene superlattice. *App. Phys. Lett.*, **98**, 2011.

[44] H. Minowa H. Nitta, T. Kudo. Motion of a wave packet in the Klein paradox. *Am. J. Phys.*, **67.11**:966–971, 1999.

[45] L. H. Haddad and L. D. Carr. The nonlinear Dirac equation in Bose-Einstein condensates: Foundation and symmetries. *Physica D: Nonlinear Phenomena*, **238**(15):1413–1421, 2009.

[46] L. H. Haddad and L. D. Carr. Relativistic linear stability equations for the nonlinear Dirac equation in bose-einstein condensates. *arXiv:1006.3893v3*, 2011.

[47] K. Hannabuss. *An introduction to quantum theory.* Clarendon Press, Oxford, 1997.

[48] X. He, S. Chen, and G. D. Doolen. A novel thermal model of the lattice Boltzmann method in incompressible limit. *J. Comput. Phys.*, **146**:282–300, 1998.

[49] X. He and L-S. Luo. A priori derivation of the lattice Boltzmann equation. *Phys. Rev. E*, **55**(6):R6333–R6336, Jun 1997.

[50] F. J. Higuera and J. Jimenez. Boltzmann approach to lattice gas simulations. *Europhys. Lett*, **9**, 1989.

[51] Z-H. Huang, P. H. Cutler, T. E. Feuchtwang, R. H. Jr. Good, E. Kazes, H. Q. Nguyen, and S. K. Park. Computer simulation of a wave packet tunneling through a square barrier. *IEEE Trans. on Electron Devices*, **36**(11), Nov 1989.

[52] B. Huard, J. A. Sulpizio, N. Stander, K. Todd, B. Yang, and D. Goldhaber-Gordon. Transport measurements across a tunable potential barrier in graphene. *Phys. Rev. Lett.*, **92**:026807, 2007.

[53] M. Jaiswal, C. H. Lim, Q. Bao, C. T. Toh, K. P. Loh, and B. Ozyilmaz. Controlled hydrogenation of graphene sheets and nanoribbons. *ACS Nano*, **5**(2):888–896, 2011.

[54] O. Klein. Die reflexion von elektronen an einem potentialsprung nach der relativistischen dynamik von Dirac. *Z. Phys.*, **53**:157–165, 1929.

[55] P. Krekora, Q. Su, and R. Grobe. Klein paradox in spatial and temporal resolution. *Phys. Rev. Lett.*, **92**(4), Jan 2004.

[56] V. Krueckl and T. Kramer. Revivals of quantum wave packets in graphene. *New J. Phys.*, **11**:093010, 2009.

[57] R. Landauer. Spatial variation of currents and fields due to localized scatterers in metallic conduction. *IBM J. Res. Dev.*, **1**(223), 1957.

[58] D. Lapitski and P. J. Dellar. Convergence of a three-dimensional quantum lattice boltzmann scheme towards solutions of the dirac equation. *Phil. Trans. R. Soc. Lond. A*, **369**:2155–2163, 2011.

[59] D. Lapitski and P. J. Dellar. Quantum lattice boltzmann simulations of the one-dimensional klein paradox and application to monolayer graphene. *in preparation*, 2012.

[60] M.C. Lemme, T.J. Echtermeyer, M. Baus, and H. Kurz. A graphene field-effect device. *Electron Dev. Lett. IEEE*, **28**(4):282–284, 2007.

[61] Y. M. Lin, C. Dimitrakopoulos, K. A. Jenkins, D. B. Farmer, H. Y. Chiu, A. Grill, and Ph. Avouris. 100-ghz transistors from wafer-scale epitaxial graphene. *Science*, **327**(5966):662, Feb 2010.

[62] T. Low, F. Guinea, and M. I. Katsnelson. Gaps tunable by electrostatic gates in strained graphene. *Phys. Rev. B*, **93**, 2011.

[63] A. K. Geim M. I. Katsnelson, K. S. Novoselov. Chiral tunnelling and the Klein paradox in graphene. *Nature Phys.*, **2**:620–625, 2006.

[64] G. M. Maksimova, V. Ya. Demikhovskii, and E. V. Frolova. Wave packet dynamics in a monolayer graphene. *Phys. Rev. B*, **78**:235321, Dec 2008.

[65] E. McCann. Electronic properties of monolayer and bilayer graphene. *arXiv cond-mat.mes-hall 1205.4849v1*, 2012.

[66] E. McCann, D. S. L. Abergel, and V. I. Falko. Electrons in bilayer graphene. *Solid State Communications*, **143**:pp. 110–115, 2007.

[67] E. McCann and V. I. Falko. Landau-level degeneracy and quantum hall effect in graphite bilayer. *Phys. Rev. Lett.*, **96**, 2006.

[68] Guy R. McNamara and Gianluigi Zanetti. Use of the Boltzmann equation to simulate lattice-gas automata. *Phys. Rev. Lett.*, **61**:2332–2335, Nov 1988.

[69] D. A. Meyer. From quantum cellular automata to quantum lattice gases. *J. Statist. Phys.*, **85**:551–574, 1996.

[70] D. A. Meyer. Quantum mechanics of lattice gas automata: One-particle plane waves and potentials. *Phys. Rev. E*, **55**:5261–5269, 1997.

[71] G. R. Mocken, Y. I. Salamin, and C. H. Keitel. *Relativistic Quantum Dynamics in Intense Laser Fields*. Springer, Berlin, Heidelberg, 2009.

[72] S. V. Morozov, K. S. Novoselov, M. I. Katsnelson, F. Schedin, D. C. Elias, J. A. Jaszczak, and A. K. Geim. Giant intrinsic carrier mobilities in graphene and its bilayer. *Phys. Rev. Lett.*, **100**:pp. 68–71, Jan 2008.

[73] M. Mucha-Kruczynski, E. E McCann, and V. I. Falko. Electronhole asymmetry and energy gaps in bilayer graphene. *Semicond. Sci. Technol.*, **25**, 2010.

[74] C. Müller, N. Grün, and W. Scheid. Finite element formulation of the dirac equation and the problem of fermion doubling. *Phys. Lett. A*, **242**(6):245–250, 1998.

[75] K. S. Novoselov, A. K. Geim, S. V. Morozov, D. Jiang, Y. Zhang, S. V. Dubonos, I. V. Grigorieva, and A. A. Firsov. Electric field effect in atomically thin carbon films. *Science*, **306**:666–669, 2004.

[76] I. E Ovcharenko and Y. P. Stepanovsky. On some properties of 2-d Weyl equation for charged massless spin 1/2 particle. *Problems of atomic science and technology*, **N3**(1):56–60, 2007.

[77] S. Palpacelli. Results for the three-dimensional qLB model. *not published*, 2009.

[78] S. Palpacelli and S. Succi. Numerical validation of the quantum lattice Boltzmann scheme in two and three dimensions. *Phys. Rev. E*, **75**:066704–13, 2007.

[79] S. Palpacelli and S. Succi. The quantum lattice Boltzmann equation: Recent developments. *Commun. Comput. Phys.*, **4**:980–1007, 2008.

[80] S. Palpacelli, S. Succi, and R. Spigler. Ground-state computation of Bose–Einstein condensates by an imaginary-time quantum lattice Boltzmann scheme. *Phys. Rev. E*, **76**:036712–17, 2007.

[81] W. Pauli. *General Principles of Quantum Mechanics*. Springer-Verlag, Berlin HeidelBerg New York, 1980.

[82] J. M. Pereira, F. M. Peeters, A. Chaves, and G. A. Farias. Klein tunnelling in single and multiple barriers in graphene. *Semicond. Sci. Technol.*, **25**, 2010.

[83] Y. H. Qian. PhD thesis: Lattice gas and lattice kinetic theory applied to the navier-stokes equations. *Universite Pierre et Marie Curie, Paris*, 1990.

[84] Y. H. Qian, D. D'Humieres, and P. Lallemand. Lattice BGK models for navier-stokes equation. *Europhys. Lett*, **17**(6), 1992.

[85] T. M. Rusin and W. Zawadzki. Zitterbewegung of electrons in graphene in a magnetic field. *Phys. Rev. B*, **78**:125419, Sep 2008.

[86] F. Sauter. Zum "Kleinschen Paradoxon". *Zeitschrift für Physik*, **73**:547–552, 1931.

[87] A. Savchenko. Transforming graphene. *Science*, **323**:589–590, 2009.

[88] J. Schliemann. Cyclotron motion in graphene. *New J. Phys.*, **10**:043024, April 2008.

[89] F. Schwabl. *Advanced Quantum Mechanics*. Springer, 2005.

[90] F. Schwierz. Graphene transistors. *Nat. Nano.*, **5**(7):487–496, 2010.

[91] M. R. Setare and D. Jahani. Klein tunnelling of massive Dirac fermions in single-layer graphene. *Physica B: Condensed Matter*, **405**(5):1433–1436, 2010.

[92] Q. Sheng. Global error estimates for exponential splitting. *IMA J. Num. Analysis*, **14**(1):27–56, 1993.

[93] A. V. Shytov, M. S. Rudner, and L. S. Levitov. Klein backscattering and fabry-prot interference in graphene heterojunctions. *Phys. Rev. Lett.*, **101**(15), 2008.

[94] E. B. Sonin. Effect of Klein tunneling on conductance and shot noise in ballistic graphene. *Phys. Rev. B*, **79**:195438, May 2009.

[95] N. Stander, B. Huard, and D. Goldhaber-Gordon. Evidence for Klein tunnelling in graphene p-n junctions. *Phys. Rev. Lett.*, **102**:026807, 2009.

[96] G. Strang. On the construction and comparison of difference schemes. *SIAM Journal on Numerical Analysis*, **5**(3):pp. 506–517, 2008.

[97] F. W. Strauch. Relativistic quantum walks. *Phys. Rev. A*, **73**:054302, May 2006.

[98] F. W. Strauch. Relativistic effects and rigorous limits for discrete- and continuous-time quantum walks. *J. Math. Phys.*, **48**, 2007.

[99] S. Succi. Numerical solution of the Schrödinger equation using discrete kinetic theory. *Phys. Rev. E*, **53**:1969–1975, 1996.

[100] S. Succi. *The Lattice Boltzmann Equation: For Fluid Dynamics and Beyond*. Oxford University Press, Oxford, 2001.

[101] S. Succi and R. Benzi. Lattice Boltzmann equation for quantum mechanics. *Physica D*, **69**:327–332, 1993.

[102] B. Thaller. *The Dirac Equation*. Springer-Verlag, Berlin, 1992.

[103] B. Thaller. *Advanced Visual Quantum Mechanics*. Springer, New York, 2005.

[104] Miguel Alfonso Valdivieso and Jos Daniel Muñoz. Numerical comparison of 1D quantum lattice Boltzmann models. *J. Statist. Mech.: Theory & Expt.*, **2009**:P06004–8, 2009.

[105] N. G. van Kampen. Elimination of fast variables. *Phys. Rept.*, **124**:69–160, 1985.

[106] N. G. van Kampen. Chapman–Enskog as an application of the method for eliminating fast variables. *J. Statist. Phys.*, **46**:709–727, 1987.

[107] P. R. Wallace. The band theory of graphite. *Phys. Rev.*, **71.9**:622–634, 1947.

[108] X. Wang, Y. Ouyang, X. Li, H. Wang, J. Guo, and H. Dai. Room-temperature all-semiconducting sub-10-nm graphene nanoribbon field-effect transistors. *Phys. Rev. Lett.*, **100**, 2008.

[109] J. R. Williams, T. Low, M. S. Lundstrom, and C. M. Marcus. Gate-controlled guiding of electrons in graphene. *Nature Nano*, **6**:222–225, 2011.

[110] J. Yepez, G. Vahala, L. Vahala, and M. Soe. Superfluid turbulence from quantum Kelvin wave to classical Kolmogorov cascades. *Phys. Rev. Lett.*, **103**:084501, Aug 2009.

[111] A. F. Young and P. Kim. Quantum interference and Klein tunnelling in graphene heterojunctions. *Nat. Phys.*, **5**:222–226, 2009.